STRUCTURAL AND HIGH PRESSURE STUDIES OF SOME LOW AND NEGATIVE THERMAL EXPANSION MATERIALS

A Thesis
Presented to
The Academic Faculty

by

Mehmet Çetinkol

In Partial Fulfillment
of the Requirements for the Degree
Doctor of Philosophy in the
School of Chemistry and Biochemistry

Georgia Institute of Technology
December 2008

STRUCTURAL AND HIGH PRESSURE STUDIES OF SOME LOW AND NEGATIVE THERMAL EXPANSION MATERIALS

Approved by:

Dr. Angus P. Wilkinson, Advisor
School of Chemistry and Biochemistry
Georgia Institute of Technology

Dr. Jake D. Soper
School of Chemistry and Biochemistry
Georgia Institute of Technology

Dr. E. Kent Barefield
School of Chemistry and Biochemistry
Georgia Institute of Technology

Dr. Z. John Zhang
School of Chemistry and Biochemistry
Georgia Institute of Technology

Dr. Robert L. Snyder
School of Materials Science and Engineering
Georgia Institute of Technology

Date Approved: September 18, 2008

To my parents

and

my wife Özgül

ACKNOWLEDGEMENTS

First, I would like to thank my advisor Angus P. Wilkinson. This thesis would not have been possible without his encouragement, guidance, support and never-ending understanding.

I am also very grateful to all the professors of my thesis committee; E. Kent Barefield, Jake D. Soper, Z. John Zhang and Robert L.Snyder; for sharing their valuable time and for providing me with helpful feedback.

I would like to thank to the past and present members of the Wilkinson Group; Andrew C. Jupe, Tamas Varga, Kathy M. White, Mehmet N. Kütükçü, Carine Vanpeteghem, Chad Ruschman and Ben Greve; for their friendship and their invaluable support. I am especially grateful to Andrew for his unconditional help in the lab anytime of the day and sacrificing his sleep during late night data collection sessions. I will always cherish the time I spent working with Mehmet, it was the best of times.

Most of the data presented in this thesis were collected at X-Ray and neutron sources at national research laboratories. I am grateful to all the people who helped me at these facilities. I would like to thank to Peter L. Lee, Peter Chupas and Karena W. Chapman for their assistance with the synchrotron experiments at the Advanced Photon Source at Argonne National Laboratory. I thank Sarah Poulson for collection of neutron powder diffraction data at the National Institute of Standards and Technology (NIST). Some of the high pressure synchrotron x-ray diffraction work discussed in this thesis was carried out at the Cornell High Energy Synchrotron Source (CHESS). I am grateful to Chang-Sheng Zha and William A. Bassett for sharing their invaluable expertise with us.

I am really grateful to Simine Short for her great support and friendship during the time I spent at the IPNS for the He-gas cell experiments.

Finally, I would like to express my deepest gratitude to the most important person in my life. My studies at Georgia Tech would not have started or ended without the support, understanding, patience, and unconditional love of my partner in life, Özgül.

TABLE OF CONTENTS

LIST OF TABLES

LIST OF FIGURES

SUMMARY

The research presented in this thesis focuses on the structural studies and the high pressure behavior of oxide negative thermal expansion (NTE) materials that can be classified as framework materials. The reported work expands our understanding of the high pressure behavior of some low and negative thermal expansion materials, as it investigates the existence of phase transitions under pressure, the crystal structures of the new phases, and the structural compression mechanisms. The structural studies contribute to our fundamental understanding of the origin of thermal expansion and contraction.

Chapters 2 and 3 were devoted to TaO_2F which adopts the ReO_3-type cubic structure. The high pressure studies revealed a rather complicated high pressure behavior for this deceivingly simple compound. Diffraction measurements at variable temperature and high pressure indicated that pressure had a significant effect on the linear coefficient of thermal expansion for TaO_2F. The data revealed an unexpected temperature and pressure dependence for transverse displacement parameters of the O/F atoms, indicating that the local structure might not be the ideal ReO_3 type structure with 180^o angles.

In Chapters 4 - 9, compounds belonging to the $Sc_2W_3O_{12}$ family are discussed. High-pressure *in-situ* powder diffraction studies were conducted on $Zr_2WO_4(PO_4)_2$, $Zr_2MoO_4(PO_4)_2$, $Hf_2WO_4(PO_4)_2$, and $Sc_2W_3O_{12}$ in order to investigate the effects of pressure on their coefficients of thermal expansion, existence of phase transitions, phase transition pressures and structural changes associated with phase transitions. $Zr_2WO_4(PO_4)_2$, $Zr_2MoO_4(PO_4)_2$ and $Hf_2WO_4(PO_4)_2$ were studied under pressure for the

first time and the effects of cation substitution on the high pressure behavior of this structural family examined. The initial negative thermal expansion orthorhombic structure (Pnca) for $Zr_2WO_4(PO_4)_2$, $Zr_2MoO_4(PO_4)_2$ and $Hf_2WO_4(PO_4)_2$ persists to a much higher pressure when compared to $Sc_2W_3O_{12}$ and related compounds. The negative thermal expansion characteristics of these compounds are comparable to $Sc_2W_3O_{12}$, but having a first phase transition at much higher pressures is very advantageous from an applications perspective.

Chapter 10 examines the preparation and the structure of In(I)-β''-alumina. Its structure was determined by Rietveld analysis using high resolution X-ray powder diffraction data. The coordination of In(I) in this material has been found to be asymmetric.

CHAPTER 1

INTRODUCTION

1.1. THERMAL EXPANSION

Thermal expansion is somewhat overlooked but a crucially important property of materials for many engineering applications. It is well known that the majority of materials expand on heating, i.e. that their coefficient of thermal expansion is positive. The thermal expansion of a diatomic molecule is the simplest case, and it can be explained based on the asymmetric shape of a typical interatomic potential well, as shown in Figure 1.1. As energy or temperature increases, vibrations increase. Due to the asymmetry of the potential well, this will lead to an increase in time average bond distance. If the interatomic potential was perfectly harmonic, the average distance would be the same for all vibrational energies and no expansion would be observed.

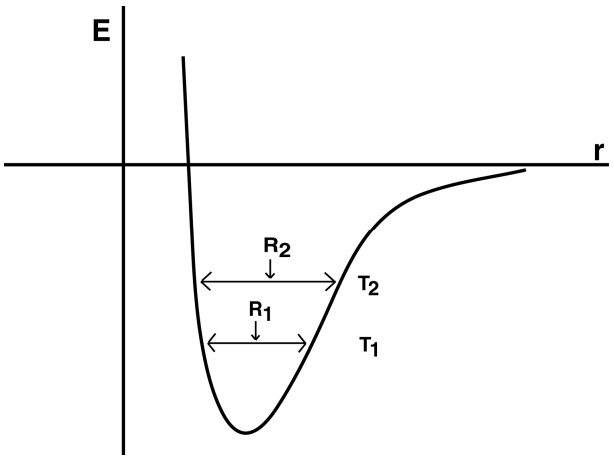

Figure1.1: Potential energy vs internuclear distance for a diatomic molecule.

For more complex systems, such as a crystalline solid, the situation becomes more complicated, the population of the entire phonon density of states as a function of temperature must be considered. In a simple sense, higher thermal energy leads to the population of higher energy vibrational modes that result in thermal expansion. In order to quantitatively measure and compare the extent of thermal expansion in solids, the thermal expansion coefficient can be calculated. The volume coefficient of thermal expansion α_V is defined as:

$$\alpha_V = \frac{d(\ln V)}{dT} = \frac{1}{V_T}\frac{d V_T}{dT}, \qquad (1)$$

where *V* is the volume and *T* the temperature. The average linear coefficient of thermal expansion (CTE) α is defined as:

$$\alpha = \frac{L - L_0}{L_0 (T - T_0)}, \qquad (2)$$

where L_0 and L are the values of the lattice constant at temperatures T_0 and T, respectively. In non-cubic materials, different values of α are usually observed for the different lattice constants. For many materials, α_V and the heat capacity C_V have a similar temperature dependence, as predicted by models for vibrations in solids[1]. The proportionality is given by the Grüneisen relationship

$$\alpha_V(T) = \frac{\gamma B_0 C_V(T)}{V_0}, \qquad (3)$$

where B_0 and V_0 are the isothermal compressibility and molar volume at T = 0 K and γ is the Grüneisen parameter. Integration gives the molar volume as a function of temperature. The variation of the molar volume with temperature is often approximated by the Debye model. Each vibrational mode has an independent Grüneisen coefficient.

As B_0 and V_0 will always have positive values, the signs of the Grüneisen parameters and the magnitude of the contribution of the associated vibrational modes to the overall expansion will determine whether a material shows positive or negative thermal expansion. Equation (3) illustrates that the expansion coefficient is not a constant, but can vary with temperature. As this variation is usually small at application temperatures, it is common to give average values of α and α_V for the temperature range over which the measurements were carried out.

Understanding and controlling the thermal expansion of materials is needed for a wide variety of applications, like cookware for oven to freezer use, electronic devices, dental applications, zero-expansion heat sinks, engine components, spark plugs, catalyst supports, high performance optical mirror substrates, etc. Understanding the origin of expansion helps design controlled thermal expansion materials.

Thermal expansion of a material can be either intrinsic or extrinsic. Intrinsic thermal expansion is based on the changes of crystallographic unit cell axes with respect to temperature and it is measured with X-ray or neutron diffraction. Intrinsic thermal expansion can be isotropic or anisotropic. Isotropic materials show the same thermal expansion in all directions; they are cubic, if crystalline, or amorphous. On the other hand; anisotropic materials have different magnitudes of thermal expansion along the different unit cell axes. When a single phase ceramic made of an anisotropic material is heated, micro cracks may form, because of the different expansion behavior of the unit cell axes. If the thermal expansion of a ceramic body is measured directly, these micro cracks affect the overall thermal expansion of the ceramic body on repeated heat treatments. Therefore, it is very hard to reproduce the same thermal expansion for the

ceramic. Materials with a high thermal expansion coefficient also show micro cracking during rapid heating or cooling. In addition, micro cracks lower the mechanical strength of the material which is undesirable. Therefore, isotropic materials with low or near-zero CTE are very important for applications.

Materials can be divided into three groups on the basis of their coefficient of thermal expansion[2]:

High Expansion Group: $\alpha > 8 \times 10^{-6} K^{-1}$

Intermediate Group: $2 < \alpha < 8 \times 10^{-6} K^{-1}$

Low Expansion Group: $\alpha < 2 \times 10^{-6} K^{-1}$

From an applications perspective, materials that belong to the low expansion group are generally the most interesting. Before the 1950s, several families of low thermal expansion materials were known. These were based on the oxides cordierite ($2MgO \cdot 2Al_2O_3 \cdot 5SiO_2$), zircon ($ZrSiO_4$) and silica glass ($SiO_2$) as well as the metal alloy Invar ($Fe_{65}Ni_{35}$). In 1948, Hummel discovered a new family of lithium aluminum silicates, β-eucryptite ($LiAlSiO_4$) and β-spodumene ($LiAlSi_2O_6$), which show negative and low thermal expansion, respectively,[3, 4] which dominated the field for almost 40 years. With the discovery of the $NaZr_2P_3O_{12}$ (NZP) family in the early 1980's [5], which shows a large tolerance towards ionic substitution and low positive to low negative thermal expansion, there was a resurgence of work on low thermal expansion materials. Some of the important low thermal expansion materials and their average coefficients of thermal expansion are listed in Table 1.1.

Table 1.1: Coefficients of thermal expansion for some low CTE materials[2]

Material	Average CTE ($^oC^{-1}$ x 10^{-6})	Temperature range (^oC)
Beryl, $Be_3Al_2Si_6O_{18}$	2.0	25-1000
Cordierite, $Mg_2Al_4Si_5O_{18}$	1.4	25-800
PMN, $Pb(Mg_{1/3}Nb_{1/3})O_3$	1.0	-100-100
β-Spodumene, $Li_2O{\cdot}Al_2O_3{\cdot}4SiO_2$	0.9	25-1000
$Ca_{0.75}Sr_{0.25}Zr_4P_6O_{24}$ (NZP)	0.6	25-1000
SiO_2 glass	0.5	25-1000
Zerodur	0.12	20-600
$SiO_2{\cdot}TiO_2$ glasses	0.05-(-0.03)	25-800
Invar	0.01	5-30
NZP, $NaZr_2P_3O_{12}$	-0.4	25-1000
β-Eucryptite, $Li_2O{\cdot}Al_2O_3{\cdot}2SiO_2$	-6.2	25-1000

1.2. NEGATIVE THERMAL EXPANSION

As pointed out in section 1.1, thermal expansion is a crucially important property of materials. Matching the thermal expansion of another device part can be important to avoid cracks or separation at interfaces between two materials, and zero expansion is needed when exact positioning of electronic or optical components in a device is crucial. In addition to the usual materials with positive CTEs, there are materials exhibiting negative thermal expansion (NTE). Use of NTE materials in composites may facilitate control of thermal expansion and should in principle allow the design of materials with a specific expansion coefficient anywhere between the values of the pure composite end members. That is the reason for renewed considerable interest in materials exhibiting negative thermal expansion (NTE) [6-12]. NTE compounds may find application as pure

phases and as components in composite materials with tailored thermal expansion coefficients [13-16].

The earliest observation of negative thermal expansion was probably related to the "density anomaly of water" [17]. Water has its highest density at 4 °C and therefore displays NTE between 0 and 4 °C. The first time that a solid was shown to contract on heating was in 1907, during experiments on quartz, silica glass and some metals by Scheel. His measurements in liquid air and up to 100 °C revealed that both crystalline and glassy quartz have negative expansion coefficients at low temperatures [18].

There are several materials that show NTE at low temperatures (e.g. Invar, SiO_2 glass) or over a narrow temperature range (e.g. water, Cu_2O, ferroelectric materials around their phase transition). Some materials display anisotropic expansion behavior, they contract along one or two axes and expand along the other axes, which can give rise to both small positive and small negative volume expansion (e.g. NZP and Li-Al silicates).

There are some general structural features that can be associated with compounds exhibiting low and negative thermal expansion [2], which include 1) strongly bonded polyhedra linked in three dimensions, 2) open, flexible structures, and 3) ferromagnetic or ferroelectric microdomains. Thus the linkages and rotations of the polyhedral network should also be examined when trying to understand bulk thermal expansion. An open, flexible framework of rigid corner sharing polyhedra is likely to accommodate transverse vibrational modes of the oxygen atoms, which can lead to a significant negative contribution to the thermal expansion if the Grüneisen parameters are large enough. It has been stated earlier that the signs and magnitude of the Grüneisen parameters and thus

the contribution of the associated vibrational modes to the overall expansion will determine the actual thermal expansion of the material. It has been shown for several NTE materials including cubic ZrW_2O_8, HfW_2O_8 and $ZrMo_2O_8$ that the NTE behavior is driven by low-frequency vibrational modes that are associated with large negative Grüneisen parameters [19-21]. Also, dimensional changes induced by thermal energy can be somewhat compensated if a ferroic microdomain distribution tends to change with temperature.

Recent research on oxide NTE materials has focused on materials that fall into the following five network types: the AM_2O_7 family [22-25], the AM_2O_8 family [26-29], the $A_2M_3O_{12}$ family [30-33], AO_2 networks or framework silicates and aluminophosphates (zeolites) [34-38] and AMO_5 [39, 40] networks. It should be noted that some MX_3 network structures, which also consist of rigid, corner-sharing metal-anion octahedra, show very low thermal expansion especially relative to typical metal oxides. These materials have the cubic ReO_3 structure [41] and include NbO_2F and TaO_2F [42]. While NbO_2F shows positive expansion, the value of CTE for TaO_2F is very small [42].

Several excellent reviews [6, 7, 11, 43] have been published on NTE materials and the possible mechanisms for their behavior. Here the focus is on framework materials and the most applicable NTE mechanism for them.

Framework materials feature low density three-dimensional networks of relatively rigid polyhedral units that share corners with each other. The mechanism, which can be considered the most applicable one in framework oxides exhibiting negative thermal expansion, is based on the transverse thermal motion of oxygen in M-O-M linkages (M = metal). This mechanism has been proposed to be responsible for the NTE in many

members of the AM_2O_7, AM_2O_8, $A_2M_3O_{12}$, AO_2 and AMO_5 families of materials, where the following requirements are met: a) open framework structure, b) oxygen in two-fold coordination, c) strong metal-oxygen bonds and d) rigid polyhedra that can freely tilt back and forth with little or no change in shape [7, 44].

This mechanism is relevant to basically all open framework oxide materials, where the oxygen is coordinated to just two metal atoms [7, 44, 45] where the M-O-M links are linear or close to linear. Provided that the M-O bonds in the structure are sufficiently strong and therefore show insignificant expansion (the polyhedra are rigid), the average metal-metal distance will decrease as the bridging oxygen in an M-O-M unit vibrates with increasing amplitude (see Figure 1.2). In a three dimensional solid, each vibration will result in a rocking motion of the polyhedra that are connected by the respective oxygen. For NTE to occur, all polyhedra must tilt back and forth in a cooperative fashion. Figure 1.2 depicts an example of how such a cooperative motion can result in a reduction in the average metal-metal distances.

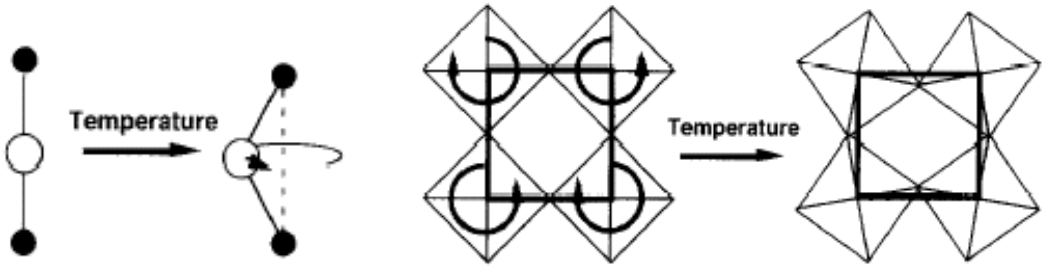

Figure 1.2: Representation of the transverse vibrational motion of an oxygen atom in a M-O-M linkage resulting in negative thermal expansion. A cooperative rotation of the polyhedral causes a decrease in the average metal-metal distances. Taken from Evans et al [46].

For a more sophisticated understanding of this mechanism, one has to consider lattice vibrational modes in the solid. Lattice vibrational modes, also called phonon modes, are cooperative vibrational modes of all atoms in a solid. If a rocking motion of the polyhedra is possible without distortions or interference with other polyhedra, a low frequency phonon mode exists that can be excited even at low temperatures [47-50]. These modes are also called "Rigid unit modes" or RUMs, as the polyhedra remain mostly undistorted (rigid). If the polyhedra in the material are essentially rigid and they can rock back and forth without significant distortions or interference with other polyhedra, then low-energy vibrational modes may be present that can result in NTE [19, 27, 48, 49, 51-53].

1.3. MATERIALS OF INTEREST

1.3.1 $Sc_2W_3O_{12}$ family of compounds

Compounds with the general formula $A_2M_3O_{12}$ (A= many 3+ ions, M= Mo or W) are known to adopt a variety of different structures depending upon the nature of A^{3+} [54-57]. The orthorhombic $Sc_2W_3O_{12}$ structure (Pnca), which is often associated with volume NTE, has been observed for A=Al, Sc, Cr, Fe, Y, In and the smaller rare earths from Lu to Ho. Some of these orthorhombic materials show anisotropic negative thermal expansion behavior. Both the a and c axes contract on heating, the b axis can either expand or contract depending on the identity of the A cation [11, 30-32, 44-46, 58, 59]. The $Sc_2W_3O_{12}$ structure consists of corner-sharing ScO_6 octahedra and WO_4 tetrahedra [56] as shown in Figure 1.3. Each ScO_6 octahedra is bound to six MO_4 tetrahedra and each MO_4 unit is connected to four ScO_6 units. It displays anisotropic thermal expansion

with the *a*- and *c*-axes contracting and the *b*-axis expanding on heating. The contraction can be viewed as arising from a dynamic cooperative tilting of the quasi-rigid polyhedral units that make up the framework [31]. The changes of the expansion behavior with the

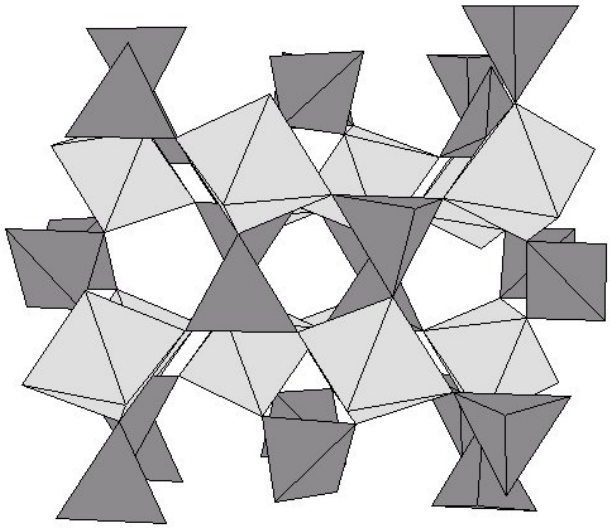

Figure 1.3: Crystal structure of orthorhombic $Sc_2W_3O_{12}$ viewed down the a axis. Octahedra (light): ScO_6; tetrahedral (dark): WO_4

A cation size are also intimately related to the $Sc_2W_3O_{12}$ structure. The b axis tend to contract when Sc is substituted with an A^{3+} ion of larger size (e.g. Y, Lu, Er, Yb) [32, 59, 60]. With an increasing size of the A^{3+} cation, the thermal contraction along the b-axis becomes more negative [60]. The reason is that $A_2M_3O_{12}$ compounds with larger A^{3+} ion size can be more flexible towards rocking motion of the polyhedra. The main force that keeps the polyhedra regular is the repulsive interaction between oxygens [61]. This interaction becomes weaker as the size of the polyhedra increases. Several members of the $Sc_2(WO_4)_3$ family have been shown to undergo a structure-collapse phase transition to

a monoclinic structure on cooling [54, 55, 57, 62, 63]. The monoclinic structure does not show negative volume expansion [62].

It is noteworthy that the anisotropic thermal expansion behavior results in different values for the CTE when it is determined by different methods. Dilatometer experiments give systematically more negative values than diffraction, suggesting that there is an intrinsic and an extrinsic contribution to the negative thermal expansion [33]. Due to the anisotropic expansion behavior, micro cracks can develop during thermal cycling of the material leading to an extrinsic negative expansion that can change between cycles. This is a hindrance from the applications point of view as the thermal expansion behavior is not necessarily repeatable as temperature is cycled.

The $Sc_2W_3O_{12}$ framework is amenable to a wide range of substitutions beyond the simple replacement of Sc^{3+} with other trivalent ions, for example, materials such as $A_2(MO_4)(PO_4)_2$ (A = Zr or Hf, M = W or Mo) [64-67], $(HfMg)(WO_4)_3$ [68-70], and $Zr_2(SO_4)(PO_4)_2$ [71] have been reported to have related structures. The wide range of possible substitutions allows for tuning of both thermal and high pressure behavior. The use of $A_2(MO_4)(PO_4)_2$ (A = Zr or Hf; M = W or Mo) in controlled thermal expansion applications is covered by several patents including [72, 73].

1.3.2 TaO_2F and NbO_2F

TaO_2F and NbO_2F were structurally characterized by Frevel and Rinn in 1956 [41]. Under ambient conditions they adopt the cubic ReO_3 structure, space group Pm-3m, which can be thought of as an undistorted ABX_3 perovskite with the A sites empty, see Figure 1.4. For both TaO_2F and NbO_2F, the O and F atoms occupy the same crystallographic site. Thus, their long range average structures are very simple.

The ReO_3 structure is relatively low in density and there is potentially considerable flexibility associated with tilting of the MO_6 octahedra. These are both characteristics typical of frameworks that show negative thermal expansion. While both ReO_3 and NbO_2F show positive thermal expansion [74, 75], TaO_2F exhibits very low thermal expansion from 20 to 400 K [75].

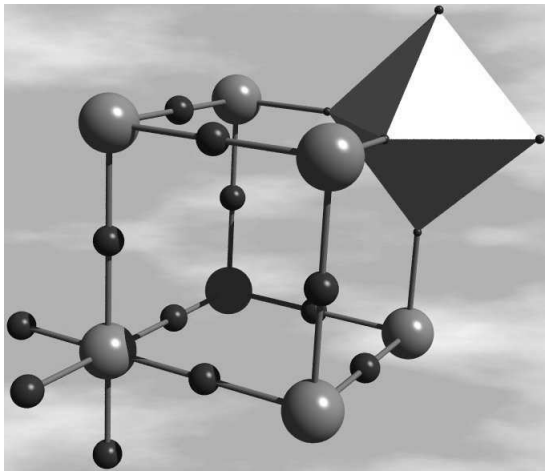

Figure 1.4: Average structure of TaO_2F and NbO_2F. Ta and Nb atoms are on the corners. O/F occupy the positions in between.

These same characteristics also predispose ReO_3 type materials to interesting behavior on modest compression. While the framework octahedra are quite rigid, the void spaces between them readily allow for volume reduction by tilting of the octahedra. Structural changes resulting from octahedral rotations in perovskite related materials have been carefully explored by several workers [76, 77].

1.4. HIGH PRESSURE BEHAVIOR OF NTE MATERIALS AND OTHER FRAMEWORK MATERIALS

NTE compounds may find application as pure phases and as components in composite materials with tailored thermal expansion coefficients [13-16]. During the manufacture and use of these materials, pressures above ambient may be encountered leading to phase transitions and a loss of NTE behavior [78, 79]. Many NTE materials have open frameworks and, owing to their flexibility and relatively low densities, commonly display crystalline-to-crystalline phase transitions [80-84], and pressure induced amorphization [80, 85-89] upon application of modest pressures. As a consequence, high pressure studies of NTE materials are of some importance from a practical standpoint as well as being of fundamental interest.

Phase transitions at pressures above ambient have been reported for many NTE materials (cubic $ZrMo_2O_8$ [80, 90], cubic $HfMo_2O_8$ [90], cubic ZrW_2O_8 [82, 91-95], cubic HfW_2O_8 [83, 96], cubic ZrV_2O_7 [97], $Sc_2Mo_3O_{12}$ [98], $Sc_2W_3O_{12}$ [99] and $Al_2W_3O_{12}$ [100, 101]). In general, these pressure-induced phase transitions involve tilting of rigid polyhedral units with an associated decrease in unit cell volume and lowering of the symmetry. From an applications perspective, the most important aspect of these phase transitions is that the linear thermal expansion coefficient exhibited by the ambient pressure structure is changed drastically. The cubic-to-orthorhombic phase transformation in ZrW_2O_8 occurring around 0.2 GPa results in a reduction of the negative coefficient of thermal expansion by almost ten-fold [82, 93]. This variation or loss of the NTE property on compression adversely affects their applicability in structural materials,

as they may be subjected to high pressures during processing of composites with tailored thermal expansion [78, 102, 103].

1.4.1 Effect of Pressure on CTE

There have been numerous studies concerning crystalline to crystalline and crystalline to amorphous phase transitions in NTE materials. These studies are important because stresses might be encountered during the manufacture and use of a controlled thermal expansion composite. In addition to leading to phase transitions and a loss of NTE behavior, the pressure (stress) might affect the coefficient of thermal expansion before any phase transitions. However, little attention has been paid to the effect of compression on the expansion coefficients of a particular phase. It was reported by Chapman and Chupas that the thermal expansion coefficient for the NTE material $Zn(CN)_2$ became more negative on compression [104]. The average linear coefficient of thermal expansion (CTE) changed from -17.4(2) $\times 10^{-6}$ K^{-1} to -19.4(2) $\times 10^{-6}$ K^{-1} on going from ambient to 0.4 GPa. From the definitions of the coefficient of thermal expansion and the bulk modulus, it has been shown that the effect of applied pressure on the expansivity of a solid is given by the following equation[105].

$$\left(\frac{\partial \alpha_V}{\partial P}\right)_T = \frac{1}{K^2}\left(\frac{\partial K}{\partial T}\right)_P , \qquad (4)$$

K is the bulk modulus. In this equation, one needs to know the temperature dependence of bulk modulous, or term $(\partial K / \partial T)_P$. Watchman et al.[106] suggested the following equation for the temperature dependence of the bulk modulus.

$$K = K_o - bTe^{(-T_0/T)}, \tag{5}$$

Where K_0 is the bulk modulus at absolute zero, T is the temperature and b and T_0 are constants. It has been theoretically shown by Anderson[107] and Garai et al. [108] that, in general, b will be positive and $(\partial K/\partial T)_P$ will be negative for materials with positive Grüneisen parameters. Grüneisen parameters are positive for materials with positive volume coefficient expansion α_V, hence pressure will decrease α_V if it is positive. For NTE materials which have negative Grüneisen parameters, α_V would increase with increasing pressure. This contradicts with the results of Chapman and Chupas [104].

1.5. REFERENCES

[1] Bruesch P. Phonons: Theory and Experiments. Berlin, Germany: Springer Verlag, 1982.

[2] Roy R, Agrawal DK, McKinstry HA. Very Low Thermal Expansion Coefficient Materials. Annu. Rev. Mater. Sci. 1989;19:59.

[3] Hummel FA. Thermal expansion properties of natural lithia minerals. Foote Prints 1948;20:3.

[4] Hummel FA. Thermal Expansion Properties of Some Synthetic Lithia Minerals. J. Am. Ceram. Soc. 1951;34:235.

[5] Boilot JP, Salanie JP, Desplanches G, Potier DL. Phase Transformation in $Na_{1+x}Si_xZr_2P_{3-x}O_{12}$ Compounds. Mat. Res. Bull. 1979;14:1469.

[6] Sleight AW. Thermal Contraction. Endeavour 1995;19:64.

[7] Sleight AW. Compounds that Contract on Heating. Inorg. Chem. 1998;37:2854.

[8] Sleight AW. Isotropic Negative Thermal Expansion. Annual Review of Materials Science 1998;28:29.

[9] Sleight AW. Negative thermal expansion materials. Current Opinion in Solid State and Materials Science 1998;3:128.

[10] Evans JSO, Mary TA, Sleight AW. Negative thermal expansion materials. Physcia B 1998;241-243:311.

[11] Evans JSO. Negative Thermal Expansion Materials. J. Chem. Soc. Dalton Trans. 1999:3317.

[12] Evans JSO, Mary TA, Sleight AW. Negative Thermal Expansion in a Large Molybdate and Tungstate Family. J. Solid State Chem. 1997;133:580.

[13] Wetherfold RC, Wang J. Tailoring thermal deformation by using layered beams. Compos. Sci. Technol. 1995;53:1.

[14] Fleming DA, Johnson DW, Lemaire PJ. Article Comprising a Temperature Compensated Optical Fiber Refractive Index Grating. USA: Lucent Technologies, 1997.

[15] Fleming DA, Lemaire PJ, Johnson DW. Temperature compensated optical fiber refractive index grating. European Patent EP 97-306798 19970902. USA: Lucent Technologies, Inc., 1998. p.7.

[16] Balch DK, Dunand DC. Copper-Zirconium Tungstate Composites Exhibiting Low and Negative Thermal Expansion Influenced by Reinforcement Phase Transformations. Metall. Mater. Trans. A 2004;35A:1159.

[17] Balashov DB, Orlov VP. Thermal anomaly of water. I. Regional boundaries. Entropy. Heat capacities. Zh. Fiz. Khim. 1983;57:2465.

[18] Scheel K. Experiments on the Expansion of Solids and Measurements of Quartz in the Direction of the Principal Axis, Platinum, Palladium, and Quartz-glass, to the Temperature of Liquid Air. Ber. physik Ges. 1907;5:3.

[19] David WIF, Evans JSO, Sleight AW. Direct evidence for a low-frequency phonon mode mechanism in the negative thermal expansion compound ZrW_2O_8. Europhys. Lett. 1999;46:661.

[20] Yamamura Y, Nakajima N, Tsuji T, Iwasa Y, Saito K, Sorai M. Heat capacity and Grüneisen function of negative thermal expansion compound HfW_2O_8. Solid State Commun. 2002;121:213.

[21] Wang K, Reeber RR. Mode Gruneisen parameters and negative thermal expansion of cubic ZrW_2O_8 and $ZrMo_2O_8$. Appl. Phys. Lett. 2000;76:2203.

[22] Korthuis V, Khosrovani N, Sleight AW, Roberts N, Dupree R, Warren WW. Negative Thermal Expansion and Phase Transitions in the $ZrV_{2-x}P_xO_7$ Series. Chem. Mater. 1995;7:412.

[23] Khosrovani N, Korthuis V, Sleight AW, Vogt T. Unusual 180^o P-O-P Bond Angles in ZrP_2O_7. Inorg. Chem. 1996;35:485.

[24] Evans JSO, Hanson JC, Sleight AW. Room-Temperature Superstructure of ZrV_2O_7. Acta Crystallogr. 1998;B54:705.

[25] Withers RL, Evans JSO, Hanson J, Sleight AW. An *In Situ* Temperature-Dependent Electron and X-ray Diffraction Study of Structural Phase transitions in ZrV_2O_7. J. Solid State Chem. 1998;137:161.

[26] Evans JSO, Mary TA, Vogt T, Subramanian MA, Sleight AW. Negative Thermal Expansion in ZrW_2O_8 and HfW_2O_8. Chem. Mater. 1996;8:2809.

[27] Mary TA, Evans JSO, Vogt T, Sleight AW. Negative Thermal Expansion from 0.3 to 1050 Kelvin in ZrW_2O_8. Science 1996;272:90.

[28] Lind C, Wilkinson AP, Hu Z, Short S, Jorgensen JD. Synthesis and Properties of the Negative Thermal Expansion Material Cubic Zirconium Molybdate. Chem. Mater. 1998;10:2335.

[29] Closmann C, Sleight AW. Low-Temperature Synthesis of ZrW_2O_8 and Mo-Substituted ZrW_2O_8. J. Solid State Chem. 1998;139:424.

[30] Evans JSO, Mary TA, Sleight AW. Negative Thermal Expansion in a Large Molybdate and Tungstate Family. J. Solid State Chem. 1997;133:580.

[31] Evans JSO, Mary TA, Sleight AW. Negative Thermal Expansion in $Sc_2(WO_4)_3$. J. Solid State Chem. 1998;137:148.

[32] Forster PM, Yokochi A, Sleight AW. Enhanced Negative Thermal Expansion in $Lu_2W_3O_{12}$. J. Solid State Chem. 1998;140:157.

[33] Mary TA, Sleight AW. Bulk thermal expansion for tungstate and molybdates of the type $A_2M_3O_{12}$. J. Mater. Res. 1999;14:912.

[34] Tschaufeser P, Parker SC. Thermal Expansion Behavior of Zeolites and $AlPO_4$s. J. Phys. Chem. 1995;99:10609.

[35] Attfield MP, Sleight AW. Strong negative thermal expansion in siliceous faujasite. Chem. Commun. 1998:601.

[36] Attfield MP, Sleight AW. Exceptional Negative Thermal Expansion in $AlPO_4$-17. Chem. Mater. 1998;10:2013.

[37] Woodcock DA, Lightfoot P, Villaescusa LA, Díaz-Cabañas M-J, Camblor MA, Engberg D. Negative Thermal Expansion in the Siliceous Zeolites Chabazite and ITQ-4: A Neutron Powder Diffraction Study. Chem. Mater. 1999;11:2508.

[38] Woodcock DA, Lightfoot P, Wright PA, Villaescusa LA, Díaz-Cabañas M-J, Camblor MA. Strong negative thermal expansion in the siliceous zeolites ITQ-1, ITQ-3 and SSZ-23. J. Mater. Chem. 1999;9:349.

[39] Amos TG, Sleight AW. Negative thermal expansion in orthorhombic $NbOPO_4$. J. Solid State Chem. 2001;160:230.

[40] Amos TG, Yokochi A, Sleight AW. Phase transition and negative thermal expansion in tetragonal $NbOPO_4$. J. Solid State Chem. 1998;141:303.

[41] Frevel LK, Rinn HW. The Crystal Structure of NbO_2F and TaO_2F. Acta Crystallogr. 1956;9:626.

[42] Tao JZ, Sleight AW. Very low thermal expansion in TaO_2F. J. Solid State Chem. 2003;173:45.

[43] Barrera GD, Bruno JAO, Barron THK, Allan NL. Negative Thermal Expansion. J. Phys. Condens. Matter 2005;17:R217.

[44] Sleight AW. Negative thermal expansion materials. Curr. Opin. Solid State Mater. Sci. 1998;3:128.

[45] Sleight AW. Isotropic Negative Thermal Expansion. Annu. Rev. Mater. Sci. 1998;28:29.

[46] Evans JSO, Mary TA, Sleight AW. Negative thermal expansion materials. Physica B 1998;241-243:311.

[47] Mary TA, Evans JSO, Vogt T, Sleight AW. Negative Thermal Expansion from 0.3 to 1050 Kelvin in ZrW_2O_8. Science 1996;272:90.

[48] Pryde AKA, Hammonds KD, Dove MT, Heine V, Gale JD, Warren MC. Origin of the Negative Thermal Expansion in ZrW_2O_8 and ZrV_2O_7. J. Phys. Condens. Matter 1996;8:10973.

[49] Pryde AKA, Hammonds KD, Dove MT, Heine V, Gale JD, Warren MC. Rigid Unit Modes and the Negative Thermal Expansion in ZrW_2O_8. Phase Transitions 1997;61:141.

[50] Heine V, Welche PRL, Dove MT. Geometrical Origin and Theory of Negative Thermal Expansion in Framework Structures. J. Am. Ceram. Soc. 1999;82:1793.

[51] Mittal R, Chaplot SL, Schober H, Mary TA. Origin of Negative Thermal Expansion in Cubic ZrW_2O_8 Revealed by High Pressure Inelastic Neutron Scattering. Phys. Rev. Lett. 2001;86:4692.

[52] Ernst G, Broholm C, Kowach GR, Ramirez AP. Phonon Density of States and Negative Thermal Expansion in ZrW_2O_8. Nature 1998;396:147.

[53] Pryde AKA, Dove MT, Heine V. Simulation studies of ZrW_2O_8 at high pressure. J. Phys.: Condens. Matter 1998;10:8417.

[54] Nassau K, Levinstein HJ, Loiacono GM. Trivalent Rare-Earth Tungstates of the Type $M_2(WO_4)_3$. J. Am. Ceram. Soc. 1964;47:363.

[55] Nassau K, Levinstein HJ, Loiacono GM. A comprehensive study of trivalent tungstates and molybdates of the type $L_2(MO_4)_3$. J. Phys. Chem. Solids 1965;26:1805.

[56] Abrahams SC, Bernstein JL. Crystal Structure of the Transition-Metal Molybdates and Tungstates. II. Diamagnetic $Sc_2(WO_4)_3$. J. Chem. Phys. 1966;45:2745.

[57] Sleight AW, Brixner LH. A New Ferroelastic Transition in Some $A_2(MO_4)_3$ Molybdates and Tungstates. J. Solid State Chem. 1973;7:172.

[58] Imanaka N, Hiraiwa M, Adachi G, Dabkowska H, Dabkowski A. Thermal contraction in $Al_2(WO_4)_3$ single crystal. J. Cryst. Growth 2000;220:176.

[59] Woodcock DA, Lightfoot P, Ritter C. Negative thermal expansion in $Y_2(WO_4)_3$. J. Solid State Chem. 2000;149:92.

[60] Sumithra S, Tyagi AK, Umarji AM. Negative thermal expansion in $Er_2W_3O_{12}$ and $Yb_2W_3O_{12}$ by high temperature X-ray diffraction. Mater. Sci. Eng., B 2005;116:14.

[61] Forster PM, Sleight AW. Negative thermal expansion in $Y_2W_3O_{12}$. Int. J. Inorg. Mater. 1999;1:123.

[62] Evans JSO, Mary TA. Structural phase transitions and negative thermal expansion in $Sc_2(MoO_4)_3$. Int. J. Inorg. Mater. 2000;2:143.

[63] Tyagi AK, Achary SN, Mathews MD. Phase transition and negative thermal expansion in $A_2(MoO_4)_3$ system (A = Fe^{3+}, Cr^{3+} and Al^{3+}). J. Alloys Compd. 2002;339:207.

[64] Tsvigunov AN, Sirotinkin VP. Preparation of $Zr_2WO_4(PO_4)_2$ and indexing of its X-ray diffraction pattern. Russ. J. Inorg. Chem. 1990;35:1740.

[65] Evans JSO, Mary TA, Sleight AW. Structure of $Zr_2(WO_4)(PO_4)_2$ from Powder X-ray Data: Cation Ordering with No Superstructure. J. Solid State Chem. 1995;120:101.

[66] Martinek CA, Hummel FA. Subsolidus Equilibria in the System ZrO_2-WO_3-P_2O_5. J. Am. Ceram. Soc. 1970;53:159.

[67] Sirotinkin VP, Tsvigunov AN. Synthesis, X-Ray-Diffraction and Thermal Analyses of $Zr_2MoO_4(PO_4)_2$. Russ. J. Inorg. Chem. 1994;39:735.

[68] Suzuki T, Omote A. Negative Thermal Expansion in $(HfMg)(WO_4)_3$. J. Am. Ceram. Soc. 2004;87:1365.

[69] Suzuki T, Omote A. Pseudo binary HfW_2O_8-$MgWO_4$ thermal expansion control system. J. Ceram. Soc. Jpn. 2006;114:833.

[70] Suzuki T, Omote A. Zero thermal expansion in $(Al_{2x}(HfMg)_{(1-x)})(WO_4)_{(3)}$. J. Am. Ceram. Soc. 2006;89:691.

[71] Piffard Y, Verbaere A, Kinoshita M. Beta - $Zr_2(PO_4)_2SO_4$ - A Zirconium Phosphato-sulfate with A $Sc_2(WO_4)_3$ Structure - A comparison between garnet, Nasicon, and $Sc_2(WO_4)_3$ structure types. J. Solid State Chem. 1987;71:121.

[72] Merkel GA. Negative Thermal Expansion Materials Including Method of Preparation and Uses Therefor. European Patent, 2001.

[73] Sleight AW, Thundathil MA, Evans JSO. Materials with Low or Negative Thermal Expansion. United States Patent, 1999.

[74] Taylor D. Thermal Expansion Data: V Miscellaneous Binary Oxides. Br. Ceram. Trans. J. 1985;84:9.

[75] Tao JZ, Sleight AW. Very low thermal expansion in TaO_2F. J. Solid State Chem. 2003;173:45.

[76] Glazer AM. Classification of Tilted Octahedra in Perovskites. Acta Crystallogr., Section B 1972;28:3384.

[77] Woodward PM. Octahedral tilting in perovskites .1. Geometrical considerations. Acta Crystallogr., Section B 1997;53:32.

[78] Holzer H, Dunand DC. Phase transformation and thermal expansion of Cu/ZrW_2O_8 metal matrix composites. J. Mater. Res. 1999;14:780.

[79] Yilmaz S. Phase transformations in thermally cycled Cu/ZrW_2O_8 composites investogated by synchrotron x-ray diffraction. J. Phys. Condens. Matter. 2002;14:365.

[80] Grzechnik A, Crichton WA. Structural transformations in cubic $ZrMo_2O_8$ at high pressures and high temperatures. Solid State Sci. 2002;4:1137.

[81] Muthu DVS, Chen B, Wrobel JM, Krogh Andersen AM, Carlson S, Kruger MB. Pressure-induced phase transitions in α–$ZrMo_2O_8$. Phys. Rev. B 2002;65:064101.

[82] Evans JSO, Hu Z, Jorgensen JD, Argyriou DN, Short S, Sleight AW. Compressibility, Phase Transitions, and Oxygen Migration in Zirconium Tungstate, ZrW_2O_8. Science 1997;275:61.

[83] Jorgensen JD, Hu Z, Short S, Sleight AW, Evans JSO. Pressure-induced cubic-to-orthorhombic phase transfromation in the negative thermal expansion material HfW_2O_8. J. Appl. Phys. 2001;89:3184.

[84] Varga T, Wilkinson AP, Lind C, Bassett WA, Zha C-S. High pressure synchrotron x-ray powder diffraction study of $Sc_2Mo_3O_{12}$ and $Al_2W_3O_{12}$ J. Phys.: Condens. Matter 2005;17:4271.

[85] Chen B, Muthu DVS, Liu ZX, Sleight AW, Kruger MB. High-pressure Raman and infrared study of HfW_2O_8. Phys. Rev. B 2001;64:214111.

[86] Perottoni CA, de Jornada JAH. Pressure-Induced Amorphization and Negative Thermal Expansion in ZrW_2O_8. Science 1998;280:886.

[87] Varga T, Wilkinson AP, Lind C, Bassett WA, Zha C-S. Pressure-induced amorphization of cubic ZrW_2O_8 studied in-situ and ex-situ by synchrotron x-ray absorption spectroscopy and diffraction. Phys. Rev. B 2005;72:024117.

[88] Varga T, Wilkinson AP, Lind C, Basset WA, Zha C-S. Pressure-induced amorphization of cubic $ZrMo_2O_8$ studied in-situ by x-ray absorption spectroscopy and diffraction. Solid State Communications 2005;135:739.

[89] Secco RA, Liu H, Imanaka N, Adachi G. Pressure-induced amorphization in negative thermal expansion $Sc_2(WO_4)_3$. Journal of Materials Science Letters 2001;20:1339.

[90] Lind C, VanDerveer DG, Wilkinson AP, Chen J, Vaughan MT, Weidner DJ. New high pressure form of the negative thermal expansion materials zirconium molybdate and hafnium molybdate. Chem. Mater. 2001;13:487.

[91] Ravindran TR, Arora AK, Mary TA. High Pressure Behavior of ZrW_2O_8: Gruneisen Parameter and Thermal Properties. Phys. Rev. Lett. 2000;84:3879.

[92] Ravindran TR, Arora AK, Mary TA. High-pressure Raman spectroscopic study of zirconium tungstate. J. Phys.: Condens. Matter 2001;13:11573.

[93] Hu Z, Jorgensen JD, Teslic S, Short S, Argyriou DN, Evans JSO, Sleight AW. Pressure-induced phase transformation in ZrW_2O_8 - Compressibility and thermal expansion of the orthorhombic phase. Physica B 1998;241-243:370.

[94] Jorgensen JD, Hu Z, Teslic S, Argyriou DN, Short S, Evans JSO, Sleight AW. Pressure -induced cubic-to-orthorhombic phase transition in ZrW_2O_8. Phys. Rev. B 1999;59:215.

[95] Gallardo-Amores JM, Amador U, Moran E, Alario-Franco MA. XRD study of ZrW_2O_8 versus temperature and pressure. Int. J. Inorg. Mater. 2000;2:123.

[96] Chen B, Muthu DVS, Liu ZX, Sleight AW, Kruger MB. High-pressure Raman and infrared study of HfW_2O_8. Phys. Rev. B 2001;64:214111.

[97] Carlson S, Krogh Andersen AM. High-pressure properties of TiP_2O_7, ZrP_2O_7 and ZrV_2O_7. J. Appl. Crystallogr. 2000;34:7.

[98] Paraguassu W, Maczka M, Souza Filho AG, Freire PTC, Mendes Filho J, Melo FEA, Macalik L, Gerward L, Staun Olsen J, Waskowska A, Hanuza J. Pressure-induced structural transformations in the molybdate $Sc_2(MoO_4)_3$. Phys. Rev. B 2004;69:094111.

[99] Varga T, Wilkinson AP, Lind C, Bassett WA, Zha C-S. In-situ high pressure synchrotron x-ray diffraction study of $Sc_2W_3O_{12}$ at up to 10 GPa. Phys. Rev. B 2005;71:214106.

[100] Maczka M, Paraguassu W, Souza Filho AG, Freire PTC, Mendes Filho J, Melo FEA, Hanuza J. High-pressure Raman study of $Al_2(WO_4)_3$. J. Solid State Chem. 2004;177:2002.

[101] Mukherjee GD, Achary SN, Tyagi AK, Vaidya SN. High pressure AC resistivity and compressibility study on $Al_2(WO_4)_3$. J. Phys. Chem. Solids 2003;64:611.

[102] Verdon C, Dunand DC. High-Temperature Reactivity in the ZrW_2O_8-Cu System. Scr. Mater. 1997;36:1075.

[103] Balch DK, Dunand D, C. Copper-Zirconium Tungstate Composites Exhibiting Low and Negative Thermal Expansion Influenced by Reinforcement Phase Transformations. Metall. Mater. Trans. A 2004;35A:1159.

[104] Chapman KW, Chupas PJ. Pressure enhancement of negative thermal expansion behavior and induced framework softening in zinc cyanide. Journal of the American Chemical Society 2007;129:10090.

[105] Touloukian YS, Kirby RK, Taylor RE, Lee TYR. Thermal Expansion: Nonmetallic Solids. New York: Plenum, 1970.

[106] Wachtman JB, Tefft WE, Lam DG, Apstein CS. Exponential Temperature Dependence of Youngs Modulus for Several Oxides. Physical Review 1961;122:1754.

[107] Anderson OL. Derivation of Wachtmans Equation for Temperature Dependence of Elastic Moduli of Oxide Compounds. Physical Review 1966;144:553.

[108] Garai J, Laugier A. The temperature dependence of the isothermal bulk modulus at 1 bar pressure. J. Appl. Phys. 2007;101:4.

CHAPTER 2

HIGH PRESSURE POWDER DIFFRACTION STUDY OF TaO_2F[1]

2.1. INTRODUCTION

TaO_2F and NbO_2F were structurally characterized by Frevel and Rinn in 1956 [1]. Under ambient conditions they adopt the cubic ReO_3 structure, space group Pm-3m, which can be thought of as an undistorted ABX_3 perovskite with the A sites empty. For both TaO_2F and NbO_2F, the O and F atoms occupy the same crystallographic site. Thus, their long range average structures are very simple.

The ReO_3 structure is relatively low in density and there is potentially considerable flexibility associated with tilting of the MO_6 octahedra. These are both characteristics typical of frameworks that show negative thermal expansion. While both ReO_3 and NbO_2F show positive thermal expansion [2, 3], TaO_2F does exhibit very low thermal expansion from 20 to 400 K [3]. These same characteristics also predispose ReO_3 type materials to interesting behavior on modest compression. While the framework octahedra are quite rigid, the void spaces between them readily allow for volume reduction by tilting of the octahedra. Structural changes resulting from octahedral rotations in perovskite related materials have been carefully explored by several workers [4, 5].

---

[1] The majority of the work presented in this chapter was previously published in Çetinkol, M., et al.,*J. Phys. Chem. Solids.*, **2007,** *68*, 611-616.

ReO_3 itself has been studied extensively at high pressure and undergoes several phase transitions, some of which are still under discussion. The first evidence of a high pressure transition came from measurements at low temperature and pressures close to 0.3 GPa [6]. X-ray diffraction at room temperature showed that the compressibility of the high pressure phase was an order of magnitude larger than that of the ambient pressure phase and the term 'compressibility collapse' was proposed [7]. Many reports on the high pressure behavior of ReO_3 subsequently appeared [8-14]. At ambient temperature ReO_3 has Pm-3m symmetry up to ~0.5 GPa, at which point it transforms to a structure with Im-3 symmetry [13]. This second cubic phase transforms into a rhombohedral phase, with R-3c symmetry, at around ~8 GPa [12]. At around 38 GPa, the R-3c phase transforms into another rhombohedral phase with the same space group. However, there is some controversy over the possible existence of a monoclinic phase between the cubic (Im-3) and first rhombohedral (R-3c) phases [11-13].

NbO_2F has been studied recently at high pressure using synchrotron powder diffraction and diamond anvil cells [15, 16]. It was reported to transform from the cubic (Pm-3m) ambient pressure structure, with a bulk modulus (K_0) of 24.8 GPa ($K_p = 4$), to a rhombohedral (R-3c) structure at 0.47 GPa [15, 16], with $K_0 \sim 9.6$ GPa ($K_p \sim 11.7$). Above 18.5 GPa amorphization was seen. While there is an increase in compressibility after going through the first phase transition on compression, it is much less dramatic than that seen for ReO_3. The transformation to the VF_3-type structure, space group R-3c, involves tilting of octahedra around one of the cubic triad axes. The volume reduction mechanism was shown to involve compression of Nb-(O/F) distances and a slight distortion of the $Nb(O/F)_6$ octahedra, in addition to octahedral tilting.

Many materials have a VF_3-type structure under ambient conditions, including AF_3 (A= Al, Cr, Fe, Ga, In, Ti, V), and they typically transform to a cubic ReO_3-type structure at elevated temperatures [17-20]. TiF_3 and FeF_3 have been studied at up to 7.67 and 9.00 GPa, respectively, and no phase transitions were observed for either compound [20]. Volume reduction on compression of these R-3c materials was attributed to the rotation of octahedra along with octahedral distortions. CrF_3 has recently been studied under pressure by time-of-flight neutron diffraction experiments up to 9.12 GPa and no structural phase transitions were observed [21].

This chapter examines TaO_2F at room-temperature and high pressure using monochromatic synchrotron powder diffraction and diamond anvil cells. The material's behavior is compared with that of its structural relatives. There have been no prior high pressure studies of this compound.

2.2. EXPERIMENTAL PROCEDURES

2.2.1 Sample Preparation

TaO_2F was prepared by dissolving Ta_2O_5 (Strem, 99.8%) in a Pt crucible with concentrated HF (Mallinckrodt, 48%) followed by slow evaporation of HF to dryness. The remaining off-white powder was transferred to a Teflon container and heated in an oven at 180 ^oC for 10 h. X-ray powder diffraction data showed it to be single phase TaO_2F.

2.2.2. Diffraction Data Collection

For the initial characterization, powder X-ray diffraction data were obtained using a Scintag X1 diffractometer equipped with a Peltier cooled solid state detector. High pressure powder diffraction data were collected at room temperature using the B-2 line of the Cornell High Energy Synchrotron Source (CHESS), Wilson Lab, Cornell University, Ithaca, NY. Data were obtained using two different diamond anvil cell (DAC) designs with different pressure-transmitting media to ensure that the effects observed by diffraction were intrinsic to the sample.

For the first series of measurements, a Hydrothermal DAC (HDAC) [22] with a rhenium gasket of initial thickness 125 μm and a hole diameter of 300 μm, was used with anhydrous isopropyl alcohol as the pressure-transmitting medium. The diamonds were 1.6 mm thick with 600 μm culets. Data were collected up to ~10.6 GPa, and then the cell was decompressed and a final data set was measured at ~0.14 GPa. Isopropyl alcohol was claimed to provide hydrostatic conditions up to 4.3 GPa [23].

For the second set of measurements, a four-post DAC with a methanol-ethanol (4:1) pressure medium was used. This DAC had 2.1 mm thick diamonds with 600 μm culet faces. A preindented fully hardened stainless steel gasket with 250 μm initial thickness and a 150 μm diameter hole was used. The methanol-ethanol (4:1) medium was claimed to be hydrostatic up to 10.4 GPa [23]. In total, 58 powder patterns were recorded on compression up to ~12.8 GPa and subsequent decompression back to ambient pressure in small steps.

For both sets of experiments, the X-ray wavelength was selected using a Ge(111) double-crystal monochromator and the beam collimated with a ~50 μm pin hole. The

first run used X-rays of wavelength 0.4940 Å, whereas the second used a wavelength of 0.4960 Å. The diffraction patterns were recorded on a Mar345 imaging plate detector. In each case, the starting pressure was ambient, as indicated by ruby fluorescence measurements, and the sample-to-plate distance was calibrated using diffraction from the TaO_2F sample. A few small ruby chips were loaded into the cells along with the samples so that the pressure could be determined using the ruby fluorescence technique [24], where pressure calibration errors of 0.05-0.1 GPa are possible [25].

2.2.3. Data Processing

The two-dimensional diffraction images were integrated using the program FIT2D [26]. I(2θ) data were initially processed in JADE [27], and then further analyzed by a combination of the Rietveld [28] and Le Bail [29] methods using GSAS [30] with the EXPGUI [31] interface. After carrying out initial Le Bail fits on the integrated patterns, it was found that a further correction, for radial offset of the read head in the Mar345 detector, had to be applied to get high quality fits. These corrected patterns were used for the final analyses.

2.3. RESULTS AND DISCUSSION

Diffraction data from the two sets of high pressure measurements are shown in Figures 2.1 and 2.2. Both show an obvious phase transition at ~0.7 GPa that is reversible on decompression, and they are generally in good agreement with one another. We primarily present an analysis of the measurements performed with a methanol-ethanol medium due to the greater number of pressure points (54 measurements) and the higher hydrostatic limit for this medium.

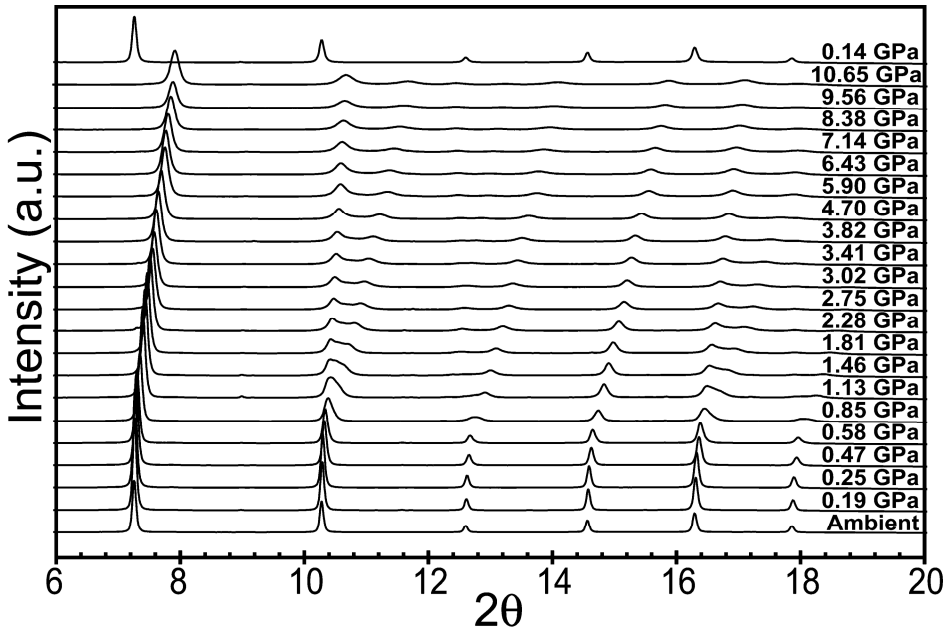

Figure 2.1: Complete set of diffraction patterns obtained with the HDAC using isopropanol as a pressure transmitting medium. The X-ray wavelength was 0.4940 Å.

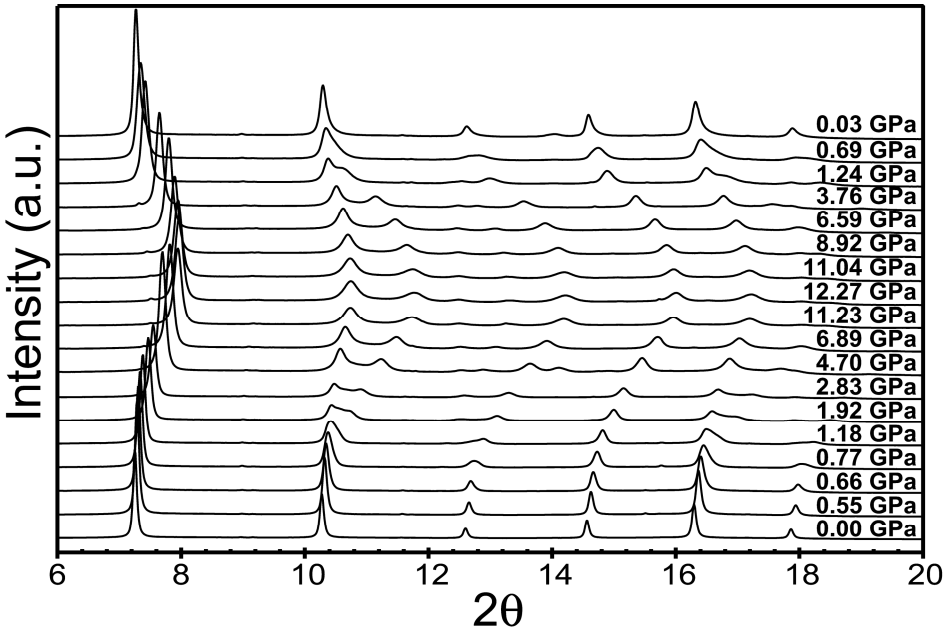

Figure 2.2: Selected diffraction patterns obtained in a 4-post DAC using methanol:ethanol (4:1) as a pressure transmitting medium. The X-ray wavelength was 0.4960 Å. The 4.70 GPa data set shows a gasket peak at $2\theta \sim 14^{o}$.

Up to ~0.7 GPa the diffraction patterns could be indexed on a cubic unit cell (Pm-3m). Above this pressure, some of the cubic peaks started to split, and a new peak emerged at around 13^{o} 2θ. This new peak indicates a unit cell volume increase on going through the transition. An examination of its intensity, normalized to that of the first peak in the diffraction patterns (Figure 2.3), suggests a phase transition onset pressure of between 0.55 and 0.66 GPa. The transition is probably largely complete by 0.66 GPa if this normalized intensity is viewed as primarily measuring the sample fraction that has been transformed.

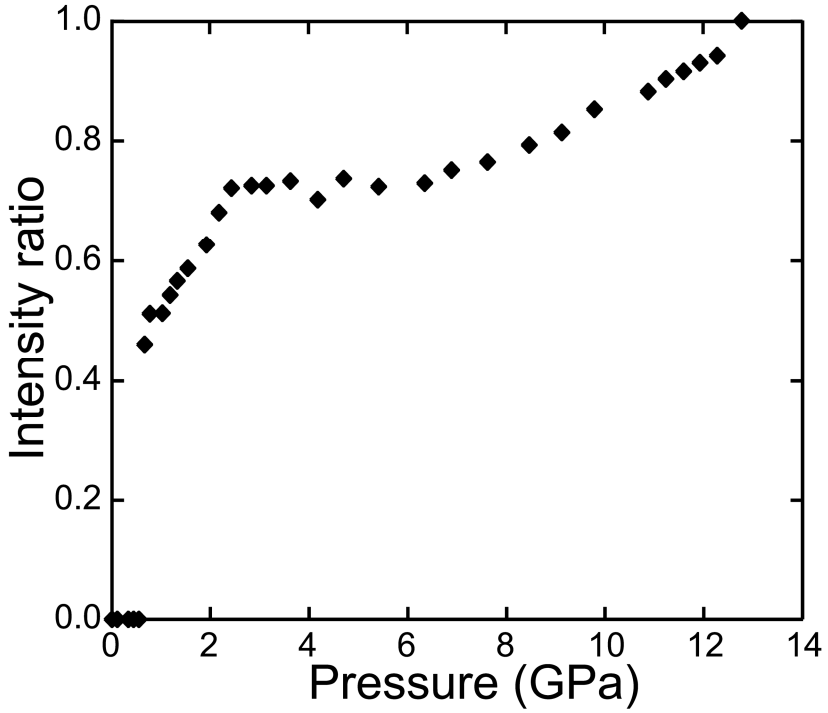

Figure 2.3: The intensity of the peak developing at 2θ ~13º on compression suggests a transition onset pressure between 0.55 and 0.66 GPa. This intensity was difficult to estimate reliably between ~1.2 and ~2.4 GPa, due to extensive overlap with another Bragg peak. To take into account differences in exposure time between diffraction images, the intensity was scaled to that of the strongest peak in the diffraction pattern. The resulting values were normalized to that for the 12.8 GPa measurement.

These values are similar to those reported for NbO_2F [15]; onset at ~ 0.3 GPa and completion at ~0.6 GPa. A transition to a VF_3 type structure with R-3c space group, as reported for NbO_2F, seemed most likely. While the major features of the data above 0.7 GPa could be explained based on a R-3c model, careful examination of the patterns showed scattering that was not consistent with single phase R-3c material. This is shown in Figure 2.4, where the cubic (110) peak is expected to split into two components during such a transition, but an additional component between the expected two is seen. The relative intensity of this "extra" scattering decreases as the pressure is increased and does not vanish until ~10.8 GPa. Interestingly, a close inspection of the diffraction data for NbO_2F given as a supplementary data to Carlson's paper [15] also seems to show some signs of "extra" scattering in this region. The diffraction data collected for TaO_2F above 10.8 GPa during compression, and on decompression down to ~4 GPa can be explained quite well with a single phase rhombohedral (R-3c) model. Below 4 GPa on decompression the "extra" scattering features reappear and remain until almost ambient pressure.

Initially, we considered the possibility that the "extra" scattering might be attributed to cubic (Pm-3m) material that had not yet transformed to the rhombohedral phase, as phase coexistence over an extended pressure range had previously been reported for cubic (Im-3) and rhombohedral (R-3c) ReO_3 [12]. However, the existence of isolated grains of cubic (Pm-3m) material above 0.7 GPa in our sample is not supported by the diffraction data.

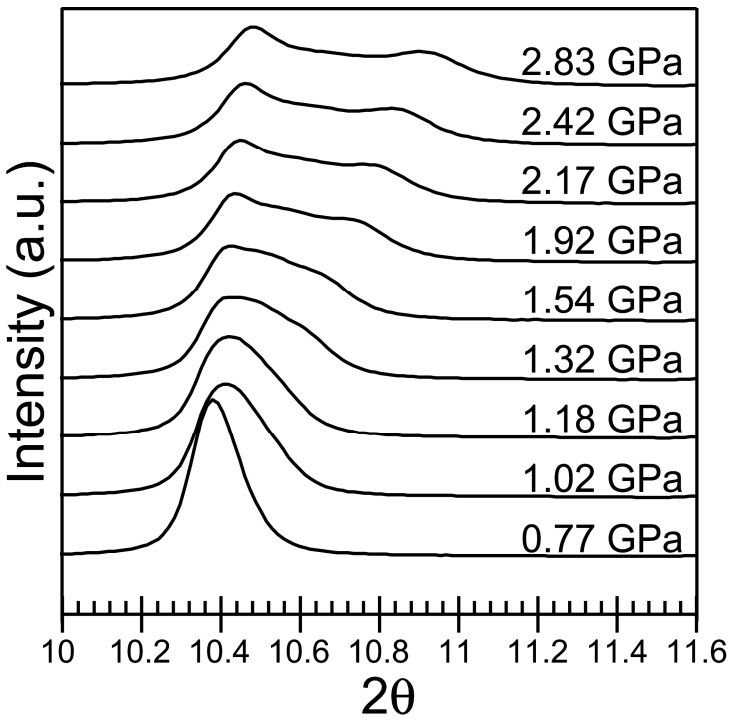

Figure 2.4: The cubic (110) peak is expected to split into two components if a Pm-3m (cubic ReO_3 structure) to single phase R-3c (VF_3 structure) transition is occurring, but a third component is visible between the two major maxima in the data above 1.5 GPa.

In Figure 2.5, the first peak in our diffraction patterns is shown as a function of pressure (all the patterns have been normalized and offset from the x-axis in proportion to the pressure). If the cubic phase persisted above 0.7 GPa, in a form that was not subjected to any stress other than that imposed by the pressure transmitting medium, there would be scattering above this pressure at the position indicated by the trend line drawn in the figure, as the compressibility of the cubic (Pm-3m) phase should be approximately the same both above and below this pressure. However, there is no scattering maximum at the trend line position above 0.7 GPa, suggesting that isolated grains of the cubic phase do not persist above this pressure. However, it seems possible

that extra scattering could come from cubic domains that are under stresses imposed by neighboring domains of rhombohedral material.

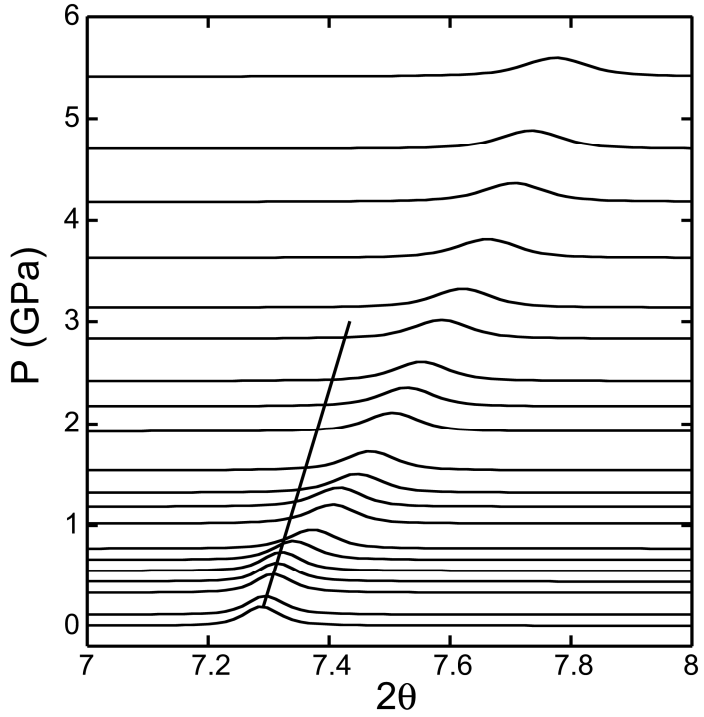

Figure 2.5: The cubic (110) peak is expected to split into two components if a Pm-3m (cubic ReO_3 structure) to single phase R-3c (VF_3 structure) transition is occurring, but a third component is visible between the two major maxima in the data above 1.5 GPa.

To gain further insight into the behavior of TaO_2F, the full widths at half maximum (FWHM) for the cubic reflections (100) and (200) were examined as a function of pressure. As their behavior was very similar, only data for the (100) peak is shown in Figure 2.6. These peaks are not expected to split on going to R-3c symmetry, and our diffraction data show no resolved splittings, shoulders, or significant asymmetry at any pressure examined. However, on compression a pronounced discontinuity in the FWHM versus pressure data is seen at ~0.7 GPa, and there is an obvious change in slope

at just below 4 GPa, followed by a more subtle change in slope at 9-10 GPa. We believe that the first two changes are associated with phase transitions. Any symmetry lowering transition is likely to produce twinning of the original crystallites and the associated strain field could lead to the observed peak broadening. The change in slope at 9-10 GPa may be due to the loss of hydrostaticity in the methanol-ethanol (4:1) medium. This explanation is supported by a close examination of our Ruby fluorescence pressure calibration data; the ruby R1 line starts to broaden at ~10 GPa. On decompression, the FWHM of the cubic (100) peak follows that seen on compression down to ~ 4 GPa. At this point the decompression curve departs from what was seen on compression, indicating that the transition at 4 GPa is not readily reversible. The powder diffraction patterns from the experiment using anhydrous isopropanol as a pressure transmitting medium showed essentially the same behavior, for pressures below 8 GPa, as that seen in methanol:ethanol and discussed above. This indicates that the transition at around 0.7 GPa, the presence of scattering that can not be explained by a single R-3c phase above 0.7 GPa on compression, and the occurrence of a second transition at ~ 4 GPa are intrinsic to the material and not artifacts of the way the DAC was loaded or of the pressure transmitting medium that was used.

We explored a wide range of possibilities for the nature of the phase or phases that were present between 0.7 and ~ 4 GPa on compression. However, due to a combination of the limited angular resolution and d-spacing range of the data, and the intrinsically poor sensitivity of x-ray data to super cell reflections arising from oxygen displacements, we were unable to determine the true nature of the sample in this pressure range.

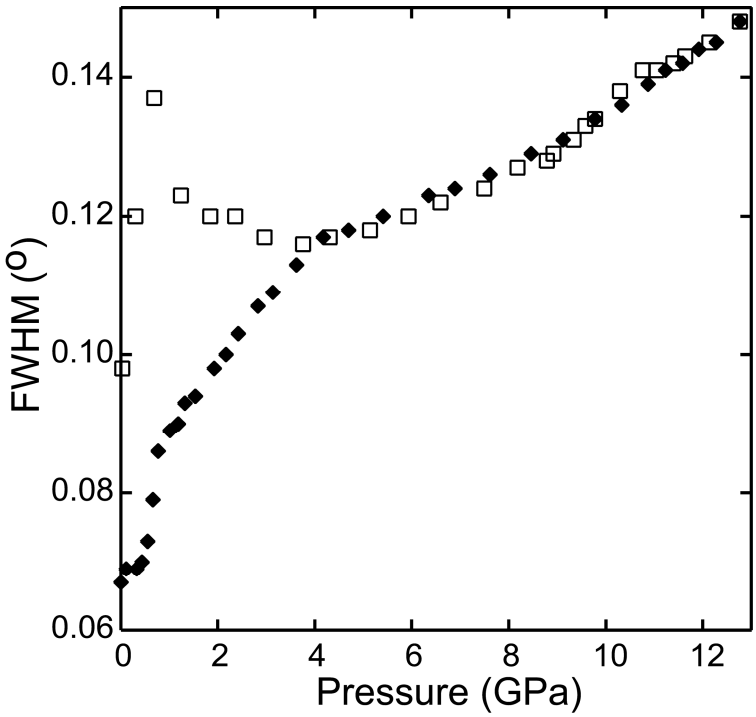

Figure 2.6: Full width at half maximum of the cubic (100) peak as a function of pressure. Filled and open symbols represent the data collected during compression and decompression, respectively.

Unit cell volume data for TaO_2F below 0.7 GPa (single phase Pm-3m) were fit using EOS-FIT (v5.2) to a third order Birch-Murnaghan equation-of-state to estimate a bulk modulus for this phase [32]. As we have data from two separate experiments, we analyzed the unit cell volumes from each run separately and also performed an analysis of the pooled data. In each case, K_p was fixed at 4.0, as the available data range did not constrain this parameter and the prior work on NbO_2F [15] adopted this value for K_p. The ambient pressure unit cell volume was very heavily weighted relative to the other data during fitting. The unit cell volumes and the corresponding fit to the equation of state are shown in Figure 2.7 for the pooled data. K_0 was estimated to be 41(6) GPa based on the measurements in methanol:ethanol only, 34(4) GPa based on the measurements in

isopropanol only, and 36(3) GPa based on the pooled measurements. Within the estimated errors, these values are equivalent. In Table 2.1 we compare the bulk modulus for cubic TaO_2F, from the pooled data analysis, with those in the literature for its structural relatives NbO_2F and ReO_3. The bulk moduli (K_0) for cubic (Pm-3m) TaO_2F and NbO_2F are much lower than that reported for ReO_3, and K_0 for the tantalum compound is only slightly higher than that for the niobium analogue. In the cubic phase, compression involves a reduction of the average M-O bond length. The ease of doing this is partly dependent upon O-O repulsions within the MO_6 octahedra, and as octahedral Re^{6+} is significantly smaller (r_+ = 69 pm) [33] than Nb^{5+} and Ta^{5+} (78 pm) [33], these repulsions will be bigger for ReO_3 and contribute to the higher bulk modulus of this compound. While the difference in K_0 for TaO_2F and NbO_2F is small, it is consistent with literature reports that halides of tantalum have larger force constants for their M-X stretching modes than their niobium analogs [34, 35].

Table 2.1: Equation of state (EOS) parameters for cubic TaO_2F , NbO_2F and ReO_3

Compound	**V_0(Å^3)**	**K_0(GPa)**	**Kp**	**EOS Type**
TaO_2F (Pm-3m)	59.21(1)	36(3)	4[a]	BM3[b]
NbO_2F (Pm-3m) [15]	59.43(2)	24.8(11)	4[a]	Vinet
ReO_3 (Pm-3m) [11]	52.810[a]	100(18)	0[a]	Birch

a) Variables that were kept constant during the equation of state fit.
b) Birch Murnaghan third order equation of state.

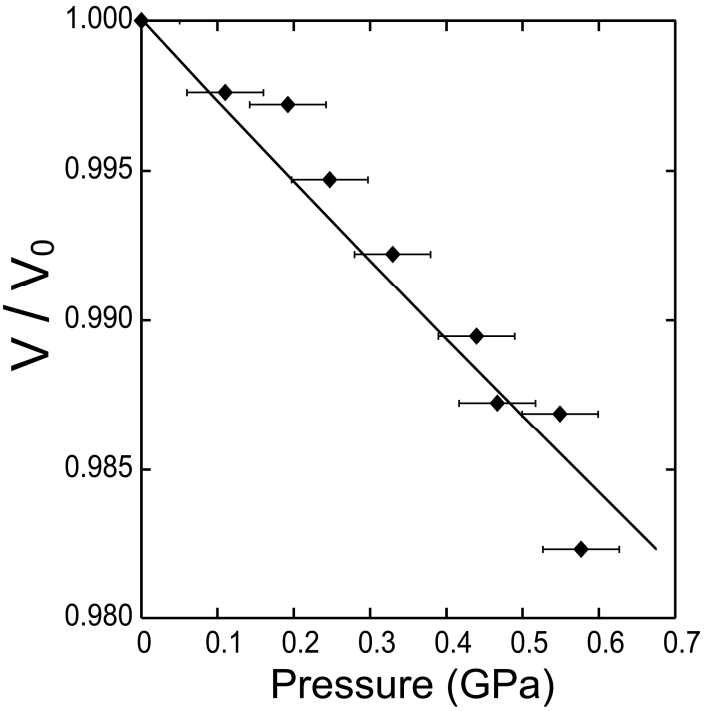

Figure 2.7: Unit cell volume versus pressure for cubic TaO_2F along with a fit to the third order Birch-Murnaghan equation-of-state: K_0=36(3) GPa, K_p=4.0, V_0=59.21(1) Å^3. Estimated errors on the unit cell volumes are smaller than the symbols.

As the data obtained between 8 and 4 GPa on decompression could be indexed with an R-3c model of the type previously reported for NbO_2F [16], we were able to perform a quantitative evaluation of this phase's compressibility. Our attempts to fit the small number of data points that are available to an equation of state invariably led to V_0 values that seemed unreasonable, so we employed a straight line fit of ln(V) versus P to obtain an average compressibility, in the range 4 - 8 GPa, of 16.7 $\times 10^{-3}$ GPa^{-1} (corresponding to an average bulk modulus of ~60 GPa). The data and fit are shown in Figure 2.8. This compressibility is very close to that calculated from the reported equation of state (EOS) for NbO_2F in this pressure range [16] (16 $\times$ 10^{-3} GPa^{-1}, R-3c, VF_3-type structure) and slightly larger than that calculated for ReO_3 based on its reported EOS [13] (15.3 $\times$ 10^{-3}

GPa^{-1}, Im-3 structure). For these structures, the compressibility is likely to be dominated by the resistance to polyhedral tilting rather than the compression of individual octahedra.

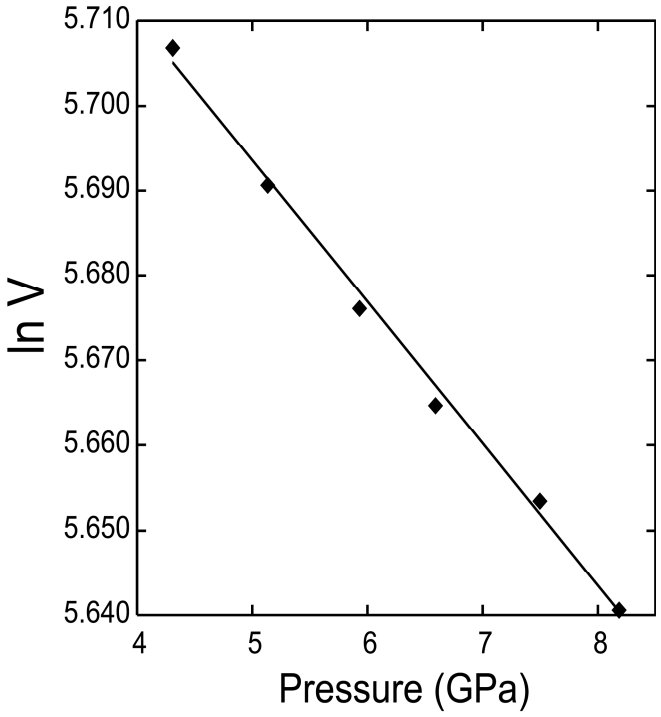

Figure 2.8: The compressibility of TaO_2F (R-3c) in the pressure range 4.3 to 8.2 GPa is estimated to be 16.7×10^{-3} GPa^{-1} using a straight line fit to ln(V) *versus* P. The errors in ln(V) are estimated to be smaller than the symbols and those for the pressure are comparable to the size of the symbols.

2.4. CONCLUSIONS

We have investigated TaO_2F, with a ReO_3-type structure, at up to 12.8 GPa using monochromatic synchrotron powder diffraction and diamond anvil cells. Two phase transitions at ~0.7 and 4 GPa were observed on compression. Below ~0.7 GPa the cubic material was found to have a bulk modulus (K_0) of 36(3) GPa (Kp fixed at 4.0), similar to that reported for NbO_2F but much smaller than that of ReO_3. Immediately above 0.7 GPa

on compression, the diffraction data were not fully consistent with a VF_3 type structure as previously proposed for NbO_2F. On decompression, the data between 8 and 4 GPa could be satisfactorily attributed to a single R-3c phase with a VF_3 type structure and an average volume compressibility of 16.7×10^{-3} GPa-1. On further decompression, there was evidence of hysteresis. However, cubic material was recovered on complete decompression.

2.5. REFERENCES

[1] Frevel LK, Rinn HW. The Crystal Structure of NbO_2F and TaO_2F. Acta Crystallogr. 1956;9:626.

[2] Taylor D. Thermal Expansion Data: V Miscellaneous Binary Oxides. Br. Ceram. Trans. J. 1985;84:9.

[3] Tao JZ, Sleight AW. Very low thermal expansion in TaO_2F. J. Solid State Chem. 2003;173:45.

[4] Glazer AM. Classification of Tilted Octahedra in Perovskites. Acta Crystallogr., Section B 1972;28:3384.

[5] Woodward PM. Octahedral tilting in perovskites .1. Geometrical considerations. Acta Crystallogr., Section B 1997;53:32.

[6] Razavi FS, Altounian Z, Datars WR. Pressure-Induced Anomaly in Fermi-Surface of ReO_3. Solid State Commun. 1978;28:217.

[7] Schirber JE, Morosin B. Compressibility Collapse Transition in ReO_3. Phys. Rev. Lett. 1979;42:1485.

[8] Batlogg B, Maines RG, Greenblatt M, DiGregorio S. Novel p-V relationship in ReO_3 under pressure. Phys. Rev. B 1984;29:3762.

[9] Axe JD, Fujii Y, Batlogg B, Greenblatt M, Di Gregorio S. Neutron Scattering Study of the Pressure Induced Phase Transformation in ReO_3. Phys. Rev. B 1985;31:663.

[10] Jorgensen J-E, Jorgensen JD, Batlogg B, Remeika JP, Axe JD. Order parameter and critical exponent for the pressure-induced phase transitions in ReO_3. Phys. Rev. B 1986;33:4793.

[11] Jorgensen JE, Olsen JS, Gerward L. Phase transitions in ReO_3 studied by high-pressure X-ray diffraction. J. Appl. Crystallogr. 2000;33:279.

[12] Suzuki E, Kobayashi Y, Endo S, Kikegawa T. Structural phase transition in ReO_3 under high pressure. J. Phys.: Condens. Matter 2002;14:10589.

[13] Jorgensen JE, Marshall WG, Smith RI, Olsen JS, Gerward L. High-pressure neutron powder diffraction study of the Im-3 phase of ReO_3. J. Appl. Crystallogr. 2004;37:857.

[14] Chatterji T, McIntyre GJ. Pressure-induced structural phase transition in ReO_3. Solid State Commun. 2006;139:12.

[15] Carlson S. High-pressure studies of the cubic to rhombohedral transformation in NbO_2F. J. Appl. Crystallogr. 2000;33:1175.

[16] Carlson S, Larsson A-K, Rohrer FE. High-pressure transformations of NbO_2F. Acta Crystallogr., Sect. B 2000;56:189.

[17] Mogusmilankovic A, Ravez J, Chaminade JP, Hagenmuller P. Ferroelastic Properties of TiF_3, VF_3, CrF_3, FeF_3, GaF_3 Compounds. Mater. Res. Bull. 1985;20:9.

[18] Daniel P, Bulou A, Rousseau M, Nouet J, Leblanc M. Raman-Scattering Study of Crystallized MF_3 Compounds (M=Al,Cr,Ga,V,Fe,In) - an Approach to the Short-Range-Order Force-Constants. Phys. Rev. B 1990;42:10545.

[19] Daniel P, Bulou A, Rousseau M, Nouet J. Structural Phase-Transitions and Lattice-Dynamics in the Trifluorides MF_3 (M = Al, Cr, Ga, V, Fe, In...). Phase Trans. 1991;33:91.

[20] Sowa H, Ahsbahs H. Pressure-induced octahedron strain in VF_3-type compounds. Acta Crystallogr., Section B 1998;54:578.

[21] Jorgensen JE, Marshall WG, Smith RI. The compression mechanism of CrF_3. Acta Crystallogr., Section B 2004;60:669.

[22] Bassett WA, Shen AH, Bucknum M, Chou I-M. A new diamond anvil cell for hydrothermal studies to 2.5 GPa and from -190 to 1200 C. Rev. Sci. Inst. 1993;64:2340.

[23] Piermarini GJ, Block S, Barnett JD. Hydrostatic limits in liquids and solids to 100 kbar. J. Appl. Phys. 1973;44:5377.

[24] Barnett JD, Block S, Piermarini GJ. An Optical Fluorescence System for Quantitative Pressure Measurement in the Diamond-Anvil Cell. Rev. Sci. Instrum. 1973;44:1.

[25] Miletich R, Allan D, R., Kuhs W, F. High-Pressure Single-Crystal Techniques. Rev. Mineral. Geochem. 2001;41:445.

[26] Hammersley AP, Svensson SO, Hanfland M, Fitch AN, Hausermann D. Two-dimensional detector software: From real detector to idealised image or two-theta scan. High Pressure Research 1996;14:235.

[27] JADE. computer code JADE. Livermore, CA: Materials Data, Inc., 1995-2005.

[28] Rietveld HM. A Profile Refinement Method for Nuclear and Magnetic Structures. J. Appl. Crystallogr. 1969;2:65.

[29] Le Bail A, Duroy H, Fourquet JL. Abinitio Structure Determination of $LiSbWO_6$ by X-Ray-Powder Diffraction. Mater. Res. Bull. 1988;23:447.

[30] Larson AC, Von Dreele RB. GSAS - General Structure Analysis System. Los Alamos Laboratory: Report LA-UR-86-748, 1987.

[31] Toby BH. EXPGUI, a graphical user interface for GSAS. J. Appl. Crystallogr. 2001;34:210.

[32] Angel RJ. Equations of state. High-Temperature and High-Pressure Crystal Chemistry 2000;41:35.

[33] Shannon RD. Revised Effective Ionic Radii and Systematic Studies of Interatomic Distances in Halides and Chalcogenides. Acta Cryst. A 1976;32:751.

[34] Mehta ML, Avasthi MN. Normal Coordinate Analysis of Tantalum(I) and Niobium(I) Hexahalide Anions. J. Cryst. Mol. Struct. 1972;2:299.

[35] So SP. Normal Coordinate Analysis and Thermodynamic Functions of Niobium and Tantalum Pentahalides. J. Mol. Struct. 1973;16:311.

CHAPTER 3

PRESSURE DEPENDENCE OF NEGATIVE THERMAL EXPANSION IN TaO_2F

3.1. INTRODUCTION

Under ambient conditions TaO_2F adopts the cubic ReO_3 structure [1], space group Pm-3m, which can be thought of as an undistorted ABX_3 perovskite with the A sites empty. ReO_3 type structure has many of the structural features typical of negative thermal expansion oxides (open flexible frameworks with two coordinate anions), although none of the compounds ReO_3, TaO_2F and NbO_2F display NTE. While both ReO_3 and NbO_2F show positive thermal expansion [2, 3], TaO_2F does exhibit very low thermal expansion from 20 to 400 K [3]. Most negative thermal expansion oxides are framework materials which feature low density three-dimensional networks of relatively rigid polyhedral units that share corners with each other. The mechanism, which can be considered the most applicable one in framework oxides exhibiting negative thermal expansion, is based on the transverse thermal motion of oxygen in M-O-M linkages (M = metal). This transverse thermal motion pulls M atoms closer to one another giving rise to NTE. In a 3-dimensional lattice, a simple way to describe the likely correlations of the thermal motions of various oxygen atoms is to consider rocking motions of polyhedra as rigid unit modes (RUMs) [4]. Compounds with ReO_3 type structures are very simple prototypes to study this kind of mechanism.

In general, framework NTE materials show rich behavior on compression, due to their structural flexibility and low density, and transitions leading to a loss of NTE often occur at pressures that may be achieved during the processing of composites containing the NTE material. Phenomena occurring on compression include low pressure crystalline-to-crystalline phase transitions [5-8], and pressure induced amorphization [9-13]. As a result, high pressure studies of NTE materials are of some importance from a practical standpoint as well as being of fundamental interest. Little attention has been paid to the effect of compression on the expansion coefficients of a particular phase. Recently, it was reported by Chapman and Chupas that the thermal expansion coefficient for the NTE material $Zn(CN)_2$ became more negative on compression [14]. The average linear coefficient of thermal expansion (CTE) changed from -17.4(2) 10^{-6} K^{-1} to -19.4 10^{-6} K^{-1} on going from ambient to 0.4 GPa. Here, we report experiments that were undertaken to examine the effect of pressure on the coefficients of thermal expansion for TaO_2F.

3.2. EXPERIMENTAL PROCEDURES

3.2.1 Sample Preparation

TaO_2F was prepared by dissolving Ta_2O_5 (Strem, 99.8%) in a Pt crucible with concentrated HF (Mallinckrodt, 48%) followed by slow evaporation of HF to dryness. The remaining off-white powder was transferred to a Teflon container and heated in an oven at 200 ^oC for 10 h. X-ray powder diffraction data showed it to be single phase TaO_2F.

3.2.2 Neutron diffraction data collection and analyses

Approximately 10 grams of polycrystalline TaO_2F was loaded into a helium-gas pressure cell [15] and time-of-flight neutron powder diffraction data were collected on the Special Environment Powder Diffractometer [16], at the Intensed Pulsed Neutron Source (IPNS), Argonne National Laboratory, Argonne, IL. The helium-gas pressure cell allowed us to apply precisely measured, perfectly hydrostatic pressure onto the sample. Measurements as a function of pressure at room temperature were made at 0, 0.05, 0.1, 0.2, 0.25, 0.3 and 0.4 GPa. Low temperature measurements were made at 200 K and 60 K under 0.3 GPa and at 60 K at 0.2 GPa and ambient pressure. Data collection times were about 30 minutes, with approximately an hour of equilibration time in between changes to either pressure or temperature.

The program suite GSAS [17] with the EXPGUI [18] graphical interface was used to perform Rietveld [19] analyses. Lattice constants were refined except for the ambient pressure and room temperature data set for which lattice constants were kept fixed at the values obtained from Rietveld refinement of laboratory X-ray powder diffraction data obtained using a Scintag X1 diffractometer equipped with a copper tube and a Peltier cooled solid-state detector. DIFC value and an absorption coefficient were refined only for the ambient pressure and room temperature data set and were not refined for the remaining data. The background was fitted with an 18 term reciprocal interpolation function. Independent isotropic atomic displacement parameters for each atom were also refined.

3.3. RESULTS AND DISCUSSION

The average structure for TaO_2F from diffraction experiments is cubic with ReO_3-type structure, with O and F occupying the same crystallographic position. As an example Rietveld fit to the data, the fit to the data at room temperature and ambient pressure is shown in Figure 3.1. A good fit to the neutron diffraction data for TaO_2F, under all conditions examined, could be obtained using a simple cubic ReO_3-type structure model. Our prior high pressure x-ray diffraction work [20] on this phase revealed a phase transition at ~0.7 GPa and ambient temperature that would be expected to occur at lower pressure on cooling, but no evidence for this transition was observed down to 60 K at 0.3 GPa (lowest temperature and highest pressure examined).

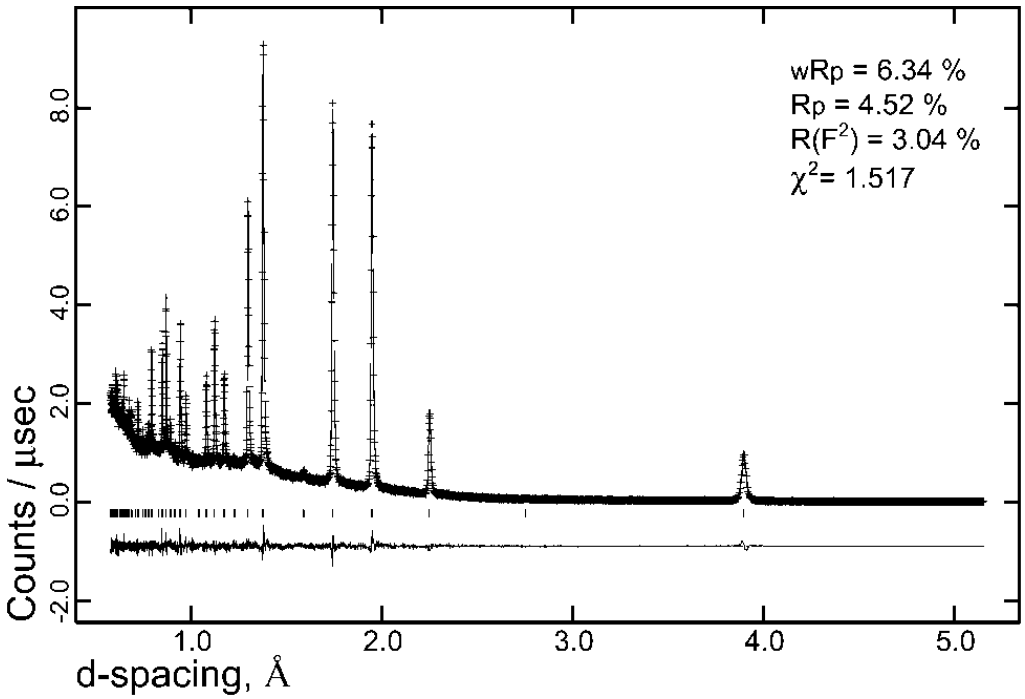

Figure 3.1: Example of a Rietveld fit - Observed(+), calculated(-), and difference (lower trace) of TaO_2F at ambient pressure and room temperature

Unit cell volume and lattice constants obtained from Rietveld refinements of all the diffraction data sets are given in Table 3.1, and Figure 3.2 shows a plot of lattice constants. There is a continuous reduction of unit cell volume by 0.75 % during compression to 0.4 GPa at room temperature.

Table 3.1: Lattice constants and unit cell volume for TaO_2F as a function of pressure and temperature, determined from Rietveld analyses of neutron diffraction data.

P(GPa) at 296 K	***a(Å)***	***V(Å^3)***
0.00	3.89649(4)	59.159(2)
0.05	3.89542(8)	59.110(4)
0.10	3.89430(6)	59.059(3)
0.20	3.89191(4)	58.951(2)
0.25	3.89074(4)	58.897(2)
0.30	3.88932(4)	58.833(2)
0.40	3.88669(8)	58.714(4)
T(K) at 0GPa		
296	3.89649(4)	59.159(2)
60	3.89637(7)	59.154(3)
T(K) at 0.2GPa		
296	3.89191(4)	58.951(2)
60	3.88797(8)	58.772(4)
T(K) at 0.3GPa		
296	3.88932(4)	58.833(2)
200	3.88735(9)	58.744(4)
60	3.8817(1)	58.491(5)

Fitting a 3rd order Birch-Murnaghan equation of state (EOS) using EOSFIT [21] to the volume data gave us (V_0=59.169(5) Å^3, K_0= 52(1) GPa, K_p= fixed at 4) at ambient temperature. Plots of normalized unit cell volume and corresponding equation of state fit are shown in Figure 3.3. The average volume coefficients of thermal expansion obtained

from the analysis of variable-temperature data at constant pressures of 0, 0.2, and 0.3 GPa are shown in Table 3.2. The linear thermal expansion coefficient increased from almost zero (0.1 10^{-6} K^{-1}) at ambient pressure to 8.4 10^{-6} K^{-1} at 0.3 GPa. This indicates that thermal expansion behavior of TaO_2F is significantly affected by pressure.

Table 3.2: Coefficients of thermal expansion for TaO_2F as a function of pressure

P (GPa)	α_v	α_a
0.0	0.4 x 10^{-6} K^{-1}	0.1 x 10^{-6} K^{-1}
0.2	12.9 x 10^{-6} K^{-1}	4.3 x 10^{-6} K^{-1}
0.3	24.7 x 10^{-6} K^{-1}	8.4 x 10^{-6} K^{-1}

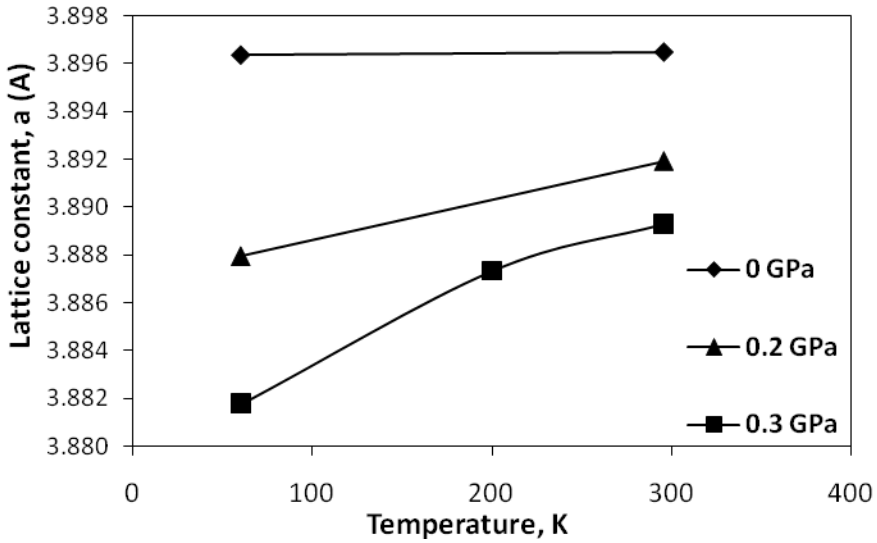

Figure 3.2: Lattice constants for TaO_2F at varying temperature and pressure

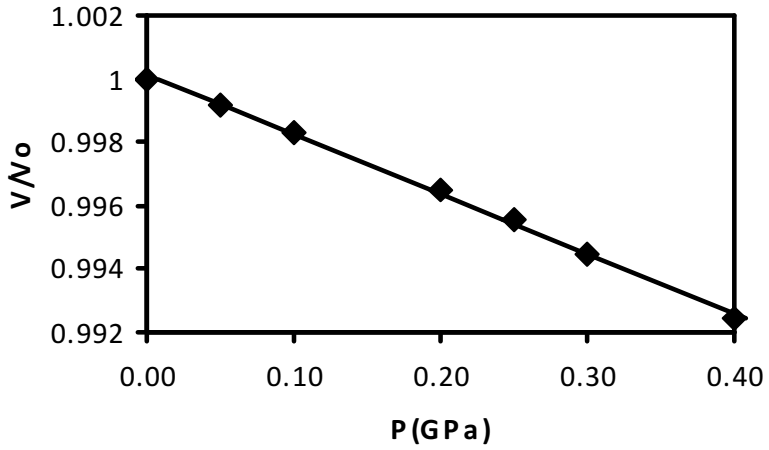

Figure 3.3: EOS fit to the P-V data for TaO_2F (Vo=59.169(5) $Å^3$, Ko= 52(1) GPa, Kp= fixed at 4)

The pressure and temperature dependence of the atomic displacement parameters for this material are unusual. At ambient pressure, the atomic displacement parameters (ADPs) (see Figures 3.4 and 3.5) for the O/F position are highly anisotropic, with a large transverse component even at 60K, suggesting static disorder perpendicular to the Ta-Ta direction. The transverse component of the O/F displacement parameter increases significantly on compression, particularly at low temperature, but pressure does not have a strong effect on the apparent ADP for Ta (see Figure 3.6) or the longitudinal component for the O/F site.

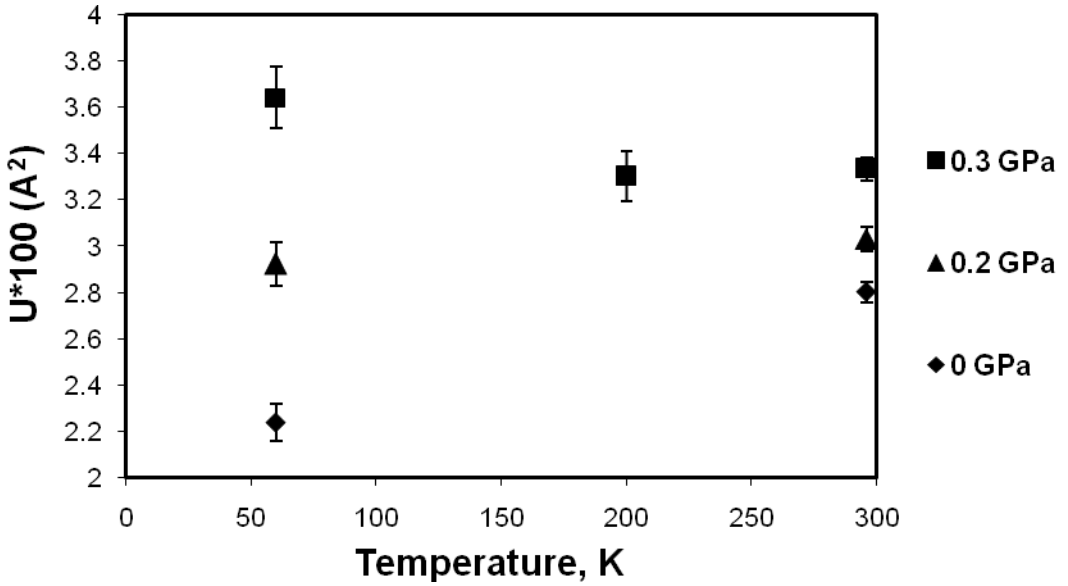

Figure 3.4: Transverse displacement parameters for O/F as a function of temperature at different pressures

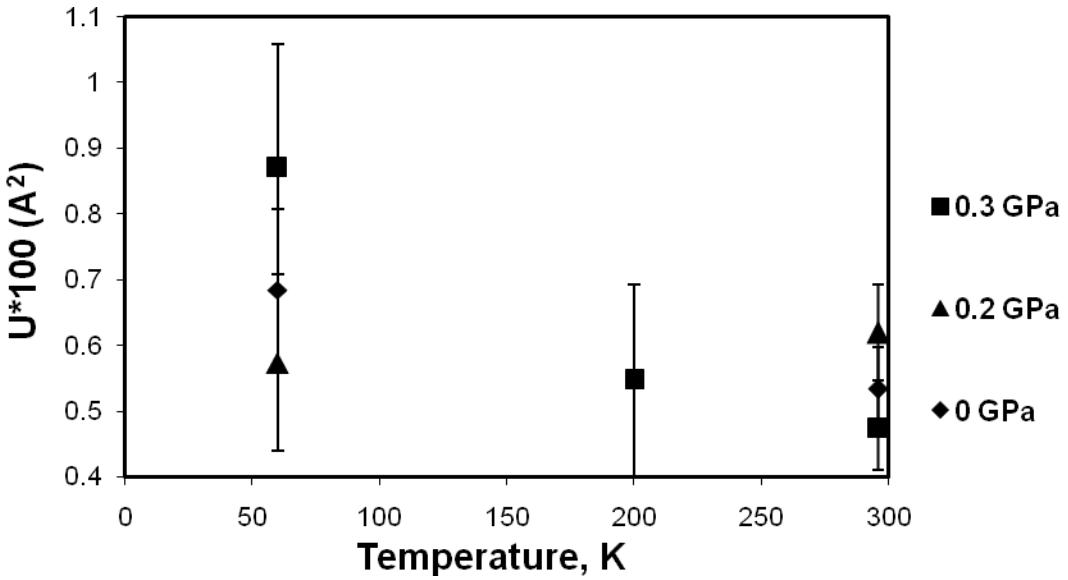

Figure 3.5: Longitudinal displacement parameters for O/F as a function of temperature at different pressures

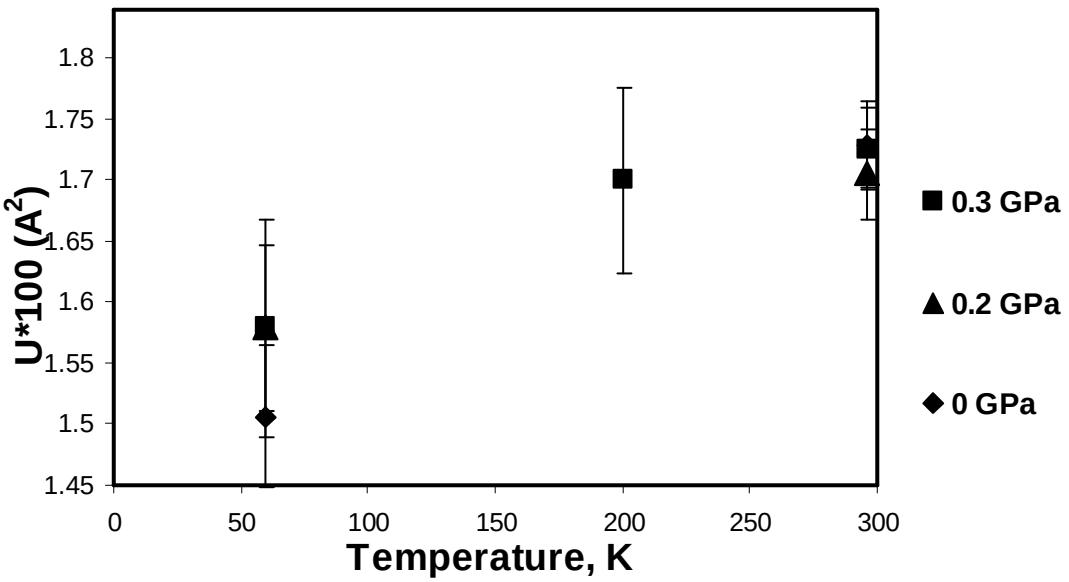

Figure 3.6: Atomic displacement parameters for Ta as a function of temperature at different pressures. Transverse and longitudinal values are equivalent.

Tao et al. [3] conducted a variable temperature diffraction study on TaO_2F, and observed that transverse anion displacement factors remain high to very low temperatures. They pointed to a likely existence of a static tilting and the possibility of Ta-(O/F)-Ta bonds not being linear. The above observations suggest that locally the octahedra in TaO_2F may be tilted, perhaps in a similar fashion to what is seen in compounds such as VF_3 at ambient temperature. If this is true, compression would probably lead to a decrease of the "true" Ta-X-Ta angles (consistent with increasing transverse O/F on compression) giving rise to a volume reduction. The expansion of the nearest neighbor Ta-Ta distance on heating is likely to be dependent on this angle and the increase in macroscopic CTE may arise because this expansion becomes more pronounced as the Ta-X-Ta angle decreases. Total scattering experiments are planned to

directly probe the local structure of this material and attempt to verify the above hypothesis.

3.4. CONCLUSIONS

TaO_2F is a framework material with the cubic ReO_3 structure. At ambient pressure TaO_2F displays zero thermal expansion. Variable-temperature high-pressure neutron powder diffraction measurements were undertaken using SEPD at IPNS to investigate the pressure dependence of thermal expansion in TaO_2F. The neutron diffraction measurements at variable temperature (300 to 60 K) and high pressure (up to 0.3 GPa) indicated that pressure had a significant effect on the linear coefficient of thermal expansion (from 0.1 10^{-6} K^{-1} at 0 GPa to 8.4 10^{-6} K^{-1} at 0.3 GPa) of TaO_2F. Rietveld analysis of the data resulted in unexpected temperature and pressure dependence for transverse displacement parameters of O/F atoms, indicating the local structure might not be the ideal ReO_3 type structure with 180^o angles.

3.5. REFERENCES

[1] Frevel LK, Rinn HW. The Crystal Structure of NbO_2F and TaO_2F. Acta Crystallogr. 1956;9:626.

[2] Taylor D. Thermal Expansion Data: V Miscellaneous Binary Oxides. Br. Ceram. Trans. J. 1985;84:9.

[3] Tao JZ, Sleight AW. Very low thermal expansion in TaO_2F. J. Solid State Chem. 2003;173:45.

[4] Hammonds KD, Dove MT, Giddy AP, Heine V, Winkler B. Rigid-unit modes and structural phase transitions in framework silicates. American Mineralogist 1996;81:1057.

[5] Varga T, Wilkinson AP, Lind C, Bassett WA, Zha C-S. High pressure synchrotron x-ray powder diffraction study of $Sc_2Mo_3O_{12}$ and $Al_2W_3O_{12}$ J. Phys.: Condens. Matter 2005;17:4271.

[6] Grzechnik A, Crichton WA. Structural transformations in cubic $ZrMo_2O_8$ at high pressures and high temperatures. Solid State Sci. 2002;4:1137.

[7] Muthu DVS, Chen B, Wrobel JM, Krogh Andersen AM, Carlson S, Kruger MB. Pressure-induced phase transitions in α–$ZrMo_2O_8$. Phys. Rev. B 2002;65:064101.

[8] Evans JSO, Hu Z, Jorgensen JD, Argyriou DN, Short S, Sleight AW. Compressibility, Phase Transitions, and Oxygen Migration in Zirconium Tungstate, ZrW_2O_8. Science 1997;275:61.

[9] Secco RA, Liu H, Imanaka N, Adachi G. Pressure-induced amorphization in negative thermal expansion $Sc_2(WO_4)_3$. Journal of Materials Science Letters 2001;20:1339.

[10] Varga T, Wilkinson AP, Lind C, Bassett WA, Zha C-S. Pressure-induced amorphization of cubic ZrW_2O_8 studied in-situ and ex-situ by synchrotron x-ray absorption spectroscopy and diffraction. Phys. Rev. B 2005;72:024117.

[11] Chen B, Muthu DVS, Liu ZX, Sleight AW, Kruger MB. High-pressure Raman and infrared study of HfW_2O_8. Phys. Rev. B 2001;64:214111.

[12] Perottoni CA, de Jornada JAH. Pressure-Induced Amorphization and Negative Thermal Expansion in ZrW_2O_8. Science 1998;280:886.

[13] Varga T, Wilkinson AP, Lind C, Basset WA, Zha C-S. Pressure-induced amorphization of cubic $ZrMo_2O_8$ studied in-situ by x-ray absorption spectroscopy and diffraction. Solid State Communications 2005;135:739.

[14] Chapman KW, Chupas PJ. Pressure enhancement of negative thermal expansion behavior and induced framework softening in zinc cyanide. Journal of the American Chemical Society 2007;129:10090.

[15] Jorgensen JD, Pei S, Lightfoot P, Hinks DG, Veal BW, Dabrowski B, Paulikas AP, Kleb R, Brown ID. Pressure-induced charge transfer and dT_c/dP in Y $Ba_2Cu_3O_{7-x}$. Physica C 1990;171:93.

[16] Jorgensen JD, Faber Jr. J, Carpenter JM, Crawford RK, Haumann JR, Hitterman RL, Kleb R, Ostrowski GE, Rotella FJ, Worlton TG. Electronically Focused Time-of-Flight Powder Diffractometers at the Intense Pulsed Neutron Source. J. App. Crystallogr. 1989;22:321.

[17] Larson AC, Von Dreele RB. GSAS - General Structure Analysis System. Los Alamos Laboratory: Report LA-UR-86-748, 1987.

[18] Toby BH. EXPGUI, a graphical user interface for GSAS. J. Appl. Crystallogr. 2001;34:210.

[19] Rietveld HM. A Profile Refinement Method for Nuclear and Magnetic Structures. Journal of Applied Crystallography 1969;2:65.

[20] Cetinkol M, Wilkinson AP, Lind C, Bassett WA, Zha C-S. High-pressure powder diffraction study of TaO_2F. Journal of Physics and Chemistry of Solids 2007;68:611.

[21] Angel RJ. EOS-FIT. computer code EOS-FIT. Blacksburg, VA: Virginia Tech, 2001.

CHAPTER 4

IN SITU HIGH-PRESSURE SYNCHROTRON X-RAY DIFFRACTION STUDY OF $Zr_2(WO_4)(PO_4)_2$

4.1. INTRODUCTION

Materials exhibiting low and negative thermal expansion (NTE) have been of considerable recent interest [1-7]. Many oxides displaying NTE belong to one of the following families: NZP-type [8-12], ZrW_2O_8-type [13-15], ZrV_2O_7-type [16] and $Sc_2W_3O_{12}$-type [7]. NTE compounds may find application as pure phases and as components in composite materials with tailored thermal expansion coefficients [17-20]. During the manufacture and use of these materials, pressures above ambient may be encountered leading to phase transitions and a loss of NTE behavior [21, 22]. Many NTE materials, owing to their flexible frameworks and relatively low densities, display crystalline-to-crystalline phase transitions [13, 23-26], and pressure induced amorphization [15, 23, 27-30] upon application of modest pressures. As a consequence, high pressure studies of NTE materials are of some importance from a practical standpoint as well as being of fundamental interest.

Compounds with the general formula $A_2M_3O_{12}$ (A= many 3+ ions, M= Mo or W) are known to adopt a variety of different structures depending upon the nature of A^{3+} [31-34]. The orthorhombic $Sc_2W_3O_{12}$ structure (Pnca), which is often associated with volume NTE, has been observed for A=Al, Sc, Cr, Fe, Y, In and the smaller rare earths from Lu to Ho. With decreasing temperatures, several compounds in the $Sc_2W_3O_{12}$ family display

a ferroelastic phase transition to a monoclinic ($P2_1/a$) structure which does not exhibit NTE [34-36]. The temperature for this transition has been proposed to be dependent on the electronegativity of the A^{3+} cation [34]. Several members of the $Sc_2W_3O_{12}$ family have been studied under pressure, and were reported to display a variety of crystalline-to-crystalline phase transitions and undergo pressure induced amorphization [26, 30, 37-41].

Many compounds that are structurally related to $Sc_2W_3O_{12}$ can be prepared by substitution on the scandium and tungsten sites. These include simple substitutions, for example, $(ScAl)W_3O_{12}$ and $(ErIn)W_3O_{12}$ [7], as well as more complicated substitutions such as $HfMgW_3O_{12}$ [42], and $Zr_2WO_4(PO_4)_2$, $Zr_2MoO_4(PO_4)_2$ and their Hf analogs [7]. The effect of the more complex substitutions on the high pressure behavior of this structure type is unknown.

In this chapter, a high-pressure *in-situ* monochromatic synchrotron powder diffraction study of $Zr_2WO_4(PO_4)_2$ at room temperature in a diamond anvil cell is presented. The existence of $Zr_2WO_4(PO_4)_2$ was first reported by Martinek [43] in 1970. Evans *et al.* [44] reported its crystal structure (Pnca) as being comprised of ZrO_6 octahedra sharing corners with WO_4 and PO_4 tetrahedra. Dilatometer and x-ray diffraction measurements indicate mean linear coefficients of thermal expansion -6×10^{-6} and $-3 \times 10^{-6}\ K^{-1}$ respectively [7].

4.2. EXPERIMENTAL PROCEDURES

4.2.1 Sample Preparation

$Zr_2(WO_4)(PO_4)_2$ was prepared using a literature method [44]. Stoichiometric amounts of ZrO_2 (Alfa Aesar, 99.7%), WO_3 (Strem Chemicals, 99.8 %) and ZrP_2O_7 were

ground together in an agate mortar, heated in a Pt crucible for 5 h at 900 ºC followed by 8 h at 1250 ºC in air. ZrP_2O_7 was prepared by heating stoichiometric amounts of dehydrated $ZrO(NO_3)_2 \cdot xH_2O$ (Alfa Aesar) and $(NH_4)_2HPO_4$ (J.T. Baker, 99.2%) for 20 h at 700 ºC in a Pt crucible.

4.2.2 Diamond Anvil Cell and Diffraction Data Collection

High pressure *in-situ* powder diffraction data were collected at room temperature using the B-2 line of the Cornell High Energy Synchrotron Source (CHESS), Wilson Lab, Cornell University, Ithaca, NY. Data were obtained from two separate runs using a four-post DAC with a methanol-ethanol (4:1) pressure medium. The DAC had 2.1 mm thick diamonds with 600 μm culet faces. A pre-indented fully hardened stainless steel gasket with 250 μm initial thickness and a 150 μm diameter hole was used. The medium was claimed to be hydrostatic up to 10.4 GPa [45]. For both runs, X-rays of wavelength 0.4960 Å was selected using a Ge(111) double-crystal monochromator and the beam collimated with a ~50 μm pin hole. Diffraction patterns were recorded on a Mar345 imaging plate detector. A few small ruby chips were loaded into the cells along with the samples so that the pressure could be determined using the ruby fluorescence technique [46], where pressure calibration errors of 0.05-0.1 GPa are possible [47].

For the first run, the initial pressure was ambient and 23 diffraction patterns were collected up to 5.35 GPa on compression and 21 patterns were collected during decompression to 0.08 GPa. For the second set of measurements, the starting pressure was 0.44 GPa and 18 patterns were collected up to 16 GPa and the cell was decompressed to ~1.4 GPa in 4 large steps. The sample-to-detector distance was

calibrated using ambient pressure diffraction from a TaO_2F sample in a previous experiment [48].

4.2.3 Data Processing

The two-dimensional diffraction images were integrated using the program FIT2D [49]. I(2θ) data were initially processed in JADE [50]. The high pressure phases were indexed with Treor [51] implemented in the program CMPR [52] and then further analyzed by a combination of the Rietveld [53] and Le Bail [54] methods using GSAS [55] with the EXPGUI [56] interface. The calculated unit cell volumes were fitted to the Birch-Murnaghan equation of state (EOS) [57] using the EOS-FIT program (v5.2) [58].

4.3. RESULTS

Two reversible crystalline-to-crystalline phase transitions are apparent based on the data shown in Figure 4.1. The Bragg peaks at ~3.8^o and ~6.4^o 2θ get broader and ultimately split during the first transition. The transition onset pressure, as suggested by an examination of the full width at half maximum for these peaks as a function of pressure (Figure 4.2) during compression is ~ 1.4 GPa. This new phase was indexed as monoclinic, possible space group $P2_1/n11$, using Treor.

When the pressure was increased above 3.41 GPa, another phase formed as indicated by the emergence of new peaks. This second transition is most likely discontinuous, as two phases seem to coexist over a narrow range of pressures. The new phase was also indexed as monoclinic**,** probable space group $P2_1/n11$. Both transitions were reversible on decompression. Lattice constants from Le Bail fits to each diffraction

pattern from this run are given in Table 4.1. Unit cell volume as a function of pressure is shown in Figure 4.3 for this run. It is notable that while the normalized unit cell volumes on compression and decompression are the same within experimental error between 3.5 and 5.5 GPa, the values below 3.5 GPa are different from one another.

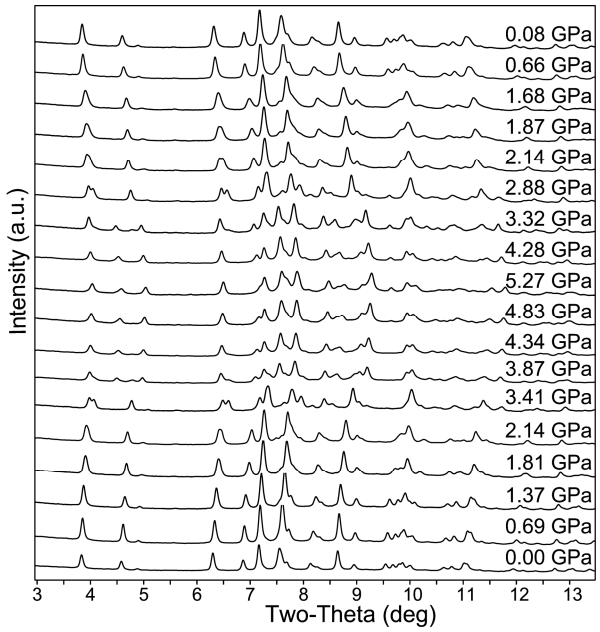

Figure 4.1: Selected diffraction patterns for $Zr_2WP_2O_{12}$ on compression to 5.27 GPa followed by decompression. Phase transitions occur at ~1.4 and ~3.7 GPa. These changes are reversible on decompression.

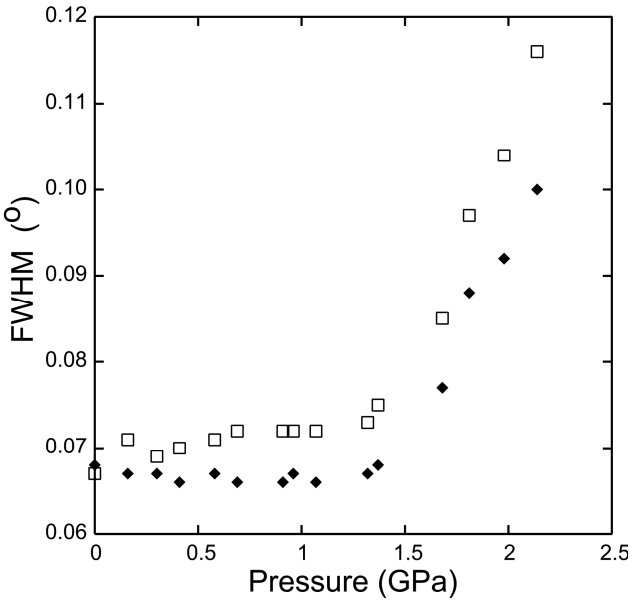

Figure 4.2: Full width at half maximum for the Bragg peaks located at ~3.8° (filled diamonds) and ~6.4° (open squares) 2θ in the data shown in Figure 1. These data suggest a phase transition on set pressure of ~1.4 GPa.

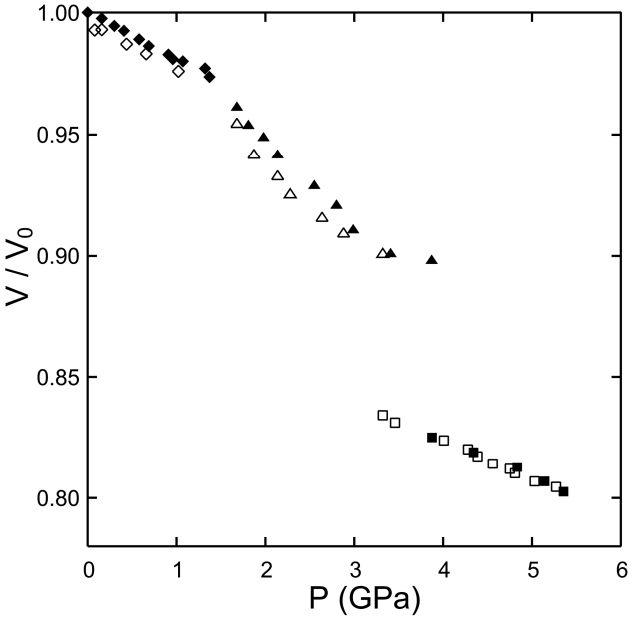

Figure 4.3: Normalized unit cell volumes from run 1 for $Zr_2WP_2O_{12}$. Closed symbols are values on compression and open symbols are on decompression.

In principle, this could be a consequence of an experimental error, such as the sample to image plate distance changing during our experiment, or to hysteresis. An examination of the individual lattice constants on compression and decompression (Figures 4.4 and 4.5), indicates that the observed phenomenon is not due to a change in sample to plate distance, or any similar experimental error, as some of the lattice constants change in a reversible way on compression and decompression, but others do not. For the second run (Figure 4.6), the pressure range was more extensive than in the first and, 3 crystalline-to-crystalline phase transitions were seen along with a disordering, or partial amorphization, above 14 GPa. The disordering was not reversible and remnant Bragg peaks suggestive of the highest pressure crystalline phase persisted on decompression. The diffraction patterns from this run could be indexed on an orthorhombic unit cell (Pnca) for pressures up to 1.2 GPa.

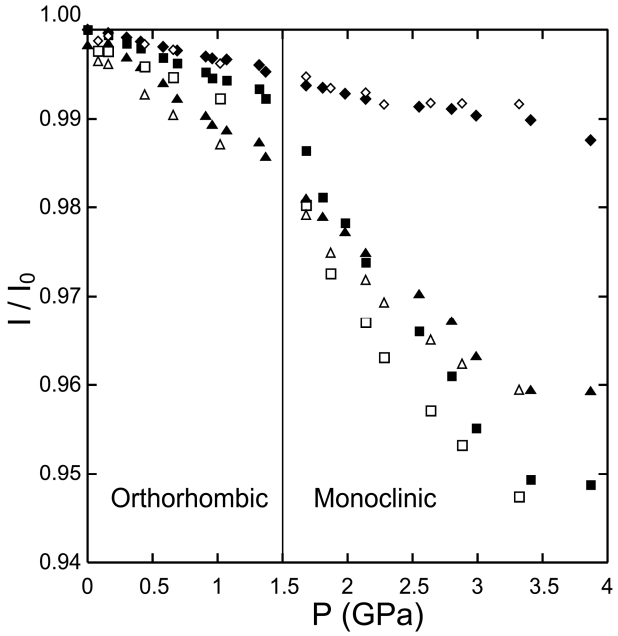

Figure 4.4: Normalized unit cell constants for $Zr_2WP_2O_{12}$ from run 1 Filled symbols are values determined on compression and open symbols are on decompression. a-axis diamonds; b-axis triangles; c-axis squares.

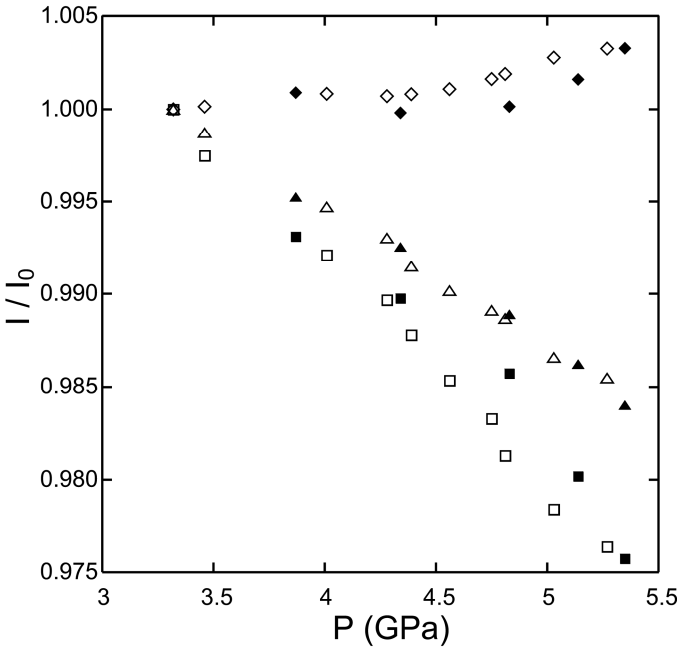

Figure 4.5: Normalized unit cell constants for the second monoclinic phase of $Zr_2WP_2O_{12}$ from run 1 Filled symbols are values determined on compression and open symbols are on decompression. a-axis diamonds; b-axis triangles; c-axis squares.

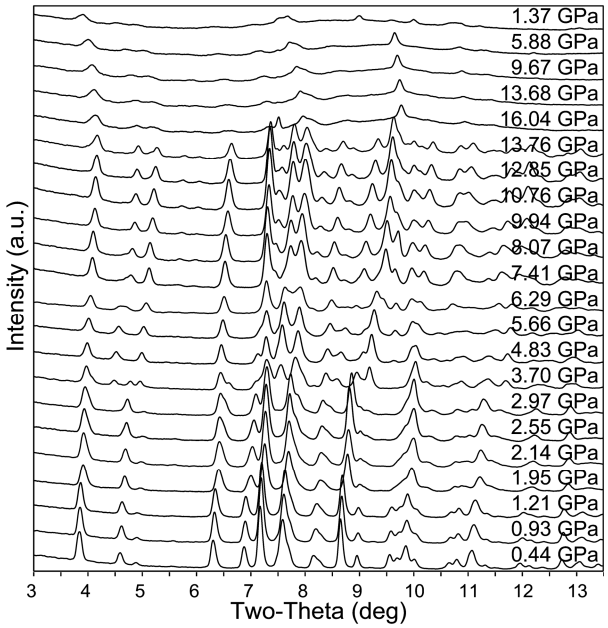

Figure 4.6: Selected diffraction patterns for $Zr_2WP_2O_{12}$ on compression to ~16 GPa followed by decompression. In addition to the phase transitions seen in the earlier run, another transition is observed at 7.4 GPa. The partial amorphization seen at >14 GPa is not reversible on decompression.

At the next pressure point (1.94 GPa), the pattern could be indexed as monoclinic. A transition leading to a second monoclinic phase was observed between 2.97 and 3.70 GPa. In the pressure range 5.66 - 9.94 GPa the behavior of the second Bragg peak in the diffraction pattern suggests another crystalline-to-crystalline phase transition with some phase coexistence. This is followed by partial amorphization above 14 GPa. The highest pressure crystalline phase could be indexed on a triclinic unit cell using Treor [51] implemented in the program CMPR [52]. Lattice constants derived from Le Bail fits to the data from run 2 are given in Table 4.2. Normalized unit cell volumes from run 1 and 2 on compression are compared in Figure 4.7. The agreement between the two sets of measurements is not perfect, perhaps in part reflecting different sample to detector calibration errors for the two runs. As more extensive data are available at low pressure from run 1, this run is the basis of most subsequent discussion for pressures below 6 GPa.

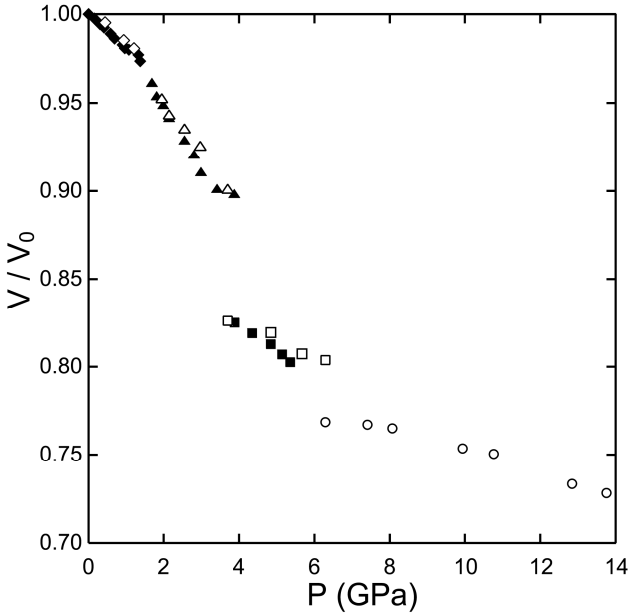

Figure 4.7: Normalized unit cell volumes for $Zr_2WP_2O_{12}$ from runs 1 (closed symbols) and 2 (open symbols) on compression only.

Normalized lattice constants for phases 1 and 2 are shown in Figure 4.4. There appear to be no discontinuities in the lattice constants at the first phase transition, suggestive of second order behavior. Both phases are anisotropically compressible, with the second (monoclinic) phase showing much greater anisotropy. The compressibilities of the a and b-axes are almost continuous through the transition, but the c-axis softens considerably on going to the monoclinic phase. Average linear compressibility's for the initial orthorhombic phase were estimated to be β_a= 3.3(1) x 10^{-3} GPa^{-1}, β_b= 10.3(3) x 10^{-3} GPa^{-1}, β_c= 5.5(2) x 10^{-3} GPa^{-1} by least squares fits of a straight line. The corresponding values for the monoclinic phase existing below ~4 GPa are β_a= 2.3(1) x 10^{-3} GPa^{-1}, β_b= 13.0(4) x 10^{-3} GPa^{-1}, β_c= 22.0(8) x 10^{-3} GPa^{-1}. Normalized lattice constants for the second monoclinic phase (Figure 5) also indicate considerable anisotropy for the compressibility of this phase. Average linear compressibility's for this phase were estimated to be β_a= -1(1) x 10^{-3} GPa^{-1}, β_b= 7.6(4) x 10^{-3} GPa^{-1}, β_c= 12(2) x 10^{-3} GPa^{-1}. Compressibilities on compression and decompression are summarized in Table 4.4.

For all the phases observed, a third order Birch-Murnaghan equation of state was fit to the P-V data shown in Tables 4.1 and 4.2. During the fitting, the pressure derivative of the bulk modulous (K_p) was fixed at 4.0 while varying the zero pressure volume (V_0) and bulk modulus (K_0). Additionally, average bulk moduli were estimated using a straight line fit to ln(V) vs. P. These moduli are presented in Table 4.3.

4.4. DISCUSSION

The behavior of $Zr_2P_2WO_{12}$ on compression is different from that previously observed for other orthorhombic $A_2M_3O_{12}$ phases such as $Sc_2W_3O_{12}$, $Sc_2Mo_3O_{12}$ and $Al_2W_3O_{12}$. A summary of the high pressure behavior for these compounds is presented in Table 4.5.

The initial negative thermal expansion orthorhombic structure (Pnca) for $Zr_2P_2WO_{12}$ persists to a much higher pressure ~1.4 GPa when compared to $Sc_2Mo_3O_{12}$ (~0.25 GPa) and $Al_2W_3O_{12}$ (~0.1 GPa). Orthorhombic $Zr_2P_2WO_{12}$ has a bulk modulous (K_0) 49(2) GPa that is greater than that for the scandium containing phases (~31 GPa) but similar to that for aluminum tungstate (~48 GPa), in line with the observed volumes per oxide ion for these phases: $Zr_2P_2WO_{12}$, 22.0 $Å^3$; $Al_2W_3O_{12}$, 21.7 $Å^3$; $Sc_2W_3O_{12}$, 25.7 $Å^3$; $Sc_2Mo_3O_{12}$, 25.4 $Å^3$.

On compressing the scandium and aluminum phases [26], they transform to the same monoclinic structure (Pnca $\rightarrow$ $P2_1/a$) that occurs on cooling $Al_2W_3O_{12}$, or $Sc_2Mo_3O_{12}$ [35], via discontinuous pathway. This monoclinic structure has twice as many formula units per primitive unit cell as the original Pnca phase. However, the first monoclinic structure formed on compressing $Zr_2P_2WO_{12}$ (Pnca $\rightarrow$ $P2_1/n11$) has essentially the same unit cell volume as the starting orthorhombic phase and the new phase is formed in an apparently continuous fashion. This new monoclinic phase has a bulk modulous (K_0) of 17(1) GPa, that is almost identical to those for low pressure monoclinic $Sc_2Mo_3O_{12}$ and $Sc_2W_3O_{12}$ [16(1) and 14(1) GPa respectively] but much less than that for monoclinic $Al_2W_3O_{12}$ (K_0 = 28(1) GPa). All of these compounds display a reduction in bulk modulus on going through the orthorhombic to monoclinic phase

transition. Similar behavior has previously been reported for materials with a ReO_3 type structure [59]. This structure type also has many of the structural features typical of negative thermal expansion oxides (open flexible frameworks with two coordinate anions), although none of the compounds ReO_3, TaO_2F and NbO_2F display strong NTE. This initial monoclinic $Zr_2P_2WO_{12}$ structure displays highly anisotropic compressibility ($\beta_c \sim 10 \times \beta_a$) whereas the other $A_2M_3O_{12}$ type monoclinic phases show almost isotropic behavior. Structure determination for the monoclinic $Zr_2P_2WO_{12}$ phase is needed to help explain the origin of these differences.

The second monoclinic phase observed on compression of $Zr_2WP_2O_{12}$ to > ~3 GPa is apparently similar in structure to the phases that were previously observed on compression of $Sc_2W_3O_{12}$ and $Sc_2Mo_3O_{12}$ to greater than ~2.8 and ~2.5 GPa respectively, and presumably similar to the phase reported to form on compressing $Sc_2W_3O_{12}$ to > 1.6 GPa by Garg et al [37]. While Varga et al. were unable to index the diffraction data for $Sc_2W_3O_{12}$ at the time, a unit cell derived from the one proposed for $Zr_2WP_2O_{12}$ satisfactorily explains the high pressure $Sc_2W_3O_{12}$ data. This second monoclinic phase for $Zr_2WP_2O_{12}$ has a ~8% smaller volume per formula unit than the lower pressure monoclinic phase that it forms from at ~3 GPa. Phase coexistence was observed consistent with the discontinuous nature of the transition. The bulk modulous of this phase (K_0 ~36(4) GPa) is similar to that of the starting orthorhombic material and it shows anisotropic compressibility with the a-axis expanding during compression.

At > 6.3 GPa a further crystalline phase formed. As far as we are aware, this apparently triclinic material is not structurally related to any previously seen $A_2M_3O_{12}$ type phases, although structure determination and confirmation of this unit cell requires

better quality diffraction data. Its estimated bulk modulous (K_0 ~ 76(7) GPa) is greater than that of the starting orthorhombic phase.

The pressure induced amorphization seen at > 14 GPa for $Zr_2WP_2O_{12}$ occurs in a regimen where the pressure transmitting medium is not expected to be pseudohydrostatic [45]. Pressure induced amorphization in NTE materials is a common phenomenon that has received much recent discussion including the possibility that it is somehow related to NTE [15]. Its occurrence can be dependent on how hydrostatic the compression is[60] [61, 62]. An amorphization pressure of ~ 14 GPa is high when compared to other NTE oxides such as ZrW_2O_8 (1.5 - 3.5 GPa) and $ZrMo_2O_8$ (< 4 GPa).

4.5. CONCLUSIONS

The high pressure behavior of $Zr_2WP_2O_{12}$ is significantly different from that reported for $A_2M_3O_{12}$ phases (A - +3 ion, M – W or Mo) that adopt a $Sc_2W_3O_{12}$ structure under ambient conditions. Three crystalline to crystalline phase transitions were observed followed by irreversible amorphization at > 14 GPa. The first phase transition, leading to a loss of the orthorhombic $Sc_2W_3O_{12}$ structure that is associated with negative thermal expansion, occurred at much high pressure (~1.4 GPa) than has been seen for related materials (< 0.5 GPa). The first high pressure phase that is formed apparently has a different structure from that seen in previous work on $A_2M_3O_{12}$. The second high pressure phase formed on compression of $Zr_2WP_2O_{12}$ is probably structurally related to the high pressure form of $Sc_2W_3O_{12}$ seen at ~3 GPa.

Table 4.1: $Zr_2WP_2O_{12}$ lattice constants, determined by Le Bail fits, from experimental run1.

P (GPa)	*phase*	*a (Å)*	*b (Å)*	*c (Å)*	*α (deg)*	*Vol (Å^3)*
0.00	**Ortho**	**9.3543(3)**	**12.3288(5)**	**9.1708(4)**		**1057.65(5)**
0.16	**Ortho**	**9.3507(3)**	**12.3107(5)**	**9.1656(4)**		**1055.08(5)**
0.30	**Ortho**	**9.3462(4)**	**12.2911(5)**	**9.1566(4)**		**1051.87(5)**
0.41	**Ortho**	**9.3419(4)**	**12.2780(5)**	**9.1517(4)**		**1049.70(5)**
0.58	**Ortho**	**9.3363(3)**	**12.2558(4)**	**9.1422(4)**		**1046.09(5)**
0.69	**Ortho**	**9.3326(3)**	**12.2342(4)**	**9.1365(4)**		**1043.18(5)**
0.91	**Ortho**	**9.3265(4)**	**12.2106(6)**	**9.1273(5)**		**1039.44(6)**
0.96	**Ortho**	**9.3242(4)**	**12.1983(5)**	**9.1211(5)**		**1037.43(6)**
1.07	**Ortho**	**9.3232(4)**	**12.1909(5)**	**9.1189(5)**		**1036.44(6)**
1.32	**Ortho**	**9.3174(4)**	**12.1743(6)**	**9.1102(5)**		**1033.40(6)**
1.37	**Ortho**	**9.3101(3)**	**12.1540(8)**	**9.1003(6)**		**1029.74(7)**
1.68	**Mono 1**	**9.2959(6)**	**12.0950(8)**	**9.0466(8)**	**89.60(1)**	**1017.13(8)**
1.81	**Mono 1**	**9.2935(5)**	**12.0699(8)**	**8.9978(5)**	**89.495(7)**	**1009.26(7)**
1.98	**Mono 1**	**9.2872(6)**	**12.049(1)**	**8.9716(7)**	**89.398(7)**	**1003.86(8)**
2.14	**Mono 1**	**9.2818(6)**	**12.0199(9)**	**8.9308(7)**	**89.306(8)**	**996.30(8)**
2.55	**Mono 1**	**9.2738(3)**	**11.9633(6)**	**8.8597(5)**	**89.149(5)**	**982.83(6)**
2.80	**Mono 1**	**9.2712(6)**	**11.9253(8)**	**8.8131(8)**	**89.089(7)**	**974.27(8)**
2.99	**Mono 1**	**9.2642(7)**	**11.876(1)**	**8.7596(7)**	**88.897(1)**	**963.58(8)**
3.41	**Mono 1**	**9.2595(4)**	**11.8297(6)**	**8.7057(5)**	**88.646(5)**	**953.33(5)**
3.87	**Mono 1**	**9.238(2)**	**11.828(2)**	**8.701(2)**	**88.39(2)**	**950.4(2)**
	Mono 2	**9.3473(8)**	**11.4280(7)**	**8.2372(7)**	**97.261(7)**	**872.84(7)**
4.34	**Mono 2**	**9.3371(6)**	**11.3967(6)**	**8.2095(5)**	**97.374(5)**	**866.37(5)**
4.83	**Mono 2**	**9.3403(8)**	**11.3549(8)**	**8.1760(8)**	**97.443(8)**	**859.83(8)**
5.14	**Mono 2**	**9.3539(8)**	**11.3243(7)**	**8.1302(8)**	**97.621(7)**	**853.60(8)**
5.35	**Mono 2**	**9.3694(9)**	**11.2988(9)**	**8.0931(9)**	**97.672(8)**	**849.09(8)**
5.27	**Mono 2**	**9.3693(8)**	**11.3157(7)**	**8.0985(8)**	**97.616(6)**	**851.03(8)**
5.03	**Mono 2**	**9.3649(8)**	**11.3283(8)**	**8.1153(9)**	**97.579(7)**	**853.42(9)**
4.81	**Mono 2**	**9.3566(7)**	**11.3522(7)**	**8.1393(9)**	**97.554(6)**	**857.03(8)**
4.75	**Mono 2**	**9.3540(7)**	**11.3573(7)**	**8.1557(7)**	**97.546(6)**	**858.93(7)**
4.56	**Mono 2**	**9.3489(7)**	**11.3694(8)**	**8.1729(6)**	**97.506(6)**	**861.28(6)**
4.39	**Mono 2**	**9.3465(7)**	**11.3845(7)**	**8.1931(6)**	**97.424(6)**	**864.49(6)**
4.28	**Mono 2**	**9.3455(7)**	**11.4024(7)**	**8.2086(6)**	**97.370(6)**	**867.49(6)**
4.01	**Mono 2**	**9.3466(5)**	**11.4217(5)**	**8.2289(5)**	**97.310(5)**	**871.33(5)**
3.46	**Mono 2**	**9.3403(8)**	**11.4679(7)**	**8.2734(7)**	**97.216(7)**	**879.17(7)**
3.32	**Mono 2**	**9.3388(6)**	**11.4824(6)**	**8.2944(5)**	**97.254(6)**	**882.31(6)**
	Mono 1	**9.2766(7)**	**11.8291(8)**	**8.6883(9)**	**88.652(8)**	**953.1(1)**
2.88	**Mono 1**	**9.2773(6)**	**11.8649(8)**	**8.7421(6)**	**88.649(8)**	**962.01(7)**
2.64	**Mono 1**	**9.2774(6)**	**11.8985(9)**	**8.7778(7)**	**88.83(1)**	**968.76(8)**
2.28	**Mono 1**	**9.2762(5)**	**11.9511(9)**	**8.8324(7)**	**89.051(8)**	**979.03(8)**
2.14	**Mono 1**	**9.2884(5)**	**11.9824(7)**	**8.8685(6)**	**89.122(6)**	**986.92(7)**
1.87	**Mono 1**	**9.2933(5)**	**12.0196(8)**	**8.9194(6)**	**89.228(7)**	**996.22(8)**

Table 4.1 (continued):

1.68	**Mono 1**	**9.3054(5)**	**12.0718(9)**	**8.9899(7)**	**89.417(8)**	**1009.81(9)**
1.02	**Ortho**	**9.3188(6)**	**12.1707(8)**	**9.1001(8)**		**1032.10(9)**
0.66	**Ortho**	**9.3334(7)**	**12.2111(8)**	**9.1222(8)**		**1039.67(9)**
0.44	**Ortho**	**9.3392(7)**	**12.2397(9)**	**9.1330(8)**		**1043.98(9)**
0.16	**Ortho**	**9.3476(7)**	**12.281(1)**	**9.1488(8)**		**1050.3(1)**
0.08	**Ortho**	**9.3428(7)**	**12.2855(9)**	**9.1490(8)**		**1050.13(9)**

Table 4.2: $Zr_2WP_2O_{12}$ lattice constants, determined by Le Bail fits, from experimental run2.

P (GPa)	*phase*	*a (Å)*	*b (Å)*	*c (Å)*	*α (deg)*	*β (deg)*	*γ (deg)*	*Vol (Å^3)*
0.44	**Ortho**	**9.3479(6)**	**12.292(1)**	**9.1608(7)**				**1052.6(1)**
0.93	**Ortho**	**9.3294(6)**	**12.2345(8)**	**9.1304(7)**				**1042.14(9)**
1.21	**Ortho**	**9.3226(6)**	**12.2069(9)**	**9.1135(7)**				**1037.11(9)**
1.95	**Mono 1**	**9.2719(7)**	**12.107(1)**	**8.9766(9)**	**89.56(1)**			**1007.7(1)**
2.14	**Mono 1**	**9.2775(7)**	**12.037(1)**	**8.9375(8)**	**89.27(1)**			**998.0(1)**
2.55	**Mono 1**	**9.2747(8)**	**11.9952(2)**	**8.8960(8)**	**89.12(1)**			**989.6(1)**
2.97	**Mono 1**	**9.2774(7)**	**11.9503(2)**	**8.8335(7)**	**88.95(1)**			**979.2(1)**
3.70	**Mono 1**	**9.239(1)**	**11.8474(2)**	**8.712(1)**	**88.45(2)**			**953.2(1)**
	Mono 2	**9.301(1)**	**11.467(1)**	**8.259(1)**	**97.289(8)**			**873.7(1)**
4.83	**Mono 2**	**9.2925(7)**	**11.4186(8)**	**8.2383(6)**	**97.392(7)**			**866.88(7)**
5.66	**Mono 2**	**9.3130(6)**	**11.3435(8)**	**8.1571(8)**	**97.593(7)**			**854.18(6)**
6.29	**Mono 2**	**9.355(1)**	**11.301(1)**	**8.116(1)**	**97.78(1)**			**850.1(1)**
	Tric	**11.204(2)**	**9.374(2)**	**12.499(2)**	**88.229(8)**	**141.717(5)**	**91.43(2)**	**812.9(2)**
7.41	**Tric**	**11.1475(8)**	**9.3759(7)**	**12.515(1)**	**88.866(4)**	**141.654(2)**	**90.930(7)**	**811.34(7)**
8.07	**Tric**	**11.1388(7)**	**9.389(1)**	**12.464(1)**	**88.875(5)**	**141.622(2)**	**90.947(8)**	**809.15(9)**
9.94	**Tric**	**11.0392(9)**	**9.370(1)**	**12.408(1)**	**89.280(5)**	**141.610(2)**	**90.591(9)**	**796.97(8)**
10.76	**Tric**	**10.996(1)**	**9.377(1)**	**12.363(1)**	**89.209(5)**	**141.495(3)**	**90.67(2)**	**793.64(8)**
12.85	**Tric**	**10.9258(6)**	**9.3460(6)**	**12.2423(7)**	**89.472(3)**	**141.641(2)**	**90.420(5)**	**775.76(2)**
13.76	**Tric**	**10.877(1)**	**9.3407(9)**	**12.196(1)**	**89.474(5)**	**141.578(3)**	**90.40(1)**	**770.02(6)**
16.04		-	-	-	-	-	-	-
13.68		-	-	-	-	-	-	-
9.67		-	-	-	-	-	-	-
5.88		-	-	-	-	-	-	-
1.37		-	-	-	-	-	-	-

Table 4.3: Phase transition pressures and parameters from fitting a 3rd order Birch-Murnaghan equations of state to the P-V data for $Zr_2WP_2O_{12}$ shown in Tables 4.1 and 4.2. In each case, K_p was fixed at 4 during the fit to the EOS.

		Run 1 compression	Run 1 decompression	Run 2	Pooled
phase 1	**P-range (GPa)**	0.0 - 1.37	1.02 - 0.08	0.44 - 1.2	0.0-1.37
	Vo (Å^3)	1058(1)	1053(1)	1062(2)	1057(1)
	Ko (GPa)	49(2)	50(3)	48(5)	49(5)
	Average K (GPa)	52.36	51.81	51.55	
phase 2	**P-range (GPa)**	1.68 - 3.41	2.88 - 1.68	1.95 - 2.97	1.68-3.41
	Vo (Å^3)	1104(5)	1096(10)	1071(10)	1108(15)
	Ko (GPa)	17(1)	17(2)	27(4)	16(2)
	Average K (GPa)	26.74	25.71	37.45	
phase 3	**P-range (GPa)**	3.87 - 5.35	5.27 - 3.32	3.7 - 6.3	3.7-6.3
	Vo (Å^3)	956(9)	954(3)	921(10)	941(9)
	Ko (GPa)	36(4)	37(1)	66(12)	44(6)
	Average K (GPa)	54.64	52.91	89.29	
phase 4	**P-range (GPa)**			7.41 - 13.76	
	Vo (Å^3)			885(8)	
	Ko (GPa)			76(7)	
	Average K (GPa)			119.05	

Table 4.4: Average linear compressibilities for the different phases observed during the compression of $Zr_2WP_2O_{12}$. The values were obtained from linear fits to ln(lattice constant) vs P

		Run 1	Run 1	Run 2
phase 1	**P-range (GPa)**	0.0 - 1.37	1.02 - 0.08	0.44 - 1.2
	a (GPa^{-1})	$-3.3(1)\times10^{-3}$	$-3.0(5)\times10^{-3}$	$-3.6(4)\times10^{-3}$
	b (GPa^{-1})	$-10.3(3)\times10^{-3}$	$-10.3(4)\times10^{-3}$	$-9.1(4)\times10^{-3}$
	c (GPa^{-1})	$-5.5(2)\times10^{-3}$	$-5.8(3)\times10^{-3}$	$-6.74(5)\times10^{-3}$
phase 2	**P-range (GPa)**	1.68 - 3.41	2.88 - 1.68	1.95 - 2.97
	a (GPa^{-1})	$-2.3(1)\times10^{-3}$	$-2.4(7)\times10^{-3}$	$0.4(4)\times10^{-3}$
	b (GPa^{-1})	$-13.0(4)\times10^{-3}$	$-14.0(7)\times10^{-3}$	$-12(2)\times10^{-3}$
	c (GPa^{-1})	$-22.0(8)\times10^{-3}$	$-22(2)\times10^{-3}$	$-15(1)\times10^{-3}$
phase 3	**P-range (GPa)**	3.87 - 5.35	5.27 - 3.32	3.7 - 6.3
	a (GPa^{-1})	$1(1)\times10^{-3}$	$1.5(2)\times10^{-3}$	$2(1)\times10^{-3}$
	b (GPa^{-1})	$-7.6(4)\times10^{-3}$	$-7.6(2)\times10^{-3}$	$-5.8(6)\times10^{-3}$
	c (GPa^{-1})	$-12(2)\times10^{-3}$	$-12.3(4)\times10^{-3}$	$-7(2)\times10^{-3}$
phase 4	**P-range (GPa)**			7.41 - 13.76
	a (GPa^{-1})			$-3.9(2)\times10^{-3}$
	b (GPa^{-1})			$-0.7(2)\times10^{-3}$
	c (GPa^{-1})			$-4.0(2)\times10^{-3}$

Table 4.5: Summary of the high pressure behavior of $Sc_2W_3O_{12}$ related materials.

		$Sc_2W_3O_{12}$	$Sc_2Mo_3O_{12}$	$Al_2W_3O_{12}$	$Zr_2WP_2O_{12}$
phase 1		Pnca	Pnca	Pnca	Pnca
	Ko (GPa)	31(3)[41]	32(2)[26]; 6[39]	48[26]	49(2)
	P_T (GPa)	0.3[41]; 0.6[37]	0.29[40]	0.1[26]; 0.28[63]	1.4; 1.2
			0.25-0.6[26]	0.5[64]	
phase 2		$P2_1/a$	$P2_1/a$	$P2_1/a$	$P2_1/n$
	Ko (GPa)	14(1)[41]	16(1)[26]	28(1)[26]	17(1)
	P_T (GPa)	2.8[41]	2.5 - 3[26]		3.4
		1.6[37]	2.7[40]		
phase 3		Unidentified	Unidentified	N/A	$P2_1/n$
	Ko (GPa)				36(4)
	P_T (GPa)				6.3
phase 4					P1 or P-1
	Ko (GPa)				76(7)

4.6. REFERENCES

[1] Sleight AW. Thermal Contraction. Endeavour 1995;19:64.

[2] Sleight AW. Compounds that Contract on Heating. Inorg. Chem. 1998;37:2854.

[3] Sleight AW. Isotropic Negative Thermal Expansion. Annual Review of Materials Science 1998;28:29.

[4] Sleight AW. Negative thermal expansion materials. Current Opinion in Solid State and Materials Science 1998;3:128.

[5] Evans JSO, Mary TA, Sleight AW. Negative thermal expansion materials. Physcia B 1998;241-243:311.

[6] Evans JSO. Negative Thermal Expansion Materials. J. Chem. Soc. Dalton Trans. 1999:3317.

[7] Evans JSO, Mary TA, Sleight AW. Negative Thermal Expansion in a Large Molybdate and Tungstate Family. J. Solid State Chem. 1997;133:580.

[8] Breval E, Agrawal DK. Thermal-Expansion Characteristics of [NZP], $NaZr_2P_3O_{12}$-Type Materials - a Review. Brit Ceram T 1995;94:27.

[9] Roy R, Agrawal DK, McKinstry HA. Very Low Thermal Expansion Coefficient Materials. Annu. Rev. Mater. Sci. 1989;19:59.

[10] Lenain GE, McKinstry HA, Alamo J, Agrawal DK. Structural model for thermal expansion in alkali metal zirconium phosphates $MZr_2P_3O_{12}$ (M = Li, Na, K, Rb, Cs). J. Mater. Sci. 1987;22:17.

[11] Woodcock DA, Lightfoot P, Ritter C. Mechanism of low thermal expansion in the cation-ordered Nasicon structure. Chem. Commun. 1998:107.

[12] Woodcock DA, Lightfoot P, Smith RI. Powder neutron diffraction studies of three low thermal expansion phases in the NZP family: $K_{0.5}Nb_{0.5}Ti_{1.5}(PO_4)_3$, $Ba_{0.5}Ti_2(PO_4)_3$ and $Ca_{0.25}Sr_{0.25}Zr_2(PO_4)_3$. J. Mater. Chem. 1999;9:2631.

[13] Evans JSO, Hu Z, Jorgensen JD, Argyriou DN, Short S, Sleight AW. Compressibility, Phase Transitions, and Oxygen Migration in Zirconium Tungstate, ZrW_2O_8. Science 1997;275:61.

[14] Mary TA, Evans JSO, Vogt T, Sleight AW. Negative Thermal Expansion from 0.3 to 1050 Kelvin in ZrW_2O_8. Science 1996;272:90.

[15] Perottoni CA, de Jornada JAH. Pressure-Induced Amorphization and Negative Thermal Expansion in ZrW_2O_8. Science 1998;280:886.

[16] Korthuis V, Khosrovani N, Sleight AW, Roberts N, Dupree R, Warren WW. Negative Thermal Expansion and Phase Transitions in the $ZrV_{2-x}P_xO_7$ Series. Chem. Mater. 1995;7:412.

[17] Wetherfold RC, Wang J. Tailoring thermal deformation by using layered beams. Compos. Sci. Technol. 1995;53:1.

[18] Fleming DA, Johnson DW, Lemaire PJ. Article Comprising a Temperature Compensated Optical Fiber Refractive Index Grating. USA: Lucent Technologies, 1997.

[19] Fleming DA, Lemaire PJ, Johnson DW. Temperature compensated optical fiber refractive index grating. European Patent EP 97-306798 19970902. USA: Lucent Technologies, Inc., 1998. p.7.

[20] Balch DK, Dunand DC. Copper-Zirconium Tungstate Composites Exhibiting Low and Negative Thermal Expansion Influenced by Reinforcement Phase Transformations. Metall. Mater. Trans. A 2004;35A:1159.

[21] Holzer H, Dunand DC. Phase transformation and thermal expansion of Cu/ZrW_2O_8 metal matrix composites. J. Mater. Res. 1999;14:780.

[22] Yilmaz S. Phase transformations in thermally cycled Cu/ZrW_2O_8 composites investogated by synchrotron x-ray diffraction. J. Phys. Condens. Matter. 2002;14:365.

[23] Grzechnik A, Crichton WA. Structural transformations in cubic $ZrMo_2O_8$ at high pressures and high temperatures. Solid State Sci. 2002;4:1137.

[24] Muthu DVS, Chen B, Wrobel JM, Krogh Andersen AM, Carlson S, Kruger MB. Pressure-induced phase transitions in α–$ZrMo_2O_8$. Phys. Rev. B 2002;65:064101.

[25] Jorgensen JD, Hu Z, Short S, Sleight AW, Evans JSO. Pressure-induced cubic-to-orthorhombic phase transfromation in the negative thermal expansion material HfW_2O_8. J. Appl. Phys. 2001;89:3184.

[26] Varga T, Wilkinson AP, Lind C, Bassett WA, Zha C-S. High pressure synchrotron x-ray powder diffraction study of $Sc_2Mo_3O_{12}$ and $Al_2W_3O_{12}$ J. Phys.: Condens. Matter 2005;17:4271.

[27] Chen B, Muthu DVS, Liu ZX, Sleight AW, Kruger MB. High-pressure Raman and infrared study of HfW_2O_8. Phys. Rev. B 2001;64:214111.

[28] Varga T, Wilkinson AP, Lind C, Bassett WA, Zha C-S. Pressure-induced amorphization of cubic ZrW_2O_8 studied in-situ and ex-situ by synchrotron x-ray absorption spectroscopy and diffraction. Phys. Rev. B 2005;72:024117.

[29] Varga T, Wilkinson AP, Lind C, Basset WA, Zha C-S. Pressure-induced amorphization of cubic $ZrMo_2O_8$ studied in-situ by x-ray absorption spectroscopy and diffraction. Solid State Communications 2005;135:739.

[30] Secco RA, Liu H, Imanaka N, Adachi G. Pressure-induced amorphization in negative thermal expansion $Sc_2(WO_4)_3$. Journal of Materials Science Letters 2001;20:1339.

[31] Nassau K, Levinstein HJ, Loiacono GM. Trivalent Rare-Earth Tungstates of the Type $M_2(WO_4)_3$. J. Am. Ceram. Soc. 1964;47:363.

[32] Nassau K, Levinstein HJ, Loiacono GM. A comprehensive study of trivalent tungstates and molybdates of the type $L_2(MO_4)_3$. J. Phys. Chem. Solids 1965;26:1805.

[33] Abrahams SC, Bernstein JL. Crystal Structure of the Transition-Metal Molybdates and Tungstates. II. Diamagnetic $Sc_2(WO_4)_3$. J. Chem. Phys. 1966;45:2745.

[34] Sleight AW, Brixner LH. A New Ferroelastic Transition in Some $A_2(MO_4)_3$ Molybdates and Tungstates. J. Solid State Chem. 1973;7:172.

[35] Evans JSO, Mary TA. Structural Phase Transitions and negative thermal expansion in $Sc_2(MoO_4)_3$. International Journal of Inorganic Materials 2000;2:143.

[36] Tyagi AK, Achary SN, Mathews MD. Phase transition and negative thermal expansion in $A_2(MoO_4)_3$ system (A = Fe^{3+}, Cr^{3+} and Al^{3+}). J. Alloys Compd. 2002;339:207.

[37] Garg N, Murli C, Tyagi AK, Sharma SM. Phase transitions in $Sc_2(WO_4)_3$ under high pressure. Phys. Rev. B 2005;72.

[38] Arora AK, Nithya R, Yagi T, Miyajima N, Mary TA. Two-stage amorphziation of scandium molybdate at high pressure. Solid State Commun. 2004;129:9.

[39] Arora AK, Yagi T, Miyajima N, Mary TA. Amorphization and decomposition of scandium molybdate at high pressure. J. Appl. Phys. 2005;97:013508.

[40] Paraguassu W, Maczka M, Souza Filho AG, Freire PTC, Mendes Filho J, Melo FEA, Macalik L, Gerward L, Staun Olsen J, Waskowska A, Hanuza J. Pressure-induced structural transformations in the molybdate $Sc_2(MoO_4)_3$. Phys. Rev. B 2004;69:094111.

[41] Varga T, Wilkinson AP, Lind C, Bassett WA, Zha C-S. In-situ high pressure synchrotron x-ray diffraction study of $Sc_2W_3O_{12}$ at up to 10 GPa. Phys. Rev. B 2005;71:214106.

[42] Suzuki T, Omote A. Negative Thermal Expansion in $(HfMg)(WO_4)_3$. J. Am. Ceram. Soc. 2004;87:1365.

[43] Martinek CA, Hummel FA. Subsolidus Equilibria in System ZrO_2-WO_3-P_2O_5. J. Am. Ceram. Soc. 1970;53:159.

[44] Evans JSO, Mary TA, Sleight AW. Structure of $Zr_2(WO_4)(PO_4)_2$ from Powder X-ray Data: Cation Ordering with No Superstructure. J. Solid State Chem. 1995;120:101.

[45] Piermarini GJ, Block S, Barnett JD. Hydrostatic limits in liquids and solids to 100 kbar. J. Appl. Phys. 1973;44:5377.

[46] Barnett JD, Block S, Piermarini GJ. An Optical Fluorescence System for Quantitative Pressure Measurement in the Diamond-Anvil Cell. Rev. Sci. Instrum. 1973;44:1.

[47] Miletich R, Allan D, R., Kuhs W, F. High-Pressure Single-Crystal Techniques. Rev. Mineral. Geochem. 2001;41:445.

[48] Cetinkol M, Wilkinson AP, Lind C, Bassett WA, Zha C-S. High-pressure powder diffraction study of TaO_2F. J. Phys. Chem. Solids 2007;68:611.

[49] Hammersley AP, Svensson SO, Hanfland M, Fitch AN, Hausermann D. Two-dimensional detector software: From real detector to idealised image or two-theta scan. High Pressure Research 1996;14:235.

[50] JADE. computer code JADE. Livermore, CA: Materials Data, Inc., 1995-2005.

[51] Werner PE, Eriksson L, Westdahl M. Treor, a Semi-Exhaustive Trial-and-Error Powder Indexing Program for All Symmetries. J. Appl. Crystallogr. 1985;18:367.

[52] Toby BH. CMPR - a powder diffraction toolkit. J. Appl. Crystallogr. 2005;38:1040.

[53] Rietveld HM. A Profile Refinement Method for Nuclear and Magnetic Structures. Journal of Applied Crystallography 1969;2:65.

[54] Le Bail A, Duroy H, Fourquet JL. Abinitio Structure Determination of $LiSbWO_6$ by X-Ray-Powder Diffraction. Mater. Res. Bull. 1988;23:447.

[55] Larson AC, Von Dreele RB. GSAS - General Structure Analysis System. Los Alamos Laboratory: Report LA-UR-86-748, 1987.

[56] Toby BH. EXPGUI, a graphical user interface for GSAS. J. Appl. Crystallogr. 2001;34:210.

[57] Birch F. Finite elastic strain of cubic crystals. Phys. Rev. 1947;71:809.

[58] Angel RJ. EOS-FIT. computer code EOS-FIT. Blacksburg, VA: Virginia Tech, 2001.

[59] Schirber JE, Morosin B. Compressibility Collapse Transition in ReO_3. Phys. Rev. Lett. 1979;42:1485.

[60] Sharma SM, Sikka SK. Pressure Induced Amorphization of Materials. Prog. Mater. Sci. 1996;40:1.

[61] Lind C, VanDerveer DG, Wilkinson AP, Chen J, Vaughan MT, Weidner DJ. New high pressure form of the negative thermal expansion materials zirconium molybdate and hafnium molybdate. Chem. Mater. 2001;13:487.

[62] Kingma KJ, Meade C, Hemley RJ, Mao HK, Veblen DR. Microstructural Observations of Alpha-Quartz Amorphization. Science 1993;259:666.

[63] Maczka M, Paraguassu W, Souza Filho AG, Freire PTC, Mendes Filho J, Melo FEA, Hanuza J. High-pressure Raman study of $Al_2(WO_4)_3$. J. Solid State Chem. 2004;177:2002.

[64] Mukherjee GD, Vijaykumar V, Achary SN, Tyagi AK, Godwal BK. Phase transitions in $Al_2(WO_4)_3$: high pressure investigations of low frequency dielectric constant and crystal structure. J. Phys.: Condens. Matter 2004;16:7321.

CHAPTER 5

PRESSURE DEPENDENCE OF NEGATIVE THERMAL EXPANSION IN $Zr_2(WO_4)(PO_4)_2$

5.1. INTRODUCTION

Recent work on negative thermal expansion (NTE) materials has been driven by a combination of fundamental interest in this relatively unusual property and the possibility of applications [1-4]. During the manufacture and use of controlled thermal expansion composites, stresses may be encountered leading to phase transitions and a loss, or change, of NTE behavior**.** For example, phase transitions in composites containing ZrW_2O_8, due to stresses occurring during processing or thermal expansion mismatch between the filler and matrix, have been observed [5, 6]. Such transitions are an impediment to application. Little attention has been paid to the effect of compression on the expansion coefficients of a particular phase. The pressure dependence of the volume coefficient of thermal expansion, α_V, is related to the temperature dependence of the bulk modulus by (5.1).

$$\left(\frac{\partial \alpha_V}{\partial P}\right)_T = \frac{1}{K^2}\left(\frac{\partial K}{\partial T}\right)_p \quad (5.1)$$

The temperature dependence of the bulk modulus, $(\delta K/\delta T)_p$, has been examined theoretically [7, 8] and experimentally for many materials and it is typically negative, indicating that the volume coefficient of thermal expansion usually decreases on compression [9].

Chapman and Chupas reported that the thermal expansion coefficient for the NTE material $Zn(CN)_2$ became more negative on compression [10], with the average linear coefficient of thermal expansion (CTE) changing from -17.4(2) $\times 10^{-6}$ K^{-1} to -19.4(2) $\times 10^{-6}$ K^{-1} on going from ambient pressure to 0.4 GPa. As part of our general exploration of how modest pressures affect thermal expansion in very low and NTE materials, we recently found that pressure dramatically enhances expansion in TaO_2F[11] (see Chapter 3). Here, we report results for $Zr_2(WO_4)(PO_4)_2$ [12], one of many NTE materials that are close structural relatives of $Sc_2W_3O_{12}$. Prior dilatometer and x-ray diffraction measurements indicate mean linear coefficients of thermal expansion -6 $\times 10^{-6}$ and -3$\times 10^{-6}$ K^{-1} respectively [13].

5.2. EXPERIMENTAL PROCEDURES

5.2.1. Sample Preparation

$Zr_2(WO_4)(PO_4)_2$ was prepared using stoichiometric amounts of ZrO_2 (Alfa Aesar, 99.7%), WO_3 (Strem Chemicals, 99.8 %) and $NH_4H_2PO_4$ (J.T. Baker, 99.2 %). The starting compounds were ground together in an agate mortar, heated in an alumina crucible for 4 hours at 900 ºC, and 4 h at 1250 ºC in air. This treatment was followed by grinding and heating the powder mixture for another 2h at 1250 ºC and resulted in an off-white homogeneous product.

5.2.2. Neutron diffraction data collection and analyses

$Zr_2(WO_4)(PO_4)_2$ was loaded into a helium-gas pressure cell [14]. Powder diffraction data were collected on the Special Environment Powder Diffractometer [15],

at the Intense Pulsed Neutron Source (IPNS), Argonne National Laboratory, Argonne, IL. The gas cell allowed us to apply precisely measured, hydrostatic pressure. At room temperature, data were recorded at 0, 0.1, 0.15, 0.2, 0.3 and 0.4 GPa. Then, at constant pressures of 0.0 GPa, 0.2 GPa and 0.3 GPa, measurements were made at 225, 125, and 60 K. Data collection times were about 4 hours, with approximately an hour of equilibration time in between each measurement.

The program suite GSAS [16] with the EXPGUI [17] graphical interface was used to perform Rietveld [18] analyses on the data from the 90 degree detector banks of the instrument. The reported $Zr_2(WO_4)(PO_4)_2$ (Pnca) structure [12] was used as a starting model. Initially, the room temperature ambient pressure data were analyzed with the lattice constants fixed at the values obtained from the analysis of a laboratory powder x-ray pattern and the diffractometer constant, DIFC, was varied. Subsequently, all the data sets were analyzed with freely varying lattice constants and the diffractometer constants fixed at the values initially determined by analysis of the ambient data set. An absorption coefficient was refined only for the ambient pressure and room temperature data set and this value applied to the remaining data sets. In each case, the atomic coordinates and independent isotropic atomic displacement parameters were refined for each atom. A representative Rietveld fit to the data is shown in Figure 5.1. The lattice constants and unit cell volumes obtained from the Rietveld analyses are shown in Table 5.1.

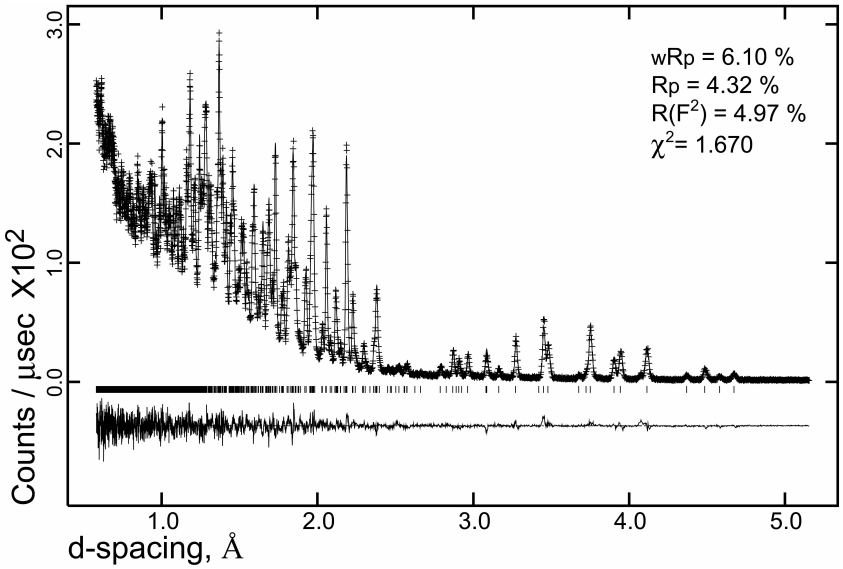

Figure 5.1: Rietveld fit to the neutron diffraction data for $Zr_2(WO_4)(PO_4)_2$ recorded at ambient pressure and room temperature. Observed(+), calculated(-), and difference (lower trace).

Table 5.1: Lattice constants and unit cell volume for $Zr_2(WO_4)(PO_4)_2$ as a function of pressure and temperature, determined from Rietveld analyses of neutron diffraction data.

P(GPa) at 296 K	a (Å)	b (Å)	c (Å)	V (Å^3)
0.000	9.3462(3)	12.3313(4)	9.1606(3)	1055.77(4)
0.100	9.3427(3)	12.3205(4)	9.1566(3)	1054.00(4)
0.150	9.3424(3)	12.3148(4)	9.1548(3)	1053.26(4)
0.200	9.3405(3)	12.3087(4)	9.1527(3)	1052.29(4)
0.294	9.3377(3)	12.2996(4)	9.1483(3)	1050.70(5)
0.372	9.3355(5)	12.2920(5)	9.1458(5)	1049.50(5)
T(K) at 0 GPa				
296	9.3462(3)	12.3313(4)	9.1606(3)	1055.77(4)
225	9.3511(3)	12.3278(4)	9.1657(3)	1056.61(4)
125	9.3576(3)	12.3244(4)	9.1739(3)	1058.00(4)
60	9.3640(3)	12.3243(4)	9.1793(3)	1059.34(4)
T(K) at 0.2 GPa				
296	9.3405(3)	12.3087(4)	9.1527(3)	1052.29(4)
225	9.3458(3)	12.3062(4)	9.1584(3)	1053.32(5)
125	9.3533(3)	12.3040(4)	9.1662(3)	1054.88(5)
60	9.3586(3)	12.3020(5)	9.1718(3)	1055.95(5)
T(K) at 0.3 GPa				
296	9.3377(3)	12.2996(4)	9.1483(3)	1050.70(5)
225	9.3424(3)	12.2955(5)	9.1536(3)	1051.47(5)
125	9.3506(4)	12.2923(5)	9.1623(3)	1053.13(5)
60	9.3549(4)	12.2911(5)	9.1682(3)	1054.17(5)

5.3. RESULTS AND DISCUSSION

$Zr_2(WO_4)(PO_4)_2$ adopts the orthorhombic $Sc_2W_3O_{12}$ structure [19] consisting of ZrO_6 octahedra sharing corners with two WO_4 tetrahedra and four PO_4 tetrahedra. Some compounds with this structure undergo a volume reducing transition to a monoclinic phase on cooling [20] although $Sc_2W_3O_{12}$ itself does not go through a transition down to 10 K [21]. $Zr_2(WO_4)(PO_4)_2$ remained orthorhombic under all the conditions examined in the present study, consistent with our diamond anvil cell high pressure x-ray work where the first transition observed for $Zr_2(WO_4)(PO_4)_2$ at ambient temperature occurred at ~ 1.4 GPa. (see Chapter 4)

Plots of normalized unit cell volume and lattice constants as a function of temperature, at different pressures, are shown in Figures 5.2 and 5.3, respectively.

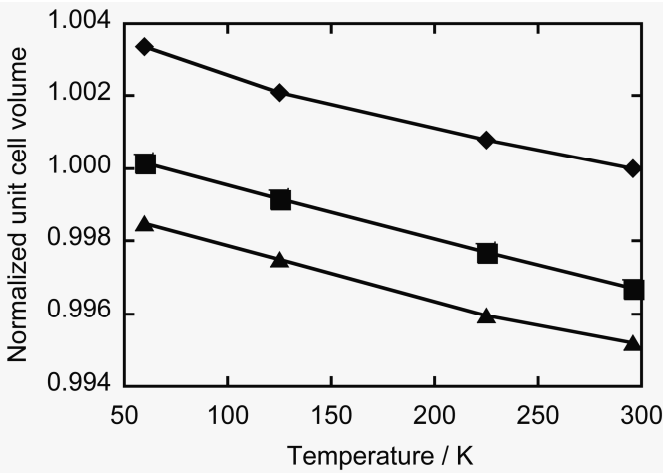

Figure 5.2: Variation of the unit cell volume for $Zr_2(WO_4)(PO_4)_2$ on cooling at 0 GPa (diamonds), 0.2 GPa (squares) and 0.3 GPa (triangles). All values are normalized to the volume for 296K and 0 GPa.

Fitting a 3rd order Birch-Murnaghan equation of state (EOS), using EOSFIT [22], to the room temperature volume data resulted in V_0=1055.76(5) $Å^3$, K_0= 61.3(8) GPa

with K_p fixed at 4 (see Figure 5.4 for fit). Freely varying K_p led to similar results, but with larger estimated standard deviations; V_0 = 1055.78(7) Å^3, K_0 = 60(3) GPa, K_p = 11(15). Linear compressibility values were estimated to be $\beta_a = 3.0(1) \times 10^{-3}$ GPa^{-1}, $\beta_b = 8.6(2) \times 10^{-3}$ GPa^{-1}, $\beta_c = 4.4(1) \times 10^{-3}$ GPa^{-1} by straight line fits over 0 – 0.37 GPa range using the lattice constants at room temperature. Our estimated bulk modulus, 61.3(8) GPa, is significantly larger than those reported for orthorhombic $Sc_2W_3O_{12}$ (31 GPa [23], 32 GPa [24]), $Sc_2Mo_3O_{12}$ (32 GPa [25]), and $Y_2W_3O_{12}$ (~25 GPa [26]) but similar to that for aluminum tungstate (~48 GPa [25]). This trend is broadly in agreement with the observed volumes per oxide ion for these phases: $Zr_2P_2WO_{12}$, 22.0 Å^3; $Al_2W_3O_{12}$, 21.7 Å^3; $Sc_2W_3O_{12}$, 25.7 Å^3; $Y_2W_3O_{12}$, 29.1 Å^3.

Volume and linear thermal expansion coefficients at pressures of 0, 0.2, and 0.3 GPa were obtained by straight line fits to the lattice constants and unit cell volume (see Table 2). It is clear that pressure has little if any effect on these parameters, in contrast to our recent observations in Chapter 3 on the low thermal expansion material TaO_2F and reports on the negative thermal expansion material $Zn(CN)_2$ [10]. The same data can be looked at from the perspective of the temperature dependence of the bulk modulus. Using straight line fits to ln(V) versus P, bulk moduli for this phase were estimated to be 61(1), 65(2), 62(2) and 62(1) GPa at 60, 125, 225 and 296 K respectively.

Previous studies of compounds adopting the $Sc_2W_3O_{12}$ structure have shown that negative thermal expansion in these materials can be associated with systematic changes in crystallographic M-O-M' bond angles as a function temperature [27, 28]. At least for $Sc_2W_3O_{12}$, the structural changes accompanying volume reduction on compression are not the same as those seen on volume reduction due to heating [24]. An examination of

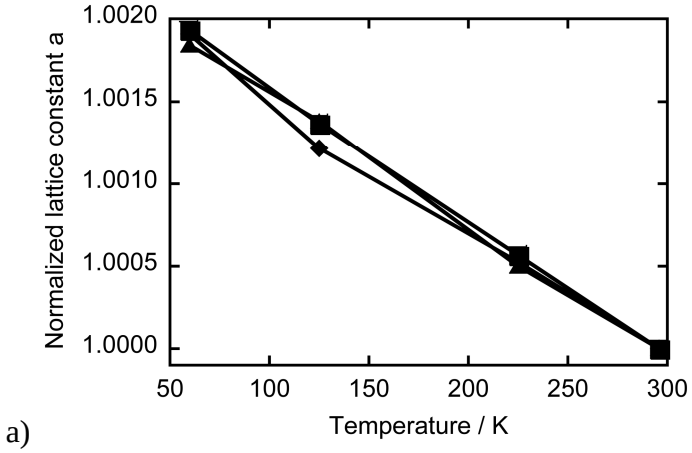

a)

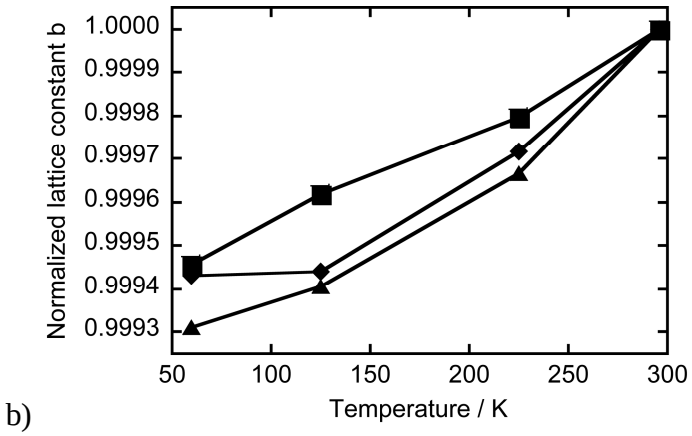

b)

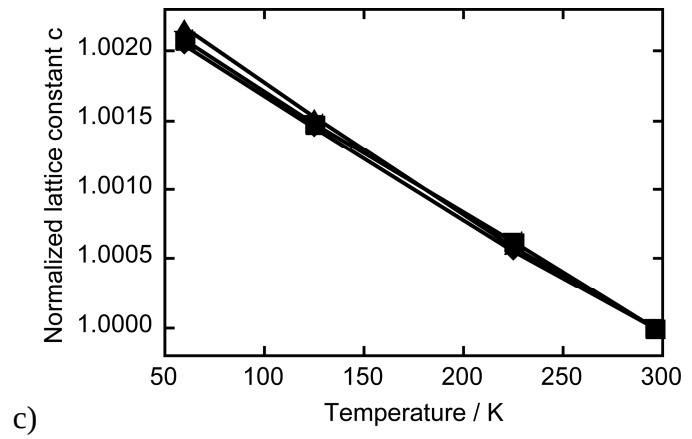

c)

Figure 5.3: Variation of the unit cell axes for $Zr_2(WO_4)(PO_4)_2$ on cooling at 0 GPa (diamonds), 0.2 GPa (squares) and 0.3 GPa (triangles). Panel (a) shows data for the a-axis, panel (b) shows data for the b-axis, and panel (c) shows data for the c-axis. All values are normalized to the lattice constant at 296 K for the pressure in question.

Table 5.2 Coefficients of thermal expansion for $Zr_2(WO_4)(PO_4)_2$ as a function of pressure

P (GPa)	α_V	α_a	α_b	α_c
0.0	-1.4(1) x 10^{-5} K^{-1}	-7.9(5) x 10^{-6} K^{-1}	2.5(5) x 10^{-6} K^{-1}	-8.7(2) x 10^{-6} K^{-1}
0.2	-1.47(3) x 10^{-5} K^{-1}	-8.2(1) x 10^{-6} K^{-1}	2.2(2) x 10^{-6} K^{-1}	-8.7(1) x 10^{-6} K^{-1}
0.3	-1.42(8) x 10^{-5} K^{-1}	-7.9(3) x 10^{-6} K^{-1}	2.9(5) x 10^{-6} K^{-1}	-9.2(2) x 10^{-6} K^{-1}

crystallographic Zr-O-P and Zr-O-W bond angles in $Zr_2WP_2O_{12}$, derived from our Rietveld fits, as a function of temperature or pressure, shows considerable scatter (values not shown) and no obvious trends. The temperature dependence of the atomic displacement parameters (ADPs) for all crystallographic sites in $Zr_2WP_2O_{12}$ is well behaved (values not shown) and pressure does not have any effect on the apparent atomic displacement parameters (ADPs) of any atom, unlike our observations for TaO_2F [11].

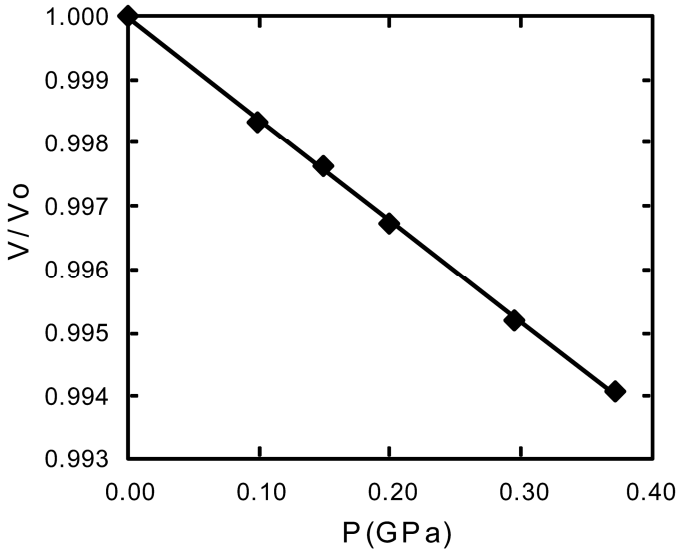

Figure 5.4: Fit to the P-V data for ambient temperature using a Birch-Murnaghan equation of state (V_0=1055.76(5) $Å^3$, K_0= 61.3(8) GPa, K_p fixed at 4).

5.4. CONCLUSIONS

$Zr_2WP_2O_{12}$ is orthorhombic (Pnca) throughout the P-T range examined (0 – 0.3 GPa, 60 – 300K). Under ambient conditions it displays anisotropic negative thermal expansion (NTE) (α_v = -14.0(10) x 10^{-6} K^{-1}, α_a = -7.9(5) x 10^{-6} K^{-1}, α_b = 2.5(5) x 10^{-6} K^{-1}, α_c = -8.7(2) x 10^{-6} K^{-1} at 0 GPa). It has a bulk modulous, $K_{0,}$ of 61.3(8) GPa at ambient temperature, significantly stiffer than structurally related compounds with larger available volumes per oxide ion. Unlike $Zn(CN)_2$ and TaO_2F, pressure has no detectable effect on thermal expansion (α_v = -14.2(8) x 10^{-6} K^{-1}, α_a = -7.9(3) x 10^{-6} K^{-1}, α_b = 2.9(5) x 10^{-6} K^{-1}, α_c = -9.2(2) x 10^{-6} K^{-1} at 0.3 GPa)

5.5. REFERENCES

[1] Wetherfold RC, Wang J. Tailoring thermal deformation by using layered beams. Compos. Sci. Technol. 1995;53:1.

[2] Fleming DA, Johnson DW, Lemaire PJ. Article Comprising a Temperature Compensated Optical Fiber Refractive Index Grating. USA: Lucent Technologies, 1997.

[3] Fleming DA, Lemaire PJ, Johnson DW. Temperature compensated optical fiber refractive index grating. European Patent EP 97-306798 19970902. USA: Lucent Technologies, Inc., 1998. p.7.

[4] Balch DK, Dunand DC. Copper-Zirconium Tungstate Composites Exhibiting Low and Negative Thermal Expansion Influenced by Reinforcement Phase Transformations. Metall. Mater. Trans. A 2004;35A:1159.

[5] Holzer H, Dunand DC. Phase transformation and thermal expansion of Cu/ZrW_2O_8 metal matrix composites. J. Mater. Res. 1999;14:780.

[6] Yilmaz S. Phase transformations in thermally cycled Cu/ZrW_2O_8 composites investogated by synchrotron x-ray diffraction. J. Phys. Condens. Matter. 2002;14:365.

[7] Garai J, Laugier A. The temperature dependence of the isothermal bulk modulus at 1 bar pressure. J. Appl. Phys. 2007;101.

[8] Anderson OL. Derivation of Wachtman's Equation for the Temperature Dependence of Elastic Moduli of Oxide Compounds. Physical Review 1966;144:553.

[9] Touloukian YS, Kirby RK, Taylor RE, Lee TYR. Thermal Expansion: Nonmetallic Solids. New York: Plenum, 1970.

[10] Chapman KW, Chupas PJ. Pressure Enhancement of Negative Thermal Expansion Behavior and Induced Framework Softening in Zinc Cyanide. J. Am. Chem. Soc. 2007;129:10090.

[11] Cetinkol M, Wilkinson AP. manuscript in preparation.

[12] Evans JSO, Mary TA, Sleight AW. Structure of $Zr_2(WO_4)(PO_4)_2$ from Powder X-ray Data: Cation Ordering with No Superstructure. J. Solid State Chem. 1995;120:101.

[13] Evans JSO, Mary TA, Sleight AW. Negative Thermal Expansion in a Large Molybdate and Tungstate Family. J. Solid State Chem. 1997;133:580.

[14] Jorgensen JD, Pei S, Lightfoot P, Hinks DG, Veal BW, Dabrowski B, Paulikas AP, Kleb R, Brown ID. Pressure-induced charge transfer and dT_c/dP in Y $Ba_2Cu_3O_{7-x}$. Physica C 1990;171:93.

[15] Jorgensen JD, Faber Jr. J, Carpenter JM, Crawford RK, Haumann JR, Hitterman RL, Kleb R, Ostrowski GE, Rotella FJ, Worlton TG. Electronically Focused Time-of-Flight Powder Diffractometers at the Intense Pulsed Neutron Source. J. App. Crystallogr. 1989;22:321.

[16] Larson AC, Von Dreele RB. GSAS - General Structure Analysis System. Los Alamos Laboratory: Report LA-UR-86-748, 1987.

[17] Toby BH. EXPGUI, a graphical user interface for GSAS. J. Appl. Crystallogr. 2001;34:210.

[18] Rietveld HM. A Profile Refinement Method for Nuclear and Magnetic Structures. Journal of Applied Crystallography 1969;2:65.

[19] Abrahams SC, Bernstein JL. Crystal Structure of the Transition-Metal Molybdates and Tungstates. II. Diamagnetic $Sc_2(WO_4)_3$. J. Chem. Phys. 1966;45:2745.

[20] Sleight AW, Brixner LH. A New Ferroelastic Transition in Some $A_2(MO_4)_3$ Molybdates and Tungstates. J. Solid State Chem. 1973;7:172.

[21] Evans JSO. Negative Thermal Expansion Materials. J. Chem. Soc. Dalton Trans. 1999:3317.

[22] Angel RJ. EOS-FIT. computer code EOS-FIT. Blacksburg, VA: Virginia Tech, 2001.

[23] Varga T, Wilkinson AP, Lind C, Bassett WA, Zha C-S. In-situ high pressure synchrotron x-ray diffraction study of $Sc_2W_3O_{12}$ at up to 10 GPa. Phys. Rev. B 2005;71:214106.

[24] Varga T, Wilkinson AP, Jorgensen JD, Short S. Neutron powder diffraction study of the orthorhombic to monoclinic transition in $Sc_2W_3O_{12}$ on compression. Solid State Sciences 2006;8:289.

[25] Varga T, Wilkinson AP, Lind C, Bassett WA, Zha C-S. High pressure synchrotron x-ray powder diffraction study of $Sc_2Mo_3O_{12}$ and $Al_2W_3O_{12}$ J. Phys.: Condens. Matter 2005;17:4271.

[26] Karmakar S, Deb SK, Tyagi AK, Sharma SM. Pressure-induced amorphization in $Y_2(WO_4)_3$: in situ X-ray diffraction and Raman studies. J. Solid State Chem. 2004;177:4087.

[27] Evans JSO, Mary TA, Sleight AW. Negative Thermal Expansion in $Sc_2(WO_4)_3$. J. Solid State Chem. 1998;137:148.

[28] Weller MT, Henry P, Wilson CC. An analysis of the thermal motion in the negative thermal expansion material $Sc_2(WO_4)_3$ using isotopes in neutron diffraction. J. Phys. Chem. B 2000;104:12224.

CHAPTER 6

STRUCTURAL CHANGES ACCOMPANYING NEGATIVE THERMAL EXPANSION IN $Zr_2(MoO_4)(PO_4)_2$

6.1. INTRODUCTION

Negative thermal expansion materials continue to attract attention due to intrinsic interest in this phenomenon and their potential for application in controlled thermal expansion composites and other areas. Many compositions are known to form with structures related to that of orthorhombic $Sc_2W_3O_{12}$ [1-3]. They typically display anisotropic volume negative thermal expansion while orthorhombic, but are susceptible to symmetry lowering phase transitions [4], with a concomitant loss of negative thermal expansion, on cooling or modest compression [5-8]. The $Sc_2W_3O_{12}$ framework is amenable to a wide range of substitutions beyond the simple replacement of Sc^{3+} with other trivalent ions, for example, materials such as $A_2(MO_4)(PO_4)_2$ (A – Zr or Hf, M – W or Mo) [9-12], $(HfMg)(WO_4)_3$ [13-15], and $Zr_2(SO_4)(PO_4)_2$ [16] have been reported to have related structures. The wide range of possible substitutions allows for tuning of both thermal and high pressure behavior. The use of $A_2(MO_4)(PO_4)_2$ (A = Zr or Hf; M = W or Mo) in controlled thermal expansion applications is covered by several patents including [17, 18]. As a prelude to exploring the behavior of $Zr_2(MoO_4)(PO_4)_2$ under pressure, we have examined the expansion of this compound and the structural changes underlying its behavior by a combination of neutron, high resolution synchrotron x-ray and variable temperature medium resolution synchrotron powder diffraction. The results of this work

are reported in this chapter. The complicated high pressure behavior of this compound is discussed in the next chapter.

6.2. EXPERIMENTAL PROCEDURES

6.2.1 Sample Preparation

Two separate batches of $Zr_2(MoO_4)(PO_4)_2$ were prepared using stoichiometric amounts of ZrO_2 (Alfa Aesar, 99.7%), $NH_4H_2PO_4$ (J.T. Baker, 99.2 %) and 20% excess MoO_3 (J.T. Baker, 99.8 %). The starting compounds were ground together in an agate mortar, heated in an alumina crucible for 4 hours at 600 ºC, 2 hours at 900 ºC and, finally, 30 minutes at 1000 ºC. This treatment was followed by grinding and heating for another 5 hours at 900 ºC resulting in off white powders. Laboratory powder diffraction data, obtained using a Scintag X1 diffractometer equipped with a copper tube and a Peltier cooled solid-state detector, indicated that the batch used for the variable temperature x-ray study was single phase. The second batch was used for neutron diffraction and the high -resolution X-ray experiments.

6.2.2 Synchrotron High Resolution X-ray Diffraction Study

High resolution synchrotron X-ray powder diffraction data for $Zr_2(MoO_4)(PO_4)_2$ were obtained at room temperature using the 11-BM-B beamline of the Advanced Photon Source, Argonne National Laboratory. A Si(111) double crystal monochromator provided 0.4017 Å x-rays from a bending magnet. A triple axis geometry was employed with 12 scintillation detectors each with its own Si(111) analyzer crystal. The sample

was contained in a 0.8 mm diameter capillary and data collected over the range 2-36^{o} 2θ in 0.001^{o} steps.

The program suite GSAS [19] with the EXPGUI [20] graphical interface was used for the Rietveld [21] analysis of this powder X-ray diffraction data. Initial analysis showed the presence of MoO_3 (<1% by weight) and ZrO_2 (~2% by weight) as trace impurities. The final Rietveld refinement included these impurities (fit shown in Figure 6.1). Only the lattice constants, two Lorentzian profile coefficients and scale factors were refined for the impurities. The $Zr_2(WO_4)(PO_4)_2$ structure reported by Evans [10] (Pnca) was used as a starting model. The background was fitted with a 15 term Chebyshev polynomial. Peak profiles were modeled using a pseudo-Voigt function. Independent isotropic atomic displacement parameters were used for all atoms. An absorption correction was applied assuming a 30% packing density for the capillary and a computed linear absorption coefficient of 13.12 cm^{-1}. Some of the peaks for the main phase showed an asymmetry (see Figure 6.2) that was attributed to the presence of a range of lattice constants where the distribution of lattice constants was not symmetrical. Similar issues were reported by Evans for $Zr_2(WO_4)(PO_4)_2$ [10]. This unusual peak shape was modeled by using two $Zr_2MoP_2O_{12}$ "phases" in the refinement that were constrained to be structurally identical to one another, but allowed to have different lattice constants and peak shapes. The structural parameters resulting from this analysis are summarized in Table 6.1.

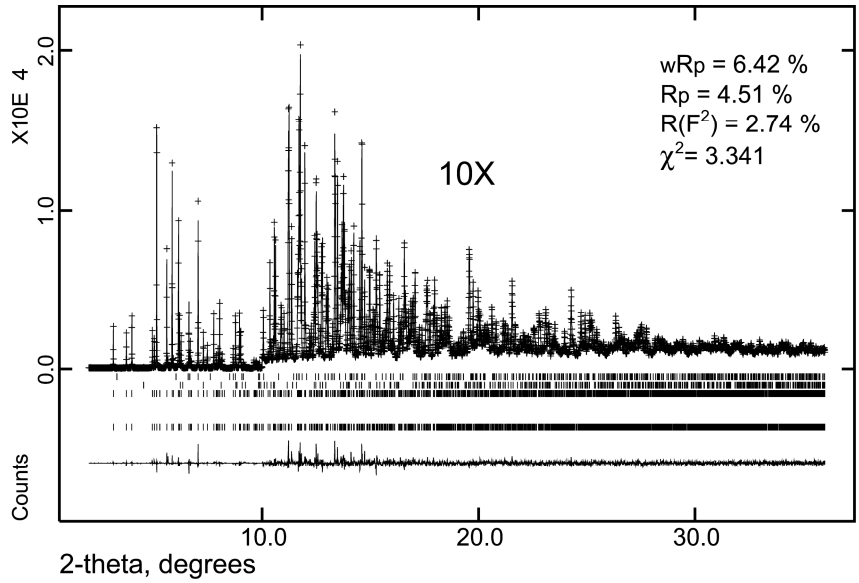

Figure 6.1: Rietveld fit to the 300 K high resolution synchrotron data for $Zr_2(MoO_4)(PO_4)_2$. Observed (+), calculated (-), and difference (bottom trace) powder diffraction patterns are shown along with tag marks indicating the Bragg peak positions for trace MoO_3 (top) and ZrO_2 (second from top) impurities and the two "phases" of $Zr_2(MoO_4)(PO_4)_2$ (lower set of marks).

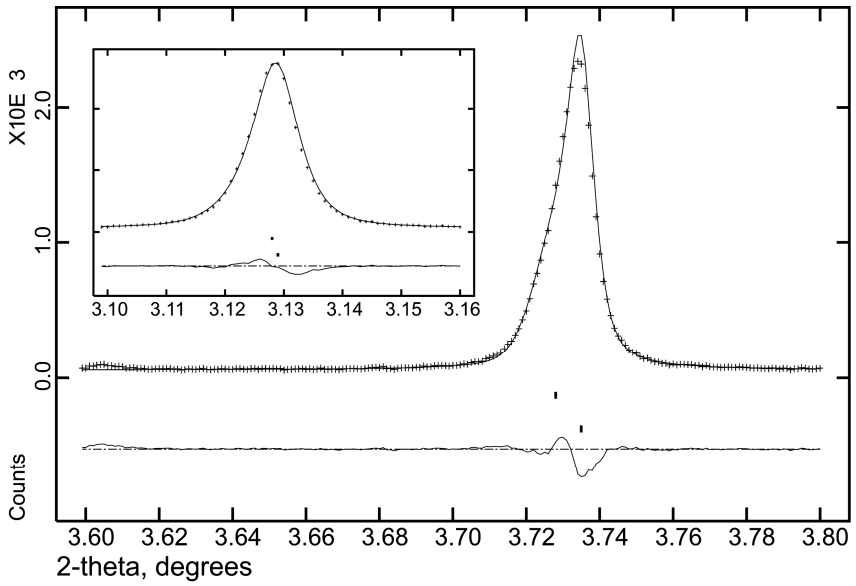

Figure 6.2: Examples of peak asymmetry in the 300 K high resolution synchrotron data for $Zr_2(MoO_4)(PO_4)_2$.

Table 6.1: Structural parameters for $Zr_2(MoO_4)(PO_4)_2$ at 300 K determined by Rietveld analysis of the synchrotron high resolution X-ray data. Lattice constants for the two "phases" used to model the complex observed peak shape were a = 9.33504(3), b = 12.32430(4), c = 9.16613(3) Å for the main component, and a = 9.32849(8), b = 12.3473(1), c = 9.16300(7) Å for the minor component.

Atom	x	y	z	U_{iso}*100
Zr1	0.047437(30)	0.370039(22)	0.226064(30)	0.377(8)
Mo1	0.25	0	0.03890(4)	0.449(11)
P1	0.60513(9)	0.85615(8)	0.38301(10)	0.250(25)
O1	0.92935(19)	0.34922(15)	0.04470(20)	0.56(6)
O2	0.86967(21)	0.42745(16)	0.34905(21)	1.35(7)
O3	-0.00437(21)	0.21956(15)	0.30054(21)	0.36(6)
O4	0.15646(21)	0.40740(16)	0.42713(20)	1.08(7)
O5	0.08112(18)	0.52818(17)	0.17145(19)	0.47(6)
O6	0.23974(23)	0.32418(14)	0.14179(19)	0.55(6)

6.2.3 Variable Temperature Powder Neutron Diffraction

Neutron powder diffraction data were collected using the 32 detector BT-1 instrument at the NIST Center for Neutron Research reactor, NBSR. A Ge(311) monochromator with a 75° take-off angle, λ = 2.0787 Å, and in-pile collimation of 15 minutes of arc were used. The instrument is described in the NCNR website (http://ncnr.nist.gov). The sample was sealed in a 15.6 mm diameter vanadium can inside a dry He-filled glovebox. Data were collected over the range of 3-165° 2θ, with a step size of 0.05°, at both 298 and 9K, using a closed cycle refrigerator. The program suite GSAS [19] with the EXPGUI [20] graphical interface was used to perform Rietveld [21] analyses. The background was fitted with a Chebyshev polynomial function with 20 coefficients. The Bragg peak profiles were modeled using a pseudo-Voigt function. Independent isotropic atomic displacement parameters were used for all atoms. The

Rietveld fit to the 9 K data is shown in Figure 6.3. Structural parameters resulting from these analyses are summarized in Tables 6.2 and 6.3.

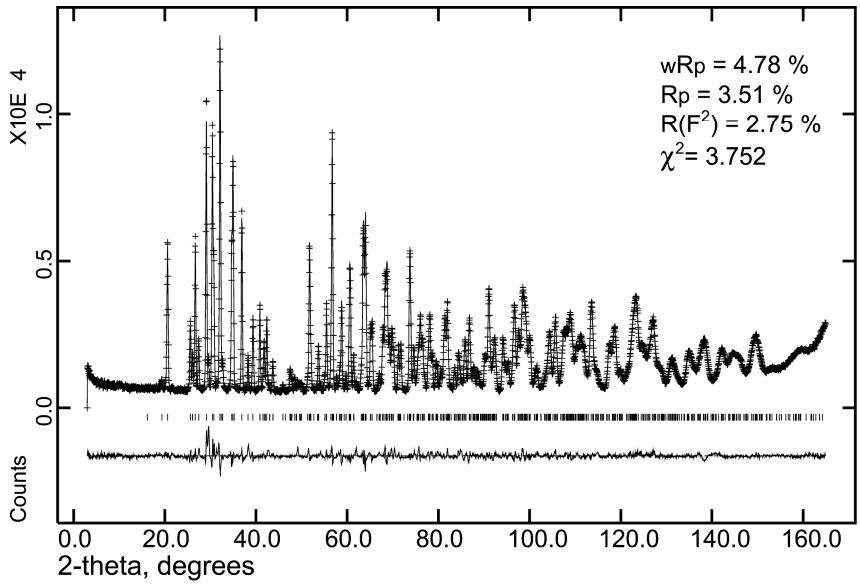

Figure 6.3: Rietveld fit to the 9 K high neutron diffraction data for $Zr_2(MoO_4)(PO_4)_2$. Observed (+), calculated (-), and difference (bottom trace) powder diffraction patterns are shown along with tag marks indicating the Bragg peak positions for $Zr_2(MoO_4)(PO_4)_2$.

Table 6.2: Structural parameters for $Zr_2(MoO_4)(PO_4)_2$ at 298 K determined by the Rietveld analysis of neutron diffraction data. The refined lattice constants were a = 9.3383(1), b = 12.3367(2) and c = 9.1701(1) Å.

Atom	x	y	z	U_{iso}*100
Zr1	0.04776(22)	0.36980(17)	0.22615(22)	1.00(8)
Mo1	0.25	0	0.03816(34)	0.53(9)
P1	0.60483(28)	0.85576(24)	0.38149(30)	0.56(8)
O1	0.92797(29)	0.34873(21)	0.04465(29)	1.76(8)
O2	0.86971(29)	0.42894(22)	0.35063(30)	2.28(9)
O3	-0.00498(25)	0.21975(20)	0.30081(28)	1.59(7)
O4	0.15861(30)	0.40768(21)	0.42819(29)	1.87(9)
O5	0.08136(27)	0.52915(19)	0.17230(31)	1.60(8)
O6	0.23781(26)	0.32405(21)	0.14135(25)	1.55(8)

Table 6.3: Structural parameters for $Zr_2(MoO_4)(PO_4)_2$ at 9 K determined by the Rietveld analysis of neutron diffraction data. The refined lattice constants were a = 9.3594(1), b = 12.3277(2) and c = 9.1923(1) Å.

Atom	x	y	z	U_{iso}*100
Zr1	0.04785(21)	0.36901(16)	0.22533(21)	0.59(7)
Mo1	0.25	0	0.03857(31)	-0.06(8)
P1	0.60551(27)	0.85594(23)	0.38255(29)	0.29(7)
O1	0.92734(27)	0.34904(19)	0.04591(26)	0.71(7)
O2	0.87216(26)	0.43016(20)	0.35029(26)	0.85(8)
O3	-0.00409(23)	0.21922(19)	0.30084(26)	0.70(7)
O4	0.16091(28)	0.40694(19)	0.42662(26)	0.76(8)
O5	0.08373(24)	0.52862(17)	0.17013(29)	0.51(7)
O6	0.23837(24)	0.32257(19)	0.14153(23)	0.53(7)

6.2.4 Variable Temperature Powder X-ray Diffraction

17.53 keV (λ = 0.70736 Å) X-rays were used at the APS beamline 1-BM-C, Argonne National Laboratory, in combination with a MAR-345 imaging plate detector, to record 2-D diffraction patterns for $Zr_2(MoO_4)(PO_4)_2$ in a 0.7 mm diameter glass capillary. The detector was vertically offset to increase the 2θ range, such that the X-ray beam was centered close to the bottom of the imaging plate. 86 diffraction patterns were recorded (2.5 second exposures plus readout time) on cooling from 400 K to 85 K at 120 Khr^{-1} using an Oxford Cryosystems Cryostream 700. Powder diffraction data were also collected for a 1:3 mixture of silicon and alpha alumina under identical conditions. The measured lattice constants for these standards were compared with those expected based on their known thermal expansion [22, 23] to verify the temperature calibration. The raw 2-D images were processed using Fit2D [24]. The sample to detector distance (ca. 340 mm) and tilt of the image plate relative to the beam were refined using data from a LaB_6

calibrant. Analysis of the integrated diffraction patterns was undertaken using the GSAS suite and the SeqGSAS utility was used to process all of the patterns sequentially. The Rietveld analyses were done assuming single phase $Zr_2(MoO_4)(PO_4)_2$. The background was fitted with a Chebyshev polynomial function with 20 coefficients. The Bragg peak profiles were modeled using a pseudo-Voigt function. Isotropic atomic displacement parameters were used. μR for the sample was estimated to be ~0.35, a value that is sufficiently low that no absorption correction was applied. The Rietveld fit to the 300 K data is shown in Figure 6.4. The structural parameters resulting from the analysis of these data are summarized in Table 6.4. The variation of the unit cell volume and the cell constants with temperature are shown in Figure 6.5 and 6.6 respectively. Selected geometrical parameters, as a function of temperature, are shown in Figures 6.7 – 6.12.

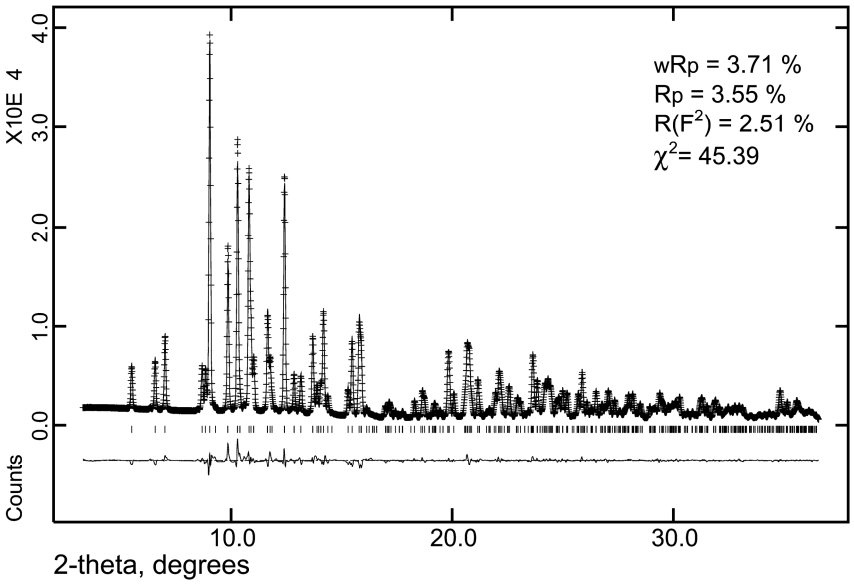

Figure 6.4: Rietveld fit to the image plate x-ray data for $Zr_2(MoO_4)(PO_4)_2$ recorded at approximately 300 K. Observed (+), calculated (-), and difference (bottom trace) powder diffraction patterns are shown along with tag marks indicating the Bragg peak positions for $Zr_2(MoO_4)(PO_4)_2$.

Table 6.4: Structural parameters for $Zr_2(MoO_4)(PO_4)_2$ at 300 K determined by Rietveld analysis of the synchrotron image plate data. The refined lattice constants were a = 9.3284(1), b = 12.3374(2) and c = 9.1621(1) Å.

Atom	x	y	z	U_{iso}*100
Zr1	0.04754(8)	0.37025(6)	0.22622(8)	1.061(31)
Mo1	0.25	0	0.03943(11)	0.463(35)
P1	0.60591(20)	0.85535(20)	0.38344(24)	-0.54(7)
O1	0.9289(5)	0.34931(40)	0.0441(5)	-0.22(14)
O2	0.8685(6)	0.43101(41)	0.3499(6)	0.48(17)
O3	-0.0049(4)	0.21812(34)	0.3007(5)	-0.85(14)
O4	0.1573(6)	0.40866(41)	0.4286(5)	0.55(17)
O5	0.0808(5)	0.52895(44)	0.1711(5)	0.10(14)
O6	0.2403(6)	0.32566(36)	0.1403(5)	-0.32(14)

6.2.5 Joint Refinement Using Ambient Temperature Neutron and X-ray Data

A combined analysis of the 300 K high resolution X-ray data and 298 K neutron data was carried out to explore the possibility of mixed Mo/P site occupancy and/or vacancies on the tetrahedral sites. There was no evidence for mixed occupancy, or any vacancies in either site, as the deviation from the ideal occupancies were within one e.s.d.

6.3. RESULTS AND DISCUSSION

Rietveld analysis of the room temperature high resolution synchrotron data for $Zr_2(MoO_4)(PO_4)_2$ provided no evidence for symmetry lower than Pnca. This is consistent with prior work on the analogous tungstate [10]. The observed asymmetric peaks shapes (Figure 6.2) for some types of reflection are indicative of an asymmetric distribution of lattice constants within the sample, not symmetry lowering. Our fit to asymmetric peak shapes made use of two $Zr_2(WO_4)(PO_4)_2$ "phases" that were constrained to be structurally

identical but had independently refineable lattice constants and scale factors. This is a useful simplification, but a continuous distribution of lattice constants amongst separate coherent diffracting domains is expected. The predominant difference between the two "phases" used in the model was that the b lattice constant for the minor "phase" was 1.002 times that of the major "phase" (Table 6.1). The other lattice constants for the two "phases" differed by almost an order of magnitude less than this. This distribution of lattice constants is presumably associated with some type of defect in the sample that predominantly affects the b lattice constant. Using a combined analysis of the high resolution X-ray data and 298 K neutron data, we explored the possibility of vacancies and/or Mo/P substitution on the tetrahedral sites of the structure to see if this could be a possible origin of the lattice constant variation. The combined refinement was fully consistent with complete occupancy of the tetrahedral sites with a single species (Mo or P).

Many compounds with a $Sc_2W_3O_{12}$ type structure show a monoclinic to orthorhombic phase transition on heating from very low temperatures, although $Sc_2W_3O_{12}$ is orthorhombic at all temperature that have been examined [2, 3]. For example, $Sc_2Mo_3O_{12}$ goes from $P2_1/a$ to Pnca at 178 K on heating [5]. Analysis of the neutron diffraction data for $Zr_2(MoO_4)(PO_4)_2$ recorded at 9 and 298 K showed no evidence of a phase transition on cooling from room temperature.

The normalized unit cell volume and lattice constants for $Zr_2(MoO_4)(PO_4)_2$, as determined by Rietveld analysis of the data from the variable temperature X-ray experiment (cooling from 400 to 85 K) and neutron experiments (298 and 9 K), are shown in Figures 6.5 and 6.6 respectively. Thermal expansion coefficients estimated

from the neutron derived lattice constants are in good agreement with those from the variable temperature X-ray study, lending further confidence to the temperature calibration in the x-ray experiment (see Table 6.6). There is a continuous expansion of the unit cell volume on cooling, associated with a volume thermal expansion coefficient, α_v, of -13.4(1) x 10^{-6} K^{-1}. The expansion of $Zr_2(MoO_4)(PO_4)_2$ is anisotropic, such that b axis expands with increasing temperature while the a and c axes contract (α_a= -8.35(4) x 10^{-6} K^{-1} ; α_b= 3.25(3) x 10^{-6} K^{-1} ; α_c= -8.27(5) x 10^{-6} K^{-1}, obtained from straight line fits to ln(L) versus T between 400 and 122 K). The coefficients of thermal expansion for $Zr_2(MoO_4)(PO_4)_2$ are compared with those for related compounds in Table 6.6. The anisotropy of the expansion for $Zr_2(MoO_4)(PO_4)_2$ is similar to that for the listed $A^{3+}{}_2(MO_4)_3$. However, for $A^{3+}{}_2(MO_4)_3$ (M – W or Mo), α_V becomes increasingly negative as the size of the M^{3+} ion and unit cell volume increase, but $Zr_2(MoO_4)(PO_4)_2$ does not fit this unit cell volume and expansion coefficient trend. It has a unit cell volume similar to that of $Al_2(WO_4)_3$ [25], with α_v closer to that of $A^{3+}{}_2(MO_4)_3$ with much larger unit cell volumes.

As the changes in unit cell dimensions with temperature (Figures 6.5 and 6.6) must be a result of structural changes, we examined the behavior of the crystal structure as a function of temperature. The synchrotron image plate experiment spanned a significant temperature range (85 – 400 K) and included many temperature points. While the d-spacing range for these patterns (d_{min} ~ 1.13 Å) is less than that typically used for high quality structure refinements, a comparison of the bond lengths and angles derived from the high resolution synchrotron data, neutron data and image plate data all at ~300 K gives confidence that the coordinates obtained from the Rietveld analysis of the image

plate data are reliable (Table 6.5); the geometrical parameters derived from all three measurements are precise and in very good agreement with one another. However, it is worth commenting that the limited d-spacing range of the image plate data does apparently have a deleterious effect on the derived atomic displacement parameters (ADPs); there is considerable scatter amongst the various independent oxygen ADPs (Table 6.4), but little effect on the atomic coordinates. This is presumably because the systematic errors in the model for the image plate data end up being absorbed into the ADPs as a result of the small d-spacing range, but the high statistical quality of the data (low noise due to counting statistics) allows for the accurate and precise determination of atomic coordinates. An examination of the temperature dependence of the ADPs derived from this image plate data supports this reasoning; they decrease smoothly on cooling as one would expect for an ADP that is biased due to a largely unchanging systematic error, rather than being influenced by noise in the data. Graphs showing the temperature dependence of selected distances and angles for the $Zr_2(MoO_4)(PO_4)_2$ structure are shown in Figures 6.7, 6.8, 6.9, 6.10, 6.11 and 6.12. The scatter in these graphs is low, enabling an examination of structural trends with temperature.

$Zr_2(MoO_4)(PO_4)_2$ consists of corner sharing ZrO_6 octahedra and MoO_4 / PO_4 tetrahedra with only small distortions from ideal geometry (see Table 6.5 and Table 6.7). These distortions do not change significantly with temperature. The ZrO_6 octahedron is similar in size to the ScO_6 octahedron in $Sc_2W_3O_{12}$, but PO_4 is significantly smaller than MoO_4/WO_4, leading to a smaller unit cell volume for $Zr_2(MoO_4)(PO_4)_2$ than $Sc_2W_3O_{12}$ (Table 6.6). Zr-O, Mo-O and P-O bonded distances calculated from time average atomic positions are almost independent of temperature (Figure 6.7, 6.8 and 6.9) as would be

expected for strong bonds. The slight decrease for some of these distances on heating can be ascribed to the correlated (thermal) vibrational motion of the bonded pairs of atoms rather than any real reduction in instantaneous bond length [2]. Earlier work on the related compounds $Sc_2(WO_4)_3$ [2], $Sc_2(MoO_4)_3$ [5], and $Y_2(WO_4)_3$ [25] suggested that the NTE behavior in this type of material was associated with the transverse thermal vibration of bridging O atoms and related changes in A-O-M bond angles. Figure 6.10 shows the variation in six different Zr-O-Mo/P angles for $Zr_2(MoO_4)(PO_4)_2$. Evans et al. [2] reported that for $Sc_2W_3O_{12}$, the two largest A-O-M angles (Sc-O2-W and Sc-O5-W) decreased significantly on heating from 10 to 450 K, but the smallest angles (Sc-O6-W, Sc-O4-W) increased and the intermediate angles did not show a significant trend with temperature. They also described how these changes led to the observed thermal expansion characteristics of the material. A-O-M angles from a variable temperature neutron diffraction study of $Sc_2W_3O_{12}$, using three different isotopically labeled samples, showed the same overall trend [3]. Somewhat similar behavior is seen for $Zr_2(MoO_4)(PO_4)_2$. However, the largest Zr-O-Mo/P angle, Zr-O5-P, is essentially independent of temperature, only the Zr-O2-Mo angle decreases strongly on heating. The smallest angle Zr-O6-P increases strongly on heating, similar to Sc-O6-W, but there is no strong trend in Zr-O4-Mo with temperature. The other two angles Zr-O1-P and Zr-O3-P show a slight increase on heating before leveling out at the highest temperatures examined. Changes in non-bonded Zr-Mo/P separations, calculated from time average atomic positions, as a function of temperature, are shown in Figure 6.11. As would be expected from the temperature dependences of the Zr-O2-Mo and Zr-O6-P angles in a material with rigid Zr-O, P-O and Mo-O links, the Zr-Mo distances for Zr-O2-Mo

decreases quite strongly on heating and the Zr-P distance for Zr-O6-P increase on heating. However, the Zr-P separations for both Zr-O3-P and Zr-O5-P decrease significantly on heating, even though the time average bond angles for these links are essentially temperature independent; this may be due to correlations between the vibrational (thermal) motion of neighboring Zr and P. In $Zr_2(MoO_4)(PO_4)_2$, the separations between the average positions of neighboring Zr and P/Mo atoms decreases (Figure 6.12) leading to volume negative thermal expansion. The expansion coefficients for the average neighboring Zr-P, Zr-Mo and Zr-Mo/P separations, derived from linear fits (85 – 400 K), are -4.1, -7.9 and -5.5×10^{-6} K^{-1} respectively comparing quite well to the average linear expansion coefficient for the material determined from its lattice constants (-4.5×10^{-6} K^{-1}). It should be noted that, on heating, the most pronounced reductions in the separation between the time average positions of neighboring Zr and P (Zr-O3-P and Zr-O5-P) are not associated with significant reductions in the corresponding Zr-O-P crystallographic bond angles, even though Zr-O5-P is the largest Zr-O-Mo/P angle for the structure. This is contrary to what might be expected based on the view that NTE arises purely from the coupled rotation of rigid polyhedra associated with the anharmonicity of the transverse thermal motion of bridging oxygens.

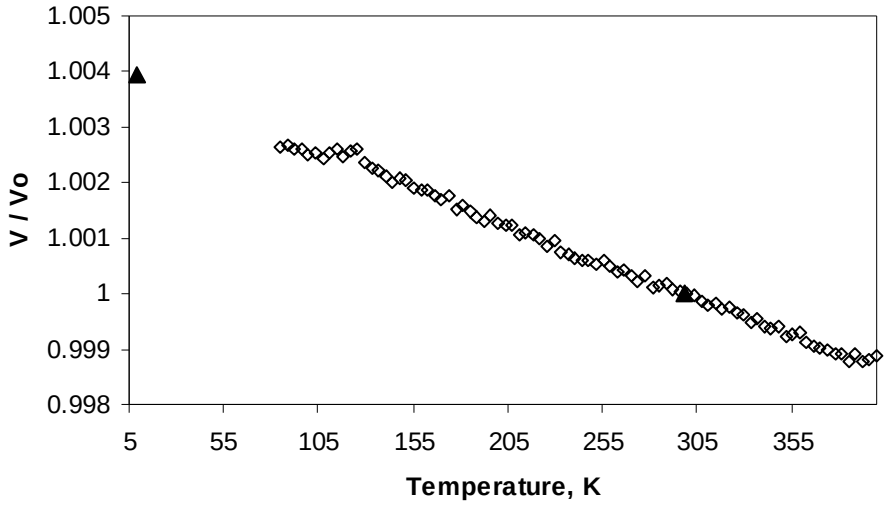

Figure 6.5: Normalized unit cell volume as a function of temperature derived from the image plate (open diamonds) and neutron data (closed triangles).

Table 6.6: Selected Bond Distances (Å) and Angles (°) High-resolution X-Ray 300K Variable T X-ray 300K Neutron 298K

	O1	**O2**	**O3**	**O4**	**O5**	**O6**
Zr1	2.011(2)	2.127(2)	2.035(2)	2.155(2)	2.037(2)	2.034(2)
	2.019(5)	2.153(5)	2.056(4)	2.170(5)	2.046(5)	2.039(5)
	2.022(3)	2.145(3)	2.034(3)	2.173(3)	2.051(3)	2.018(3)
Mo1		1.761(2)		1.765(2)		
		1.725(5)		1.746(6)		
		1.749(3)		1.744(4)		
P1	1.519(2)		1.525(2)		1.527(2)	1.518(2)
	1.509(5)		1.511(5)		1.530(6)	1.496(6)
	1.530(4)		1.513(3)		1.519(4)	1.535(4)
Zr-O-Mo		166.6(1)		150.3(1)		
		168.1(3)		150.6(3)		
		167.6(2)		150.0(2)		
Zr-O-P	156.3(1)		150.5(1)		175.1(1)	145.8(1)
	156.6(3)		149.6(3)		175.2(3)	146.7(3)
	155.3(2)		151.0(2)		175.0(2)	145.4(2)

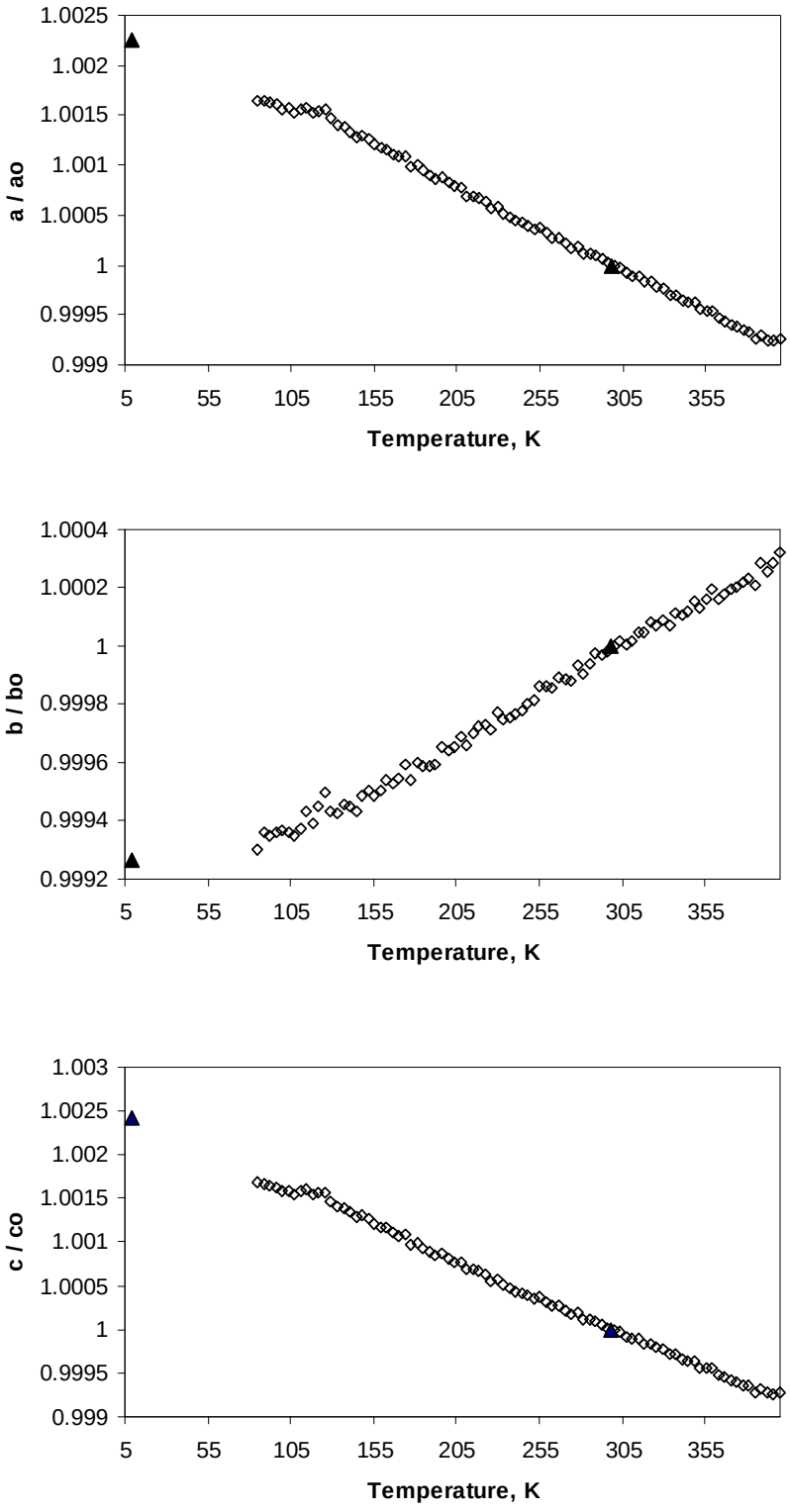

Figure 6.6: Normalized lattice constants as a function of temperature derived from the image plate (open diamonds) and neutron data (closed triangles).

Table 6.5 Coefficients of Thermal Expansion for $Zr_2(MoO_4)(PO_4)_2$ and its relatives

Compound	Radii M^{3+}/M^{4+} (pm)*	α_a (ppm K^{-1})	α_b (ppm K^{-1})	α_c (ppm K^{-1})	anisotropy#	V/Å^3	α_v (ppm K^{-1})	T range (K)	Reference
$Al_2(WO_4)_3$	53.5	-1.31	5.94	-0.099	7.25	1042	4.51	273-1073	[22]
$Sc_2(WO_4)_3$	74.5	-6.3	7.5	-5.5	13.8	1234	-6.5	50-450	[2]
$Sc_2(MoO_4)_3$	74.5	-8.41	10.82	-8.73	19.55	1220	-6.3	200-300	[5]
$Lu_2(WO_4)_3$	86.1	-9.9	-2.2	-8.3	7.7	1345	-20.4	400-900	[23]
$Y_2(WO_4)_3$	90	-10.35	-3.06	-7.62	7.29	1401	-20.9	273-1073	[22]
$Zr_2(WO_4)(PO_4)_2$	72						-9	50-450	[24]
		-7.3	1.4	-8.4	9.8	1055	-14.2	60-298	[26]
$Zr_2(MoO_4)(PO_4)_2$	72	-8.35	3.25	-8.27	11.6	1055	-13.4	85-400	Current
		-7.82	2.53	-8.34	10.87	1056	-13.6	9-298	Current

* -Ionic radii for 6 coordinate cations from Shannon 1976 [27]

- anisotropy = $\alpha_{lmax} - \alpha_{lmin}$

Table 6.7 O-M-O Angles (°)

	High-resolution X-Ray 300K	Variable T X-ray 300K	Neutron 298K
O2-Zr1-O1	93.03(7)	93.09(20)	93.04(13)
O2-Zr1-O5	86.13(7)	85.08(17)	85.45(12)
O2-Zr1-O3	86.56(8)	87.63(19)	86.72(13)
O2-Zr1-O4	81.03(7)	80.82(18)	80.93(13)
O2-Zr1-O6	169.11(8)	168.95(20)	169.10(16)
O1-Zr1-O5	90.20(7)	90.10(18)	90.55(13)
O1-Zr1-O3	91.76(8)	91.55(19)	91.49(13)
O1-Zr1-O4	173.22(8)	173.02(21)	173.15(16)
O1-Zr1-O6	97.72(8)	97.49(18)	97.66(14)
O5-Zr1-O3	172.51(8)	172.60(18)	172.00(15)
O5-Zr1-O4	86.15(7)	86.00(18)	85.77(12)
O5-Zr1-O6	92.08(7)	91.67(19)	92.34(13)
O3-Zr1-O4	91.15(8)	91.61(20)	91.38(13)
O3-Zr1-O6	94.81(7)	95.26(17)	95.05(13)
O4-Zr1-O6	88.13(7)	88.42(18)	88.27(13)
O2-Mo1-O2	108.66(13)	108.0(4)	108.66(24)
O2-Mo1-O4	110.67(8)	110.07(21)	110.59(12)
O2-Mo1-O4	108.91(8)	109.93(22)	108.82(11)
O2-Mo1-O4	108.91(8)	109.93(22)	108.82(11)
O2-Mo1-O4	110.67(8)	110.07(21)	110.59(12)
O4-Mo1-O4	109.03(12)	108.87(31)	109.36(24)
O1-P1-O5	109.90(12)	109.37(28)	109.98(23)
O1-P1-O3	108.57(12)	109.01(31)	108.68(22)
O1-P1-O6	109.49(11)	109.62(27)	108.10(21)
O5-P1-O3	108.58(12)	107.47(29)	109.16(21)
O5-P1-O6	109.48(11)	109.12(28)	109.39(21)
O3-P1-O6	110.81(12)	112.19(30)	111.51(24)

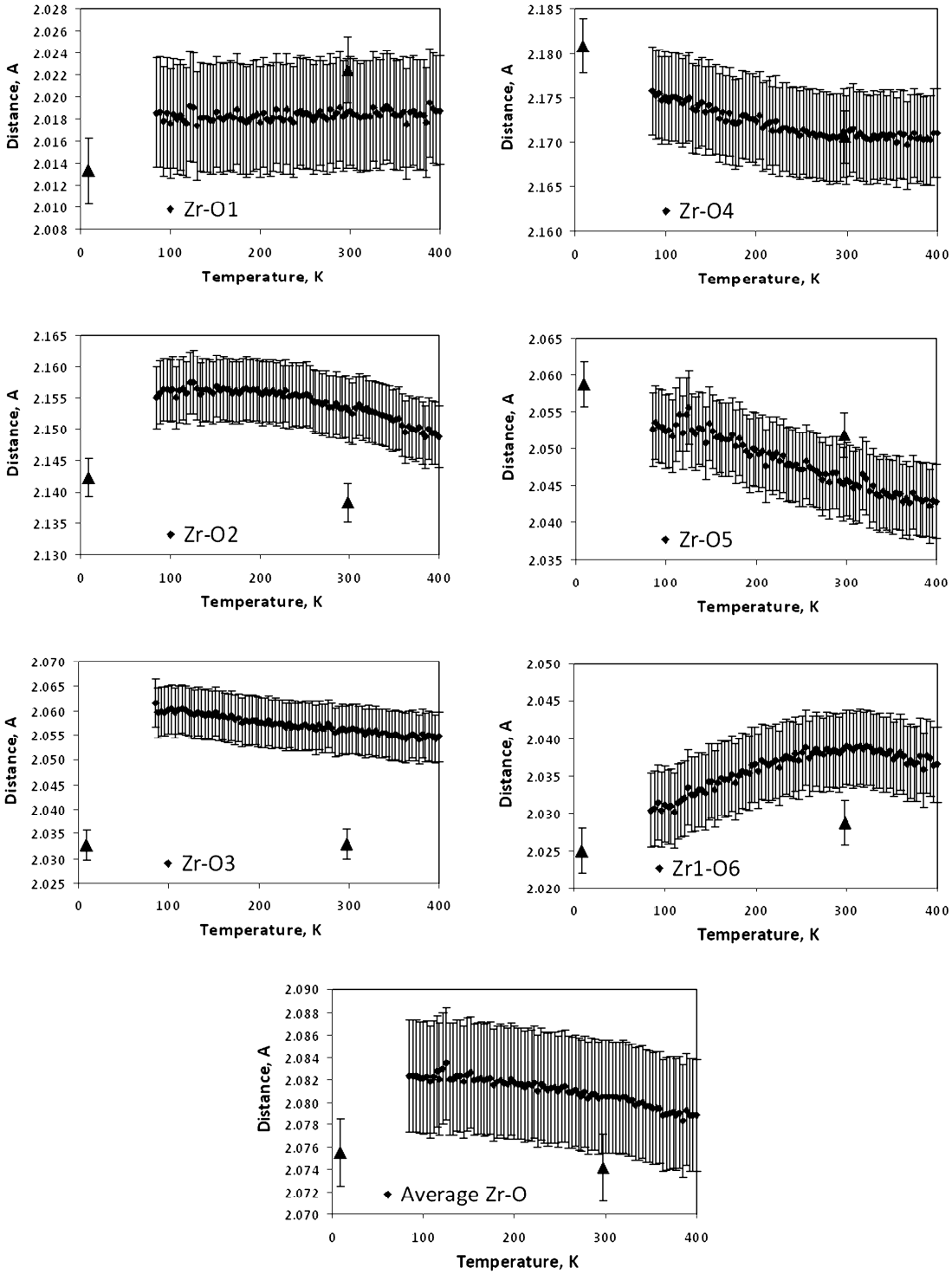

Figure 6.7: Zr-O bonded distances, as a function of temperature, from the image plate x-ray (diamonds) and neutron (triangles) diffraction data. Error bars represent typical Rietveld e.s.d.s

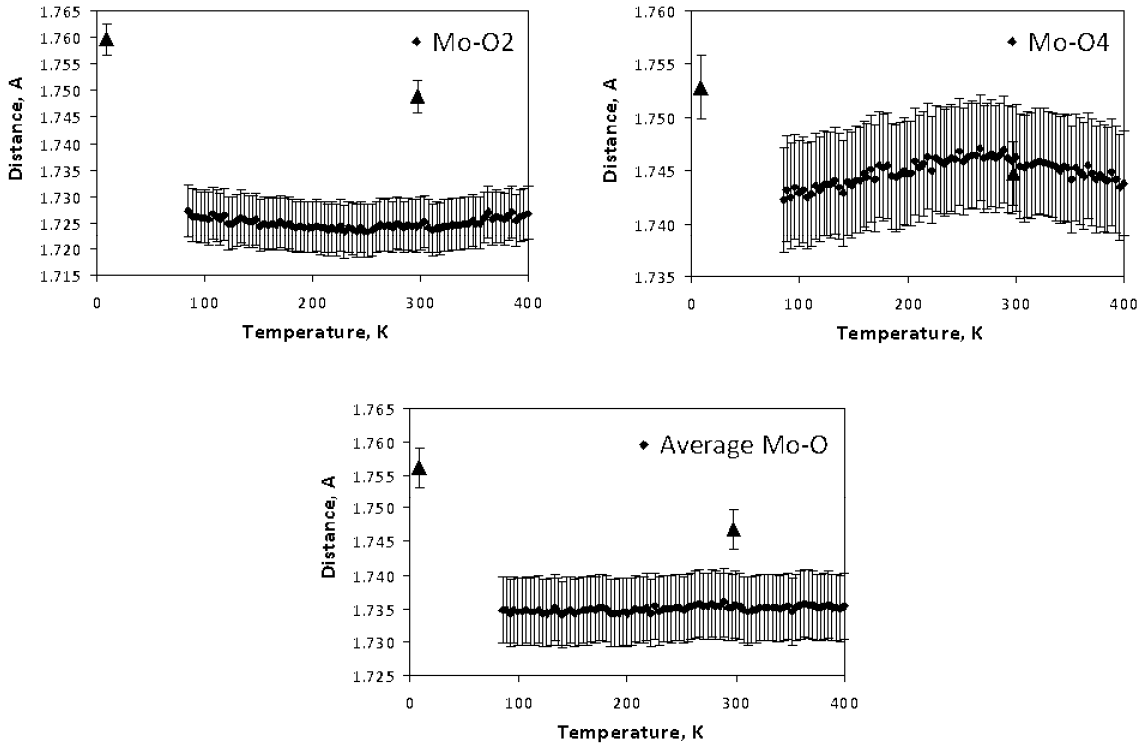

Figure 6.8: Mo-O bonded distances, as a function of temperature, from the image plate x-ray (diamonds) and neutron (triangles) diffraction data. Error bars represent typical Rietveld e.s.d.s

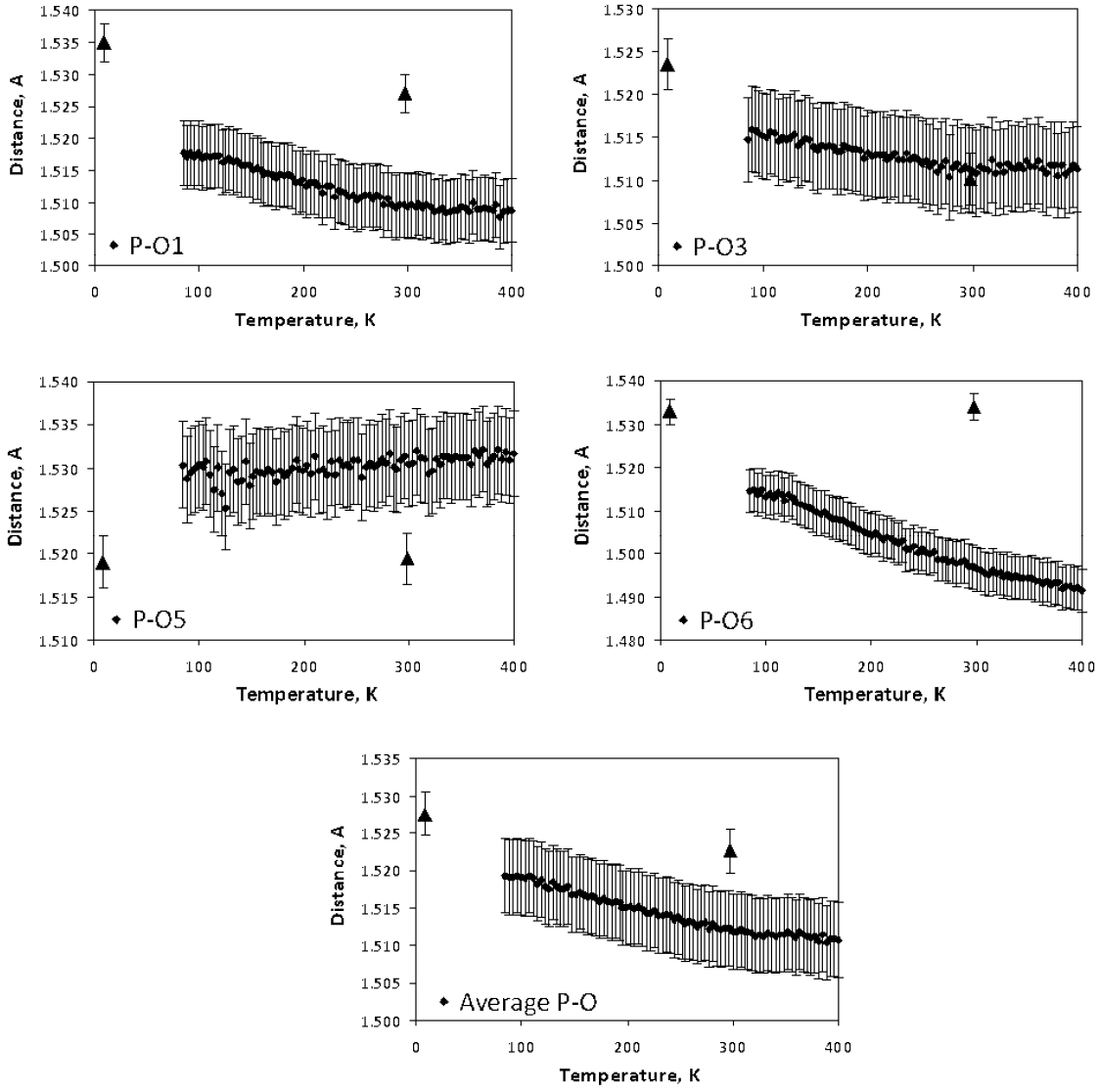

Figure 6.9: P-O bonded distances, as a function of temperature, from the image plate x-ray (diamonds) and neutron (triangles) diffraction data. Error bars represent typical Rietveld e.s.d.s

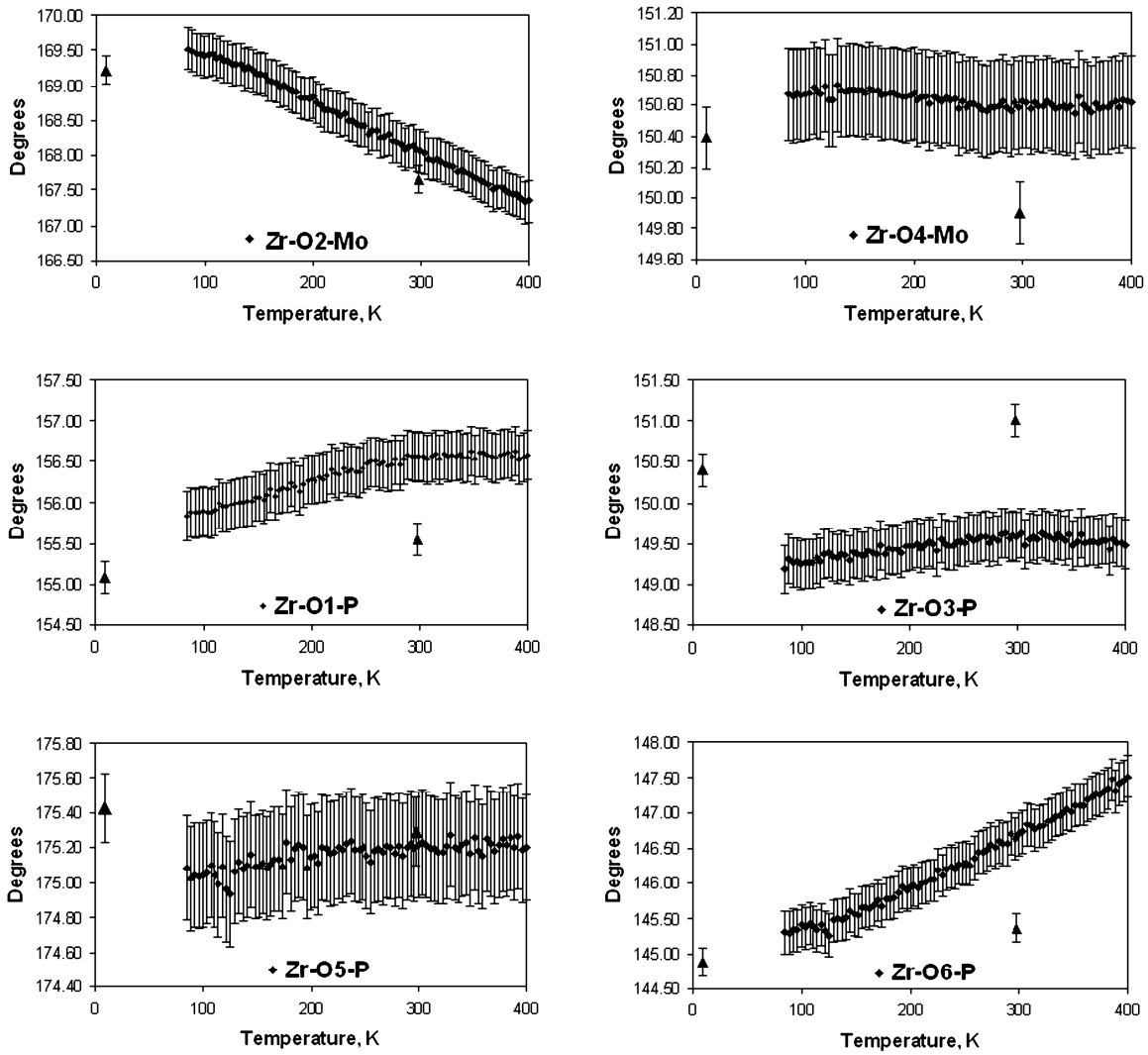

Figure 6.10: Zr-O-Mo/P angles, as a function of temperature, from the image plate x-ray (diamonds) and neutron (triangles) diffraction data. Error bars represent typical Rietveld e.s.d.s

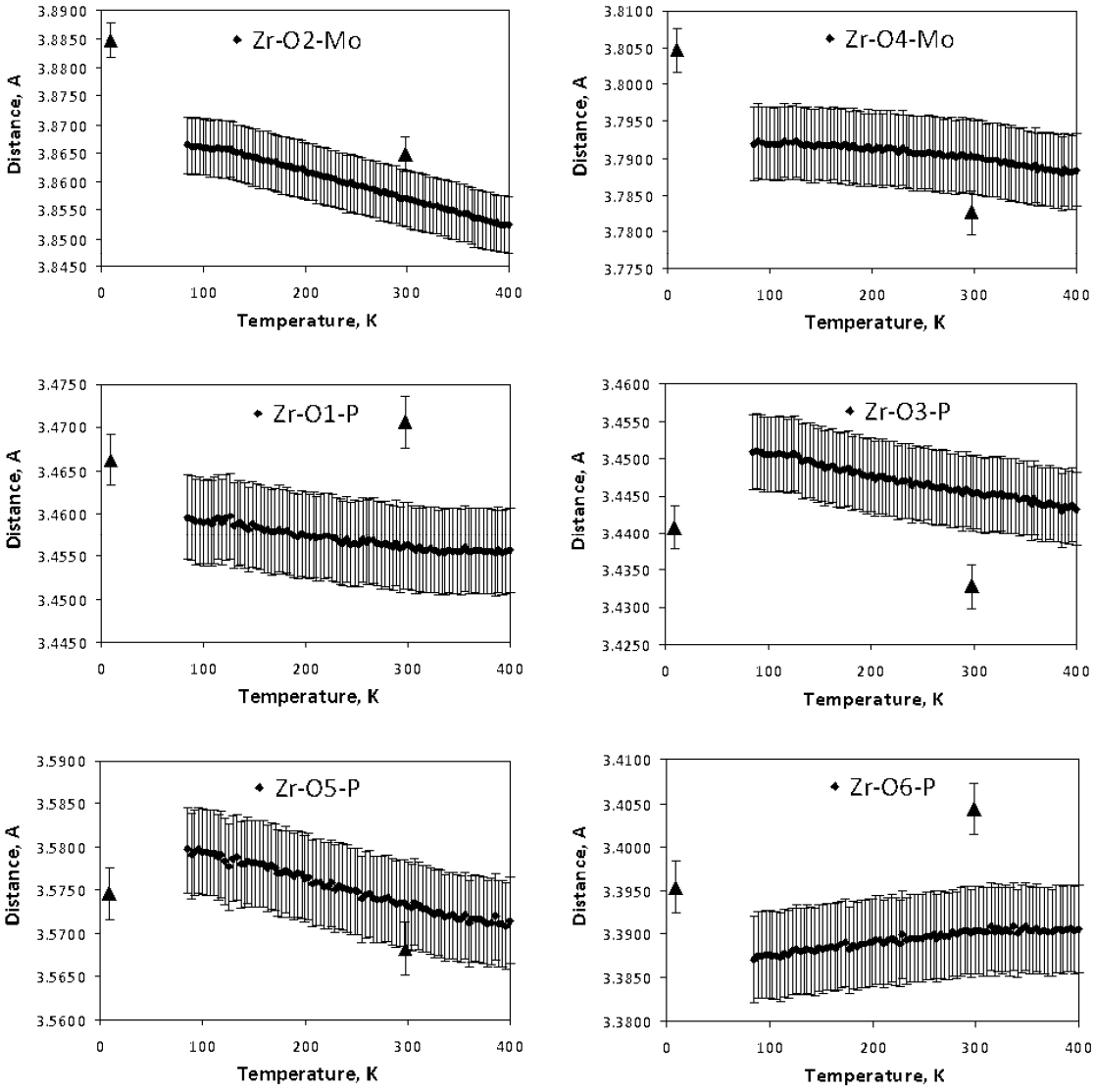

Figure 6.11: Individual nonbonding Zr-O-Mo/P distances as a function of temperature, from the image plate x-ray (diamonds) and neutron (triangles) diffraction data. Error bars represent typical Rietveld e.s.d.s

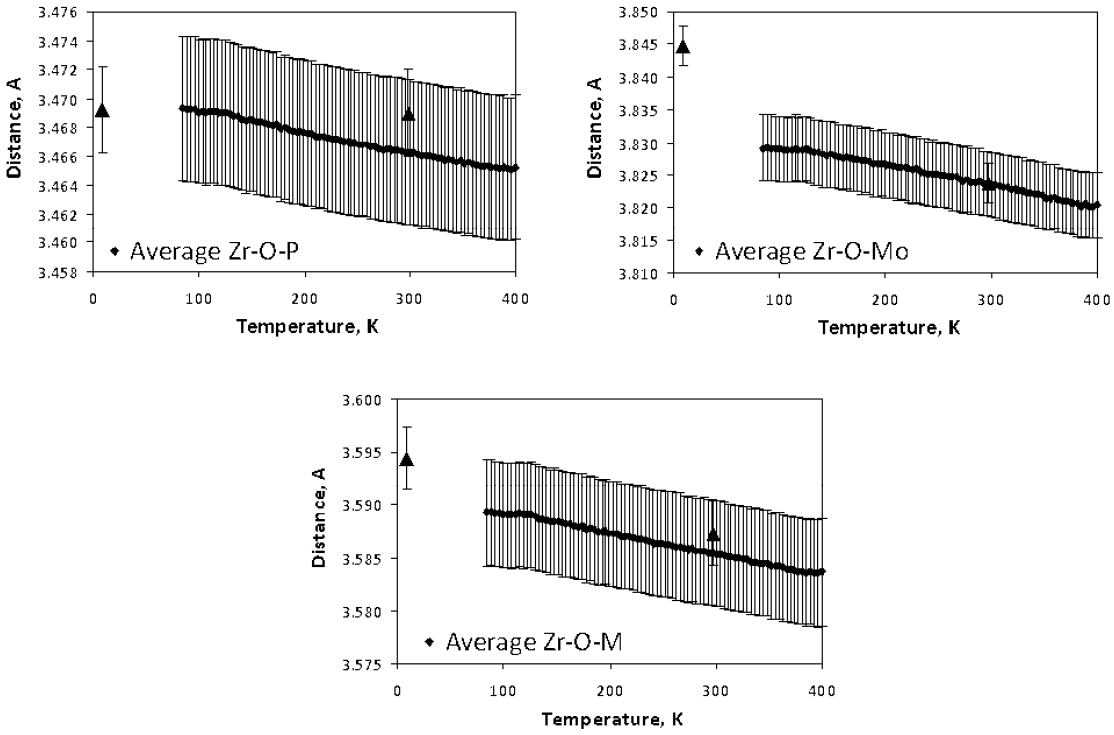

Figure 6.12: Average Nonbonding Zr-O-Mo/P distances, as a function of temperature, from the image plate x-ray (diamonds) and neutron (triangles) diffraction data. Error bars represent typical Rietveld e.s.d.s

6.4. CONCLUSIONS

$Zr_2(MoO_4)(PO_4)_2$, unlike most tungstates and molybdates in the $Sc_2W_3O_{12}$ structural family, maintains an orthorhombic structure showing negative thermal expansion down to very low temperatures (at least 9K). The compound displays anisotropic volume negative thermal expansion, with an average linear expansion coefficient (-4.5×10^{-6} K^{-1}) similar to that of $A_2(MO_4)_3$ (M = Mo or W) that have significantly larger unit cell volumes than the molybdate phosphate. The structural

changes that accompany NTE in $Zr_2(MoO_4)(PO_4)_2$ are similar, but not identical to those previously described for $Sc_2W_3O_{12}$. The most pronounced reductions in time average neighboring Zr-P distances on heating are not associated with significant reductions in the corresponding time average Zr-O-P bond angles.

6.5. REFERENCES

[1] Abrahams SC, Bernstein JL. Crystal Structure of the Transition-Metal Molybdates and Tungstates. II. Diamagnetic $Sc_2(WO_4)_3$. J. Chem. Phys. 1966;45:2745.

[2] Evans JSO, Mary TA, Sleight AW. Negative Thermal Expansion in $Sc_2(WO_4)_3$. J. Solid State Chem. 1998;137:148.

[3] Weller MT, Henry P, Wilson CC. An analysis of the thermal motion in the negative thermal expansion material $Sc_2(WO_4)_3$ using isotopes in neutron diffraction. J. Phys. Chem. B 2000;104:12224.

[4] Sleight AW, Brixner LH. A New Ferroelastic Transition in Some $A_2(MO_4)_3$ Molybdates and Tungstates. J. Solid State Chem. 1973;7:172.

[5] Evans JSO, Mary TA. Structural Phase Transitions and negative thermal expansion in $Sc_2(MoO_4)_3$. International Journal of Inorganic Materials 2000;2:143.

[6] Varga T, Wilkinson AP, Lind C, Bassett WA, Zha C-S. In-situ high pressure synchrotron x-ray diffraction study of $Sc_2W_3O_{12}$ at up to 10 GPa. Phys. Rev. B 2005;71:214106.

[7] Varga T, Wilkinson AP, Lind C, Bassett WA, Zha C-S. High pressure synchrotron x-ray powder diffraction study of $Sc_2Mo_3O_{12}$ and $Al_2W_3O_{12}$ J. Phys.: Condens. Matter 2005;17:4271.

[8] Varga T, Wilkinson AP, Jorgensen JD, Short S. Neutron powder diffraction study of the orthorhombic to monoclinic transition in $Sc_2W_3O_{12}$ on compression. Solid State Sciences 2006;8:289.

[9] Tsvigunov AN, Sirotinkin VP. Preparation of $Zr_2WO_4(PO_4)_2$ and indexing of its X-ray diffraction pattern. Russ. J. Inorg. Chem. 1990;35:1740.

[10] Evans JSO, Mary TA, Sleight AW. Structure of $Zr_2(WO_4)(PO_4)_2$ from Powder X-ray Data: Cation Ordering with No Superstructure. J. Solid State Chem. 1995;120:101.

[11] Martinek CA, Hummel FA. Subsolidus Equilibria in the System ZrO_2-WO_3-P_2O_5. J. Am. Ceram. Soc. 1970;53:159.

[12] Sirotinkin VP, Tsvigunov AN. Synthesis, X-Ray-Diffraction and Thermal Analyses of $Zr_2MoO_4(PO_4)_2$. Russ. J. Inorg. Chem. 1994;39:735.

[13] Suzuki T, Omote A. Negative Thermal Expansion in $(HfMg)(WO_4)_3$. J. Am. Ceram. Soc. 2004;87:1365.

[14] Suzuki T, Omote A. Zero thermal expansion in $(Al_{2x}(HfMg)_{(1-x)})(WO_4)_{(3)}$. J. Am. Ceram. Soc. 2006;89:691.

[15] Suzuki T, Omote A. Pseudo binary HfW_2O_8-$MgWO_4$ thermal expansion control system. J. Ceram. Soc. Jpn. 2006;114:833.

[16] Piffard Y, Verbaere A, Kinoshita M. Beta - $Zr_2(PO_4)_2SO_4$ - A Zirconium Phosphato-sulfate with A $Sc_2(WO_4)_3$ Structure - A comparison between garnet, Nasicon, and $Sc_2(WO_4)_3$ structure types. J. Solid State Chem. 1987;71:121.

[17] Sleight AW, Thundathil MA, Evans JSO. Materials with Low or Negative Thermal Expansion. United States Patent, 1999.

[18] Merkel GA. Negative Thermal Expansion Materials Including Method of Preparation and Uses Therefor. European Patent, 2001.

[19] Larson AC, Von Dreele RB. GSAS - General Structure Analysis System. Los Alamos Laboratory: Report LA-UR-86-748, 1987.

[20] Toby BH. EXPGUI, a graphical user interface for GSAS. J. Appl. Crystallogr. 2001;34:210.

[21] Rietveld HM. A Profile Refinement Method for Nuclear and Magnetic Structures. Journal of Applied Crystallography 1969;2:65.

[22] Stinton GW, Evans JSO. Parametric Rietveld refinement. J. Appl. Crystallogr. 2007;40:87.

[23] Taylor D. Thermal Expansion Data: III Sesquioxides M_2O_3, with the corundum and the A-, B- and C-M_2O_3 structures. Br. Ceram. Trans. J. 1984;83:92.

[24] Hammersley AP, Svensson SO, Hanfland M, Fitch AN, Hausermann D. Two-dimensional detector software: From real detector to idealised image or two-theta scan. High Pressure Research 1996;14:235.

[25] Woodcock DA, Lightfoot P, Ritter C. Negative Thermal Expansion in $Y_2(WO_4)_3$. J. Solid State Chem. 2000;149:92.

[26] Cetinkol M, Wilkinson AP. manuscript in preparation.

[27] Shannon RD. Revised Effective Ionic Radii and Systematic Studies of Interatomic Distances in Halides and Chalcogenides. Acta Cryst. A 1976;32:751.

CHAPTER 7

IN SITU HIGH-PRESSURE SYNCHROTRON X-RAY DIFFRACTION STUDY OF $Zr_2(MoO_4)(PO_4)_2$

7.1. INTRODUCTION

Materials exhibiting negative thermal expansion continue to attract attention due to intrinsic interest in this phenomenon and their potential for application in controlled thermal expansion composites. $Zr_2(MoO_4)(PO_4)_2$ is a negative thermal expansion material that is structurally related to orthorhombic $Sc_2W_3O_{12}$. Many compositions are known to form with structures related to that of orthorhombic $Sc_2W_3O_{12}$ [1-3]. They typically display anisotropic volume negative thermal expansion while orthorhombic, but are susceptible to symmetry lowering phase transitions [4], with a concomitant loss of negative thermal expansion, on cooling or modest compression [5-8]. The $Sc_2W_3O_{12}$ framework is amenable to a wide range of substitutions beyond the simple replacement of Sc^{3+} with other trivalent ions, for example, materials such as $A_2(MO_4)(PO_4)_2$ (A = Zr or Hf, M = W or Mo) [9-12], $(HfMg)(WO_4)_3$ [13-15], and $Zr_2(SO_4)(PO_4)_2$ [16] have been reported to have related structures. The wide range of possible substitutions allows for tuning of both thermal and high pressure behavior. The use $A_2(MO_4)(PO_4)_2$ (A = Zr or Hf; M = W or Mo) in controlled thermal expansion applications is covered by several patents including [17, 18].

NTE compounds may find application as pure phases and as components in composite materials with tailored thermal expansion coefficients [19-22]. During the manufacture and use of these materials, pressures above ambient may be encountered

leading to phase transitions and a loss of NTE behavior [23, 24]. Many NTE materials, owing to their flexible frameworks and relatively low densities, commonly display crystalline-to-crystalline phase transitions [7, 25-28], and pressure induced amorphization [25, 29-33] upon application of modest pressures. As a consequence, high pressure studies of NTE materials are of some importance from a practical standpoint as well as being of fundamental interest.

The existence of $Zr_2MoO_4(PO_4)_2$ was first reported by Sirotinkin et al. [34]. It has been shown to display negative thermal expansion [35, 36]. Dilatometer measurements indicated a mean linear coefficients of thermal expansion -6×10^{-6} [36]. We have recently conducted a detailed investigation on $Zr_2MoO_4(PO_4)_2$, investigating the structural changes accompanying the thermal expansion behavior. In this paper, we present a high-pressure *in-situ* monochromatic synchrotron powder diffraction study of $Zr_2MoO_4(PO_4)_2$ at room temperature in a diamond anvil cell.

7.2. EXPERIMENTAL PROCEDURES

7.2.1. Sample Preparation

$Zr_2(MoO_4)(PO_4)_2$ were prepared using stoichiometric amounts of ZrO_2 (Alfa Aesar, 99.7%), $NH_4H_2PO_4$ (J.T. Baker, 99.2 %) and 20% excess MoO_3 (J.T. Baker, 99.8 %). The starting compounds were ground together in an agate mortar, heated in an alumina crucible for 4 hours at 600 ºC, 2 hours at 900 ºC and, finally, 30 minutes at 1000 ºC. This treatment was followed by grinding and heating for another 5 hours at 900 ºC resulting in an off white powder.

7.2.2. Diamond Anvil Cell and Diffraction Data Collection

High pressure *in-situ* powder diffraction data were collected at room temperature on the beamline 1-BM-C at the Advanced Photon Source (APS), Argonne National Laboratory. Data were obtained using a four-post diamond anvil cell (DAC). The DAC had 2.1 mm thick diamonds with 600 μm culet faces. A pre-indented fully hardened stainless steel gasket with 250 μm initial thickness and a 300 μm diameter hole was used. A methanol-ethanol (4:1) liquid mixture was used as the pressure medium. This liquid medium was claimed to be hydrostatic up to 10.4 GPa [37]. X-rays of wavelength 0.6194 Å was selected using a Si (111) double-crystal monochromator and the beam collimated with a ~200 μm pin hole. Diffraction patterns were recorded on a Mar345 imaging plate detector. A few small ruby chips were loaded into the cells along with the samples so that the pressure could be determined using the ruby fluorescence technique [38], where pressure calibration errors of 0.05-0.1 GPa are possible [39].

At each pressure point, 2 exposures were taken at 2 different sample-to-detector distances (600 mm and 1000 mm). The initial data collection was done with no pressure medium and with no pressure. 18 diffraction patterns were collected up to 7.2 GPa on compression. The sample-to-detector distance was calibrated using ambient pressure diffraction from LaB_6 (NIST SRM 660a) sample that was loaded into the DAC.

7.2.3. Data Processing

The two-dimensional diffraction images were integrated using the program FIT2D [40]. I(2θ) data were initially processed in JADE [41]. The high pressure phases were indexed with Treor [42] implemented in the program CMPR [43] and then further analyzed by a combination of the Rietveld [44] and Le Bail [45] methods using GSAS

[46] with the EXPGUI [47] interface. The calculated unit cell volumes were fitted to the Birch-Murnaghan equation of state (EOS) [48] using the EOS-FIT program (v5.2) [49].

7.3. RESULTS AND DISCUSSION

All of the diffraction patterns, collected at a sample-to-detector distance of 600 mm, are shown in Figures 7.1. A more detailed version of diffraction patterns are presented in Figure 7.2 for selected pressure points. The Bragg peaks at ~4.8^o and ~6.1^o 2θ get broader during the first transition. The transition onset pressure, as suggested by an examination of the full width at half maximum for these peaks as a function of pressure (Figure 7.3 and 7.4) during compression is 1.5 GPa. The diffraction patterns could be indexed on an orthorhombic unit cell (Pnca) for pressures up to 1.2 GPa. The next pressure point (1.5 GPa), the pattern could be indexed as monoclinic. All the features in the diffraction patterns for the new phase could be fit very well using monoclinic ($P2_1/n$) unit cell up to 3.1 GPa. LeBail fits to the data at 0.0 GPa with orthorhombic (Pnca) structure and 1.5 GPa with monoclinic ($P2_1/n$) structure are shown in Figures 7.5 and 7.6, respectively. When the pressure was increased to 3.3 GPa, another phase formed as indicated by the splitting of some of the Bragg peaks. This new phase could not be clearly identified, but might be an another monoclinic phase as we have observed for $Zr_2(WO_4)(PO_4)_2$ previously. The Bragg peaks start to broaden around 4 GPa showing signs of pressure induced amorphization.

Lattice constants derived from LeBail fits to each diffraction pattern up to 3.1 GPa are given in Table 7.1. Normalized unit cell volume as a function of pressure is shown in Figure 7.7. Normalized lattice constants for phases 1 and 2 are shown in Figure

7.8. There appear to be no discontinuities in the lattice constants at the first phase transition, suggestive of second order behavior. Progression of the monoclinic angle α is also very continuous, as seen in Figure 7.9. It is apparent from normalized lattice constants that both phases are anisotropically compressible. Linear compressibility's for the initial orthorhombic phase were estimated to be β_a= 4.2(3) x 10^{-3} GPa^{-1}, β_b= 11(1) x 10^{-3} GPa^{-1}, β_c= 6.0(5) x 10^{-3} GPa^{-1} by least squares fits of a straight line. The corresponding values for the monoclinic phase existing up to 3.1 GPa are β_a= 11(1) x 10^{-3} GPa^{-1}, β_b= 6.1(4) x 10^{-3} GPa^{-1}, β_c= 17(1) x 10^{-3} GPa^{-1}. The b-axis stiffens slightly, but the a- and c-axes softens considerably on going to the monoclinic phase.

For the two phases observed, a third order Birch-Murnaghan equation of state was fit to the P-V data and the fits are shown in Figure 7.10 and 7.11. During the fitting, the pressure derivative of the bulk modulus (K_p) was fixed at 4.0 while varying the zero pressure volume (V_0) and bulk modulus (K_0). Bulk moduli estimated using a Birch - Murnaghan equation of state, were 45(4) GPa for the orthorhombic phase, and 20(2) GPa for the monoclinic phase. The bulk modulous values with phase transition pressures for $Zr_2(WO_4)(PO_4)_2$ and some of the related compounds are shown in Table 7.2. The behavior of $Zr_2(MoO_4)(PO_4)_2$ on compression is very similar to the behavior of $Zr_2(WO_4)(PO_4)_2$, and different from that previously observed for other orthorhombic $A_2M_3O_{12}$ phases such as $Sc_2W_3O_{12}$, $Sc_2Mo_3O_{12}$ and $Al_2W_3O_{12}$.

7.4. CONCLUSIONS

$Zr_2(MoO_4)(PO_4)_2$ adopts the orthorhombic (Pnca) $Sc_2W_3O_{12}$ structure under ambient conditions. Synchrotron x-ray powder diffraction was used to study its behavior

on compression in a diamond anvil cell up to 7.2 GPa. Two crystalline-to-crystalline phase transitions were observed: orthorhombic (Pnca) between 0.0-1.2 GPa, monoclinic ($P2_1/n$) between 1.5-3.1 GPa, and unidentified phase above 3.2 GPa. Bulk modulous estimated using a Birch-Murnaghan equation of state, were 45(4) GPa for the orthorhombic phase, and 20(2) GPa for the monoclinic phase. Amorphization was observed above 4 GPa.

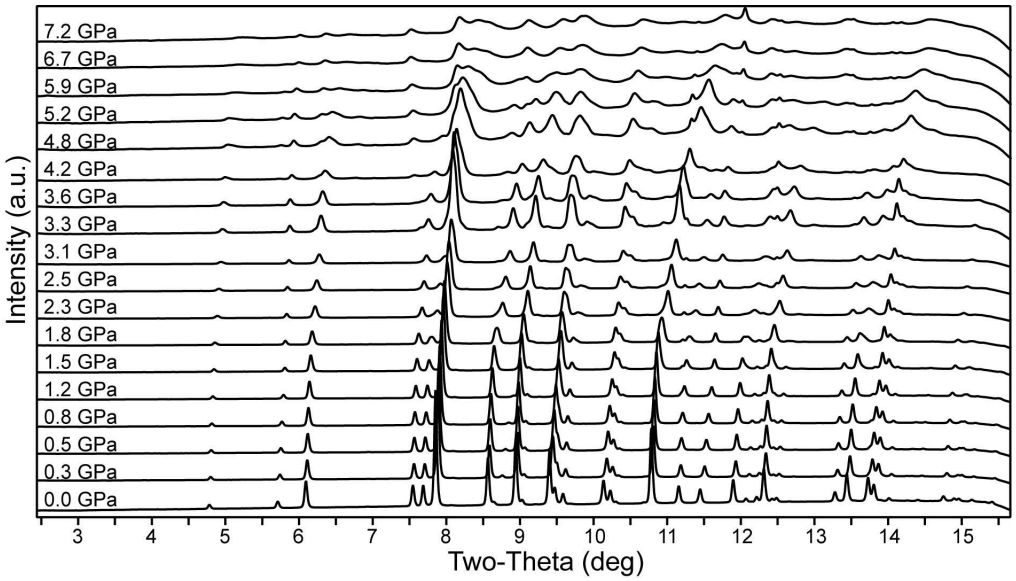

Figure 7.1: Diffraction patterns for $Zr_2(MoO_4)(PO_4)_2$ as a function of pressure (The sample-to-detector distance is 600 mm)

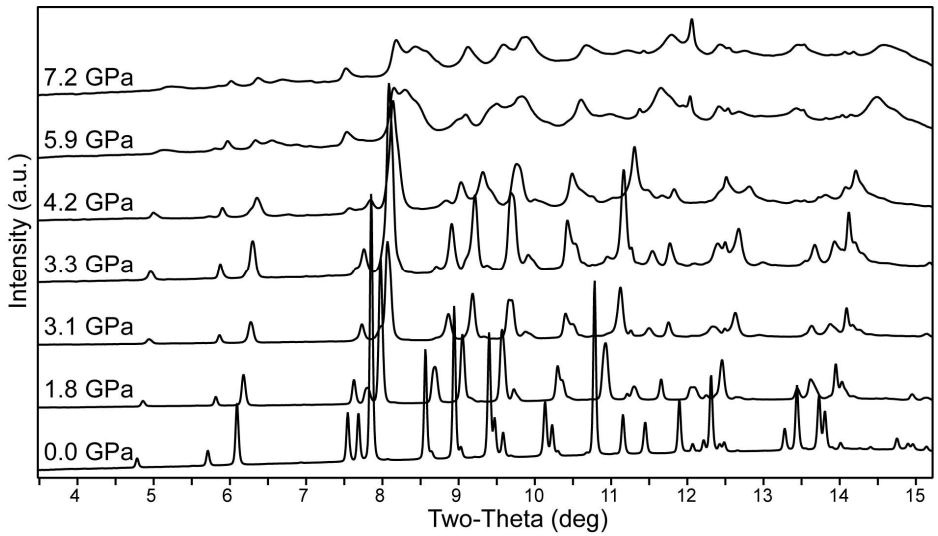

Figure 7.2: Selected diffraction patterns for $Zr_2(MoO_4)(PO_4)_2$ as a function of pressure (The sample-to-detector distance is 600 mm)

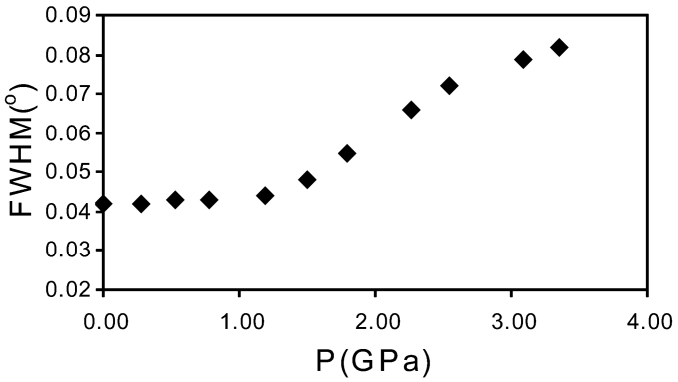

Figure 7.3: Full width at half maximum for the Bragg peak located at ~4.8°

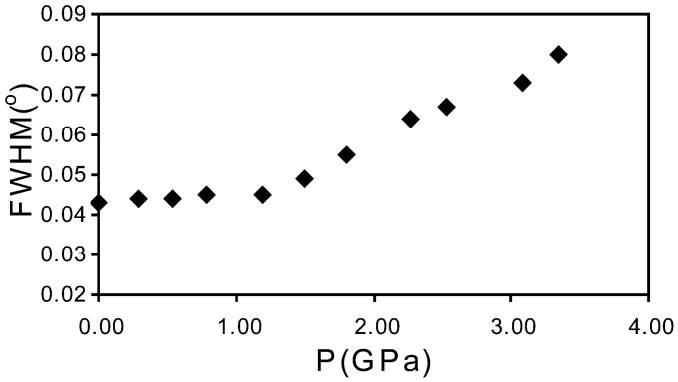

Figure 7.4: Full width at half maximum for the Bragg peak located at ~6.1°

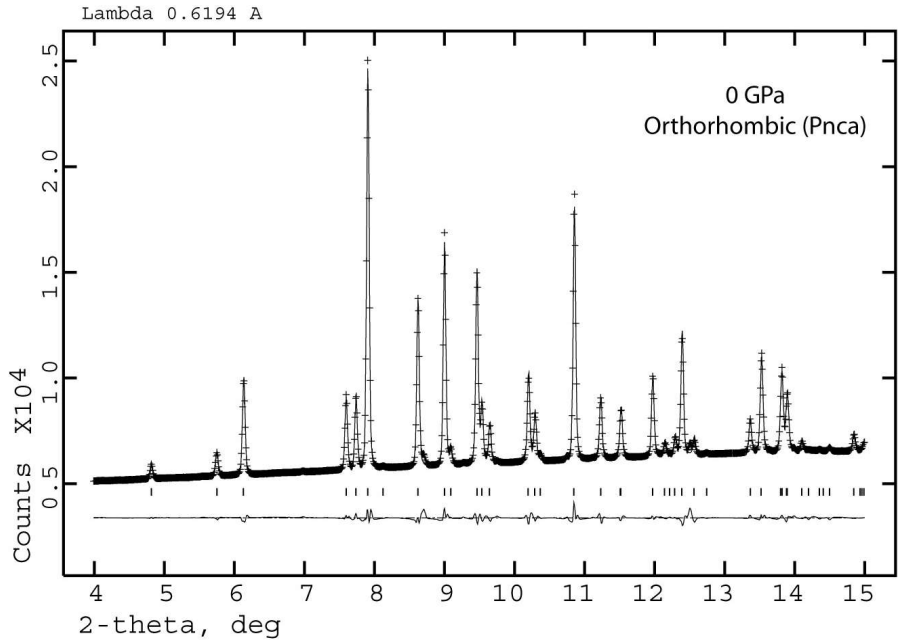

Figure 7.5: Le Bail fit for $Zr_2(MoO_4)(PO_4)_2$ at ambient pressure. Observed (+), calculated (-), and difference (bottom trace) powder diffraction patterns are shown along with tag marks indicating the calculated peak positions.

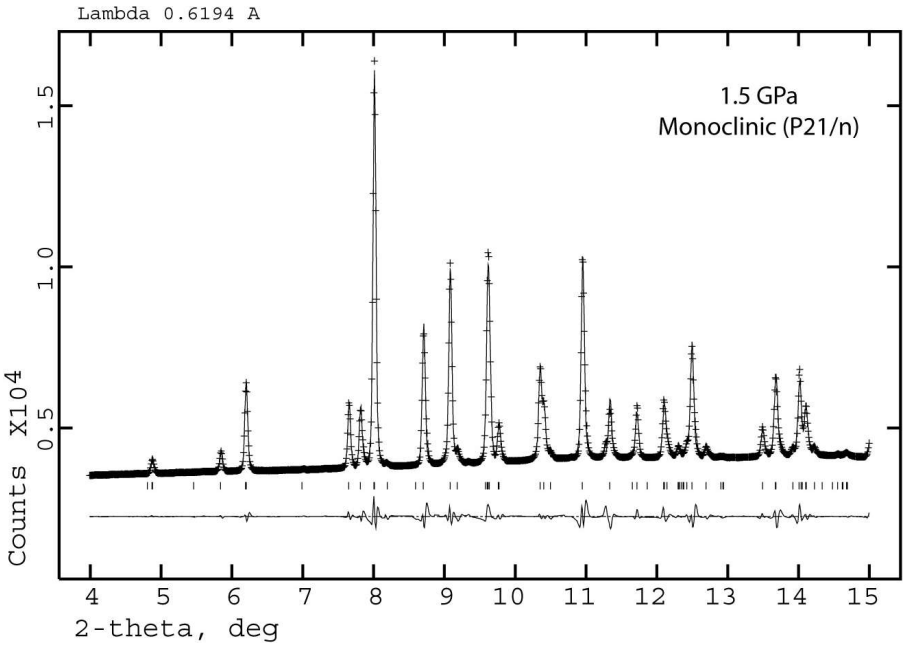

Figure 7.6: Le Bail fit for monoclinic phase of $Zr_2(MoO_4)(PO_4)_2$ at 1.5 GPa. Observed (+), calculated (-), and difference (bottom trace) powder diffraction patterns are shown along with tag marks indicating the calculated peak positions.

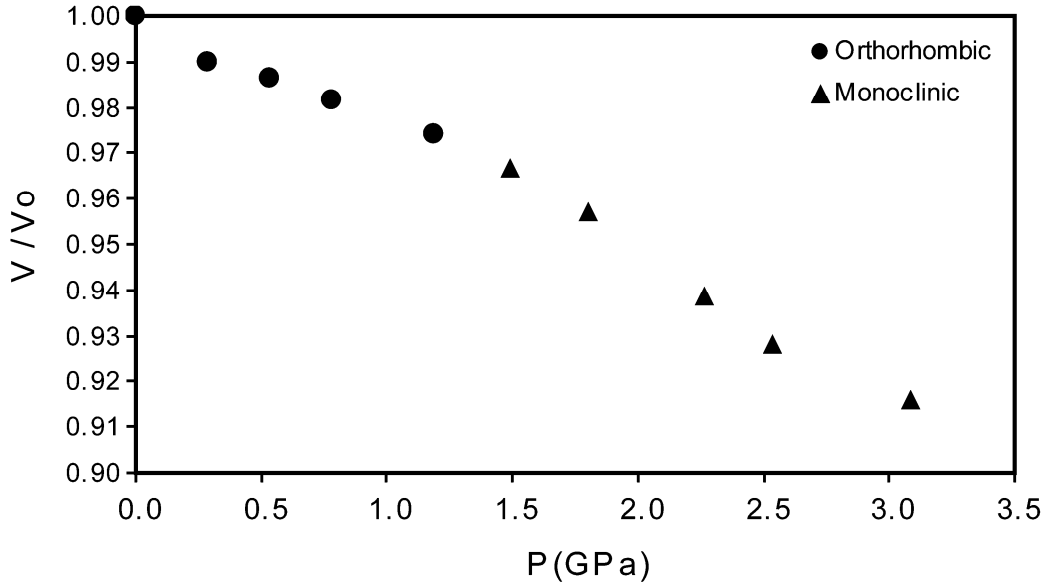

Figure 7.7: Normalized unit cell volume as a function of pressure.

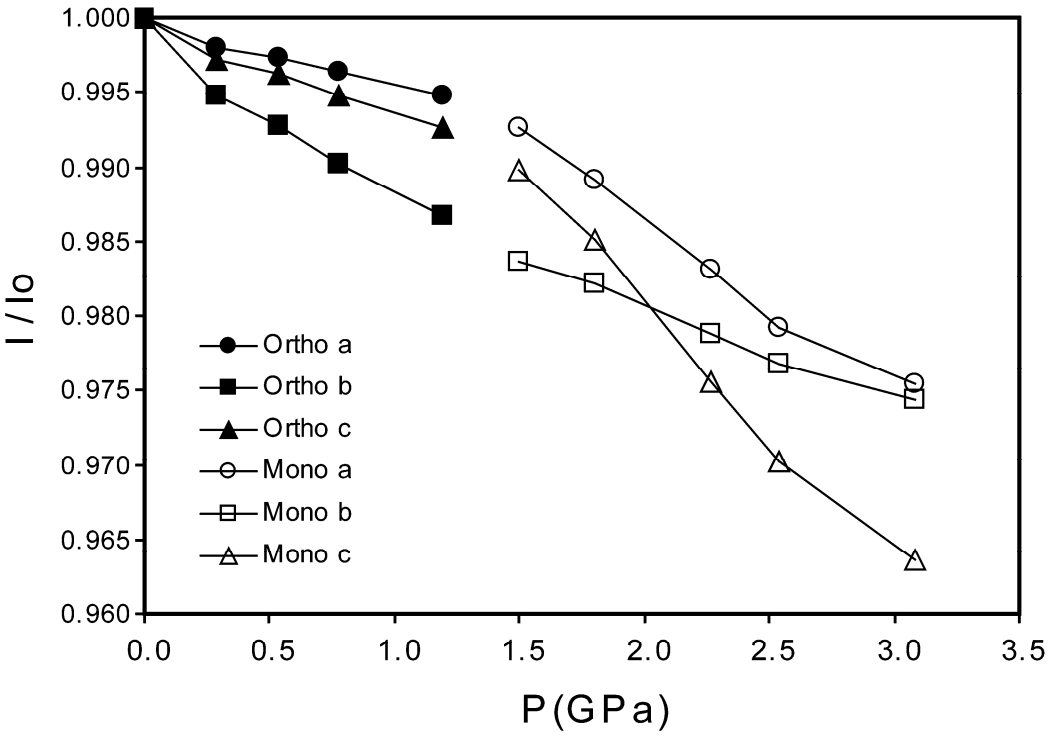

Figure 7.8: Normalized unit cell constants for orthorhombic and monoclinic phases.

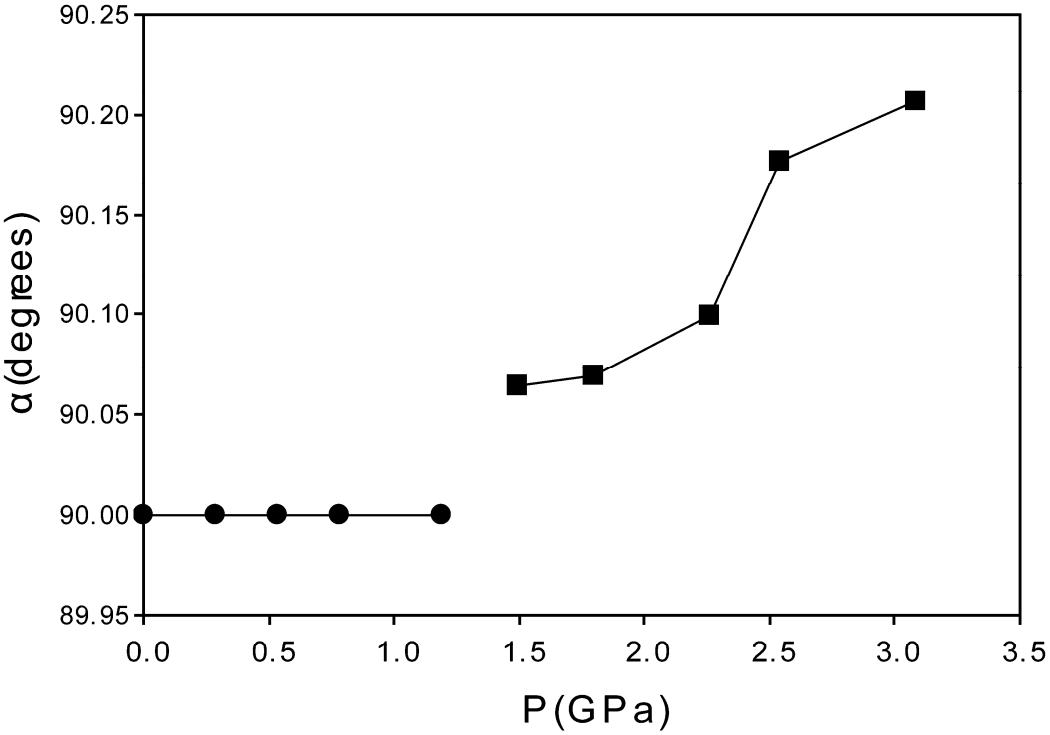

Figure 7.9: Evolution of monoclinic angle α as a function of pressure

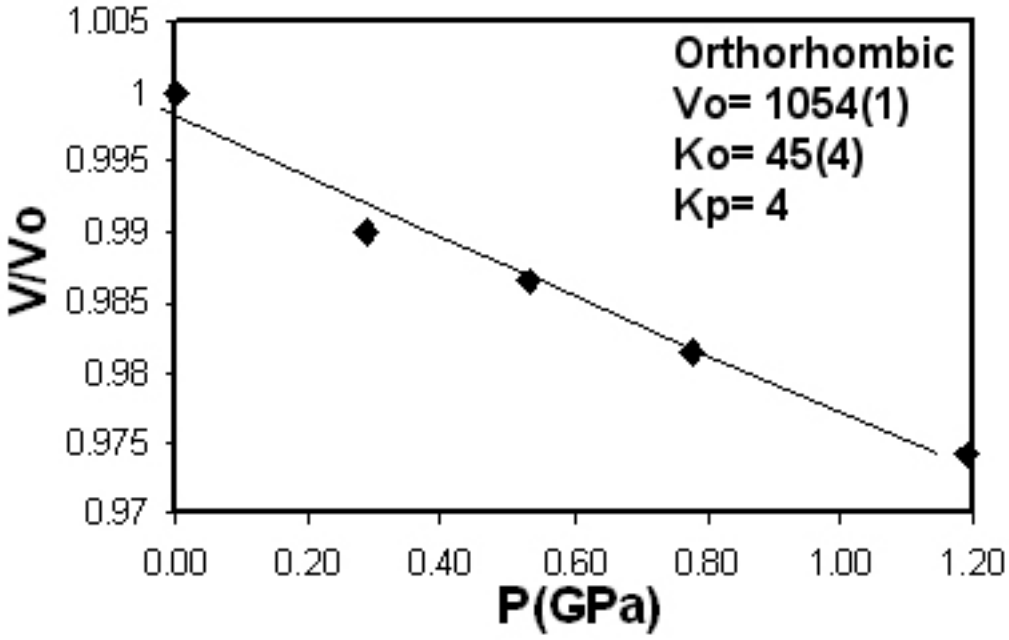

Figure 7.10: Normalized unit cell volume versus pressure for orthorhombic $Zr_2(MoO_4)(PO_4)_2$ along with a fit to the Birch-Murnaghan equation-of-state.

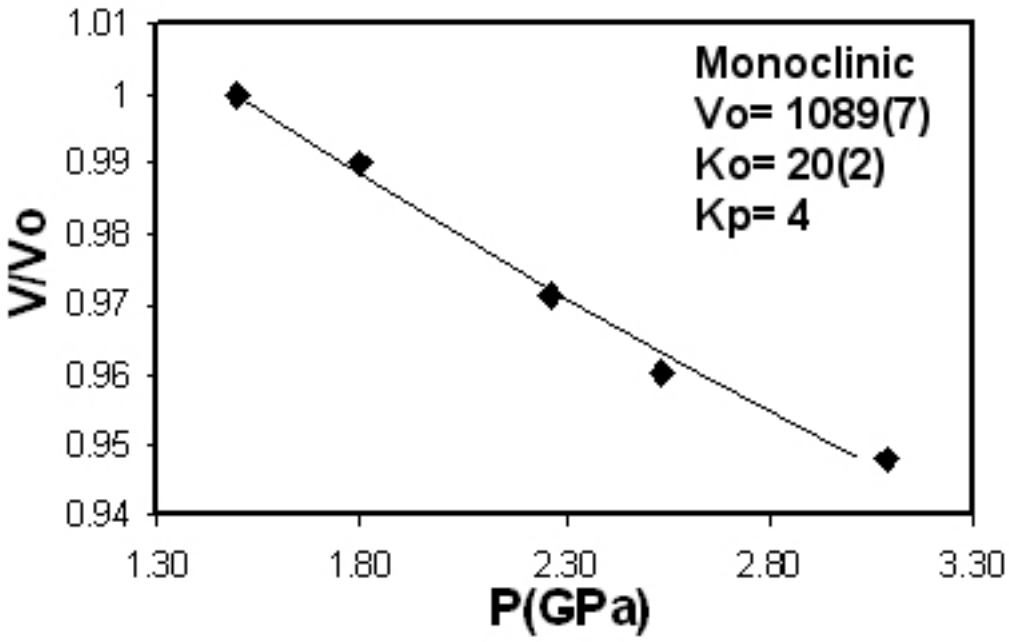

Figure 7.11: Normalized unit cell volume versus pressure for monoclinic $Zr_2(MoO_4)(PO_4)_2$ along with a fit to the Birch-Murnaghan equation-of-state.

Table 7.1: $Zr_2MoP_2O_{12}$ Lattice constants from LeBail fits

P	*phase*	*a (Å)*	*b (Å)*	*c (Å)*	*α (deg)*	*Vol (Å^3)*
0.0	Ortho	9.3378(2)	12.3285(3)	9.1684(2)		1055.48(7)
0.3	Ortho	9.3190(2)	12.2648(4)	9.1426(2)		1044.95(8)
0.5	Ortho	9.3133(3)	12.2393(4)	9.1337(2)		1041.13(8)
0.8	Ortho	9.3038(2)	12.2083(3)	9.1208(2)		1035.98(7)
1.2	Ortho	9.2890(2)	12.1639(4)	9.1005(2)		1028.27(8)
1.5	Mono	9.2694(5)	12.1260(4)	9.0753(5)	90.06(2)	1020.1(1)
1.8	Mono	9.237(1)	12.108(1)	9.032(1)	90.07(1)	1010.1(3)
2.3	Mono	9.180(1)	12.067(2)	8.944(1)	90.10(2)	990.7(4)
2.5	Mono	9.1430(9)	12.042(1)	8.895(1)	90.18(1)	979.4(3)
3.1	Mono	9.1090(9)	12.013(1)	8.835(1)	90.21(1)	966.8(3)

Table 7.2: High pressure behavior of $A_2M_3O_{12}$ type compounds. Ko and P_T denotes bulk modulus and phase transition pressure, respectively.

		$Sc_2W_3O_{12}$	***$Sc_2Mo_3O_{12}$***	***$Al_2W_3O_{12}$***	***$Zr_2WP_2O_{12}$***	***$Zr_2MoP_2O_{12}$***
phase 1		Pnca	Pnca	Pnca	Pnca	**Pnca**
	Ko (GPa)	31(3)[6]	32(2)[7]; 6[50]	48[7]	49(2)	**45(4)**
	P_T (GPa)	0.3[6]; 0.6[51]	0.29[52]	0.1[7]; 0.28[53]	1.4; 1.2	**1.2-1.5**
			0.25-0.6[7]	0.5[54]		
phase 2-A		$P2_1/a$	$P2_1/a$	$P2_1/a$		
	Ko (GPa)	14(1)[6]	16(1)[7]	28(1)[7]		
	P_T (GPa)	2.8[6] ; 1.6[51]	2.5 - 3[7] ; 2.7[52]			
phase 2-B					$P2_1/n$	**$P2_1/n$**
	Ko (GPa)				17(1)	**20(2)**
	P_T (GPa)				3.4	3.3
phase 3		**$P2_1/n$**	Unidentified	N/A	$P2_1/n$	
	Ko (GPa)	**90(3)**			36(4)	
	P_T (GPa)	**2.7**			6.3	
phase 4					P1 or P-1	
	Ko (GPa)				76(7)	
	P_T (GPa)					

7.5. REFERENCES

[1] Abrahams SC, Bernstein JL. Crystal Structure of the Transition-Metal Molybdates and Tungstates. II. Diamagnetic $Sc_2(WO_4)_3$. J. Chem. Phys. 1966;45:2745.

[2] Evans JSO, Mary TA, Sleight AW. Negative Thermal Expansion in $Sc_2(WO_4)_3$. J. Solid State Chem. 1998;137:148.

[3] Weller MT, Henry P, Wilson CC. An analysis of the thermal motion in the negative thermal expansion material $Sc_2(WO_4)_3$ using isotopes in neutron diffraction. J. Phys. Chem. B 2000;104:12224.

[4] Sleight AW, Brixner LH. A New Ferroelastic Transition in Some $A_2(MO_4)_3$ Molybdates and Tungstates. J. Solid State Chem. 1973;7:172.

[5] Evans JSO, Mary TA. Structural Phase Transitions and negative thermal expansion in $Sc_2(MoO_4)_3$. International Journal of Inorganic Materials 2000;2:143.

[6] Varga T, Wilkinson AP, Lind C, Bassett WA, Zha C-S. In-situ high pressure synchrotron x-ray diffraction study of $Sc_2W_3O_{12}$ at up to 10 GPa. Phys. Rev. B 2005;71:214106.

[7] Varga T, Wilkinson AP, Lind C, Bassett WA, Zha C-S. High pressure synchrotron x-ray powder diffraction study of $Sc_2Mo_3O_{12}$ and $Al_2W_3O_{12}$ J. Phys.: Condens. Matter 2005;17:4271.

[8] Varga T, Wilkinson AP, Jorgensen JD, Short S. Neutron powder diffraction study of the orthorhombic to monoclinic transition in $Sc_2W_3O_{12}$ on compression. Solid State Sciences 2006;8:289.

[9] Tsvigunov AN, Sirotinkin VP. Preparation of $Zr_2WO_4(PO_4)_2$ and indexing of its X-ray diffraction pattern. Russ. J. Inorg. Chem. 1990;35:1740.

[10] Evans JSO, Mary TA, Sleight AW. Structure of $Zr_2(WO_4)(PO_4)_2$ from Powder X-ray Data: Cation Ordering with No Superstructure. J. Solid State Chem. 1995;120:101.

[11] Martinek CA, Hummel FA. Subsolidus Equilibria in the System ZrO_2-WO_3-P_2O_5. J. Am. Ceram. Soc. 1970;53:159.

[12] Sirotinkin VP, Tsvigunov AN. Synthesis, X-Ray-Diffraction and Thermal Analyses of $Zr_2MoO_4(PO_4)_2$. Russ. J. Inorg. Chem. 1994;39:735.

[13] Suzuki T, Omote A. Negative Thermal Expansion in $(HfMg)(WO_4)_3$. J. Am. Ceram. Soc. 2004;87:1365.

[14] Suzuki T, Omote A. Pseudo binary HfW_2O_8-$MgWO_4$ thermal expansion control system. J. Ceram. Soc. Jpn. 2006;114:833.

[15] Suzuki T, Omote A. Zero thermal expansion in $(Al_{2x}(HfMg)_{(1-x)})(WO_4)_{(3)}$. J. Am. Ceram. Soc. 2006;89:691.

[16] Piffard Y, Verbaere A, Kinoshita M. Beta - $Zr_2(PO_4)_2SO_4$ - A Zirconium Phosphato-sulfate with A $Sc_2(WO_4)_3$ Structure - A comparison between garnet, Nasicon, and $Sc_2(WO_4)_3$ structure types. J. Solid State Chem. 1987;71:121.

[17] Sleight AW, Thundathil MA, Evans JSO. Materials with Low or Negative Thermal Expansion. United States Patent, 1999.

[18] Merkel GA. Negative Thermal Expansion Materials Including Method of Preparation and Uses Therefor. European Patent, 2001.

[19] Wetherfold RC, Wang J. Tailoring thermal deformation by using layered beams. Compos. Sci. Technol. 1995;53:1.

[20] Fleming DA, Johnson DW, Lemaire PJ. Article Comprising a Temperature Compensated Optical Fiber Refractive Index Grating. USA: Lucent Technologies, 1997.

[21] Fleming DA, Lemaire PJ, Johnson DW. Temperature compensated optical fiber refractive index grating. European Patent EP 97-306798 19970902. USA: Lucent Technologies, Inc., 1998. p.7.

[22] Balch DK, Dunand DC. Copper-Zirconium Tungstate Composites Exhibiting Low and Negative Thermal Expansion Influenced by Reinforcement Phase Transformations. Metall. Mater. Trans. A 2004;35A:1159.

[23] Holzer H, Dunand DC. Phase transformation and thermal expansion of Cu/ZrW_2O_8 metal matrix composites. J. Mater. Res. 1999;14:780.

[24] Yilmaz S. Phase transformations in thermally cycled Cu/ZrW_2O_8 composites investogated by synchrotron x-ray diffraction. J. Phys. Condens. Matter. 2002;14:365.

[25] Grzechnik A, Crichton WA. Structural transformations in cubic $ZrMo_2O_8$ at high pressures and high temperatures. Solid State Sci. 2002;4:1137.

[26] Muthu DVS, Chen B, Wrobel JM, Krogh Andersen AM, Carlson S, Kruger MB. Pressure-induced phase transitions in α–$ZrMo_2O_8$. Phys. Rev. B 2002;65:064101.

[27] Evans JSO, Hu Z, Jorgensen JD, Argyriou DN, Short S, Sleight AW. Compressibility, Phase Transitions, and Oxygen Migration in Zirconium Tungstate, ZrW_2O_8. Science 1997;275:61.

[28] Jorgensen JD, Hu Z, Short S, Sleight AW, Evans JSO. Pressure-induced cubic-to-orthorhombic phase transfromation in the negative thermal expansion material HfW_2O_8. J. Appl. Phys. 2001;89:3184.

[29] Chen B, Muthu DVS, Liu ZX, Sleight AW, Kruger MB. High-pressure Raman and infrared study of HfW_2O_8. Phys. Rev. B 2001;64:214111.

[30] Perottoni CA, de Jornada JAH. Pressure-Induced Amorphization and Negative Thermal Expansion in ZrW_2O_8. Science 1998;280:886.

[31] Varga T, Wilkinson AP, Lind C, Bassett WA, Zha C-S. Pressure-induced amorphization of cubic ZrW_2O_8 studied in-situ and ex-situ by synchrotron x-ray absorption spectroscopy and diffraction. Phys. Rev. B 2005;72:024117.

[32] Varga T, Wilkinson AP, Lind C, Basset WA, Zha C-S. Pressure-induced amorphization of cubic $ZrMo_2O_8$ studied in-situ by x-ray absorption spectroscopy and diffraction. Solid State Communications 2005;135:739.

[33] Secco RA, Liu H, Imanaka N, Adachi G. Pressure-induced amorphization in negative thermal expansion $Sc_2(WO_4)_3$. Journal of Materials Science Letters 2001;20:1339.

[34] Sirotinkin VP, Tsvigunov AN. Synthesis, X-Ray-Diffraction and Thermoanalytical Study of $Zr_2MoO_4(PO_4)_2$ compounds. Zhurnal Neorg. Khimii 1994;39:768.

[35] Mary TA, Sleight AW. Bulk thermal expansion for tungstate and molybdates of the type $A_2M_3O_{12}$. J. Mater. Res. 1999;14:912.

[36] Evans JSO, Mary TA, Sleight AW. Negative Thermal Expansion in a Large Molybdate and Tungstate Family. J. Solid State Chem. 1997;133:580.

[37] Piermarini GJ, Block S, Barnett JD. Hydrostatic limits in liquids and solids to 100 kbar. J. Appl. Phys. 1973;44:5377.

[38] Barnett JD, Block S, Piermarini GJ. An Optical Fluorescence System for Quantitative Pressure Measurement in the Diamond-Anvil Cell. Rev. Sci. Instrum. 1973;44:1.

[39] Miletich R, Allan D, R., Kuhs W, F. High-Pressure Single-Crystal Techniques. Rev. Mineral. Geochem. 2001;41:445.

[40] Hammersley AP, Svensson SO, Hanfland M, Fitch AN, Hausermann D. Two-dimensional detector software: From real detector to idealised image or two-theta scan. High Pressure Research 1996;14:235.

[41] JADE. computer code JADE. Livermore, CA: Materials Data, Inc., 1995-2005.

[42] Werner PE, Eriksson L, Westdahl M. Treor, a Semi-Exhaustive Trial-and-Error Powder Indexing Program for All Symmetries. J. Appl. Crystallogr. 1985;18:367.

[43] Toby BH. CMPR - a powder diffraction toolkit. J. Appl. Crystallogr. 2005;38:1040.

[44] Rietveld HM. A Profile Refinement Method for Nuclear and Magnetic Structures. Journal of Applied Crystallography 1969;2:65.

[45] Le Bail A, Duroy H, Fourquet JL. Abinitio Structure Determination of $LiSbWO_6$ by X-Ray-Powder Diffraction. Mater. Res. Bull. 1988;23:447.

[46] Larson AC, Von Dreele RB. GSAS - General Structure Analysis System. Los Alamos Laboratory: Report LA-UR-86-748, 1987.

[47] Toby BH. EXPGUI, a graphical user interface for GSAS. J. Appl. Crystallogr. 2001;34:210.

[48] Birch F. Finite elastic strain of cubic crystals. Phys. Rev. 1947;71:809.

[49] Angel RJ. EOS-FIT. computer code EOS-FIT. Blacksburg, VA: Virginia Tech, 2001.

[50] Arora AK, Yagi T, Miyajima N, Mary TA. Amorphization and decomposition of scandium molybdate at high pressure. J. Appl. Phys. 2005;97:013508.

[51] Garg N, Murli C, Tyagi AK, Sharma SM. Phase transitions in $Sc_2(WO_4)_3$ under high pressure. Phys. Rev. B 2005;72.

[52] Paraguassu W, Maczka M, Souza Filho AG, Freire PTC, Mendes Filho J, Melo FEA, Macalik L, Gerward L, Staun Olsen J, Waskowska A, Hanuza J. Pressure-induced structural transformations in the molybdate $Sc_2(MoO_4)_3$. Phys. Rev. B 2004;69:094111.

[53] Maczka M, Paraguassu W, Souza Filho AG, Freire PTC, Mendes Filho J, Melo FEA, Hanuza J. High-pressure Raman study of $Al_2(WO_4)_3$. J. Solid State Chem. 2004;177:2002.

[54] Mukherjee GD, Vijaykumar V, Achary SN, Tyagi AK, Godwal BK. Phase transitions in $Al_2(WO_4)_3$: high pressure investigations of low frequency dielectric constant and crystal structure. J. Phys.: Condens. Matter 2004;16:7321.

CHAPTER 8

SCANDIUM TUNGSTATE ABOVE 2.5 GPA

8.1. INTRODUCTION

$Sc_2W_3O_{12}$ adopts an orthorhombic (Pnca) structure under ambient conditions that is regarded as the structural prototype for a family of compounds with the general formula $A_2M_3O_{12}$ (A = variety of 3+ cations, M = W or Mo). It displays anisotropic negative thermal expansion with (α_a= -6.3 x 10^{-6} K^{-1}, α_b= +7.5 x 10^{-6} K^{-1} and α_c = -5.5 x 10^{-6} K^{-1}) at ambient pressure [1]. Many NTE materials, owing to their flexible frameworks and relatively low densities, display crystalline-to-crystalline phase transitions [2-6], and pressure induced amorphization [2, 7-11] upon application of modest pressures. NTE phases are of interest for application in composite materials with tailored thermal expansion coefficients [12-15]. During the manufacture and use of such materials, stresses may be encountered leading to phase transitions and/or changes in expansion characteristics [16, 17]**.** As a consequence, high pressure studies of NTE materials are of some importance from a practical standpoint as well as being of fundamental interest.

Several members of the $Sc_2W_3O_{12}$ family have been studied under pressure, and display a variety of crystalline-to-crystalline phase transitions and, in some cases, undergo pressure induced amorphization [6, 11, 18-23]. The first high pressure diffraction study of $Sc_2W_3O_{12}$ was done on samples recovered from a Walker-type high pressure device [11]. No crystalline-to-crystalline phase transitions were observed, and $Sc_2W_3O_{12}$ was shown to amorphize partially above 4 GPa, and completely by 8 GPa.

Subsequently, in-situ x-ray diffraction experiments were performed by two groups. Varga et al. examined polycrystalline $Sc_2W_3O_{12}$ using diamond anvil cells and different pressure media up to 10 GPa [22]. They reported an orthorhombic to monoclinic ($P2_1/a$) transition at around 0.3 GPa, and a second irreversible transition to an unidentified structure at ~ 2.8 GPa. Amorphization was not observed in the studied P range. Garg et al. conducted in-situ Raman scattering and x-ray diffraction studies in diamond anvil cells [23]. They reported the same orthorhombic to monoclinic ($P2_1/a$) transition at around 0.6± 0.3 GPa and a second irreversible transition, possibly to a monoclinic phase, around 1.6 GPa, but due to the low resolution of their diffraction data they did not index the diffraction pattern. They reported amorphization starting at around 6.5 GPa. In order to reveal the structural changes accompanying compression and further details of the first phase transition, Varga et al. conducted a powder neutron diffraction experiment up to 0.6 GPa using a large volume helium gas cell [24]. In these experiments, monoclinic $Sc_2W_3O_{12}$ was first observed around 0.3 GPa with complete transformation at 0.35 GPa. On decompression, $Sc_2W_3O_{12}$ was still completely monoclinic at 0.25 GPa indicating hysteresis in the phase transition.

A further high-pressure *in-situ* monochromatic synchrotron powder diffraction study of $Sc_2W_3O_{12}$ was conducted with the aim of indexing the second high pressure phase and determining its physical characteristics under pressure.

8.2. EXPERIMENTAL PROCEDURES

8.2.1. Sample Preparation

$Sc_2W_3O_{12}$ was prepared by the high temperature solid state reaction of Sc_2O_3 (Alfa Aesar, 99.9%) and WO_3 (Strem Chemicals, 99.8 %). Stoichiometric amounts of Sc_2O_3 and WO_3 were mixed and ground together in an agate mortar. The mixture was heated in an alumina crucible for 12 h at 1000 ºC in air. This was followed by grinding and heating at 1200 ºC for 12 h in air.

8.2.2. Diamond Anvil Cell and Diffraction Data Collection

High pressure *in-situ* powder diffraction data were collected at room temperature using beamline 1-BM-C at the Advanced Photon Source (APS), Argonne National Laboratory. The sample was compressed using a Diacell Bragg-S type diamond anvil cell (DAC). A methanol-ethanol (4:1) mixture, claimed to be hydrostatic up to 10.4 GPa [25], was used as the pressure medium. The DAC had diamonds with 600 μm culet faces. A fully hardened stainless steel gasket, 250 μm initial thickness, was pre-indented to ~100 μm and a ~300 μm diameter hole was drilled. X-rays of wavelength 0.6192 Å were selected using a Si(111) double-crystal monochromator. Diffraction patterns were recorded on a Mar345 imaging plate detector. A few small ruby chips were loaded into the cell along with the sample so that the pressure could be determined using the ruby fluorescence technique [26], where pressure calibration errors of 0.05-0.1 GPa are possible [27].

At each pressure examined, 10 sec exposures were taken at 3 different sample-to-detector distances (170 mm, 370 mm and 570 mm) to provide patterns with differing 2θ ranges and resolutions. An initial pattern at ambient pressure was recorded with the sample in the DAC without any pressure medium to check particle statistics. 8 diffraction patterns were collected during compression, with the pressure medium present, up to 6.2

GPa and 2 further patterns were collected during decompression to ambient. The sample-to-detector distance was calibrated using ambient pressure diffraction from LaB_6 (NIST SRM 660a) loaded in the DAC.

8.2.3. Data Processing

The two-dimensional diffraction images were integrated using the program FIT2D [28]. I(2θ) data were initially processed in JADE [29]. Diffraction data for the second high pressure phase was indexed with Treor [30] implemented in the program CMPR [31]. Diffraction data were analyzed by the Le Bail [32] method using GSAS [33] with the EXPGUI [34] interface to obtain lattice constants and unit cell volumes (see Table 8.1). The unit cell volumes for the second high pressure phase were fitted to the Birch-Murnaghan equation of state (EOS) [35] using the EOS-FIT program (v5.2) [36].

8.3. RESULTS AND DISCUSSION

All of the diffraction patterns, collected at the sample-to-detector distance giving the highest resolution (570 mm), are shown in Figure 8.1. Two crystalline-to-crystalline phase transitions are obvious by inspection of this figure. The emergence of new peaks is apparent at ~4.3° and ~6.8° 2θ for the diffraction pattern at 0.5 GPa. While the transition onset pressure is not well determined our present data, it was established to be at 0.3 GPa by a previous neutron study [24]. This first high pressure phase was indexed previously as monoclinic ($P2_1/a$) and all the features in the diffraction patterns could be fit very well using that structural model of monoclinic $Sc_2Mo_3O_{12}$ [37]. LeBail fits to the data at 0.0

GPa with orthorhombic (Pnca) structure and 0.8 GPa with monoclinic ($P2_1/a$) structure are shown in Figures 8.2 and 8.3, respectively.

When the pressure was increased to 2.7 GPa, another phase formed as indicated by the emergence of new peaks. This new phase was observed in earlier studies, but was not indexed. The new phase was indexed as monoclinic probable space group $P2_1/n$ (a-axis unique). A LeBail fit to the data at 3.5 GPa is shown in Figure 8.4. The lattice constants derived from LeBail fits to each diffraction pattern are given in Table 8.1. After collecting data at a maximum pressure of 6.2 GPa, the diamond anvil cell was decompressed in two steps to 0 GPa. The second high pressure phase was retained to ambient pressure.

Normalized volume per formula unit is shown as a function of pressure in Figure 8.6. As our focus was on the second high pressure phase, and the first two phases were characterized previously, most of our data sets were collected above 2.7 GPa. However, data for the first two phases from Varga et al. [22] were added to the figure for comparison. Using the known equation of state for the first monoclinic phase [22], the volume reduction associated with the second phase transition was estimated to be almost 18% per formula unit at 2.7 GPa. This suggests significant structural changes, consistent with the transition being irreversible on decompression at ambient temperature. It is obvious from Figure 8.5 that the second high pressure phase is much stiffer than the low pressure phases. Fits using a Birch-Murnaghan equation of state are shown in Figure 8.6, both with and without varying K_p. The bulk moduli and phase transition pressures for $Sc_2W_3O_{12}$ and some related compounds are shown in Table 8.2. Normalized lattice constants for the second monoclinic phase are shown in Figure 8.7. It is obvious that a-

axis and b-axis behave in a very similar way under pressure, with the c-axis being slightly less compressible. Linear compressibility values for the second monoclinic phase were estimated to be $\beta_a = 3.6(1) \times 10^{-3}$ GPa^{-1}, $\beta_b = 3.7(2) \times 10^{-3}$ GPa^{-1}, $\beta_c = 2.0(1) \times 10^{-3}$ GPa^{-1} by least squares fits of a straight line to the lattice constants over the range 0 - 6.2 GPa. Changes of the monoclinic angle α on compression are shown in Figure 8.8.

The behavior of $Sc_2W_3O_{12}$ on compression is almost identical to that of $Sc_2Mo_3O_{12}$, but distinct from that of $Al_2W_3O_{12}$ and $Y_2W_3O_{12}$ (Table 8.2). $Sc_2W_3O_{12}$, $Sc_2Mo_3O_{12}$ and $Al_2W_3O_{12}$ have similar first transition pressures adopting a monoclinic $Sc_2Mo_3O_{12}$ structure below 0.5 GPa. However, $Y_2W_3O_{12}$ is reported to undergo no crystalline to crystalline phase transitions on compression, becoming disordered at high pressure. The behavior of $Sc_2W_3O_{12}$ and $Sc_2Mo_3O_{12}$ is different from that of $Al_2W_3O_{12}$ above 0.5 GPa, as there are no obvious crystalline to crystalline transitions for this compound at > 0.5 GPa. $Sc_2W_3O_{12}$, $Sc_2Mo_3O_{12}$ and $Al_2W_3O_{12}$ display a reduction in bulk modulus on going through the orthorhombic to monoclinic phase transition. Similar behavior has previously been reported for materials with a ReO_3 type structure [38]. This structure type also has many of the structural features typical of negative thermal expansion oxides (open flexible frameworks with two coordinate anions), although none of the compounds ReO_3, TaO_2F and NbO_2F display strong NTE. The second monoclinic phase observed on compression of $Sc_2W_3O_{12}$ to > ~2.7 GPa is stiff and much denser when compared to the lower pressure monoclinic phase. We speculate that this change in properties and the irreversibility of the phase transition on compression may be associated with a change in coordination of one of the metals.

8.4. CONCLUSIONS

In conclusion, the second high pressure phase transition in $Sc_2W_3O_{12}$ involves a significant reduction in volume per formula unit (~18% at 2.7 GPa), possibly associated with changes in bonding/structure that lead to irreversibility on decompression. This high pressure phase is much stiffer than either of the lower pressure phases. The sequence of high pressure phase transitions in $Sc_2W_3O_{12}$ is the same as that for $Sc_2Mo_3O_{12}$, but different from other compounds in this family that have been investigated. Structure determination for the high pressure phases would shed light on the crystal chemical origin of these differences.

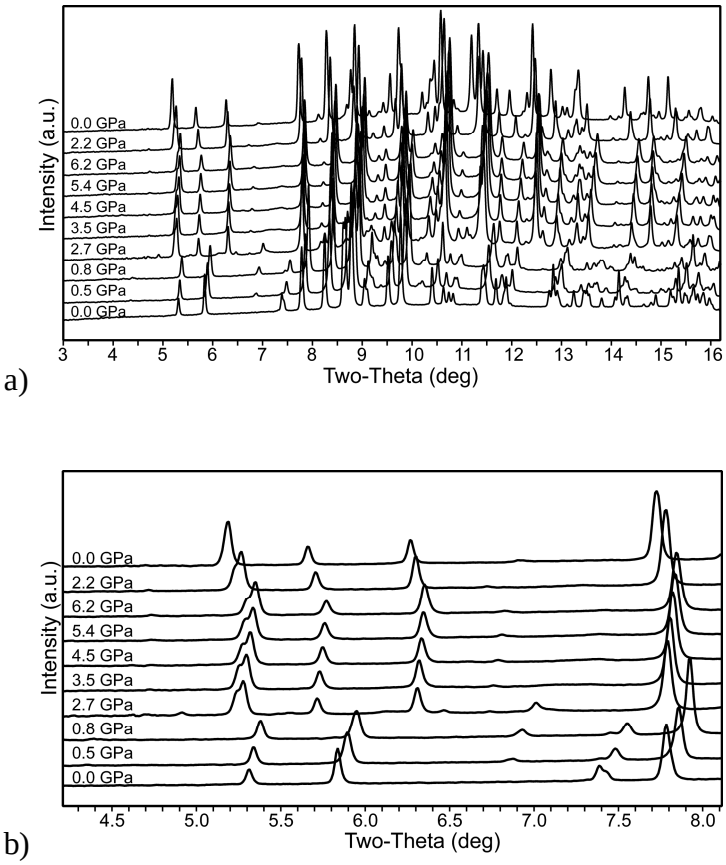

Figure 8.1: Diffraction patterns for $Sc_2W_3O_{12}$ as a function of pressure with a sample-to-detector distance of 570 mm. a) complete patterns, b) low angle region.

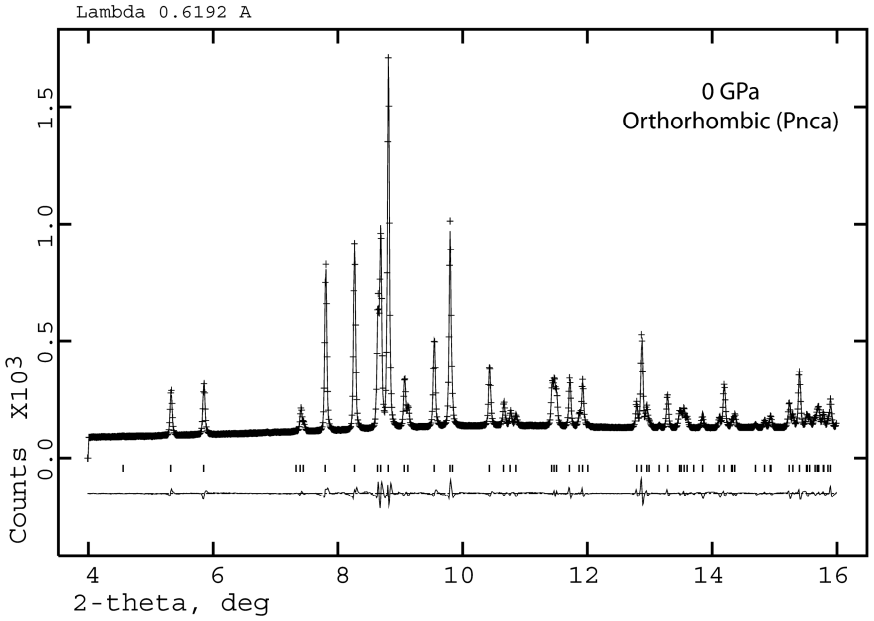

Figure 8.2 : Le Bail fit for orthorhombic $Sc_2W_3O_{12}$ at ambient pressure. Observed (+), calculated (-), and difference (bottom) powder diffraction patterns along with tag marks indicating the peak positions.

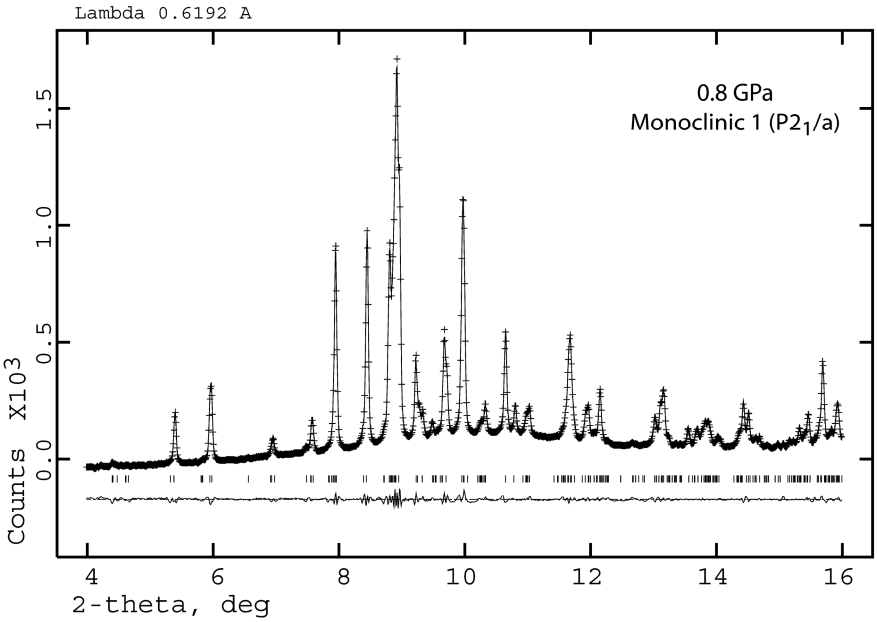

Figure 8.3: Le Bail fit for the first monoclinic phase formed on compression of $Sc_2W_3O_{12}$ (data for 0.8 GPa). Observed (+), calculated (-), and difference (bottom) powder diffraction patterns along with tag marks indicating the peak positions.

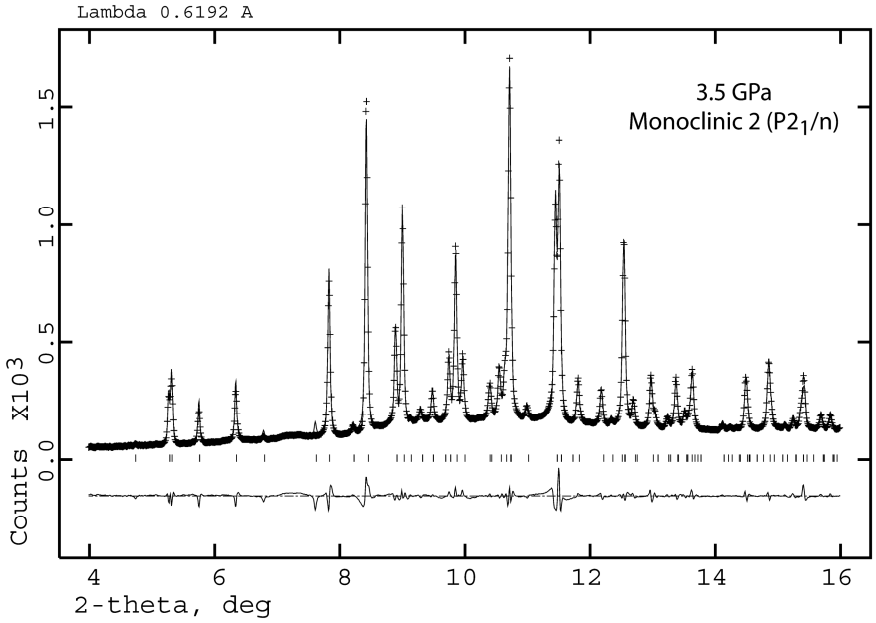

Figure 8.4: Le Bail fit for the second monoclinic phase formed on compression of $Sc_2W_3O_{12}$ (data at 3.5 GPa). Observed (+), calculated (-), and difference (bottom) powder diffraction patterns along with tag marks indicating the peak positions.

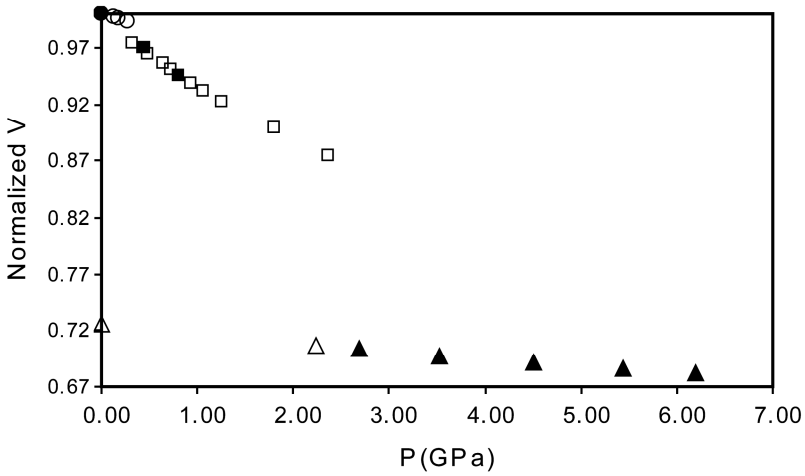

Figure 8.5: Normalized unit cell volume as a function of pressure. ●: orthorhombic, ■: first monoclinic, ▲: second monoclinic, Δ: second monoclinic during decompression, ○: orthorhombic from reference 21, □: first monoclinic from reference 21.

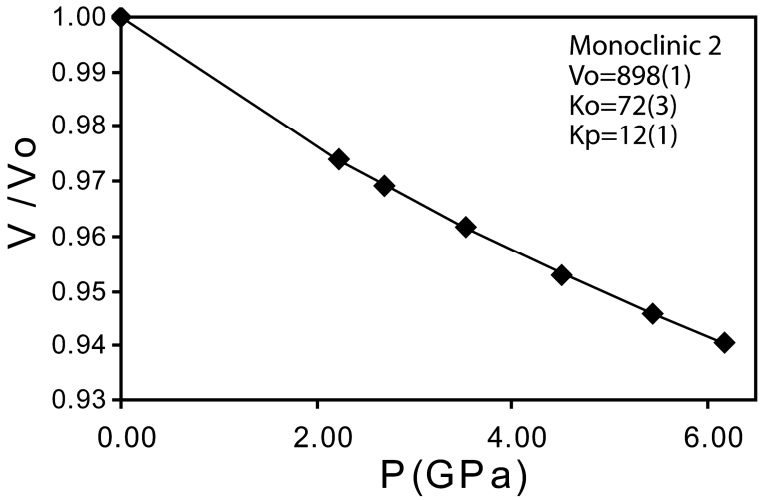

Figure 8.6: Normalized unit cell volume versus pressure for the second monoclinic form of $Sc_2W_3O_{12}$ along with fits to the Birch-Murnaghan equation-of-state with K_p as a variable.

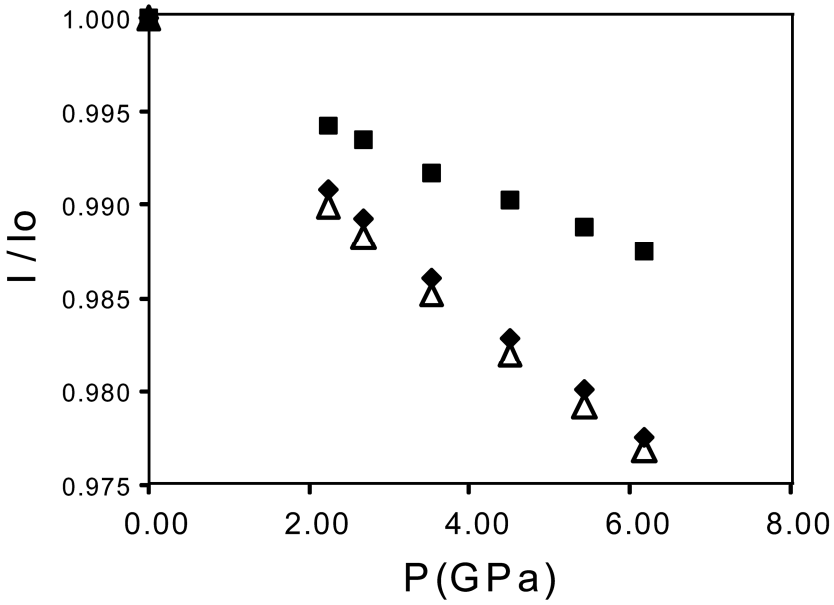

Figure 8.7: Normalized unit cell constants versus pressure for the second monoclinic form of $Sc_2W_3O_{12}$; a-axis diamonds; b-axis open triangles; c-axis squares.

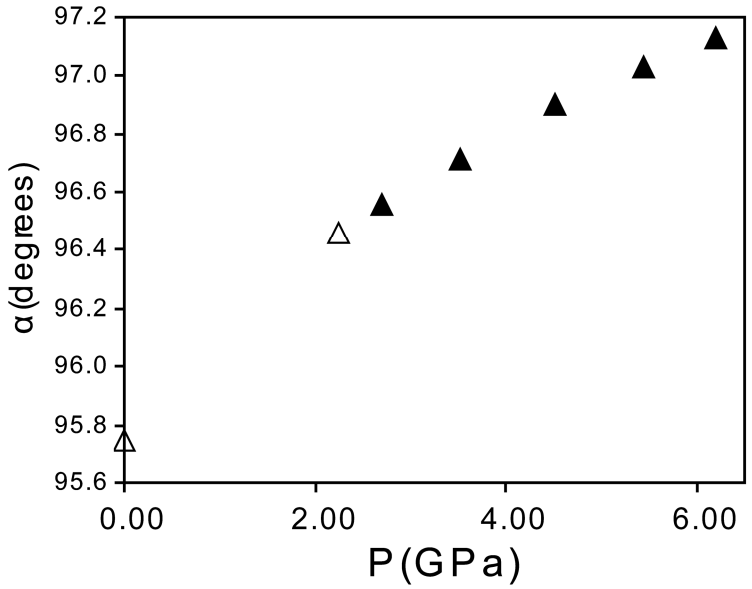

Figure 8.8: Evolution of the monoclinic angle α as a function of pressure for the second monoclinic form of $Sc_2W_3O_{12}$. Solid triangles values on compression, open triangles values on decompression.

Table 8.1: Lattice constants for $Sc_2W_3O_{12}$ as a function of pressure. Monoclinic phase 1 (M1) is b-axis unique and the monoclinic phase 2 (M2) is a-axis unique.

P	***phase***	***a (Å)***	***b (Å)***	***c (Å)***	***α (deg)***	***β (deg)***	***Vol (Å^3)***
0.0	Ortho	9.6788(1)	13.3281(2)	9.5864(2)			1236.65(3)
0.5	M1	16.2530(5)	9.5818(2)	18.9331(5)		125.384(2)	2403.89(5)
0.8	M1	16.1065(3)	9.5009(1)	18.7515(3)		125.233(1)	2343.82(4)
2.7	M2	8.4560(3)	11.3180(5)	9.1496(4)	96.561(5)		869.93(5)
3.5	M2	8.4316(1)	11.2846(2)	9.1366(2)	96.724(2)		863.35(2)
4.5	M2	8.4016(1)	11.2455(2)	9.1196(2)	96.908(2)		855.37(2)
5.4	M2	8.3782(1)	11.2144(2)	9.1069(2)	97.039(2)		849.21(2)
6.2	M2	8.3595(1)	11.1911(2)	9.0970(2)	97.127(2)		844.47(2)
2.2	M2	8.4726(2)	11.3404(3)	9.1592(2)	96.459(2)		874.45(2)
0.0	M2	8.5504(1)	11.4547(2)	9.2116(1)	95.752(2)		897.66(2)

Table 8.2: High pressure behavior of $Sc_2W_3O_{12}$ and related $A_2M_3O_{12}$ compounds. K_0 and P_T denote bulk modulus and phase transition pressure, respectively.

		$Sc_2W_3O_{12}$	***$Sc_2Mo_3O_{12}$***	***$Al_2W_3O_{12}$***	***$Y_2W_3O_{12}$***
Ortho		Pnca	Pnca	Pnca	Pnca
	Ko(GPa)	31(3)[22]	32(2)[6]; 6[20]	48[6]	25 [39]
	P_T (GPa)	0.3[22]; 0.6[18]	0.29[21]	0.1[6]; 0.28[40]	4 [39]
			0.25-0.6[6]	0.5[41]	disorders
Mono 1		$P2_1/a$	$P2_1/a$	$P2_1/a$	Not observed
	Ko(GPa)	14(1)[22]	16(1)[6]	28(1)[6]	
	P_T (GPa)	2.8[22] ; 1.6[18]	2.5 - 3[6] ; 2.7[21]		
Mono 2		**$P2_1/n$**	Same as $Sc_2W_3O_{12}$	Not observed	Not observed
	Ko(GPa)	**90(3)**			
	P_T (GPa)	**2.7**			

8.5. REFERENCES

[1] Evans JSO, Mary TA, Sleight AW. Negative Thermal Expansion in $Sc_2(WO_4)_3$. J. Solid State Chem. 1998;137:148.

[2] Grzechnik A, Crichton WA. Structural transformations in cubic $ZrMo_2O_8$ at high pressures and high temperatures. Solid State Sci. 2002;4:1137.

[3] Muthu DVS, Chen B, Wrobel JM, Krogh Andersen AM, Carlson S, Kruger MB. Pressure-induced phase transitions in α–$ZrMo_2O_8$. Phys. Rev. B 2002;65:064101.

[4] Evans JSO, Hu Z, Jorgensen JD, Argyriou DN, Short S, Sleight AW. Compressibility, Phase Transitions, and Oxygen Migration in Zirconium Tungstate, ZrW_2O_8. Science 1997;275:61.

[5] Jorgensen JD, Hu Z, Short S, Sleight AW, Evans JSO. Pressure-induced cubic-to-orthorhombic phase transfromation in the negative thermal expansion material HfW_2O_8. J. Appl. Phys. 2001;89:3184.

[6] Varga T, Wilkinson AP, Lind C, Bassett WA, Zha C-S. High pressure synchrotron x-ray powder diffraction study of $Sc_2Mo_3O_{12}$ and $Al_2W_3O_{12}$ J. Phys.: Condens. Matter 2005;17:4271.

[7] Chen B, Muthu DVS, Liu ZX, Sleight AW, Kruger MB. High-pressure Raman and infrared study of HfW_2O_8. Phys. Rev. B 2001;64:214111.

[8] Perottoni CA, de Jornada JAH. Pressure-Induced Amorphization and Negative Thermal Expansion in ZrW_2O_8. Science 1998;280:886.

[9] Varga T, Wilkinson AP, Lind C, Bassett WA, Zha C-S. Pressure-induced amorphization of cubic ZrW_2O_8 studied in-situ and ex-situ by synchrotron x-ray absorption spectroscopy and diffraction. Phys. Rev. B 2005;72:024117.

[10] Varga T, Wilkinson AP, Lind C, Basset WA, Zha C-S. Pressure-induced amorphization of cubic $ZrMo_2O_8$ studied in-situ by x-ray absorption spectroscopy and diffraction. Solid State Communications 2005;135:739.

[11] Secco RA, Liu H, Imanaka N, Adachi G. Pressure-induced amorphization in negative thermal expansion $Sc_2(WO_4)_3$. Journal of Materials Science Letters 2001;20:1339.

[12] Wetherfold RC, Wang J. Tailoring thermal deformation by using layered beams. Compos. Sci. Technol. 1995;53:1.

[13] Fleming DA, Johnson DW, Lemaire PJ. Article Comprising a Temperature Compensated Optical Fiber Refractive Index Grating. USA: Lucent Technologies, 1997.

[14] Fleming DA, Lemaire PJ, Johnson DW. Temperature compensated optical fiber refractive index grating. European Patent EP 97-306798 19970902. USA: Lucent Technologies, Inc., 1998. p.7.

[15] Balch DK, Dunand DC. Copper-Zirconium Tungstate Composites Exhibiting Low and Negative Thermal Expansion Influenced by Reinforcement Phase Transformations. Metall. Mater. Trans. A 2004;35A:1159.

[16] Holzer H, Dunand DC. Phase transformation and thermal expansion of Cu/ZrW_2O_8 metal matrix composites. J. Mater. Res. 1999;14:780.

[17] Yilmaz S. Phase transformations in thermally cycled Cu/ZrW_2O_8 composites investogated by synchrotron x-ray diffraction. J. Phys. Condens. Matter. 2002;14:365.

[18] Garg N, Murli C, Tyagi AK, Sharma SM. Phase transitions in $Sc_2(WO_4)_3$ under high pressure. Phys. Rev. B 2005;72.

[19] Arora AK, Nithya R, Yagi T, Miyajima N, Mary TA. Two-stage amorphziation of scandium molybdate at high pressure. Solid State Commun. 2004;129:9.

[20] Arora AK, Yagi T, Miyajima N, Mary TA. Amorphization and decomposition of scandium molybdate at high pressure. J. Appl. Phys. 2005;97:013508.

[21] Paraguassu W, Maczka M, Souza Filho AG, Freire PTC, Mendes Filho J, Melo FEA, Macalik L, Gerward L, Staun Olsen J, Waskowska A, Hanuza J. Pressure-induced structural transformations in the molybdate $Sc_2(MoO_4)_3$. Phys. Rev. B 2004;69:094111.

[22] Varga T, Wilkinson AP, Lind C, Bassett WA, Zha C-S. In-situ high pressure synchrotron x-ray diffraction study of $Sc_2W_3O_{12}$ at up to 10 GPa. Phys. Rev. B 2005;71:214106.

[23] Garg N, Murli C, Tyagi AK, Sharma SM. Phase transitions in Sc-2(WO4)(3) under high pressure. Physical Review B 2005;72.

[24] Varga T, Wilkinson AP, Jorgensen JD, Short S. Neutron powder diffraction study of the orthorhombic to monoclinic transition in $Sc_2W_3O_{12}$ on compression. Solid State Sciences 2006;8:289.

[25] Piermarini GJ, Block S, Barnett JD. Hydrostatic limits in liquids and solids to 100 kbar. J. Appl. Phys. 1973;44:5377.

[26] Barnett JD, Block S, Piermarini GJ. An Optical Fluorescence System for Quantitative Pressure Measurement in the Diamond-Anvil Cell. Rev. Sci. Instrum. 1973;44:1.

[27] Miletich R, Allan D, R., Kuhs W, F. High-Pressure Single-Crystal Techniques. Rev. Mineral. Geochem. 2001;41:445.

[28] Hammersley AP, Svensson SO, Hanfland M, Fitch AN, Hausermann D. Two-dimensional detector software: From real detector to idealised image or two-theta scan. High Pressure Research 1996;14:235.

[29] JADE. computer code JADE. Livermore, CA: Materials Data, Inc., 1995-2005.

[30] Werner PE, Eriksson L, Westdahl M. Treor, a Semi-Exhaustive Trial-and-Error Powder Indexing Program for All Symmetries. J. Appl. Crystallogr. 1985;18:367.

[31] Toby BH. CMPR - a powder diffraction toolkit. J. Appl. Crystallogr. 2005;38:1040.

[32] Le Bail A, Duroy H, Fourquet JL. Abinitio Structure Determination of $LiSbWO_6$ by X-Ray-Powder Diffraction. Mater. Res. Bull. 1988;23:447.

[33] Larson AC, Von Dreele RB. GSAS - General Structure Analysis System. Los Alamos Laboratory: Report LA-UR-86-748, 1987.

[34] Toby BH. EXPGUI, a graphical user interface for GSAS. J. Appl. Crystallogr. 2001;34:210.

[35] Birch F. Finite elastic strain of cubic crystals. Phys. Rev. 1947;71:809.

[36] Angel RJ. EOS-FIT. computer code EOS-FIT. Blacksburg, VA: Virginia Tech, 2001.

[37] Evans JSO, Mary TA. Structural Phase Transitions and negative thermal expansion in $Sc_2(MoO_4)_3$. International Journal of Inorganic Materials 2000;2:143.

[38] Schirber JE, Morosin B. Compressibility Collapse Transition in ReO_3. Phys. Rev. Lett. 1979;42:1485.

[39] Karmakar S, Deb SK, Tyagi AK, Sharma SM. Pressure-induced amorphization in $Y_2(WO_4)_3$: in situ X-ray diffraction and Raman studies. J. Solid State Chem. 2004;177:4087.

[40] Maczka M, Paraguassu W, Souza Filho AG, Freire PTC, Mendes Filho J, Melo FEA, Hanuza J. High-pressure Raman study of $Al_2(WO_4)_3$. J. Solid State Chem. 2004;177:2002.

[41] Mukherjee GD, Vijaykumar V, Achary SN, Tyagi AK, Godwal BK. Phase transitions in $Al_2(WO_4)_3$: high pressure investigations of low frequency dielectric constant and crystal structure. J. Phys.: Condens. Matter 2004;16:7321.

CHAPTER 9

STRUCTURE AND HIGH PRESSURE BEHAVIOR OF $Hf_2(WO_4)(PO_4)_2$

9.1. INTRODUCTION

$Hf_2(WO_4)(PO_4)_2$ is a negative thermal expansion material that is structurally related to orthorhombic $Sc_2W_3O_{12}$. Many compositions are known to form with this structure type [1-3]. They typically display anisotropic volume negative thermal expansion while orthorhombic, but are susceptible to symmetry lowering phase transitions [4], with a concomitant loss of negative thermal expansion, on cooling or modest compression [5-8]. The $Sc_2W_3O_{12}$ framework is amenable to a wide range of substitutions beyond the simple replacement of Sc^{3+} with other trivalent ions, for example, materials such as $A_2(MO_4)(PO_4)_2$ (A – Zr or Hf, M – W or Mo) [9-12], $(HfMg)(WO_4)_3$ [13-15], and $Zr_2(SO_4)(PO_4)_2$ [16] have been reported to have related structures. The wide range of possible substitutions allows for tuning of both thermal and high pressure behavior. The use $A_2(MO_4)(PO_4)_2$ (A – Zr or Hf; M - W or Mo) in controlled thermal expansion applications is covered by several patents [17, 18].

NTE compounds may find application as pure phases and as components in composite materials with tailored thermal expansion coefficients [19-22]. During the manufacture and use of these materials, pressures above ambient may be encountered leading to phase transitions and a loss of NTE behavior [23, 24]. Many NTE materials, owing to their flexible frameworks and relatively low densities, commonly display

crystalline-to-crystalline phase transitions [7, 25-28], and pressure induced amorphization [25, 29-33] upon application of modest pressures. As a consequence, high pressure studies of NTE materials are of some importance from a practical standpoint as well as being of fundamental interest.

$Hf_2(WO_4)(PO_4)_2$ has been shown to display negative thermal expansion [34, 35]. Dilatometer measurements indicated a mean linear coefficients of thermal expansion -5 $\times 10^{-6}$ [35]. Here, we present a high-resolution synchrotron powder diffraction study that confirms $Hf_2(WO_4)(PO_4)_2$ to be isostructural with $Zr_2(WO_4)(PO_4)_2$. We have also performed high-pressure *in-situ* monochromatic synchrotron powder diffraction study of $Hf_2(WO_4)(PO_4)_2$ at room temperature in a diamond anvil cell.

9.2. EXPERIMENTAL PROCEDURES

9.2.1. Sample Preparation

$Hf_2(WO_4)(PO_4)_2$ were prepared using stoichiometric amounts of HfO_2 (Alfa Aesar, 99.95%), $NH_4H_2PO_4$ (J.T. Baker, 99.2 %) and WO_3 (Strem, 99.8 %). The starting compounds were ground together in an agate mortar, heated in an alumina crucible for 4 hours at 800 ºC, and 4 hours at 1100 ºC. This treatment was followed by grinding and heating for another 2 hours at 1250 ºC resulting in an off white powder.

9.2.2. Synchrotron High Resolution X-ray Diffraction Study

High resolution synchrotron X-ray powder diffraction data for $Hf_2(WO_4)(PO_4)_2$ were obtained at room temperature using the 11-BM-B beamline of the Advanced Photon Source, Argonne National Laboratory. A Si(111) double crystal monochromator provided

0.4017 Å x-rays from a bending magnet. A triple axis geometry was employed with 12 scintillation detectors each with its own Si(111) analyzer crystal. The sample was contained in a 0.8 mm diameter capillary and data collected over the range 2-36^{o} 2θ in 0.001^{o} steps.

The program suite GSAS [36] with the EXPGUI [37] graphical interface was used for the Rietveld [38] analysis of this powder X-ray diffraction data. Initial analysis showed the presence of HfO_2 (~2% by weight) as a trace impurity. The final Rietveld refinement included this impurity (fit shown in Figure 9.1). Only the lattice constants, two Lorentzian profile coefficients and scale factors were refined for HfO_2 impurity. The $Zr_2(WO_4)(PO_4)_2$ structure reported by Evans [10] (Pnca) was used as a starting model. The background was fitted with a 15 term Chebyshev polynomial. Peak profiles were modeled using a pseudo-Voigt function. In studying the closely related compound $Zr_2(MoO_4)(PO_4)_2$, we have observed strong asymmetry in some Bragg peaks, possibly arising from lattice defects [39]. Similar issues were reported by Evans for $Zr_2(WO_4)(PO_4)_2$ [10]. For $Hf_2(WO_4)(PO_4)_2$, the degree of asymmetry was sufficiently low that the aforementioned profile function was sufficient. Independent isotropic atomic displacement parameters were used for all atoms. An absorption correction was applied assuming a 30% packing density for the capillary and a computed linear absorption coefficient of 21.19 cm^{-1}. The structural parameters resulting from this analysis are summarized in Table 9.1.

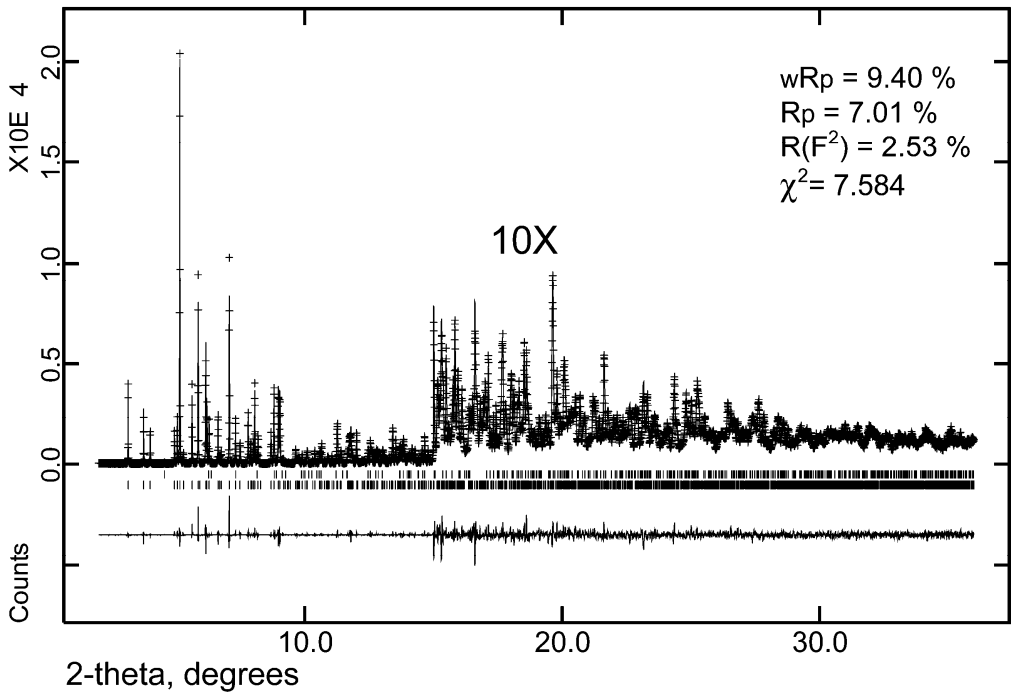

Figure 9.1: Rietveld fit to the 300 K high resolution synchrotron data for $Hf_2(WO_4)(PO_4)_2$. Observed (+), calculated (-), and difference (bottom trace) powder diffraction patterns are shown along with tag marks indicating the Bragg peak positions for trace HfO_2 (top) impurity and $Hf_2(WO_4)(PO_4)_2$ (lower set of marks).

Table 9.1: Structural parameters for $Hf_2(WO_4)(PO_4)_2$ at 300 K determined by Rietveld analysis of the synchrotron high resolution X-ray data. The refined lattice constants were a = 9.30884(4), b = 12.29909(5) and c = 9.12126(4) Å.

Atom	x	y	z	U_{iso}*100
Hf	0.04866(4)	0.369463(28)	0.22589(4)	0.366(11)
W	0.25	0	0.03997(6)	0.467(15)
P	0.60366(22)	0.85628(21)	0.38291(25)	-0.08(6)
O1	0.8694(5)	0.4273(4)	0.3460(6)	0.94(18)
O2	0.9278(5)	0.3485(4)	0.0437(5)	0.17(14)
O3	0.0836(5)	0.5266(4)	0.1697(5)	0.60(16)
O4	-0.0027(5)	0.2202(4)	0.3009(6)	0.21(15)
O5	0.1556(5)	0.4085(4)	0.4283(5)	0.47(16)
O6	0.2432(6)	0.3220(4)	0.1462(5)	0.70(15)

9.2.3. High Pressure Diffraction Data Collection and Processing

High pressure *in-situ* powder diffraction data were collected at room temperature on the beamline 1-BM-C at the Advanced Photon Source (APS), Argonne National Laboratory. Data were obtained using a four-post diamond anvil cell (DAC). The DAC had 2.1 mm thick diamonds with 600 μm culet faces. A pre-indented fully hardened stainless steel gasket with 250 μm initial thickness and a 300 μm diameter hole was used. A methanol-ethanol (4:1) liquid mixture was used as the pressure medium. This liquid medium was claimed to be hydrostatic up to 10.4 GPa [40]. X-rays of wavelength 0.6194 Å was selected using a Si (111) double-crystal monochromator and the beam collimated with a ~200 μm pin hole. Diffraction patterns were recorded on a Mar345 imaging plate detector. A few small ruby chips were loaded into the cells along with the samples so that the pressure could be determined using the ruby fluorescence technique [41], where pressure calibration errors of 0.05-0.1 GPa are possible [42].

At each pressure point, 2 exposures were taken at 2 different sample-to-detector distances (600 mm and 1000 mm). The initial data collection was done with no pressure medium and with no pressure. 21 diffraction patterns were collected at up to 8.9 GPa on compression, and one final pattern was collected after complete decompression. The sample-to-detector distance was calibrated using ambient pressure diffraction from a LaB_6 (NIST SRM 660a) sample that was loaded into the DAC.

The two-dimensional diffraction images were integrated using the program FIT2D [43]. I(2θ) data were initially processed in JADE [44]. The high pressure phases were indexed with Treor [45] implemented in the program CMPR [46] and then further analyzed by a combination of the Rietveld [38] and Le Bail [47] methods using GSAS

[36] with the EXPGUI [37] interface. The calculated unit cell volumes were fitted to the Birch-Murnaghan equation of state (EOS) [48] using the EOS-FIT program (v5.2) [49].

9.3. RESULTS AND DISCUSSION

Rietveld analysis of the room temperature high resolution synchrotron data for $Hf_2(WO_4)(PO_4)_2$ provided no evidence for symmetry lower than Pnca. This is consistent with prior work on the analogous $Zr_2(WO_4)(PO_4)_2$ [10]. The structural parameters resulting from this analysis are summarized in Table 9.1. Selected bond lengths and angles are shown in Table 9.2.

Table 9.2: Selected Bond Distances (Å) and Angles (°) - High-resolution X-Ray 300K

	O1	O2	O3	O4	O5	O6
Hf	2.119(5)	2.023(5)	2.025(5)	2.017(4)	2.152(5)	2.037(5)
W	1.766(5)				1.754(5)	
P		1.499(5)	1.530(6)	1.525(5)		1.510(5)
Hf-O-W	166.03(29)				150.83(27)	
Hf-O-P		154.72(31)	175.83(31)	150.86(33)		145.29(30)

The rest of the results pertain to the high pressure study, conducted using the DAC. All of the diffraction patterns, collected at a sample-to-detector distance of 600 mm, are shown in Figure 9.2. An enlarged version of selected diffraction patterns are presented in Figure 9.3. Looking at the diffraction patterns, some of the peaks are split at 6.0 GPa pattern, but there is no obvious evidence of a phase transition before that point. An examination of the full width at half maximum (see Figure 9.4) for some the Bragg peaks (011, 020, 111, and 200) suggest that there might be a phase transition at around 2.6 GPa. The diffraction patterns could be indexed on an orthorhombic unit cell (Pnca) for pressures up to 2.6 GPa. Rietveld fits (atomic positions are not refined) to the data at

0.0 GPa and 2.2 GPa with orthorhombic (Pnca) structure are shown in Figures 9.5 and 9.6, respectively.

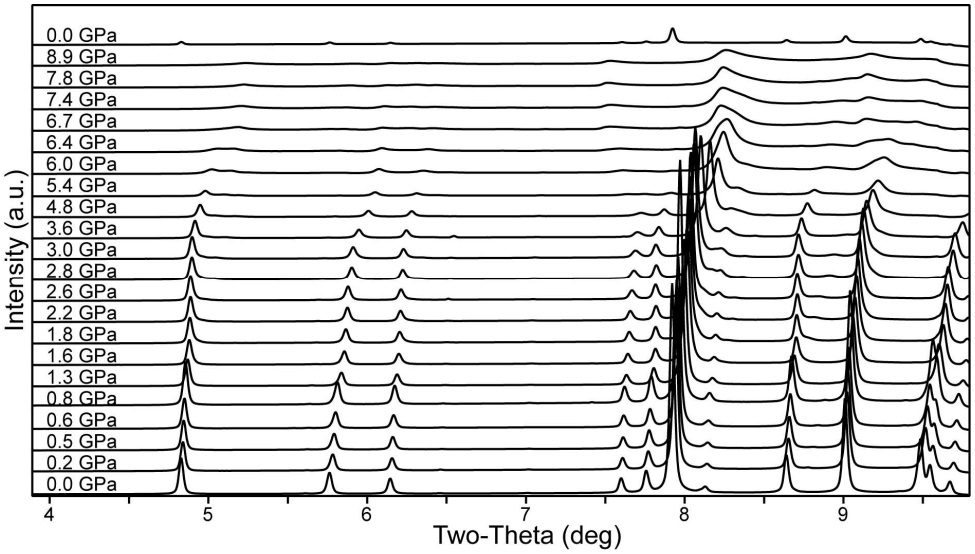

Figure 9.2: Diffraction patterns for $Hf_2(WO_4)(PO_4)_2$ as a function of pressure (The sample-to-detector distance is 600 mm)

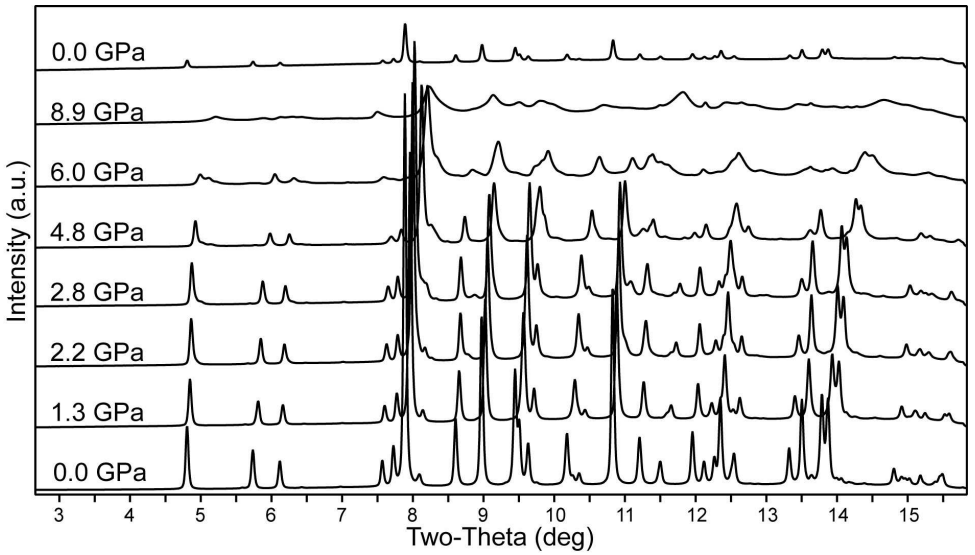

Figure 9.3: Selected diffraction patterns for $Hf_2(WO_4)(PO_4)_2$ as a function of pressure (The sample-to-detector distance is 600 mm)

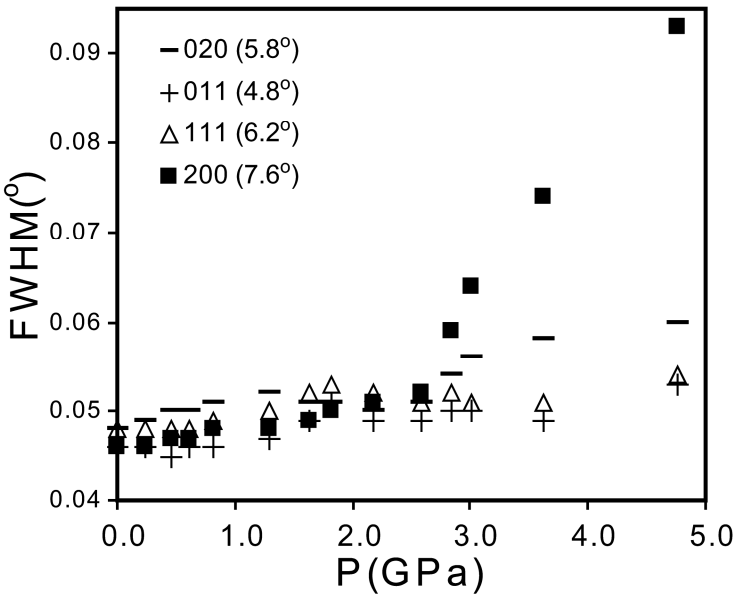

Figure 9.4: Full width at half maximum for some of the Bragg peaks

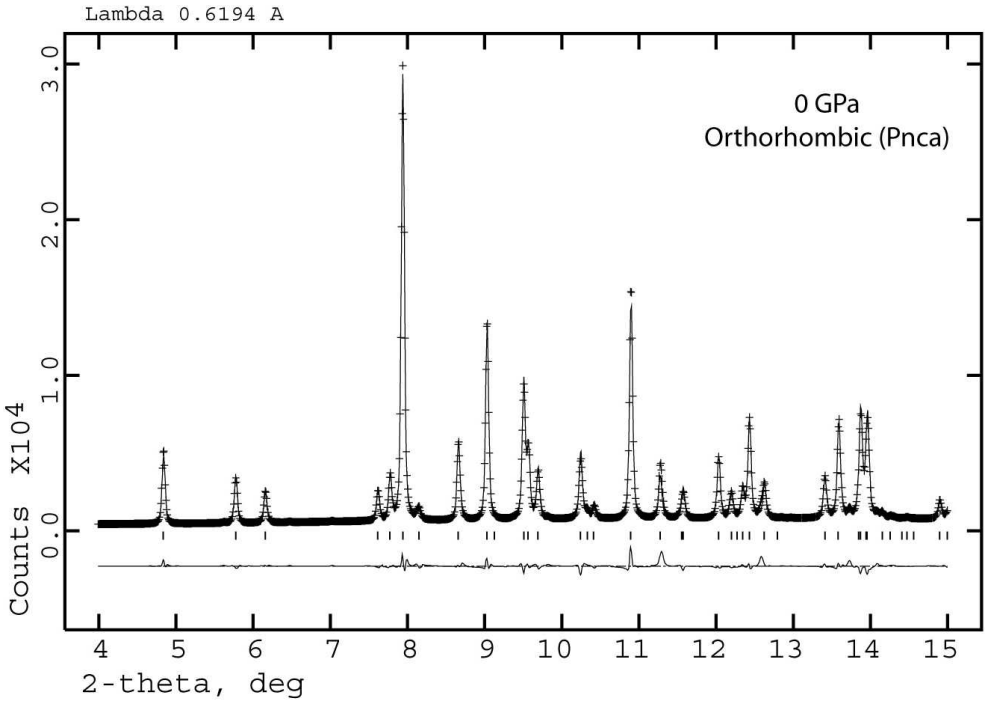

Figure 9.5: Rietveld fit for $Hf_2(WO_4)(PO_4)_2$ at ambient pressure. Observed (+), calculated (-), and difference (bottom trace) powder diffraction patterns are shown along with tag marks indicating the calculated peak positions.

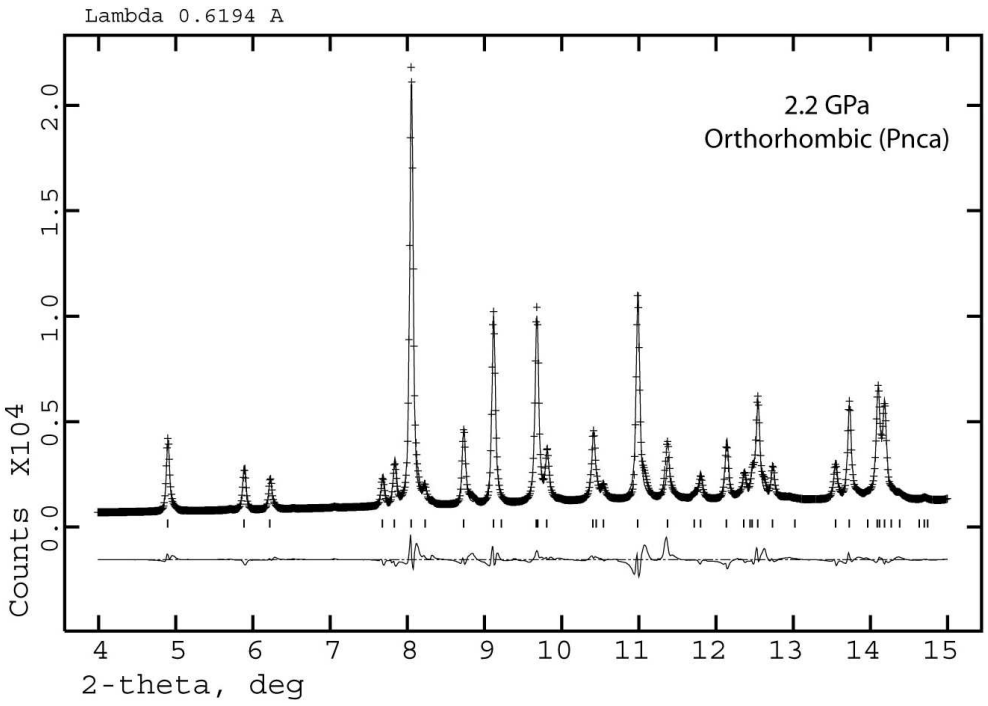

Figure 9.6: Rietveld fit for $Hf_2(WO_4)(PO_4)_2$ at 2.2 GPa. Observed (+), calculated (-), and difference (bottom trace) powder diffraction patterns are shown along with tag marks indicating the calculated peak positions.

Lattice constants derived from Rietveld fits to each diffraction pattern are given in Table 9.3. Normalized unit cell volume as a function of pressure is shown in Figure 9.7. Normalized lattice constants for the orthorhombic phase are shown in Figure 9.8. There appears to be a discontinuity in the normalized volume data and lattice constants at around 2 GPa, indicated by the dotted line. This is an indication that the true phase transition might be happening in this region. Thus, one should take 1.8 GPa powder pattern as the last point that should be indexed with the orthorhombic phase. The new phase emerging above 1.8 GPa could not be clearly identified, but might be an another monoclinic phase as we have observed for $Zr_2(WO_4)(PO_4)_2$ previously. The Bragg peaks start to broaden around 4 GPa showing signs of pressure induced amorphization.

Table 9.3: $Hf_2WP_2O_{12}$ Lattice constants from Rietveld fits to DAC data

P (GPa)	*phase*	*a (Å)*	*b (Å)*	*c (Å)*	*Vol (Å^3)*
0.0	Ortho	9.3114(3)	12.2741(4)	9.1234(3)	1042.70(9)
0.2	Ortho	9.2995(3)	12.2306(4)	9.1070(3)	1035.83(8)
0.5	Ortho	9.2955(3)	12.2126(4)	9.1012(3)	1033.19(9)
0.6	Ortho	9.2908(3)	12.1936(4)	9.0945(3)	1030.30(1)
0.8	Ortho	9.2833(3)	12.1665(5)	9.0846(3)	1026.06(1)
1.3	Ortho	9.2692(4)	12.1152(5)	9.0656(4)	1018.05(1)
1.6	Ortho	9.2565(5)	12.0800(7)	9.0536(5)	1012.36(1)
1.8	Ortho	9.2505(6)	12.0613(8)	9.0519(5)	1009.94(2)
2.2	Ortho	9.2362(6)	12.0439(8)	9.0528(6)	1007.04(2)
2.6	Ortho	9.2309(6)	12.0324(8)	9.0532(6)	1005.54(2)

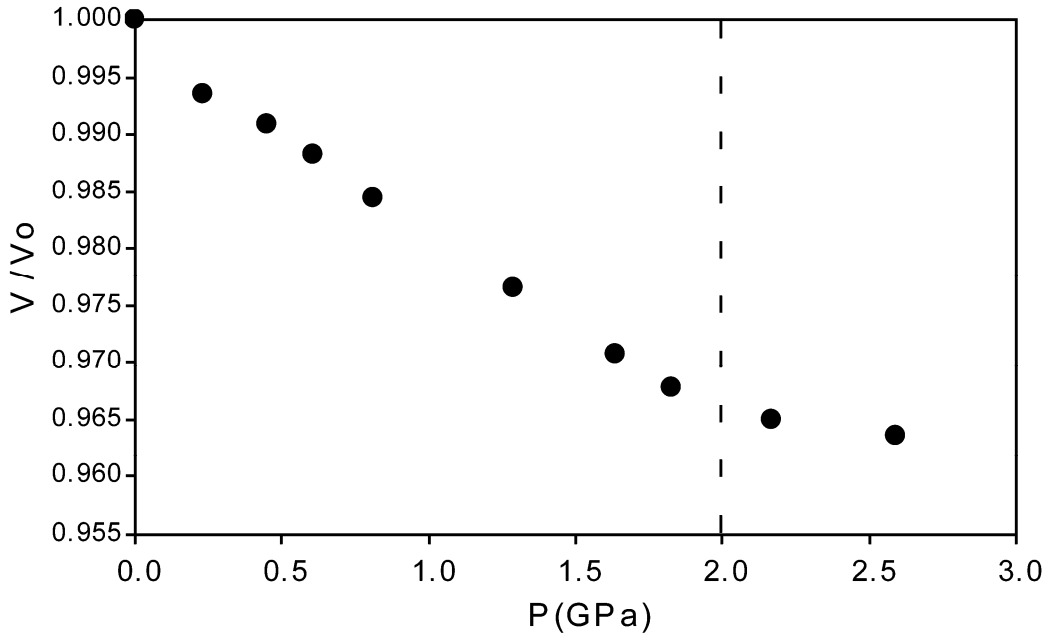

Figure 9.7: Normalized unit cell volume as a function of pressure.

It is apparent from normalized lattice constants that orthorhombic $Hf_2(WO_4)(PO_4)_2$ are anisotropically compressible, with the b-axis being slightly more compressible than a- and c-axes. Linear compressibilities for the orthorhombic phase

were estimated to be β_a= 3.5(2) x 10^{-3} GPa^{-1}, β_b= 10.0(5) x 10^{-3} GPa^{-1}, β_c= 4.3(4) x 10^{-3} GPa^{-1} by least squares fits of a straight line.

A third order Birch-Murnaghan equation of state was fit to the P-V data up to 1.8 GPa and the fit is shown in Figure 9.9. During the fitting, the pressure derivative of the bulk modulus (K_p) was fixed at 4.0 while varying the zero pressure volume (V_0) and bulk modulus (K_0). Bulk moduli estimated using a Birch -Murnaghan equation of state, were 54(1) GPa for the orthorhombic phase. The bulk moduli values with phase transition pressures for $Hf_2(WO_4)(PO_4)_2$ and some of the related compounds are shown in Table 9.4. Stability range for the orthorhombic phase, or the transition pressure for the $Hf_2(WO_4)(PO_4)_2$ is very high compared to its relatives. The bulk modulus of the first phase of $Hf_2(WO_4)(PO_4)_2$ is in line with corresponding bulk moduli values for $Zr_2(WO_4)(PO_4)_2$, $Zr_2(MoO_4)(PO_4)_2$ and $Al_2W_3O_{12}$, and different from that of $Sc_2W_3O_{12}$ and $Sc_2Mo_3O_{12}$.

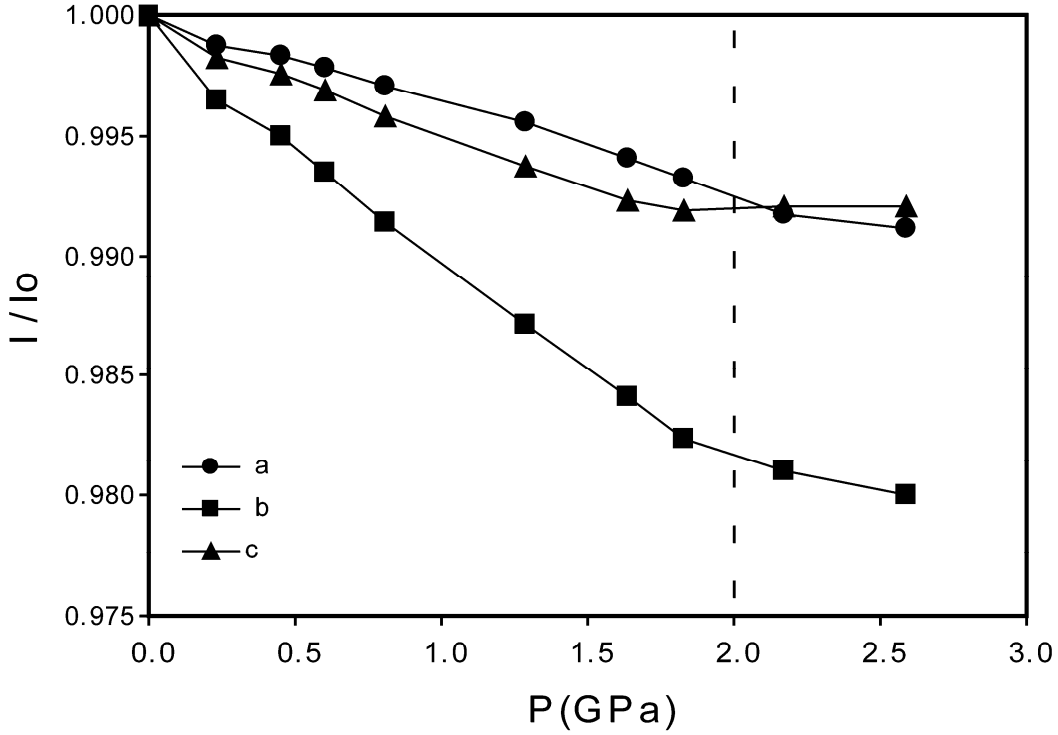

Figure 9.8: Normalized unit cell constants.

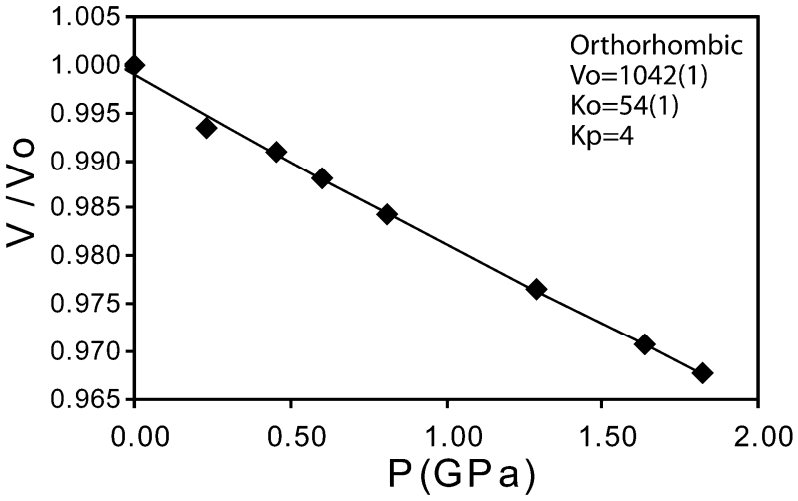

Figure 9.9: Normalized unit cell volume versus pressure for orthorhombic $Hf_2(WO_4)(PO_4)_2$ along with a fit to the Birch-Murnaghan equation-of-state.

9.4. CONCLUSIONS

High resolution synchrotron x-ray powder diffraction was used to confirm that $Hf_2(WO_4)(PO_4)_2$ is isotructural with $Zr_2(WO_4)(PO_4)_2$ which adopts the orthorhombic (Pnca) structure under ambient conditions. Synchrotron x-ray powder diffraction in conjunction with a diamond anvil cell was used to study its behavior on compression up to 8.9 GPa. One crystalline-to-crystalline phase transition was observed: orthorhombic (Pnca) between 0.0-1.8 GPa, and an unidentified phase above 2.2 GPa. Bulk modulous estimated using a Birch -Murnaghan equation of state was 54(1) GPa for the orthorhombic phase. Disordering of the crystal structure was observed above 4 GPa as evidenced by broadened Bragg peaks. Upon release of pressure, $Hf_2(WO_4)(PO_4)_2$ reverted back to its original orthorhombic phase.

Table 9.4: High pressure behavior of some $A_2M_3O_{12}$ compounds. Ko and P_T denotes bulk modulus and phase transition pressure, respectively.

		$Sc_2W_3O_{12}$	***$Sc_2Mo_3O_{12}$***	***$Al_2W_3O_{12}$***	***$Zr_2WP_2O_{12}$***	***$Zr_2MoP_2O_{12}$***	***$Hf_2WP_2O_{12}$***
phase 1		Pnca	Pnca	Pnca	**Pnca**	**Pnca**	**Pnca**
	Ko (GPa)	31(3)[6]	32(2)[7]; 6[50]	48[7]	**49(2)**	**45(4)**	**54(1)**
	P_T (GPa)	0.3[6]; 0.6[51]	0.29[52] 0.25-0.6[7]	0.1[7]; 0.28[53] 0.5[54]	**1.4; 1.2**	**1.2-1.5**	**1.8**
phase 2-A		$P2_1/a$	$P2_1/a$	$P2_1/a$			
	Ko (GPa)	14(1)[6]	16(1)[7]	28(1)[7]			
	P_T (GPa)	2.8[6] ; 1.6[51]	2.5 - 3[7] ; 2.7[52]				
phase 2-B					**$P2_1/n$**	**$P2_1/n$**	
	Ko (GPa)				**17(1)**	**20(2)**	
	P_T (GPa)				**3.4**	**3.3**	
phase 3		**$P2_1/n$**	Unidentified	N/A	**$P2_1/n$**		
	Ko (GPa)	**90(3)**			**36(4)**		
	P_T (GPa)	**2.7**			**6.3**		
phase 4					**P1 or P-1**		
	Ko (GPa)				**76(7)**		
	P_T (GPa)						

9.5. REFERENCES

[1] Abrahams SC, Bernstein JL. Crystal Structure of the Transition-Metal Molybdates and Tungstates. II. Diamagnetic $Sc_2(WO_4)_3$. J. Chem. Phys. 1966;45:2745.

[2] Evans JSO, Mary TA, Sleight AW. Negative Thermal Expansion in $Sc_2(WO_4)_3$. J. Solid State Chem. 1998;137:148.

[3] Weller MT, Henry P, Wilson CC. An analysis of the thermal motion in the negative thermal expansion material $Sc_2(WO_4)_3$ using isotopes in neutron diffraction. J. Phys. Chem. B 2000;104:12224.

[4] Sleight AW, Brixner LH. A New Ferroelastic Transition in Some $A_2(MO_4)_3$ Molybdates and Tungstates. J. Solid State Chem. 1973;7:172.

[5] Evans JSO, Mary TA. Structural Phase Transitions and negative thermal expansion in $Sc_2(MoO_4)_3$. International Journal of Inorganic Materials 2000;2:143.

[6] Varga T, Wilkinson AP, Lind C, Bassett WA, Zha C-S. In-situ high pressure synchrotron x-ray diffraction study of $Sc_2W_3O_{12}$ at up to 10 GPa. Phys. Rev. B 2005;71:214106.

[7] Varga T, Wilkinson AP, Lind C, Bassett WA, Zha C-S. High pressure synchrotron x-ray powder diffraction study of $Sc_2Mo_3O_{12}$ and $Al_2W_3O_{12}$ J. Phys.: Condens. Matter 2005;17:4271.

[8] Varga T, Wilkinson AP, Jorgensen JD, Short S. Neutron powder diffraction study of the orthorhombic to monoclinic transition in $Sc_2W_3O_{12}$ on compression. Solid State Sciences 2006;8:289.

[9] Tsvigunov AN, Sirotinkin VP. Preparation of $Zr_2WO_4(PO_4)_2$ and indexing of its X-ray diffraction pattern. Russ. J. Inorg. Chem. 1990;35:1740.

[10] Evans JSO, Mary TA, Sleight AW. Structure of $Zr_2(WO_4)(PO_4)_2$ from Powder X-ray Data: Cation Ordering with No Superstructure. J. Solid State Chem. 1995;120:101.

[11] Martinek CA, Hummel FA. Subsolidus Equilibria in the System ZrO_2-WO_3-P_2O_5. J. Am. Ceram. Soc. 1970;53:159.

[12] Sirotinkin VP, Tsvigunov AN. Synthesis, X-Ray-Diffraction and Thermal Analyses of $Zr_2MoO_4(PO_4)_2$. Russ. J. Inorg. Chem. 1994;39:735.

[13] Suzuki T, Omote A. Negative Thermal Expansion in $(HfMg)(WO_4)_3$. J. Am. Ceram. Soc. 2004;87:1365.

[14] Suzuki T, Omote A. Pseudo binary HfW_2O_8-$MgWO_4$ thermal expansion control system. J. Ceram. Soc. Jpn. 2006;114:833.

[15] Suzuki T, Omote A. Zero thermal expansion in $(Al_{2x}(HfMg)_{(1-x)})(WO_4)_{(3)}$. J. Am. Ceram. Soc. 2006;89:691.

[16] Piffard Y, Verbaere A, Kinoshita M. Beta - $Zr_2(PO_4)_2SO_4$ - A Zirconium Phosphato-sulfate with A $Sc_2(WO_4)_3$ Structure - A comparison between garnet, Nasicon, and $Sc_2(WO_4)_3$ structure types. J. Solid State Chem. 1987;71:121.

[17] Merkel GA. Negative Thermal Expansion Materials Including Method of Preparation and Uses Therefor. European Patent, 2001.

[18] Sleight AW, Thundathil MA, Evans JSO. Materials with Low or Negative Thermal Expansion. United States Patent, 1999.

[19] Wetherfold RC, Wang J. Tailoring thermal deformation by using layered beams. Compos. Sci. Technol. 1995;53:1.

[20] Fleming DA, Johnson DW, Lemaire PJ. Article Comprising a Temperature Compensated Optical Fiber Refractive Index Grating. USA: Lucent Technologies, 1997.

[21] Fleming DA, Lemaire PJ, Johnson DW. Temperature compensated optical fiber refractive index grating. European Patent EP 97-306798 19970902. USA: Lucent Technologies, Inc., 1998. p.7.

[22] Balch DK, Dunand DC. Copper-Zirconium Tungstate Composites Exhibiting Low and Negative Thermal Expansion Influenced by Reinforcement Phase Transformations. Metall. Mater. Trans. A 2004;35A:1159.

[23] Holzer H, Dunand DC. Phase transformation and thermal expansion of Cu/ZrW_2O_8 metal matrix composites. J. Mater. Res. 1999;14:780.

[24] Yilmaz S. Phase transformations in thermally cycled Cu/ZrW_2O_8 composites investogated by synchrotron x-ray diffraction. J. Phys. Condens. Matter. 2002;14:365.

[25] Grzechnik A, Crichton WA. Structural transformations in cubic $ZrMo_2O_8$ at high pressures and high temperatures. Solid State Sci. 2002;4:1137.

[26] Muthu DVS, Chen B, Wrobel JM, Krogh Andersen AM, Carlson S, Kruger MB. Pressure-induced phase transitions in α–$ZrMo_2O_8$. Phys. Rev. B 2002;65:064101.

[27] Evans JSO, Hu Z, Jorgensen JD, Argyriou DN, Short S, Sleight AW. Compressibility, Phase Transitions, and Oxygen Migration in Zirconium Tungstate, ZrW_2O_8. Science 1997;275:61.

[28] Jorgensen JD, Hu Z, Short S, Sleight AW, Evans JSO. Pressure-induced cubic-to-orthorhombic phase transfromation in the negative thermal expansion material HfW_2O_8. J. Appl. Phys. 2001;89:3184.

[29] Chen B, Muthu DVS, Liu ZX, Sleight AW, Kruger MB. High-pressure Raman and infrared study of HfW_2O_8. Phys. Rev. B 2001;64:214111.

[30] Perottoni CA, de Jornada JAH. Pressure-Induced Amorphization and Negative Thermal Expansion in ZrW_2O_8. Science 1998;280:886.

[31] Varga T, Wilkinson AP, Lind C, Bassett WA, Zha C-S. Pressure-induced amorphization of cubic ZrW_2O_8 studied in-situ and ex-situ by synchrotron x-ray absorption spectroscopy and diffraction. Phys. Rev. B 2005;72:024117.

[32] Varga T, Wilkinson AP, Lind C, Basset WA, Zha C-S. Pressure-induced amorphization of cubic $ZrMo_2O_8$ studied in-situ by x-ray absorption spectroscopy and diffraction. Solid State Communications 2005;135:739.

[33] Secco RA, Liu H, Imanaka N, Adachi G. Pressure-induced amorphization in negative thermal expansion $Sc_2(WO_4)_3$. Journal of Materials Science Letters 2001;20:1339.

[34] Mary TA, Sleight AW. Bulk thermal expansion for tungstate and molybdates of the type $A_2M_3O_{12}$. J. Mater. Res. 1999;14:912.

[35] Evans JSO, Mary TA, Sleight AW. Negative Thermal Expansion in a Large Molybdate and Tungstate Family. J. Solid State Chem. 1997;133:580.

[36] Larson AC, Von Dreele RB. GSAS - General Structure Analysis System. Los Alamos Laboratory: Report LA-UR-86-748, 1987.

[37] Toby BH. EXPGUI, a graphical user interface for GSAS. J. Appl. Crystallogr. 2001;34:210.

[38] Rietveld HM. A Profile Refinement Method for Nuclear and Magnetic Structures. Journal of Applied Crystallography 1969;2:65.

[39] Cetinkol M, Wilkinson AP. manuscript in preparation.

[40] Piermarini GJ, Block S, Barnett JD. Hydrostatic limits in liquids and solids to 100 kbar. J. Appl. Phys. 1973;44:5377.

[41] Barnett JD, Block S, Piermarini GJ. An Optical Fluorescence System for Quantitative Pressure Measurement in the Diamond-Anvil Cell. Rev. Sci. Instrum. 1973;44:1.

[42] Miletich R, Allan D, R., Kuhs W, F. High-Pressure Single-Crystal Techniques. Rev. Mineral. Geochem. 2001;41:445.

[43] Hammersley AP, Svensson SO, Hanfland M, Fitch AN, Hausermann D. Two-dimensional detector software: From real detector to idealised image or two-theta scan. High Pressure Research 1996;14:235.

[44] JADE. computer code JADE. Livermore, CA: Materials Data, Inc., 1995-2005.

[45] Werner PE, Eriksson L, Westdahl M. Treor, a Semi-Exhaustive Trial-and-Error Powder Indexing Program for All Symmetries. J. Appl. Crystallogr. 1985;18:367.

[46] Toby BH. CMPR - a powder diffraction toolkit. J. Appl. Crystallogr. 2005;38:1040.

[47] Le Bail A, Duroy H, Fourquet JL. Abinitio Structure Determination of $LiSbWO_6$ by X-Ray-Powder Diffraction. Mater. Res. Bull. 1988;23:447.

[48] Birch F. Finite elastic strain of cubic crystals. Phys. Rev. 1947;71:809.

[49] Angel RJ. EOS-FIT. computer code EOS-FIT. Blacksburg, VA: Virginia Tech, 2001.

[50] Arora AK, Yagi T, Miyajima N, Mary TA. Amorphization and decomposition of scandium molybdate at high pressure. J. Appl. Phys. 2005;97:013508.

[51] Garg N, Murli C, Tyagi AK, Sharma SM. Phase transitions in $Sc_2(WO_4)_3$ under high pressure. Phys. Rev. B 2005;72.

[52] Paraguassu W, Maczka M, Souza Filho AG, Freire PTC, Mendes Filho J, Melo FEA, Macalik L, Gerward L, Staun Olsen J, Waskowska A, Hanuza J. Pressure-induced structural transformations in the molybdate $Sc_2(MoO_4)_3$. Phys. Rev. B 2004;69:094111.

[53] Maczka M, Paraguassu W, Souza Filho AG, Freire PTC, Mendes Filho J, Melo FEA, Hanuza J. High-pressure Raman study of $Al_2(WO_4)_3$. J. Solid State Chem. 2004;177:2002.

[54] Mukherjee GD, Vijaykumar V, Achary SN, Tyagi AK, Godwal BK. Phase transitions in $Al_2(WO_4)_3$: high pressure investigations of low frequency dielectric constant and crystal structure. J. Phys.: Condens. Matter 2004;16:7321.

CHAPTER 10

PREPARATION AND CHARACTERIZATION OF IN(I)-BETA''-ALUMINA[1]

10.1. INTRODUCTION

The chemistry of In(I) in halides and, to a lesser extent, organometallics is quite well established [1-5]. However; there are very few well characterized oxides containing this ion; examples being, In_xWO_3 [6-9], In(I)-β-alumina [10, 11] and most recently $In_2P_2O_7$[12]. In_2O itself has been examined as a matrix-isolated species and in the gas phase[13-15], but there is no definitive characterization in the solid state. The paucity of In(I) oxides in the literature is presumably because bulk In_2O is unstable with respect to disproportionation. However, ion exchange is a viable route to In(I) oxides, as illustrated by the preparation of In(I)-β-alumina.

In(I)-β-alumina was first prepared by Yao and Kummer in 1967 by treating Ag(I)-β-alumina with In metal containing a small amount of mercury [11]. It was later prepared by Pitt and Fray using Ag(I)-β-alumina in an InI melt containing excess indium [10]. Vapor transport methods have been utilized in the preparation of In(I) containing tungsten bronzes [6-8] and, recently, in the preparation of the mixed valent In(I)/(III) $In_2P_2O_7$ [12].

---

[1] The majority of the work presented in this chapter was previously published in Çetinkol, M., et al., *Mater. Res. Bull.*, **2007,** *42*, 713-719.

The current work was undertaken to expand the range of well characterized In(I) oxides and, in particular, to determine if the In(I) coordination was indicative of a stereochemically active lone pair. In our prior work on Ga(I)-β''-alumina, the Ga(I) coordination was effectively 3+0 suggesting the presence of a stereochemically active lone pair [16].

10.2. EXPERIMENTAL PROCEDURES

10.2.1. Materials

Na-β''-alumina powder ($Na_{1.6}[Al_{10.7}Li_{0.3}]O_{17}$, based on the manufacturer's batch analysis) supplied by Ceramatec, was used as a starting material. The Na-β''-alumina powder were heated with 10-fold excess silver nitrate at 300^{o}C in a quartz container for 24 hours to obtain Ag-β''-alumina. The molten salt was decanted and the residue washed with heated distilled water in order to remove the remaining nitrates. The product was vacuum-filtered and dried at 200^{o}C for 2 hours. In(I)-β''-alumina was prepared by heating 5 g of Ag-β''-alumina in an evacuated and sealed quartz ampoule along with 9 g iodine and 25 g indium metal at 300^{o}C for 3 days. The sealed tube was cooled and the excess metal physically separated from the product which was subsequently washed with 15% HCl until gas evolution ceased. The remaining insoluble powder was washed with distilled water, vacuum filtered and dried at 200^{o}C for 2 hours. The In-β''-alumina product was dark brown in color. An elemental analysis of this material was performed by Galbraith Laboratories. Thermogravimetric analysis data for the In(I)-β''-alumina were obtained using a Seiko instruments TGA/DTA 320 module. The sample was heated under flowing dry air from 25 to 1000^{o}C at 10^{o}C/min.

10.2.2 X-ray Powder Diffraction

Initial powder diffraction data for Na-β''-alumina, Ag-β''-alumina and the title compound were obtained using a Scintag X1 diffractometer equipped with copper tube and a Peltier cooled solid-state detector. The data were collected in steps of 0.02^o over the range $5\text{-}138^o$ 2θ. Subsequently, high resolution synchrotron X-ray powder diffraction data were obtained for the In(I)-β''-alumina at the 32-ID beamline of the Advanced Photon Source, Argonne National Laboratory. This experiment used λ = 0.4958 Å x-rays from an APS undulator and a double crystal diamond (111) monochromator. The diffractometer employed a triple axis geometry with 11 scintillation detectors each with its own Si(111) analyzer crystal. A 1:2 mixture of NIST standard silicon and α-alumina was used for the calibration of the instrument and the determination of the wavelength. The In(I)-β''-alumina sample was contained in a 1 mm diameter glass capillary and data were collected over the range $2\text{-}54.9^o$ 2θ in 0.001^o steps.

10.2.3 Analysis of the X-ray Diffraction Data: Rietveld Refinement

The program suite GSAS [17] with the EXPGUI [18] graphical interface was used for the Rietveld [19] analysis of the powder X-ray diffraction data. Initial analysis showed that the powder sample contained some β-alumina and elemental Ag metal as trace impurities. The final Rietveld refinement was carried out using three phases. The β-alumina impurity was assumed to be In-β-alumina, and a structural model from Pitt and Fray [10], space group *P63/mmc*, was included in the refinement. Only the lattice constants, two Lorentzian profile coefficients and scale factors were refined for the Ag metal and In-β-alumina impurities. As a starting model for the In(I)-β''-alumina, the Ga(I)-β''-alumina structure reported by Wilkinson [16] in the space group *R-3m* was

used. The background was fitted with a Chebyshev polynomial function with 20 coefficients. The Bragg peak profiles were modeled using a pseudo-Voigt function. Terms in an expression for the empirical microstrain anisotropy were refined as there was an apparent anisotropic broadening. The lithium was placed on the Al(2) site as indicated by the work of Jorgensen [20], and the Al(2) and Li atoms were constrained to have identical position and atomic displacement parameters. Fractional occupancies were not refined, except for the In atom. Isotropic thermal displacement parameters were used, except for In and O(5). Some evidence of preferred orientation was observed during the data analysis, and a spherical harmonics based correction was used to correct for this. The final texture index using a 4^{th} order correction was 1.184. The observed texture is consistent with the plate like morphology of the crystallites. The packing density of the capillary (38%) was determined by weighing the capillary before and after loading. A linear absorption coefficient of 12.54 cm^{-1} was calculated for $In_{1.6}[Al_{10.7}Li_{0.3}]O_{17}$ and an absorption correction suitable for cylindrical samples was applied within GSAS using an A_B value of 0.48. A summary of the structure refinement details is given in Table 10.1.

10.3. RESULTS AND DISCUSSION

10.3.1 Results

Lattice constants, determined by Rietveld analysis, for the Na, Ag and In(I)-β''-aluminas used in this study are given in Table 10.2 along with those for some other β''-aluminas in the literature. The lattice constants for the silver phase are fully consistent with prior reports.

Table 10.1: Summary of Crystal Data and Structure Refinement. Details for In(I)- β''-Alumina

space group	R-3m
x-ray wavelength/Å	0.4958
T/K	296
Fw	744.9
a/Å	5.604391(3)
c/Å	34.48072(3)
V/Å^3	937.916(1)
Z	3
μ_{eff} /cm^{-1a}	4.77
ρ_x/g cm^{-3}	3.957
Color	reddish brown
abs corr	yes
angular range (2θ)/deg	2.00-54.90
Minimum d-spacing/ Å	0.54
No. of data points	52900
No. of refls	897
No. of refined params	73
R_{wp}/%	4.97[b]
R_p/%	3.86[b]
χ^2	6.648
R_F^2/%	3.26[b]

[a] Linear absorption coefficient after correction for packing density
[b] $R_{wp} = \sum w(y_{io} - y_{ic})^2/\sum w(y_{io})^2$ (weights based on counting statistics); $R_p = \sum(y_{io} - y_{ic})^2/\sum(y_{io})^2$; $R_F2 = [\sum(F_o^2 - F_c^2)^2/\sum(F_o^2)^2]^{1/2}$ (F_o is estimated from the profile and may be biased by the model).

Table 10.2: Key Structural Parameters for selected M^+-β''-Alumina samples.

M^+	data[c]	a/Å	c/Å	a/c	6c occ[b]	18h occ[b]	coordinates		stabilizer
							6c	18h	
Na^+	XP[16]	5.6101	33.6355						Li
Ag^+	XP[a]	5.6096	33.3713						Li
In^+	XP[a]	5.6044	34.4807	0.1625		1.58		x=0.0076 z=-0.1774	Li
Ga^+	NP[16]	5.5951	34.367	0.1628	1.52		z=-0.1840		Li
NH_4^+	NS[21]	5.631	34.378	0.1638	1.56		z=0.16967		Mg
Ag^+	NS[22]	5.6263	33.403	0.1684		1.61		x=0.0205 z=-0.1695	Mg
Rb^+	XP[23]	5.613	34.344	0.1634					Li
K^+	NS[22]	5.6253	34.067	0.1651	0.56	1.04	z=-0.1711	x=0.0837 z=-0.1682	Mg
Na^+	NP[20]	5.6101	33.4627	0.1677	0.44	1.23	z=-0.1717	x=0.104 z=-0.166	Li

[a] Data from this study [b] Occupancy in atoms per formula unit [c] XP = X-ray powder data; NP = neutron powder data; NS = neutron single-crystal data

Elemental analysis of the In-β''-alumina indicated that it contained ~22.02% In and ~0.74% Ag, in reasonable agreement with the values expected (24.6% In) for a β''-alumina with nominal composition of $In_{1.6}[Al_{10.7}Li_{0.3}]O_{17}$ (this assumes complete exchange of the starting Na phase) given that the Rietveld analysis for this sample indicated the presence of some silver metal (~0.5%) and In(I)-β-alumina (~1.9%).

Thermogravimetric analysis of the In-β''-alumina in flowing air showed no weight gain below ~400 ^{o}C, and a gain of 3.5% on heating to 1000°C. This is consistent with the oxidation of all the In(I) in a sample of composition $In_{1.6}[Al_{10.7}Li_{0.3}]O_{17}$ to In(III); expected weight gain ~3.43%. There was a weight loss of less than 1% in the initial stages of heating that is probably due to absorbed water on the surface of the sample, but could be associated with the decomposition of some amorphous indium hydroxide that was not completely removed by the washing process.

During the Rietveld structure analysis of the In-β''-alumina, a number of different models for the In(I) distribution were examined: 1) all of the indium on a 6c site with z=-0.1775 with an anisotropic atomic displacement parameter (ADP), 2) all of the indium on a 18h site with x=0.0077 z=-0.1774 and an anisotropic ADP, and 3) a combination of these sites. These models are very similar to one another, as the 18h site is very close to the 6c position, and represent different approaches to treating disorder of the indium; pseudo thermal motion, or split sites. Model (3) gave the best fit to the data, but the indium fractional occupancies were not readily independently refineable. Model (2) gave a slightly better fit to the data than model (1) and is used in all subsequent discussion. An anisotropic ADP was used for O(5), as in an initial refinement the isotropic ADP for O(5) was approximately 10 times larger than those for the other O atoms. In other β''-

aluminas, there is also evidence for large amounts of disorder on this site [20-22, 24, 25]. While it is unusual to refine anisotropic ADPs for light atoms based on powder x-ray data, the exceptionally high quality of the current data, compared to typical data, as indicated by the large d-spacing range covered, good counting statistics and low sample absorption, enables this to be done in a well controlled fashion. It is notable that the refined indium occupancy is in excellent agreement with that expected for full ion exchange of the starting material (1.60 indium per formula unit expected, 1.58 found). Details of the refinement using model 2 are summarized in Table 10.1, the final structural parameters are given in Table 10.3, and some selected bond lengths are shown in Table 10.4. The final profile fit to the data is shown in Figure 10.1, and the oxygen coordination around In(I) is illustrated in Figure 10.2.

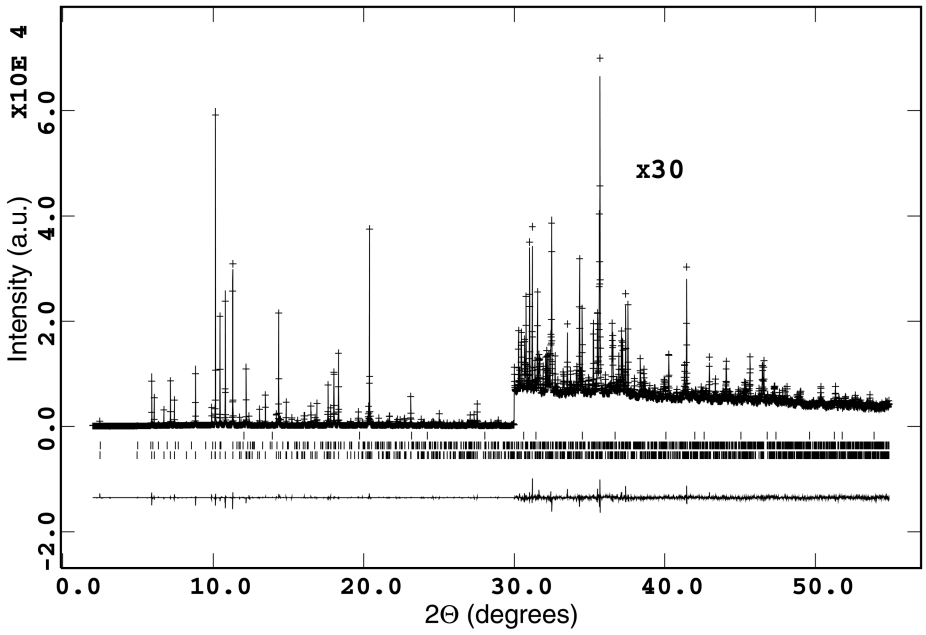

Figure 10.1: The final Rietveld fit to the powder diffraction data for the In(I)-β''-alumina sample. Crosses are the measured data points. Tick marks under the diffraction pattern indicate the expected locations of peaks for silver metal and the two alumina phases. The line across the bottom of the plot is the difference between the measured data points and the calculated pattern.

Table 10.3: Refined Coordinates and Temperature Factors for In(I)-β''-Alumina.

atom	mult	Occ	x	y	z	10^2U_{11} [a]	10^2U_{33}	10^2U_{12}
In(1)	18	0.264(0)	0.0076(4)	-0.0076(4)	-0.177367(8)	1.622(20)	1.402(18)	0.18(5)
Al(1)	3	1	0	0	0	0.119(13)		
Al(2)	6	0.85	0	0	0.349197(16)	0.076(10)		
Al(3)	18	1	0.33332(7)	0.166653(33)	0.068876(8)	0.280(6)		
Al(4)	6	1	0	0	0.450016(14)	0.221(10)		
O(1)	18	1	0.15648(6)	0.31295(12)	0.033202(16)	0.150(12)		
O(2)	6	1	0	0	0.295988(30)	0.136(20)		
O(3)	6	1	0	0	0.093421(30)	0.097(20)		
O(4)	18	1	0.16402(6)	0.32804(12)	0.236835(17)	0.115(11)		
O(5)	3	1	0	0	0.5	1.547(51)	-0.04(10)	0.77(2)
Li(1)	6	0.15	0	0	0.349197(16)	0.076(10)		

[a] Isotropic temperature factor or U_{11} if an anisotropic temperature factor was refined.

10.3.2 Discussion

Beta-aluminas have the general formula $M_2O.nAl_2O_3$, where n = 5 – 11, and occur in two structural variants, β and β''. The β'' phases are stabilized by Li^+, or Mg^{2+}, and found with n=5-7. The stabilizing Li^+ cations substitute for Al^{3+}, giving a formula for Na-β''-alumina of $Na_{1+2x}Li_xAl_{11-x}O_{17}$. The β'' phases are typically hexagonal, space group *R-3m*, and their structures consist of stacked spinel-like blocks separated by a conduction plane. The neighboring spinel blocks are held together by a combination of the ion exchangeable cations residing between the blocks and an oxygen, usually labeled O(5), that bridges the conduction plane. For β''-aluminas containing only univalent mobile cations, the exchangeable cations sit on some combination of Wyckoff positions 6c and 18h in the conduction plane. The cations on the 18h site, or sites, can be thought of as being displaced away from a 6c site toward one of its three nearest neighbor 6c sites [25-27].

The successful synthesis of In(I)-β''-alumina indicates that in the coordination environments that are available, the disproportionation of In(I) is not thermodynamically favorable. The stability of the material towards oxidation below ~ 400 ºC is almost certainly due to the poor kinetics for the process. Above 400 ºC, the In(I) ions, and perhaps In(III) ions produced by oxidation, are probably mobile enabling diffusion to the crystallite surface where they can be oxidized. Heating In(I)-β''-alumina in air, using a platinum container, at 700 ºC for 3 h decomposed the sample leaving In_2O_3 and a β-alumina phase as the only crystalline products. Further heating at 1000 ºC for 2 h gave In_2O_3 and γ-Al_2O_3 as the only crystalline phases. These observations suggest that the β-

alumina trace impurity in the original sample is most likely In(I)-β-alumina and that it has greater thermal stability on heating in air than its β''-alumina counterpart.

The lattice constants and M^+ coordinates for a range of structurally characterized M(I)-β''-aluminas are summarized in Table 10.2. In general, the lattice constant *a* is relatively insensitive to the chemical identity of M^+, but *c* varies significantly with M^+. In our previous study of Ga(I)-β''-alumina, it was found that the value *c* (34.367 Å), was large when compared to alkali metals that would be expected to have similar ionic radii (Na^+, *c* = 33.656 Å; K^+, *c* = 34.067 Å, Rb^+, *c* = 34.344 Å) and this was associated with an usual 3+0 coordination for the Ga^+ that was taken as indicative of a steroechemically active lone pair on the gallium. However, the value of *c* for the In^+ phase in the present study (34.481 Å) is only slightly larger than that observed for the Ga^+ compound, suggesting that it may not display such a strongly distorted coordination geometry.

Univalent cations that sit on a 6c site in β''-aluminas experience a distorted tetrahedral environment. For example, in Na-β''-alumina, some of the Na sit on a 6c site coordinated to three O at ~2.6 Å and one at ~2.5 Å [20]. In K-β''-alumina, the 6c cations are coordinated to three O at ~2.7 Å and one at ~2.5 Å [22]. Rb-β''-alumina is not included in this comparison as its structure was not examined in detail, but lattice constants were reported [23]. In Ga(I)-β''-alumina all of the gallium was on a 6c site coordinated to only 3 O atoms at ~2.39 Å and no other close oxygen contacts (3+0 rather than 1+3 coordination) [16]. This was attributed to the presence of a stereochemically active lone pair on the gallium. In our preferred model for In(I)- β"-alumina, the indium sits on a 18h site and is coordinated to four oxygens at 2.90, 2.64 and 2 x 2.57 Å (see Figure 10.2). This coordination geometry is different from that seen with alkali metals,

as it is effectively 3+1 rather than 1+3 coordination, and it is also different from that seen with Ga(I) where only one face of the cation was coordinated to oxygen.

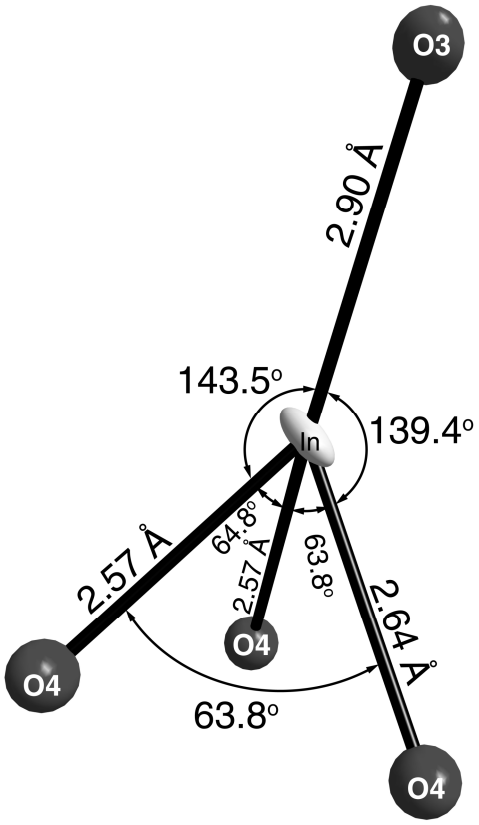

Figure 10.2: The coordination of In(I) in In(I)-β''-alumina.

Table 10.4: Selected Distances (Å) for In^{+}-β''-Alumina.

In(1)-O(3)	1 x	2.896(1)	Al(3)-O(1)	2 x	1.995(4)
In(1)-O(4)	2 x	2.574(1)	Al(3)-O(2)	1 x	1.949(7)
In(1)-O(4)	1 x	2.642(2)	Al(3)-O(3)	1 x	1.826(6)
Al(1)-O(1)	6 x	1.902(6)	Al(3)-O(4)	2 x	1.867(4)
Al(2)-O(1)	3 x	1.818(6)	Al(4)-O(4)	3 x	1.785(6)
Al(2)-O(2)	1 x	1.835(1)	Al(4)-O(5)	1 x	1.724(5)

In order to quantify the level of distortion around the cations, or alternatively the stereochemical activity of the lone pairs, we computed distortion indices, as defined by Brown [28], for In(I) and Ga(I) in all the well characterized oxides of these ions. For comparison purposes, we also examined the univalent cations in a series of alkali metal β''-aluminas. The distortion index is a vector sum of individual empirical bond strengths, S_{ij} [$S_{ij} = \exp([R_0 - r_{ij}]/B)$], where the magnitudes of these quantities are calculated according to Brown's valence sum model [29, 30]. For a regular coordination environment, this vector sum will be close to zero. A non-zero value indicates stronger coordination on one side of the cation than on the other. The bond valence parameters needed for this calculation are well known in the literature for the alkali metals, but not tabulated for In(I) and Ga(I). We used R_0= 2.20 and 2.05, for In(I) and Ga(I) respectively, as these values, when combined with B =0.37, give bond valence sums for the known In(I) and Ga(I) oxides that are close to one. We also computed a normalized distortion index (distortion index divided by the bond valence sum) to better account for any under or over bonding in the bond valence sum calculation. The results of our bond valence sum and distortion index calculations are shown in Table 10.5. With the exception of the Ga(I) and In(I)-β''-aluminas, the computed distortion indices shown in Table 10.5 are all quite close to zero. The distortion index for Ga(I) in the β''-alumina structure is large, as expected, but interestingly the distortion index for In(I) in this structure is also large, and much larger than that seen for any alkali metal β''-alumina. This suggests that the lone pair on In(I) leads to an asymmetric coordination environment for this cation in the β''-alumina structure.

Table 10.5: Results from bond valence sum and distortion index calculations for a series of In(I) and Ga(I) oxides along with comparison data for a series of alkali metal β''-aluminas.

	M^+	ΣS_{ij}	Distortion Index	Normalized Distortion Index
In(I)-β''- alumina	*In(1)*	1.19	0.672	0.564
$InZr_2P_3O_{12}$[31]	*In(1)*	0.89	0.000	0.000
$In_2P_2O_7$[12]	*In(2)*	0.99	0.176	0.177
In(I)-β-alumina[10]	*In(1)*	1.10	0.061	0.056
	In(2)	1.12	0.026	0.023
	In(3)	1.07	0.000	0.000
	In(4)	1.01	0.000	0.000
Ga-β''-alumina[16]	*Ga(1)*	1.20	0.898	0.748
$GaZr_2P_3O_{12}$[16]	*Ga(1)*	0.79	0.000	0.000
Na-β''-alumina[22]	*Na(1)*	0.58	0.172	0.297
	Na(2)	0.54	0.073	0.135
K-β''-alumina[22]	*K(1)*	1.00	0.171	0.171
	K(2)	1.03	0.108	0.105
Ag-β''-alumina[22]	*Ag(1)*	0.59	0.038	0.064

Main group metals often have highly irregular coordination environments when they have an oxidation state of 2 less than the group number. This is attributed to a stereochemically active lone pair of valence electrons occupying some space around the cation. However, the stereochemical activity of this ns^2 lone pair depends on the host structure. For example, Tl^+ shows highly irregular coordination environments in Tl_2O [32] and TlKO [33] (3+0 coordinated), but in $TlVO_3$, TlH_2PO_4 and TlS_2O_3 it sits on sites with high coordination numbers [34], with no obviously stereochemically active lone pair. This dependence on the host structure is also seen for gallium(I). In Ga(I)-β''-alumina there is a stereochemically active lone pair, but in $GaZr_2(PO_4)_3$ there are no obvious signs of stereochemical activity and the cation coordination is like that found in the alkali zirconium phosphates, with six oxygens all the same distance from the cation.

The indium(I) in In(I)-β''-alumina, is coordinated to 4 oxygen atoms in a distorted tetrahedral arrangement and appears to show some stereochemical activity (see Figure 10.2). However, the In(I) sites in In(I)-β-alumina have higher coordination numbers and show little evidence for a stereochemically active lone pair; In(I) in the tungsten bronzes In_xWO_3 and $In_2P_2O_7$ also sits on a high coordination number site with little evidence for a stereochemically active lone pair. Cation coordination around In(I) in $InZr_2(PO_4)_3$ is no different than alkali zirconium phosphates, and In(I) is coordinated with six oxygen atoms all the same same distance from the cation [31]. As pointed out by Brown, stereochemical activity, as indicated by a large distortion index, is seen when the coordinating oxygens have a high base strength leading to low coordination numbers [34].

10.4. CONCLUSIONS

Here, we have reported the preparation and the structure of In(I)-β''-alumina by ion exchange from Na-β''-alumina. In(I)-β''-alumina is stable on heating in air up to 400 ^oC. Its structure was determined by Rietveld analysis using high resolution X-ray powder diffraction data [*R-3m*, a=5.6044(1), c=34.4807(1), Z=3]. The coordination of In(I) in this material is asymmetric, as indicated by the distortion index for this cation, suggesting some stereochemical activity for the lone pair on the cation. However, the distortion is not as pronounced as that seen in the Ga(I) analogue.

10.5. REFERENCES

[1] Meyer G, Staffel T. Notiz zur Kenntnis der roten Monohalogenide des Indiums, InX (X = Cl, Br, I). Z. Anorg. Allg. Chem. 1989;574:114.

[2] Staffel T, Meyer G. The Mono-, Sequi-, and Dibromides of Indium: InBr, In_2Br_3 and $InBr_2$. Z. Anorg. Alleg. Chem. 1987;552:113.

[3] Dronskowski R. Chemical Bonding of the Binary Indium Bromides. Inorg. Chem. 1994;33:6201.

[4] Tuck DG. The Lower Oxidation States of Indium. Chemical Society Reviews 1993:269.

[5] Schmidbaur H. Arene Complexes of Univalent Gallium, Indium, and Thallium. Angewandte Chemie, International Edition in English 1985;24:893.

[6] Swanson AB, Anderson JS. Indium Tungsten Bronze. Mat. Res. Bull. 1968;3:149.

[7] Labbe P, Goreeaud M, Raveau B, Monier JC. Etude Comparative des Structures M_xWO_3 de Type Bronze Hexagonal. I. Anlyse Structurale des Bronzes de Composition $M_{0.30}WO_3$. Stereochimie des Elements M = Rb^I, Tl^I et In^I. Acta Crystallogr. 1978;B34:1433.

[8] Srivastava SK. Thin-film growth and characterization of indium-incorporated hexagonal stungsten bronze - $In_{0.4}WO_3$. J. Mater. Sci. Lett. 1994;13:832.

[9] Ekstrom T, Parmentier M, Watts KA, Tilley RJD. Tungsten Bronze Formation by the Group Iiia Metals. J. Solid State Chem. 1984;54:365.

[10] Pitt MG, Fray DJ. The Preparation and Physical Properties of Indium β-Alumina Single Crystals. J. Solid State Chem. 1982;43:227.

[11] Yao Y-FY, Kummer JT. Ion Exchange Properties of and Rates of Ionic Diffusion in Beta-Alumina. J. Inorg. Nucl. Chem. 1967;29:2453.

[12] Thauern H, Glaum R. Contributions on crystal chemistry and thermal behaviour of anhydrous phosphates. XXXIII. In2P2O7 an Indium(I)-diphosphatoindate(III), and In-4(P2O7)(3) - Synthesis, crystallization, and crystal structure. Z. Anorg. Allg. Chem. 2003;629:479.

[13] Hinchcli.Aj, Ogden JS. Matrix-Isolation Studies on Gallium-Indium-Oxygen System - Infrared-Spectra and Structures of Molecular Ga2O, in2O, and Inoga. J. Phys. Chem. 1973;77:2537.

[14] Ruscic B, Goodman GL, Berkowitz J. Photoelectron Spectra of Ga_2O, In_2O and Tl_2O. Journal of Electron Spectroscopy and Related Phenomena 1986;41:357.

[15] Lakin NM, van der Hoek G, Beattie IR, Brown JM. The identification of In_2O in the gas phase by high resolution electronic spectroscopy. J. Chem. Phys. 1997;107:4439.

[16] Wilkinson AP. Crystal Chemistry of Ga(I) in Oxides: Ga^{+}-β"-Alumina and $GaZr_2(PO_4)_3$. Inorg. Chem. 1997;36:1602.

[17] Larson AC, Von Dreele RB. GSAS - General Structure Analysis System. Los Alamos Laboratory: Report LA-UR-86-748, 1987.

[18] Toby BH. EXPGUI, a graphical user interface for GSAS. J. Appl. Crystallogr. 2001;34:210.

[19] Rietveld HM. A Profile Refinement Method for Nuclear and Magnetic Structures. J. Appl. Crystallogr. 1969;2:65.

[20] Jorgensen JD, Rotella FJ, Roth WL. Conduction Plane and Structure of Li-Stabilized Na^{+} β"-Alumina: A Powder Neutron Diffraction Study. Solid State Ionics 1981;5:143.

[21] Thomas JO, Farrington GC. Protonic Solid Electrolytes: A Single-Crystal Neutron Diffraction Study of Ammonium Hydronium β"-Alumina. Acta Crystallogr., Sect. B 1983;39:227.

[22] Brown GM, Schwinn DA, Bates JB, Brundage WE. Structures of Four Fast-Ion Conductors by Single-Crystal Neutron-Diffraction Analysis: Zn-Stabilized Naβ"-Alumina and Mg-Stabilized Na-, K-, and Agβ"-Aluminas. Solid State Ionics 1981;5:147.

[23] Masri M, Petric A. Preparation and Characterization of Rubidium Beta" Alumina. Mater. Res. Bull. 1991;26:917.

[24] Kahn A, Colomban P, Boilot JP. Silver β"-Alumina. J. Solid State Chem. 1980;33:149.

[25] Boilot JP, Collin G, Colomban P, Comes R. X-ray-scattering study of the fast-ion conductor β"-alumina. Phys. Rev. B 1980;22:5912.

[26] West AR. Solid State Chemistry and its Applications. New York: John Wiley & Sons, 1984.

[27] Farrington GC, Briant JL. Fast Ionic Transport in Solids. Science 1979;204:1371.

[28] Brown ID. What Factors Determine Cation Coordination Numbers. Acta Crystallographica Section B-Structural Science 1988;44:545.

[29] Brown ID. Predicting Bond Lengths in Inorganic Crystals. Acta Crystallographica Section B-Structural Science 1977;33:1305.

[30] Brese NE, Okeeffe M. Bond-Valence Parameters for Solids. Acta Crystallographica Section B-Structural Science 1991;47:192.

[31] Wilkinson AP. Preparation and characterization of InZr2(PO4)3 unpublished results.

[32] Sabrowsky VH. Zur Darstellung und Kristallstruktur von Tl_2O. Z. Anorg. Allg. Chem. 1971;381:266.

[33] Sabrowsky VH. Oxothallate(I) der Alkalimetalle: KTlO, RbTlO und CsTlO. Z. Anorg. Allg. Chem. 1978;438:213.

[34] Brown ID, Faggiani R. The Structure of Thallium(I) Tetraacetatothallate(III): When is the Lone Pair of Electrons on Tl(I) Stereoactive. Acta Crystallogr., Sect. B 1980;36:1802.

CHAPTER 11

CONCLUDING REMARKS

Thermal expansion is a crucially important property of materials and understanding and controlling the thermal expansion of materials is needed for a wide variety of applications, like cookware for oven to freezer use, electronic devices, dental applications, zero-expansion heat sinks, engine components, spark plugs, catalyst supports, high performance optical mirror substrates, etc.

This thesis focused on oxide negative thermal expansion (NTE) materials that can be classified as framework materials. Framework materials feature low density three-dimensional networks of relatively rigid polyhedral units that share corners with each other. The mechanism, which can be considered the most applicable one in framework oxides exhibiting negative thermal expansion, is based on the transverse thermal motion of oxygen in M-O-M linkages (M = metal). The study of these linkages and rotations of the polyhedral network should be examined when trying to understand negative thermal expansion. Understanding the origin of expansion and contraction helps design controlled thermal expansion materials. That was one of the major incentives for us to undertake structural analysis of NTE materials at various temperatures. In addition to temperature, the effect of pressure is a very important factor. The use of NTE materials in composites may facilitate control of thermal expansion and, in principle, allows the design of materials with a specific expansion coefficient anywhere between the values of the pure composite end members. That is the reason for considerable interest in materials exhibiting NTE [1-7]. However, at some stage in the manufacture and use of composite

materials, pressures above ambient may be encountered leading to phase transitions and a loss of NTE behavior [8, 9]. The phase transition to an orthorhombic phase at 0.2 GPa is the main reason hindering the use of cubic ZrW_2O_8 in composites. For these reasons, high pressure studies of NTE materials are of some importance from a practical standpoint as well as being of fundamental interest. The existence of phase transitions (phase transition might be crystalline-to-crystalline or crystalline-to-amorphous), the transition pressure, the crystal structures of the new phases and the structural compression mechanisms are things to be investigated. The pressure might also affect the coefficient of thermal expansion before any phase transitions.

The $Sc_2W_3O_{12}$ family is an important class of framework oxides that exhibit negative thermal expansion. This structural family is amenable to a wide range of substitutions beyond the simple replacement of Sc^{3+} with other trivalent ions. Materials such as $A_2(MO_4)(PO_4)_2$ (A = Zr or Hf, M = W or Mo) exhibit negative thermal expansion and have attracted attention as components suitable for use in controlled thermal expansion composites [10-12]. The effect of these complex substitutions on the high pressure behavior of the $Sc_2W_3O_{12}$-type structure has not been investigated before. Thus, we decided to conduct high-pressure *in-situ* powder diffraction studies of $Zr_2WO_4(PO_4)_2$, $Zr_2MoO_4(PO_4)_2$, $Hf_2WO_4(PO_4)_2$, and $Sc_2W_3O_{12}$ in order to investigate the effects of pressure on their coefficients of thermal expansion, the existence of phase transitions, their phase transition pressures and any structural changes occurring upon phase transitions. $Sc_2W_3O_{12}$ had already been studied under pressure along with similar compounds as discussed in chapter 8. Our only aim in studying $Sc_2W_3O_{12}$ was to structurally characterize the second high pressure phase. $Zr_2WO_4(PO_4)_2$, $Zr_2MoO_4(PO_4)_2$

and $Hf_2WO_4(PO_4)_2$ were studied under pressure for the first time and we also wanted to examine the effects of cation substitutions on the high pressure behavior of materials in the $Sc_2W_3O_{12}$ structural family. High quality powder diffraction data confirmed that the compounds, $Zr_2WO_4(PO_4)_2$, $Zr_2MoO_4(PO_4)_2$ and $Hf_2WO_4(PO_4)_2$, adopt the orthorhombic (Pnca) $Sc_2W_3O_{12}$ structure under ambient conditions. The behavior of $Zr_2WO_4(PO_4)_2$, $Zr_2MoO_4(PO_4)_2$ and $Hf_2WO_4(PO_4)_2$ on compression is different from that previously observed for other orthorhombic $A_2M_3O_{12}$ phases such as $Sc_2W_3O_{12}$, $Sc_2Mo_3O_{12}$ and $Al_2W_3O_{12}$. A summary of the high pressure behavior of these compounds is presented in Table 11.1. Most of the compounds show several phase transition under pressure. The initial negative thermal expansion orthorhombic structure (Pnca) for $Zr_2WO_4(PO_4)_2$, $Zr_2MoO_4(PO_4)_2$ and $Hf_2WO_4(PO_4)_2$ persists to a much higher pressure when compared to the scandium and aluminum phases. Negative thermal expansion characteristics for these compounds are comparable to $Sc_2W_3O_{12}$, but having a first phase transition at much higher pressures is a significant advantage from an applications perspective. Also, these change in chemical composition may lead to lower materials costs. On compressing the scandium and aluminum phases, they transform to the same monoclinic structure (Pnca $\rightarrow$ $P2_1/a$) that occurs on cooling $Al_2W_3O_{12}$, or $Sc_2Mo_3O_{12}$ [13]. This monoclinic structure has twice as many formula units per primitive unit cell as the original Pnca phase. However, the first monoclinic structure formed on compressing $Zr_2P_2WO_{12}$ and $Zr_2MoO_4(PO_4)_2$ (Pnca $\rightarrow$ $P2_1/n$) appears to have almost the same unit cell volume as the starting orthorhombic phase. The compounds $Zr_2WO_4(PO_4)_2$, $Zr_2MoO_4(PO_4)_2$ and $Hf_2WO_4(PO_4)_2$ have bulk moduli that are slightly greater than that for the scandium containing phases but similar to that for aluminum tungstate. In chapter 5, we have

examined the pressure dependence of CTE for $Zr_2WO_4(PO_4)_2$, and found out that pressure had little effect on its thermal expansion. This is one of the pioneering studies in this area.

The first two chapters of this thesis were devoted to TaO_2F which adopts the ReO_3-type cubic structure. Even though TaO_2F does not display NTE (it exhibits very low thermal expansion from 20 to 400 K [14]), its structure possesses characteristics typical of frameworks that show negative thermal expansion. There have been no prior high pressure studies of this compound and we wanted to investigate the effect of pressure on the coefficients of thermal expansion, existence of phase transitions, and structural changes occurring upon phase transitions. Our studies under pressure revealed a rather complicated high pressure behavior for this deceivingly simple looking compound, as documented in chapter 2. In chapter 3, variable-temperature high-pressure neutron powder diffraction measurements were undertaken to investigate the pressure dependence of thermal expansion in TaO_2F. The neutron diffraction measurements at variable temperature (300 to 60 K) and high pressure (up to 0.3 GPa) indicated that pressure had a significant effect on the linear coefficient of thermal expansion (from 0.1 10^{-6} K^{-1} at 0 GPa to 8.4 10^{-6} K^{-1} at 0.3 GPa) of TaO_2F. Rietveld analysis of the data revealed an unexpected temperature and pressure dependence for the transverse displacement parameters of the O/F atoms, indicating that the local structure might not be the ideal ReO_3 type with 180^o angles. In light of these observations, total scattering experiments were conducted to directly probe the local structure of this material.

Table 11.1: High pressure behavior of some $A_2M_3O_{12}$ compounds. Ko and P_T denotes bulk modulus and phase transition pressure, respectively.

		$Sc_2W_3O_{12}$	***$Sc_2Mo_3O_{12}$***	***$Al_2W_3O_{12}$***	***$Zr_2WP_2O_{12}$***	***$Zr_2MoP_2O_{12}$***	***$Hf_2WP_2O_{12}$***
phase 1		Pnca	Pnca	Pnca	**Pnca**	**Pnca**	**Pnca**
	Ko (GPa)	31(3)[15]	32(2)[16]; 6[17]	48[16]	**49(2)**	**45(4)**	**54(1)**
	P_T (GPa)	0.3[15]; 0.6[18]	0.29[19] 0.25-0.6[16]	0.1[16]; 0.28[20] 0.5[21]	**1.4; 1.2**	**1.2-1.5**	**1.8**
phase 2-A		$P2_1/a$	$P2_1/a$	$P2_1/a$			
	Ko (GPa)	14(1)[15]	16(1)[16]	28(1)[16]			
	P_T (GPa)	2.8[15] ; 1.6[18]	2.5 - 3[16] ; 2.7[19]				
phase 2-B					**$P2_1/n$**	**$P2_1/n$**	
	Ko (GPa)				**17(1)**	**20(2)**	
	P_T (GPa)				**3.4**	**3.3**	
phase 3		**$P2_1/n$**	Unidentified	N/A	**$P2_1/n$**		
	Ko (GPa)	**90(3)**			**36(4)**		
	P_T (GPa)	**2.7**			**6.3**		
phase 4					**P1 or P-1**		
	Ko (GPa)				**76(7)**		
	P_T (GPa)						

11.1. REFERENCES

[1] Sleight AW. Thermal Contraction. Endeavour 1995;19:64.

[2] Sleight AW. Compounds that Contract on Heating. Inorg. Chem. 1998;37:2854.

[3] Sleight AW. Isotropic Negative Thermal Expansion. Annual Review of Materials Science 1998;28:29.

[4] Sleight AW. Negative thermal expansion materials. Current Opinion in Solid State and Materials Science 1998;3:128.

[5] Evans JSO, Mary TA, Sleight AW. Negative thermal expansion materials. Physcia B 1998;241-243:311.

[6] Evans JSO. Negative Thermal Expansion Materials. J. Chem. Soc. Dalton Trans. 1999:3317.

[7] Evans JSO, Mary TA, Sleight AW. Negative Thermal Expansion in a Large Molybdate and Tungstate Family. J. Solid State Chem. 1997;133:580.

[8] Holzer H, Dunand DC. Phase transformation and thermal expansion of Cu/ZrW_2O_8 metal matrix composites. J. Mater. Res. 1999;14:780.

[9] Yilmaz S. Phase transformations in thermally cycled Cu/ZrW_2O_8 composites investogated by synchrotron x-ray diffraction. J. Phys. Condens. Matter. 2002;14:365.

[10] Sleight AW, Thundathil MA, Evans JSO. Materials with Low or Negative Thermal Expansion. United States Patent, 1999.

[11] Merkel GA. Negative Thermal Expansion Materials Including Method of Preparation and Uses Therefor. European Patent, 2001.

[12] Agostini G, Corvasce FG. Tire with Low Thermal Expansion Component. United States Patent, 2008.

[13] Evans JSO, Mary TA. Structural Phase Transitions and negative thermal expansion in $Sc_2(MoO_4)_3$. International Journal of Inorganic Materials 2000;2:143.

[14] Tao JZ, Sleight AW. Very low thermal expansion in TaO_2F. J. Solid State Chem. 2003;173:45.

[15] Varga T, Wilkinson AP, Lind C, Bassett WA, Zha C-S. In-situ high pressure synchrotron x-ray diffraction study of $Sc_2W_3O_{12}$ at up to 10 GPa. Phys. Rev. B 2005;71:214106.

[16] Varga T, Wilkinson AP, Lind C, Bassett WA, Zha C-S. High pressure synchrotron x-ray powder diffraction study of $Sc_2Mo_3O_{12}$ and $Al_2W_3O_{12}$ J. Phys.: Condens. Matter 2005;17:4271.

[17] Arora AK, Yagi T, Miyajima N, Mary TA. Amorphization and decomposition of scandium molybdate at high pressure. J. Appl. Phys. 2005;97:013508.

[18] Garg N, Murli C, Tyagi AK, Sharma SM. Phase transitions in $Sc_2(WO_4)_3$ under high pressure. Phys. Rev. B 2005;72.

[19] Paraguassu W, Maczka M, Souza Filho AG, Freire PTC, Mendes Filho J, Melo FEA, Macalik L, Gerward L, Staun Olsen J, Waskowska A, Hanuza J. Pressure-induced structural transformations in the molybdate $Sc_2(MoO_4)_3$. Phys. Rev. B 2004;69:094111.

[20] Maczka M, Paraguassu W, Souza Filho AG, Freire PTC, Mendes Filho J, Melo FEA, Hanuza J. High-pressure Raman study of $Al_2(WO_4)_3$. J. Solid State Chem. 2004;177:2002.

[21] Mukherjee GD, Vijaykumar V, Achary SN, Tyagi AK, Godwal BK. Phase transitions in $Al_2(WO_4)_3$: high pressure investigations of low frequency dielectric constant and crystal structure. J. Phys.: Condens. Matter 2004;16:7321.